University of Sussex

Towards high fidelity entanglement with dressed state qubits

Kimberley Lake

Submitted for the degree of Doctor of Philosophy

University of Sussex

April 2014

Declaration

I hereby declare that this thesis has not been and will not be, submitted in whole or in part to another University for the award of any other degree.

Signature: Kimberley Lake

UNIVERSITY OF SUSSEX

Kimberley Lake, Doctor of Philosophy

Towards high fidelity entanglement with dressed state qubits

To my lovely family

ABSTRACT

This thesis describes the development of an entanglement experiment for ytterbium ions making use of a new entanglement method utilizing microwaves and a static magnetic field gradient.

This thesis will begin by modelling the populations of the main levels in ytterbium using rate equations to find the optimum parameters required for the preparation and detection of qubit states. Coherent manipulation of these qubit states will be shown and coherence times of the states measured. Additionally a highly stable double resonance frequency locking setup for the ytterbium cooling lasers is built.

This thesis will go on to give an overview of the main entanglement schemes and will give a justification as to why microwaves combined with a magnetic field gradient is the most suitable method. The magnetic field gradient creates an effective Lamb-Dicke parameter which allows microwave fields to couple to the motional states of magnetic field sensitive qubit states.

The use of magnetic field sensitive states can however make the qubit highly susceptible to decoherence from magnetic field fluctuations. A method to decrease this decoherence by two orders of magnitude using a microwave dressed state qubit will be demonstrated and optimised and a new coherent manipulation method of the dressed state qubit will be presented which allows for arbitrary Bloch sphere rotations.

The production of the highest recorded magnetic field gradient of $24\,\mathrm{Tm}^{-1}$ at the position of the trapped ion using in-vacuum permanent magnets is shown and used to provide individual addressing of ions. Static gradient microwave entanglement of a single ion's internal and motional states within the bare qubit states is then demonstrated (Schrodinger cat states).

Furthermore, the first ever observation of motional coupling of the microwave dressed state qubit is shown and progress towards a two ion entanglement gate with microwave dressed state qubits is reported.

Acknowledgments

The last few years have been amazing and could not have been possible without the network of lovely people ive had around me.

Firstly id like to thank my supervisor Dr. Winfried Hensinger for giving me the opportunity to work on such an interesting and exciting experiment. Hes taught me so much in my time here and has always supported and helped me when needed.

A large thankyou goes to all my fellow phd students and postdocs who ive been working with in the lab. To the guys who started the lab, Dr. James McLoughlin, Dr. James Siverns, Dr. Robin Sterling and Dr. Altaf Nizamani for teaching me the workings of the lab and always being around to offer help, support, tea and answers to my stupid questions.To Dr. Sebastian Weidt, who ive worked with for the majority of my Phd. Seb has always applied an amazing dedication and enthusiasm to all projects throughout the good times and the bad which has always inspired me. Hes been a constant source of support, advice, humor and friendship and the last few years wouldn't have been the same without him ☺. To Eamon Standing, for teaching me how to enjoy the nightshift and whose amazing friendship kept me sane and happy in my final year especially whilst I was writing up 👉. To Dr. Simon Webster, for being a lovely postdoc and always been there to help when needed and finally, to Joe Randell, I couldn't think of anyone better to entrust the experiments future. Good luck.

Then of course there's all the people in the lab who ive never had a chance to directly work with but have always provided a nice distractionas well as many interesting conversations and nights out. Namely, Dr. Bjoern Lekic, Dr. Marcus Hughes, Darren De motte, David Murgia, Dr. Gouri Giri and Tomas Navickas.

Of course, there is life outside the lab[1] and I want to thank all my family and non Sussex friends for their support and for sticking by me over the last few years especially during the bad times when I was grumpy, uncontactable and generally not a fun person. The following people in particular deserve special mention.

Janette Mitten (mum), for always supporting and being there for me, for taking me out to lunch every week and providing a lovely platform for gossip, advice, support and the occasional shoulder to cry on and then of course to Lee Mitten for making mum so

[1] Shocking!!!

happy. Richard Lake (dad), Kate Lake and Sophie (ie. Charcott), these guys have been amazing and have been a source of constant support, advice, tea and bacon as well as providing me with a quiet place to write. To Martin Lake, Hayley Lake and Rebecca Lake for being such lovely siblings. To my wonderful Oxford friends, in particular Steven Angus and Emily Anstis for always being available to listen to my occasional rants and to my flatmate Joanna Savage and her boyfriend Steve Chalk for putting up with my grumpiness and general disorder especially over the last few months.

Detailed Acknowledgments

This thesis contains work which was performed as part of a team of people. The people involved with each experiment are outlined below.

Chapter 2

The trapping setup was designed and built in the years before I started in the lab by Dr James McLoughin, Dr James Siverns, Dr Robin Sterling, Dr Altaf Nizamani and Dr Marcus Hughes.

Chapter 3

The experimental quantum manipulation data was taken and analysed by myself and Dr. Sebastian Weidt with assistance from Dr. James McLoughin and Dr Simon Webster.

Chapter 4

The locking setup was built by myself with assistance from Dr Robin Sterling.

Chapter 6

The dressed state manipulation and optimisation data was taken and analysed by myself, Dr Sebastian Weidt and Dr Simon Webster with assistance early on from Dr James McLoughin. Dr Simon Webster developed the theory behind the new dressed-state manipulation method.

Chapter 7

The data shown within this chapter was taken and analysed by myself, Dr Sebastian Weidt, Dr Simon Webster, Joesph Randell and Eamon Standing. The magnet setup was

designed and simulated by Joesph Randell and Dr Sebastian Weidt.

Publications

Generation of spin-motion entanglement in a trapped ion using long-wavelength radiation

K. Lake, S. Weidt, J. Randall, E. Standing, S. C. Webster and W. K. Hensinger

Phys. Rev. A. 91, 012319 (2015)

Efficient preparation and detection of microwave dressed-state qubits and qutrits with trapped ions

J. Randall, S. Weidt, E. Standing, K. Lake, S. C. Webster, D. Murgia, T. Navickas, K. Roth and W. K. Hensinger

Phys. Rev. A. 91, 012322 (2015)

Fabrication and operation of a two-dimensional ion-trap lattice on a high-voltage microchip

R. C. Sterling, H. Rattanasonti, S. Weidt, K. Lake, P. Srinivasan, S. C. Webster, M. Kraft and W. K. Hensinger

Nature Commununications 5:3637 (2014)

Simple Manipulation of a Microwave Dressed-State Ion Qubit

S. C. Webster, S. Weidt, K. Lake, J. J. McLoughlin and W. K. Hensinger

Phys. Rev. Lett. 111, 140501 (2013)

Optimisation of two-dimensional ion trap arrays for quantum simulation

James D. Siverns, Seb Weidt, Kim Lake, Bjoern Lekitsch, Marcus D. Hughes, and Winfried K. Hensinger

New J. Phys. 14, 085009 (2012)

Contents

List of Tables

List of Figures

Chapter 1

Introduction

Since the invention of the ion trap in the late 1950's by Wolfgang Paul and Hans Dehmelt [5,6], trapped ions have been used in a variety of fields including atomic clocks [7–9], electrodynamics [10] and spectroscopy [11]. Arguably however, one of the largest contributions ion traps have made is to the field of quantum computing.

Quantum computing was first proposed by Feynman and Deutsch in the 1980's and uses a unit of information known as the qubit to encode information [12,13]. In contrast to the bit used within a classical computer which encodes information onto the 0 or 1 states, qubits can also exist in superposition states of 0 and 1. A three qubit system, for example, can therefore exist in eight states simultaneously, namely $|000\rangle$, $|001\rangle$, $|010\rangle$, $|011\rangle$, $|100\rangle$, $|101\rangle$, $|110\rangle$ and $|111\rangle$. The probabilities with which the system, upon measurement, will collapse into each state are used to hold information within the quantum computer. The amount of information within a system of qubits therefore increases exponentially as 2^N where N is the number of qubits. This is in contrast to a classical system of bits where the amount of information increases linearly with N. Using quantum interference and a quantum property known as entanglement, whereby the states of separate qubits become correlated, parallel quantum computing becomes possible [13] whereby a function acts simultaneously on all 2^N states. This is the basis for many quantum algorithms including Shor's algorithm [14] with which large numbers can be factorised. This will have significant applications within both cryptography and codebreaking. Other important quantum algorithms include Grover's search algorithm [15] which allows entries to be quickly found within large unordered lists and the Deutsch-Jozsa algorithm [16].

In 1995, David DiVincenzo from IBM introduced five requirements for the physical implementation of quantum computing [17]. These became known as the DiVincenzo criteria and are as follows,

1. **A scalable physical system with well defined qubits.**

2. **The ability to initialize the state of the qubits to a simple fiducial state:** Before any operations are preformed using the quantum computer, a method is needed to faithfully put the qubits in the preferred initial qubit states.

3. **A "universal" set of quantum gates:** The evolution of the qubits state within a quantum computer is controlled by the application of quantum gates. It has been shown that a universal set of quantum gates exists with which any quantum algorithm can be performed [18]. This set comprises of single qubit rotational gates and two qubit CNOT gate.

4. **Long relevant decoherence times, much longer than the gate operation time:** Decoherence results in a loss of information from the quantum computer. The time taken for this to take effect therefore needs to be a lot longer than time it takes to preform gate operations.

5. **A qubit specific measurement capability:** To gain the final result from the quantum computer, a method is needed to faithfully measure the final qubit states.

Many physical systems which show quantum behavior are currently being explored for their ability to satisfy these requirements, for example, superconducting Josephson junctions [19], photons [20], trapped ions [21] and neutral atoms confined within optical lattices [22]. Trapped ions will be the focus of this thesis and have already been proven to satisfy all five criterion [23–27]. The next step is to bring the quantum gate operations within fault tolerant levels [28] which would allow for successful error correction [29, 30] needed for the creation of a large scale quantum computer. This can be performed, for example, by reducing decoherence sources.

Trapped ion qubits normally fall into one of two categories, optical or hyperfine [31], optical qubits consist of a ground level and a metastable excited level [32] whereas hyperfine qubits consist of two hyperfine sublevels of the ions ground level [33]. This thesis focuses on the hyperfine qubit of $^{171}Yb^{+}$ and begins in chapter 2 by showing how ytterbium ions are trapped, cooled and observed within a linear Paul trap.

Chapter 3 then goes on to show how the $|0\rangle$ and $|1\rangle$ qubit states of a $^{171}Yb^{+}$ ion can be initialised by optical pumping and detected. Rate equations will then be used to find the optimum experimental parameters for both these processes. The Bloch equations are then derived which describe the evolution of quantum states within trapped ion qubits and coherent manipulation of the $^{171}Yb^{+}$ qubit will then be shown.

The fidelity of state preparation and detection can be affected by fluctuations in the frequency of the main cooling laser. This is explored in chapter 4 which goes on to describe an experimental setup used to stabilise this lasers frequency.

Chapter 5 reviews and compares the main methods of producing a two qubit entanglement gate which the lab could pursue, concluding that the most suitable method will be to use a magnetic field gradient to create an effective Lamb-Dicke parameter allowing microwave radiation to couple to the motional states of magnetic field sensitive levels [34]. This eliminates the need for Raman beams which can give rise to large amounts of decoherence from spontaneous emission and laser noise. This method does however require the use of magnetic field sensitive Zeeman levels which makes the qubit susceptible to decoherence from environmental magnetic field fluctuations. Chapter 6 will present a method of shielding the ion from these fluctuations using microwave dressed states thereby increasing the qubit coherence time by two orders of magnitude. This method will be characterized and a new coherent manipulation method allowing for arbitrary Bloch sphere rotations of the dressed state qubit will be presented.

Chapter 7 will then show the experimental progress towards the entanglement of two $^{171}Yb^{+}$ dressed state qubits within a magnetic field gradient. Firstly, the creation of a magnetic field gradient of $24\,\mathrm{Tm}^{-1}$ using in vacuum permanent magnets will be shown and used to provide individual addressing of adjacent ions. The entanglement of a single ion's motional and internal states will then be presented as well as the motional coupling of a dressed state qubit. Finally, the planned experimental method for the entanglement of two dressed state qubits is presented and explained.

Chapter 2

Trapping ytterbium ions

In order to trap and hold ytterbium ions, five main components are required.

- **A potential well**: This traps the ions and determines the position in space at which they are held. This is produced using a combination of RF and DC voltages, which are applied to several electrodes as explained in section 2.1.
- **A vacuum**: The finite depth of the potential well means that collisions with other particles can knock the ion out of the trap. In addition, unwanted collisions can perturb the system and cause decoherence of the ions' qubit states. An ultra high vacuum is therefore needed around the trap to maximise the lifetime and the coherence time of the trapped ions. The system used to produce and maintain this is described in section 2.2.
- **Ions**: Ytterbium ions are produced from neutral ytterbium using a two photon photoionisation process as described in section 2.3.
- **Lasers**: Once trapped, the ions need to be laser cooled to prevent them gaining enough kinetic energy to escape the trapping potential. The lasers and optical setup used to cool ytterbium is described in section 2.3.3.
- **An imaging system**: This allows the ions to be seen and is described in section 2.4.

This chapter will explain how the above requirements are achieved in greater detail.

2.1 RF Paul traps

As charged particles, ions can be easily manipulated and moved using electric fields. However, trapping using electric fields is more problematic due to a property of electrostatics

known as Earnshaw's theorem [35] which is described by Laplace's equation,

$$\nabla^2\phi(x,y,x) = 0 \tag{2.1}$$

Where $\phi(x,y,z)$ is the three dimensional electric field potential. This is analogous to Gauss law, $\nabla \cdot E = 0$, which states that electric field minima cannot exist in free space. A potential well for trapping ions cannot therefore be formed using static electric fields in three dimensions. If for example, a static voltage is applied to two opposite electrodes, a saddle point potential would be formed as shown in figure 2.1. An ion would simply roll off this potential and be lost to the trap.

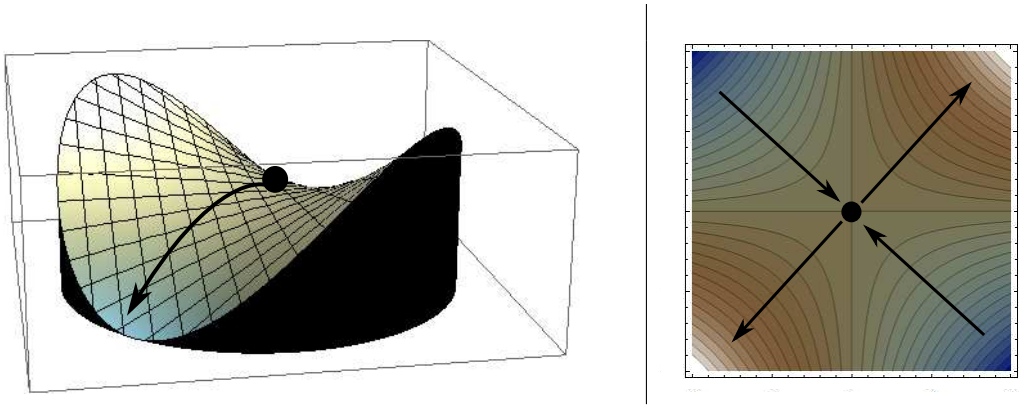

Figure 2.1: Saddle potential formed when two static voltages are applied to opposite electrodes. An ion within such a potential will be expelled outwards.

This applies however only to static fields and it is well known that a potential well can be formed using a radio frequency (RF) field. This periodically inverts the saddle potential which keeps the ion in place forming an effective potential well. The electrode structure used to accomplish this is covered in the following section. The movement of the ion within the well is covered in section 2.1.2.

2.1.1 Trap structure

For all the experiments described within this thesis, an electrode configuration known as a segmented linear Paul trap is used. This consists of two opposite RF electrodes and two opposite segmented DC electrodes, as shown in figure 2.2. The ion is held in place radially using the centre DC electrodes combined with the RF electrodes. This gives the following potential in the x-y plane [36],

$$\phi(x,y) = \kappa_0 \frac{V_{dc} - V_{RF}\cos(\Omega_{RF}t)}{2r_0^2}(x^2 - y^2) \tag{2.2}$$

where $V_{RF}\cos(\Omega_{RF}t)$ is the time dependent voltage applied to the RF electrodes, V_{dc} is the voltage applied to the DC electrodes, r_0 is the ion-electrode distance and κ_0 is a geometric factor. As I will discuss in section 2.1.2, this potential can trap the ion in the x-y plane. The ion is trapped in the z axis using static voltages applied to the endcap DC electrodes.

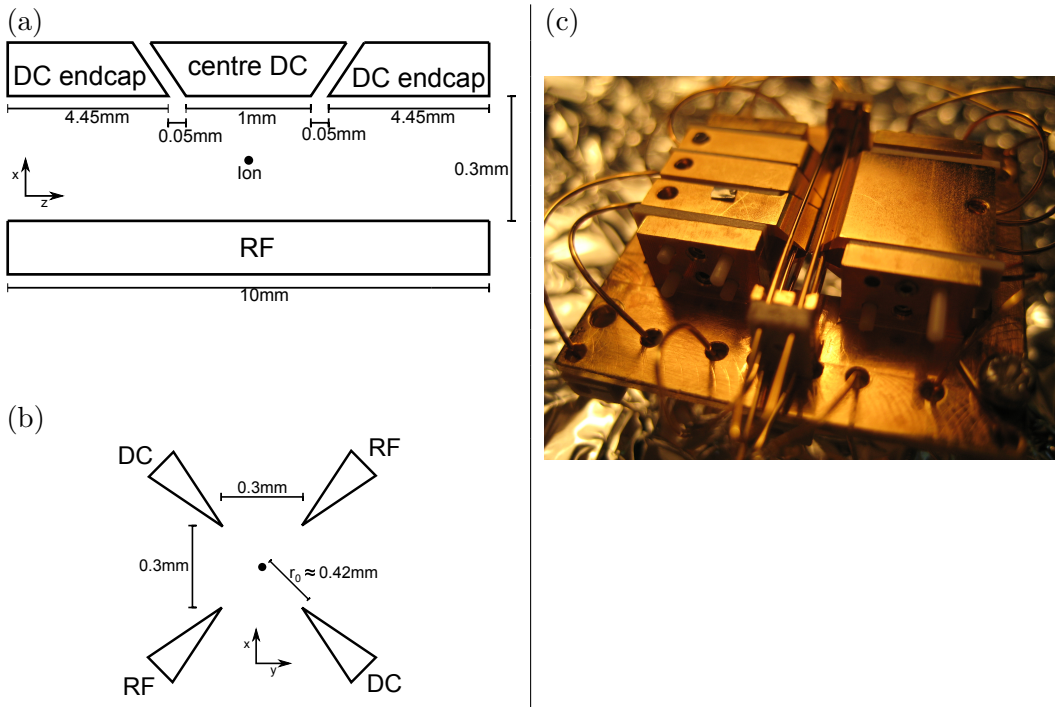

Figure 2.2: RF paul trap used for the experiments within this thesis. (a) and (b) show schematics and dimensions of the trap as observed perpendicular to and along the trap axis respectively. (c) shows a photograph of the constructed trap.

The electrodes at made out of gold-plated stainless steel and are held together using a stainless steel cage. PEEK spacers are used to separate the individual electrodes from each other and the cage to prevent electrical shorting. A photograph of the trap is shown in figure 2.2 (c).

2.1.2 Ion movement

The motion of an ion within the potential given by equation 2.2 in the x-y plane can be described using the Mathieu equations of motion. These are derived in [37] and repeated here,

$$\ddot{\mathbf{x}} + (a + 2q\cos(2\Omega_{RF}t))\mathbf{x} = 0 \tag{2.3}$$

and

$$\ddot{\mathbf{y}} - (a + 2q\cos(2\Omega_{RF}t))\mathbf{y} = 0 \tag{2.4}$$

where a and q are the stability parameters and are defined as,

$$a = \frac{4eV_{dc}}{mr_0^2 f_{RF}^2}, \qquad q = \frac{2eV_{RF}}{mr_0^2 f_{RF}^2} \tag{2.5}$$

where m is the ion mass and e is the electronic charge. A stable solution to the Mathieu equations is one in which the ion remains within the trapping potential. Figure 2.3 shows the values of the a and q parameters which will result in the ion remaining stable in the x axis (red) and the y axis (blue) of the trapping potential. The purple areas correspond

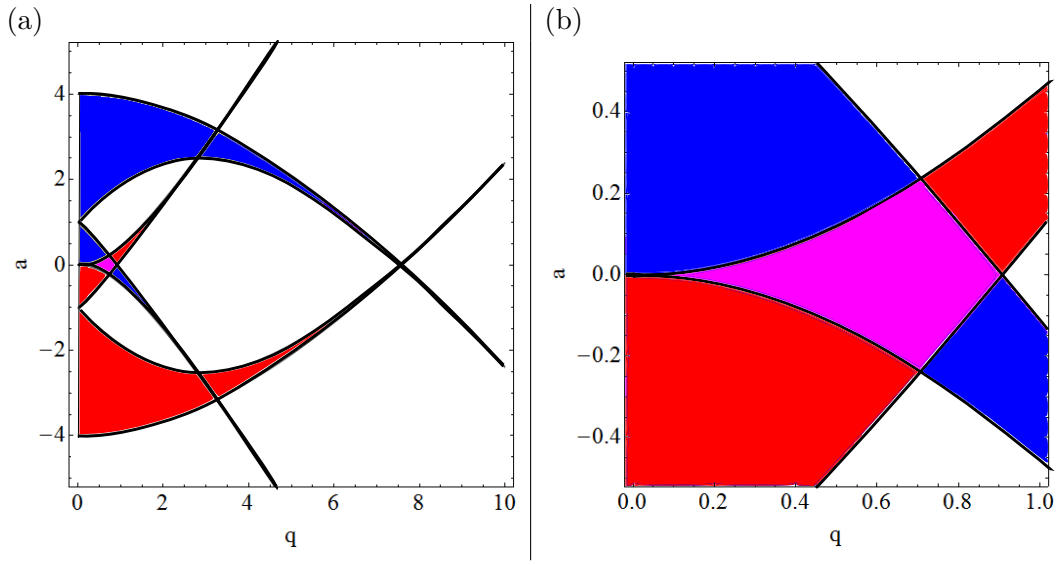

Figure 2.3: (a) Graph showing the stable regions of ion motion as a function of the a and q parameters. The red and blue regions correspond to stability in the respective x and y directions given by equations 2.3 and 2.4. The purple regions correspond to stability in both the x and y directions. (b) is a zoomed in image of the main stability region.

to a and q parameter values which provide ion stability in both the x and the y axis. By ensuring the trap operates within this region, the ions will be trapped in the x-y plane.

The main ion stability region is present at q values of less than approximately 0.9 and a values of between -0.2 and approximately 0.2. Using equation 2.5, the voltages and frequency required for stable trapping can be determined. Within this stable trapping region, the solutions to equations 2.3 and 2.4 can be found using the Floquet theorem [38]. For the example case where a is equal to 0 and q is less than 1, the solution to equation 2.3 giving the ion motion in the x-axis is given by [1],

$$\mathbf{x}(t) = A\cos(\omega t)\left(1 + \frac{q}{2}\cos(\Omega_{RF} t)\right) \tag{2.6}$$

where A is a constant which depends on the initial conditions and ω is a constant known

as the secular frequency given by

$$\omega = \frac{q\Omega_{RF}}{2\sqrt{2}} = \frac{eV_{RF}}{\sqrt{2}mr_0^2\Omega_{RF}}. \tag{2.7}$$

The motion described by equation 2.6 is plotted in figure 2.4 (a) for a q parameter equal to 0.2. As shown in figure 2.4 (a), this motion consists of a large slow oscillation at the secular frequency around the center of the RF trapping potential combined with a small fast oscillation at the RF frequency, Ω_{RF} know as micromotion. The amplitude of the micromotion is proportional to the ions' distance from the center of the RF trapping potential (known as the trap axis).

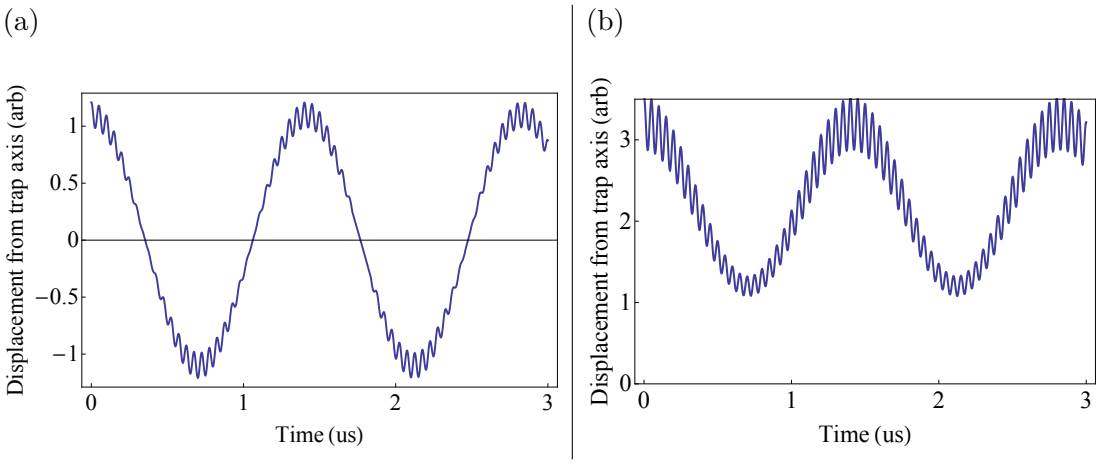

Figure 2.4: Graphs showing ion motion with a q parameter of 0.2 and a Ω_{RF} equal to $2\pi \times 20\,\text{MHz}$. (a) represents the ideal case where there is no excess micromotion present, (b) shows the excess micromotion observed when the ion is offset from the RF trapping axis.

Excess micromotion

In the above analysis there were no static electric fields within the radial directions therefore the ion motion coincided with the null of the RF trapping potential. Any additional DC fields can move the center of the ions motion from this null causing excess micromotion of a high amplitude as shown in figure 2.4 (b). Such fields can be produced, for example, by charge build up on dielectric surfaces, or, contamination or misalignment of the trap electrodes. This excess micromotion is unwanted as it can cause an increase in ion temperature, broaden the ions' transition frequencies as a result of the Doppler effect (see section 2.3.3) and reduce the ions' lifetime [39], therefore this motion needs to be minimised. Excess micromotion can be eliminated by applying compensation voltages to the DC electrodes to push the center of ion motion back to the RF nul. The exact procedure

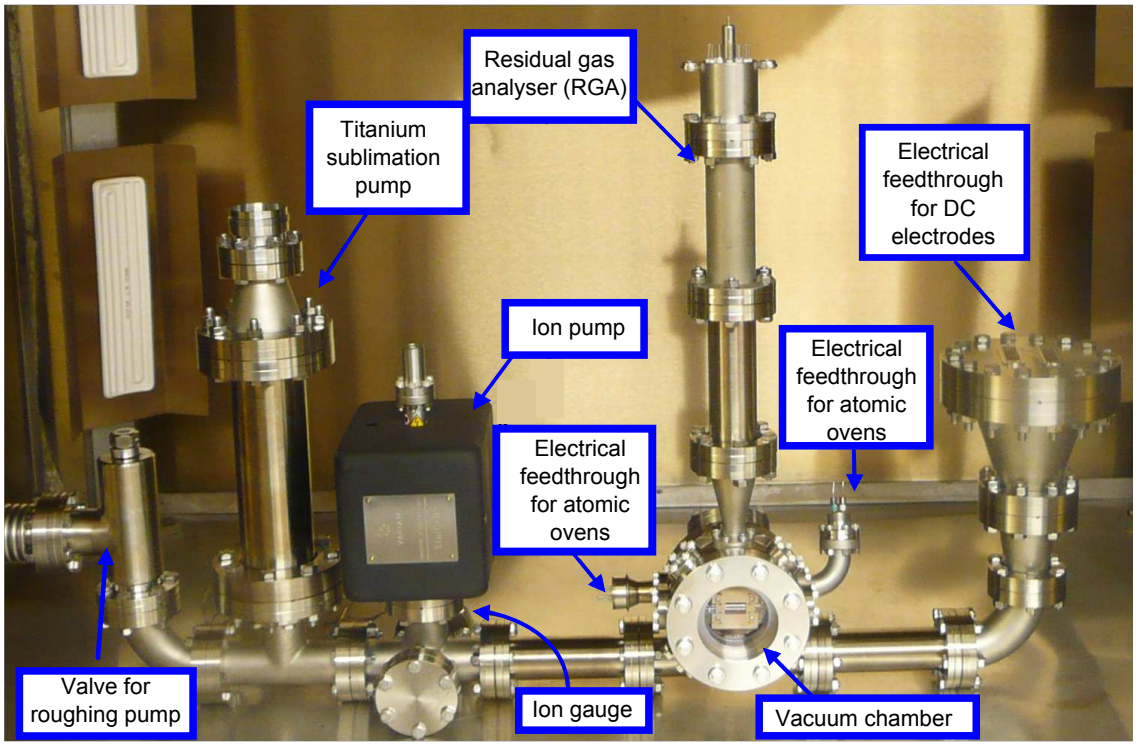

Figure 2.5: Labeled diagram showing the main components of the vacuum system used to produce and maintain the ultra high vacuum required for ion trapping

for measuring and compensating for micromotion within the experiment is based on [39] and described within [40].

2.2 UHV system

The trap needs to be situated inside a ultra high vacuum to minimises the probability of trapped ions experiencing collisions which could result in decoherence or ion loss. The system used to produce and maintain this vacuum is shown in figure 2.5 and consists of the following:

- **Electrical feedthroughs**: These allow voltages to be applied to the atomic ovens and the DC and RF electrodes from outside the system.
- **Ion gauge**[1]: This measures the system's pressure.
- **Residual gas analyser (RGA)**[2]: This measures the mass of any molecules present within the system. This is primarily used to locate leaks by passing a stream of helium molecules over each joint on the system. When helium is passed over a leak the RGA will show a peak at $4\,m_p$.

[1] Varian: 9715015
[2] ExTorr: XT200M

- **Titanium sublimation pump**[3]: When activated, this deposits a layer of titanium on the inside of the vacuum system. This reacts with any atoms or molecules within the system forming a solid layer which sticks to the surface of the inside of the system thereby reducing the vacuum pressure.

- **Ion pump**[4]: This maintains the vacuum pressure.

This system is baked at 200 degrees for two weeks using the procedure described in [37] resulting in a vacuum pressure of approximately 2×10^{-11} Torr. The trap is situated within the vacuum chamber as described in the following section.

2.2.1 Vacuum chamber

The vacuum chamber consists of an octogon[5] and a hemisphere[6]. There is a large three inch viewport on the front[7] coated for transmission of 369 nm light for imaging and several viewports at the sides for laser access. Figure 2.6 shows the inside of the chamber with the octogon removed, from (a) the front where the trap would be positioned and (b) the back. A custom PEEK chip bracket attached to the hemisphere holds the trap (not shown) in place and connects to the electrodes via gold coated pin receptacles[8] to insulated Kapton wires. These are connected to the electrical feedthroughs. Atomic ovens are located both behind and below the trap to accommodate different trap designs. For the experiments in this thesis we will use one of the ovens situated behind the trap.

2.3 Ytterbium

Ytterbium is a rare earth metal with an atomic number of 70 and seven stable isotopes. In this thesis we will only be concerned with two of these isotopes which have atomic mass numbers equal to 171 and 174. These have abundances within natural ytterbium of 14.28 % and 31.83 % respectively [37]. Ytterbium is used as its atomic structure is ideal for quantum computing applications. Ytterbium 171 has a spin half nucleus which gives its $^2S_{\frac{1}{2}}$ ground state a hyperfine structure which is ideal for use as a qubit. In addition, lasers at the wavelengths within the cooling cycle are easily obtainable.

[3]Varian: 9160050
[4]Varian StarCell: 9191145
[5]Kimball physics: MCF450-MH10204/8-A
[6]Kimball physics: MCF450-S020008-C
[7]Kurt J. Lesker: SUSO90307RHLW
[8]Mill-Max 0672-1-15-15-30-27-10-0

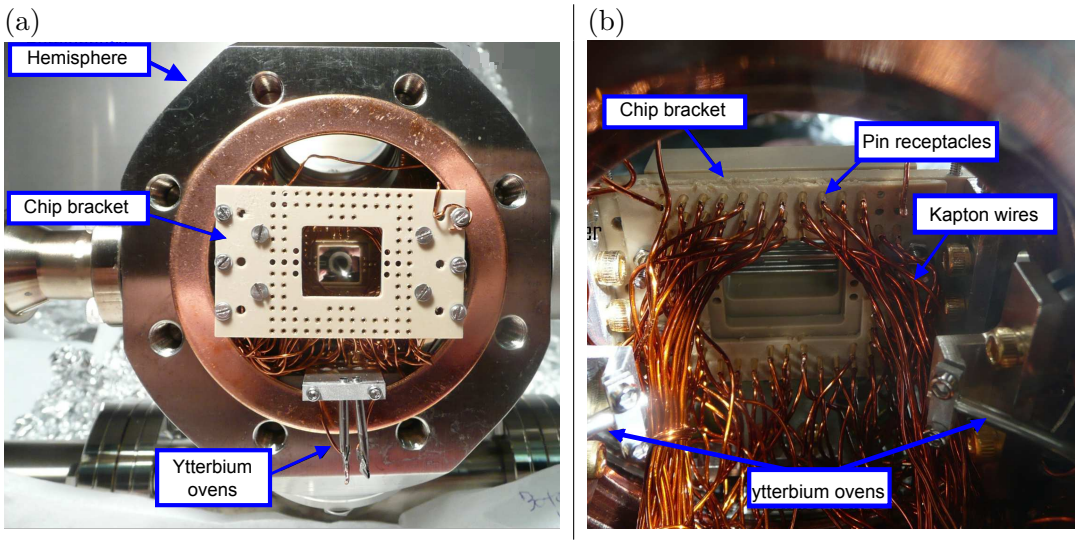

Figure 2.6: Inside of vacuum chamber as viewed from the (a) front and (b) back of the chip bracket.

2.3.1 Ionisation

Ytterbium metal is located within tubes of stainless steal inside the vacuum system. These are known as atomic ovens and are positioned so they are pointing towards the trap as shown in figure 2.6. The ovens are spot welded to copper wire which connects to the oven feedthrough. When a current is applied to this wire, the tube heats up, heating up the ytterbium which produces an atomic flux which passes through the trap. Ytterbium ions can be formed from these atoms through electron bombardment or photoionsisation. In this thesis, we use photoionisation as it allows for isotope selectivity and has higher loading rates [41]. Figure 2.7 shows the atomic levels involved in the photoionisation of ytterbium. A two photon process is used to ionise the atoms. The first photon at 398.9 nm excites an electron from the ground state up to the $^1P_1$ state. From here the electron is excited into the continuum by a second photon of a wavelength of less than 394 nm thereby ionising the atom. For this second photon we use the 369 nm photons already present for laser cooling as will be described in section 2.3.2. Once ionised, the ytterbium will, as a charged particle, become trapped in the trapping potential described in section 2.1.

2.3.2 Doppler cooling

To cool the ions once they are trapped we use Doppler cooling. When laser light is incident on a stationary ion, the ion will absorb photons which have a frequency equal to a transition frequency. When however, the ion is moving, the frequency of the incident photons will become Doppler shifted with respect to the ion. If photons are applied which

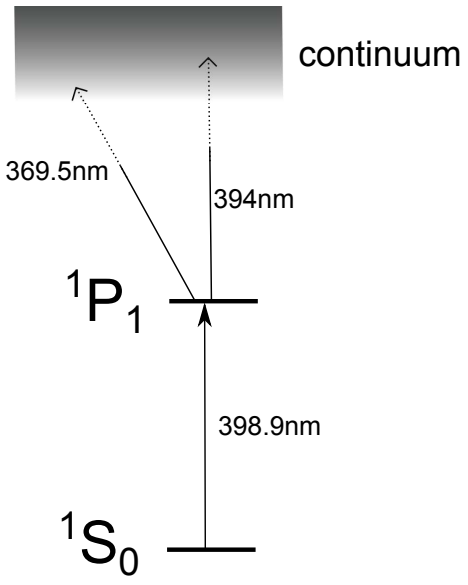

Figure 2.7: Level diagram of neutral ytterbium showing the two photon process used to ionise the atoms.

are red detuned from a transition frequency, ions traveling towards the beam will therefore absorb the photons. This will result in the ions receiving a momentum kick opposite to their direction of motion resulting in a damping force which cools the ion.

The energy level diagram for ytterbium 174 is shown in figure 2.8. The main cooling transition is between the $^2S_{\frac{1}{2}}$ level and the $^2P_{\frac{1}{2}}$ level. The ion is excited on this transition using light of a wavelength of 369.5 nm. Once in the $^2P_{\frac{1}{2}}$ level the ion will occasionally decay into the $^3D_{\frac{3}{2}}$ level with a branching ratio of 0.2 %. From this level, 935.2 nm light can be used to excite the ion into the $^3D[3/2]_{\frac{1}{2}}$ level which can decay back into the $^2S_{\frac{1}{2}}$ level. This creates a closed cooling cycle within the ion. Occasionally however (approximately once an hour), collisions with stray particles within the system can cause an ion in the $^3D_{\frac{3}{2}}$ level to fall into the $^2F_{\frac{7}{2}}$ level (not shown), from here the ion can be returned to the main cooling cycle using 638.2 nm light.

The energy level diagram for ytterbium 171 is shown in figure 2.9. The spin half nucleus of the isotope and the resulting hyperfine structure, complicate the cooling cycle. To cool, 369.5 nm light resonant with the $^2S_{\frac{1}{2}}$ F = 1 to $^2P_{\frac{1}{2}}$ F = 0 transition is applied. From here the ion can decay back to the $^2S_{\frac{1}{2}}$ F = 1 level. Off resonant scattering will also excite the ion into the $^2P_{\frac{1}{2}}$ F = 1 level where it can decay into the $^2S_{\frac{1}{2}}$ F = 0 level, microwaves at 12.6 GHz are then required to bring the ion back into the main cooling cycle. As will be explained in chapter 3, state preparation and detection will require the use of the $^2P_{\frac{1}{2}}$ F = 1 level, this level can be accessed directly by the addition of 2.1 GHz sidebands to the 369 nm light.

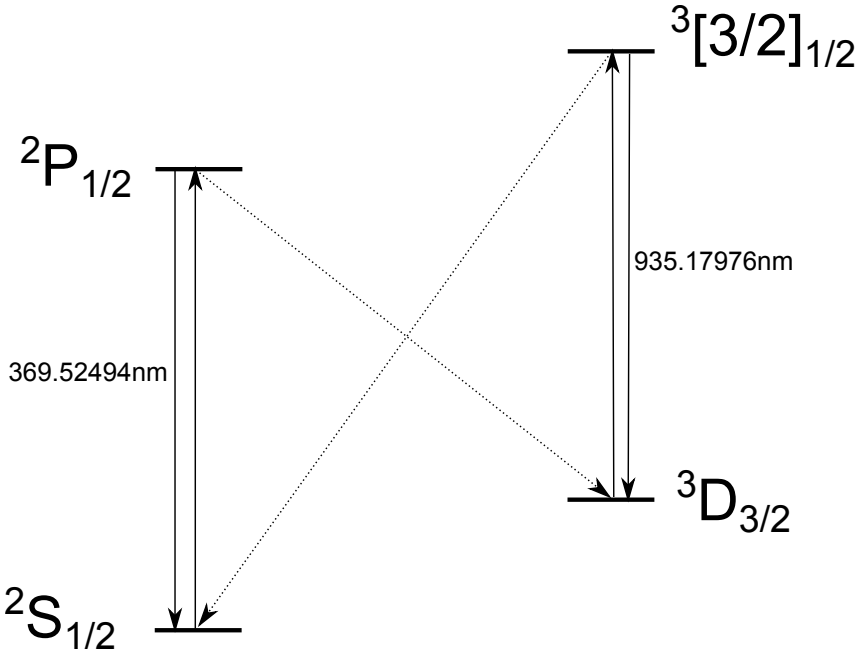

Figure 2.8: The energy level structure of ytterbium 174 showing the transitions of the main cooling cycle.

Polarisation

To effectively cool $^{171}Yb^+$, the applied 369.5 nm light should have components of linear, σ_+ and σ_- polarised light. This allows the ion to make transitions of $\Delta m_F = 0, +1$ and -1 respectively. When however, σ_+ and σ_- polarised light of the same frequency are applied simultaneously they will cancel out to form linear light. Population will therefore become trapped in the $^2S_{\frac{1}{2}}$ F = 1 $m_F = \pm 1$ levels. To avoid this, the 369 nm light should be applied at an angle with respect to the trap axis and a magnetic field should be applied to the ion [42]. This breaks the degeneracy within the $^2S_{\frac{1}{2}}$ F = 1 and $^2P_{\frac{1}{2}}$ F = 1 levels forming a Zeeman structure as shown in figure 2.9.

2.3.3 Laser setup

Figure 2.10 shows the laser setup used to produce and cool ytterbium ions. All the laser beams, upon exiting their laser cavities first travel through an optical isolator[9] to prevent reflections from reaching the laser cavity. All the lasers also travel through polarisation maintaining fibres before being sent to the trap. This allows the beam paths before the fibres to be modified without affecting the beam alignment going into the trap as well as ensuring beam stability.

The main cooling laser at 369 nm is formed by frequency doubling a 739 nm laser using

[9]LINOS: FI-760-TV

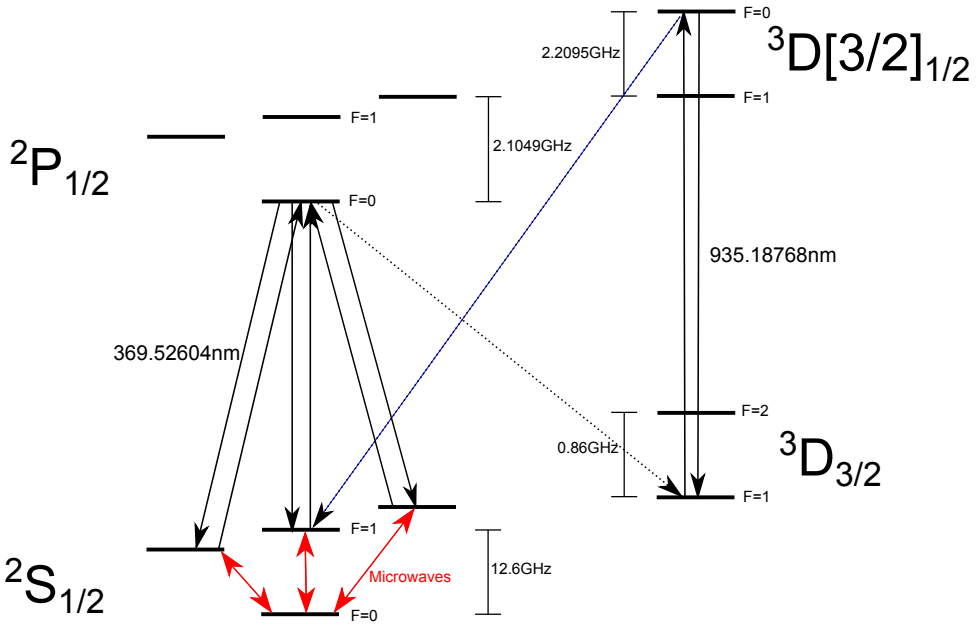

Figure 2.9: The energy level structure of ytterbium 171 showing the fine structure, hyperfine structure and transitions of the main cooling cycle.

a nonlinear lithium triborate crystal within a bow tie cavity[10]. Before doubling, the 739 nm beam first travels through an EOM which can be used to place 1.05 GHz sidebands on the light (this is required during state preparation as will be explained in chapter 3) followed by a tapered amplifier which amplifies the beam power to approximately 300 mW. A small amount of this amplified beam ($\approx 200\,\mu$W) is sent to the locking setup which provides a feedback signal to the Toptica laser cavity in order to stabilise the lasers frequency (this will be explained in chapter 4. The remaining amplified light is sent to the frequency doubler. After doubling, the beam is slightly elliptical and is therefore passed through a pair of anamorphic lenses to form a circular beam profile. This is double passed through an AOM which acts as a switch allowing the cooling light reaching the trap to be blocked. The AOM also allows the beam's frequency and power to be adjusted.

The 399 nm, 935 nm and 638 nm lasers are homebuilt external cavity diode lasers (ECDL). These are setup in the Littrow configuration as shown in figure 2.11. The laser light is produced from a diode and collimated using an aspheric lens. This is then directed towards a grating. The grating reflects the 1st order of diffracted light back to the diode to form the laser cavity and the zeroth order is used for the experiment. The exact length of the laser cavity determines the laser frequency and is determined by the grating angle.

After the fibres, the 369 nm beam is combined with the 638 nm and 399 nm beams using optical bandpass filters before being sent to the trap. Half and quarter waveplates

[10]Toptica photonics: TA-SHG 36

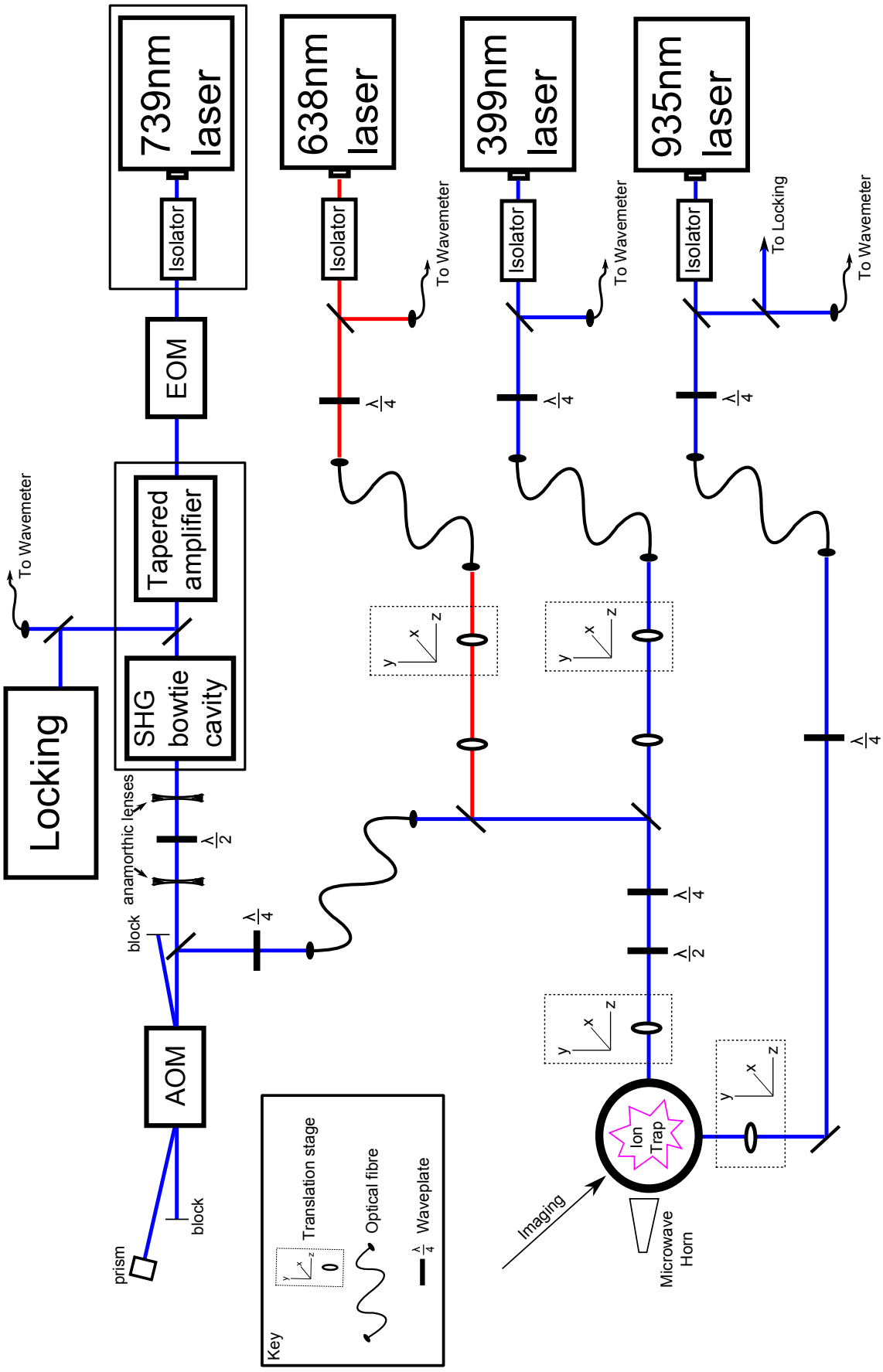

Figure 2.10: Laser setup used to ionise and cool ytterbium ions.

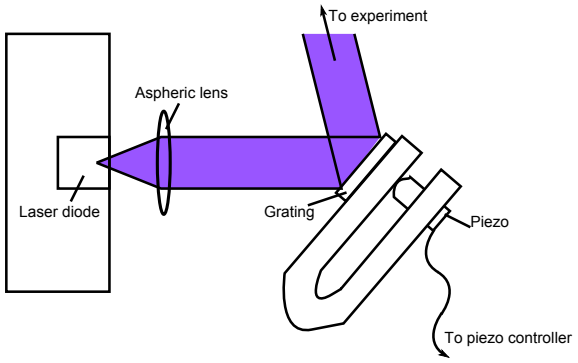

Figure 2.11: Internal structure of the external cavity diode lasers setup in the Littrow configuration.

allow the beams' polarisation to be adjusted and a final lens just before the trap focuses the light of the combined beams relative to the trap. A translation stage attached to this lens allows the exact position of the combined beams within the trap to be adjusted. To fine tune the position of the 638 nm and 399 nm beams, translation stages are connected to one of the lenses of the 1:1 telescopes present before the beams are combined. The 935 nm beam is sent into the trap at right angles to the 369 nm, 638 nm and 399 nm beams.

2.4 Imaging

In order to see the ions, the imaging system shown in figure 2.12 is used. This consists of nine main components.

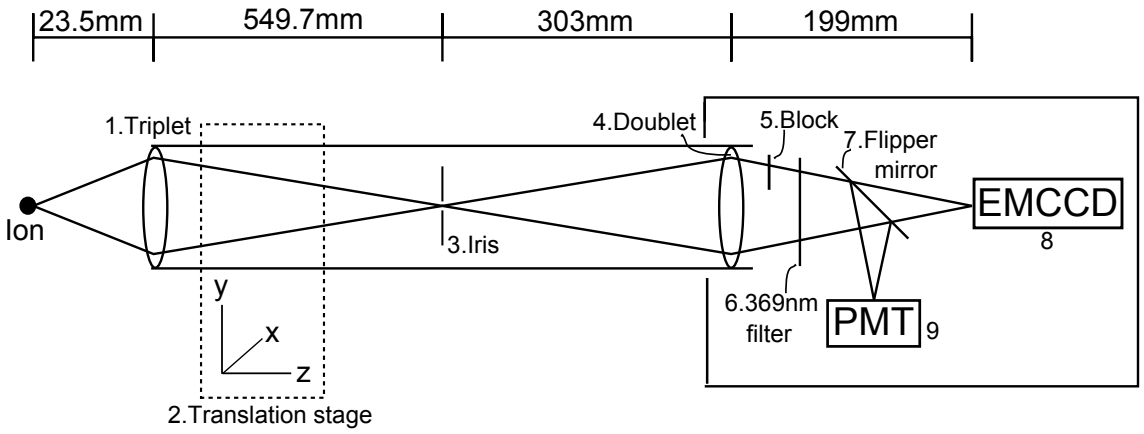

Figure 2.12: Diagram showing the setup used to image the ions.

1. **Triplet lens**: Light from the ion is collected by a triplet lens[11]. The triplet has a magnification of $M_{trip} = -17.5$ which is placed at a distance of 23.5 mm from the

[11] Special optics 54-17-29-369

ion resulting in an image distance of 550 mm.

2. **Translation stage**: This moves the imaging tube in space allowing different parts of the trap to be observed.

3. **Iris**: At the magnified image position, an iris is present to block scatter from, for example, laser light hitting the electrodes.

4. **Doublet lens**: A doublet lens reimages the light onto the photon measuring devices. The doublet consists of two lenses with focal lengths, f_1 and f_2 equal to 200 mm and 300 mm respectively. The image distance, d_i can be then be found using the following formula

$$\frac{1}{f_1} + \frac{1}{f_2} = \frac{1}{d_o} - \frac{1}{d_i}. \tag{2.8}$$

   Therefore if the doublet is placed at a distance of 303 mm from the iris, this will result in an image distance, d_i of 199 mm. The doublet has a magnification equal to $\mathrm{M}_{doub} = -\frac{d_o}{d_i} = -1.5$. The total magnification of the system is therefore equal to $\mathrm{M}_{tot} = \mathrm{M}_{trip} \times \mathrm{M}_{doub} = 26.25$.

5. **369 nm bandpass filter**: This allows only 369 nm light to pass through which reduces scatter from other wavelengths reaching the detectors.

6. **Block**: A beam block is required to prevent scatter from the trap electrodes from overlapping with the image of the ion at the detector. This is further explained in figure 2.13.

7. **Flipper mirror**: A motorised flipper mirror allows the light to be switched between hitting the PMT (photomultiplier tube) or the EMCCD (charge coupled device).

8. **EMCCD**[12]: Array of pixels which gives us the ability to align the imaging system and the lasers as well as detect trapped ions.

9. **PMT**[13]: Photomultiplier tube which emits a TTL pulse upon detection of a photon. This allows us to detect the exact number and arrival time of photons from the ion more accurately than the EMCCD. This is required for data collection during coherent manipulation experiments as described later in this thesis.

To reduce background light the whole setup is contained within light sealed tubes and boxes.

[12] Andor: iXon 885
[13] Hamamatsu H8259-01

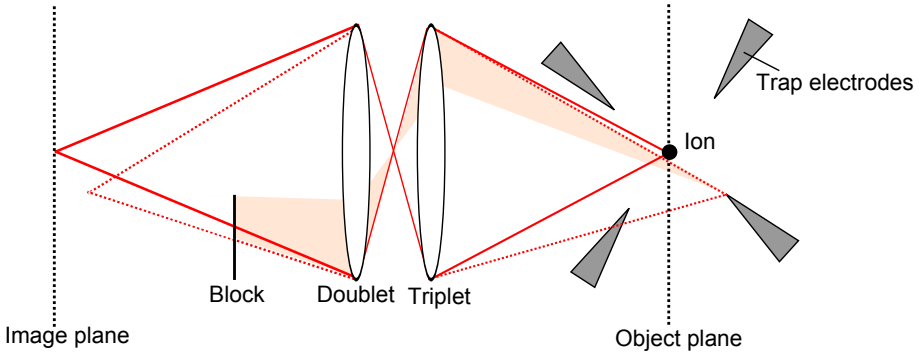

Figure 2.13: Diagram showing how a block reduces electrode scatter. Due to movement of the trap electrodes during baking, the trap is slightly tilted with respect to the plane of the imaging. As a result, out of focus light scattered from an electrode overlaps with the ion in the object plane (The path of the overlapping photons from the electrode are shown in pink). Placing a block as shown stops these photons from reaching the image plane. This block does however result in a slight reduction of photons from the ion reaching the detector. Diagram not to scale.

2.5 Electronics

The experiment is controlled and automated using two main computers. The first is known as the host computer and runs National Instruments Labview. This sends signals to a field programmable gate array[14] (FPGA) which is mounted in an external chassis[15] and connected to the host computer via a PXIe X1 card. The FPGA has 96 digital channels and 16 analogue channels to allow the input and output of signals and is mainly used to detect the output pulses from the PMT, send TTL pulses to switches and control pulse sequences as will be discussed in later chapters of this thesis.

The second computer is known as the target computer. This runs the Labview Realtime operating system which provides realtime control of signals through analogue input and output cards[16]. This is mainly used in the experiments described within this thesis to provide locking feedback (see chapter 4), monitor the vacuum pressure, operate the atomic ovens and control the amplitude of the RF trap voltage.

The remainder of this section will describe the electronics required to drive and control the main devices mentioned in this chapter.

2.5.1 Trap

DC and RF voltages need to be supplied to the electrodes of the trap. Depending on the application, the required DC voltages can be supplied by either stable DC supplies

[14] NI-PXI-7842R
[15] NI-RIOPXI-1033
[16] NI PCI-6722 and NI PCI-6143 respectively

or from the Labview realtime machine which allows for fast remote control. The voltage then passes through four stages of low pass filtering before being sent to the trap via the DC feedthrough. To supply RF to the trap electrodes a resonant circuit is used. The complete circuit diagram of this is shown in figure 2.14. The resonant circuit is designed

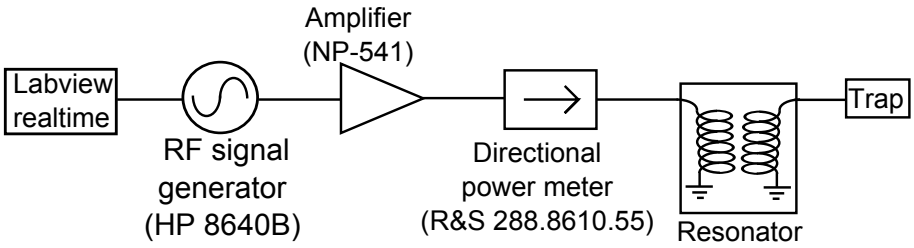

Figure 2.14: Electronics used to supply an RF voltage to the trap.

to impedance match the trap with the RF source allowing for application of the maximum possible voltage while reducing unwanted frequencies [43]. The RF voltage is supplied by a signal generator whose amplitude is controlled remotely by Labview realtime, this is then amplified to several watts and passed through a directional power meter. This allows us to monitor the power being transmitted and reflected. The signal is then sent to the trap via a helical resonator which is connected to the RF feedthrough. A full discussion of the helical resonator is given in [43]; I will give an overview here. The helical resonator consists of two resonant coils within a grounding shield as shown in figure 2.15. The resulting RF voltage applied to the electrodes is given by [43],

$$V_{RF} \approx \sqrt{2PQ\left(\frac{L}{C}\right)^{\frac{1}{2}}} \tag{2.9}$$

where P is the power applied to the resonator from the amplifier and L and C are respectively the total combined impedance and capacitance of the ion trap and resonator. Q is the quality factor and is given by [43],

$$Q = \frac{\text{energy stored in resonator}}{\text{energy dissipated}} = \frac{f_{RF}}{f_{\frac{1}{2}}} \tag{2.10}$$

where $f_{\frac{1}{2}}$ is the full width at half the maximum transmission at the resonant frequency, f_{RF}. The resonant frequency, f_{RF} is given theoretically by

$$f_{RF} = \frac{1}{2\pi\sqrt{LC}} \tag{2.11}$$

and is found to be equal to 21.49 MHz for our combination of resonator and trap. This gives a Q equal to 200 ± 20. C equals 17 ± 2 pF which allows equation 2.9 to be rewritten

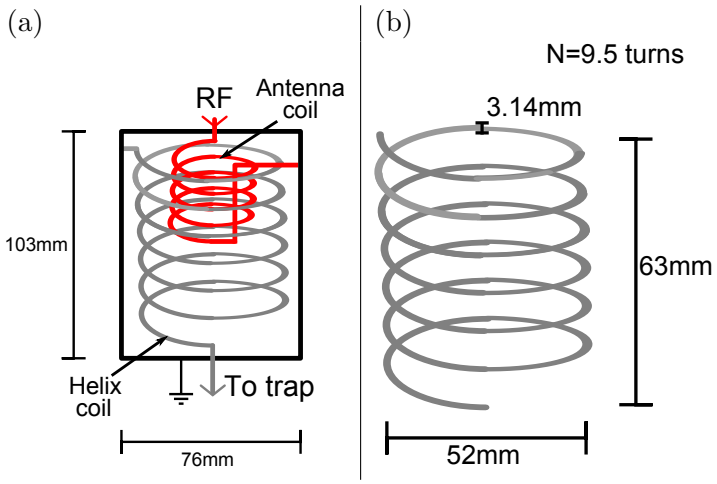

Figure 2.15: (a) Labeled diagram of the helical resonator used within this thesis showing the dimensions of the grounding shield. (b) Dimensions of the helix coil.

as $V_{RF} \approx (418 \pm 4) \times P^{\frac{1}{2}}$.

2.5.2 Laser and microwave frequencies

The following shows the electronics used to drive (a) the EOM which adds 1.05 GHz sidebands to the 739 nm laser, (b) the AOM which switches and controls the power and frequency of the 369 nm beam and (c) the microwave horn used to bridge the hyperfine splitting of ytterbium 171.

(a) EOM

The EOM is driven by a 1.05 GHz signal from a signal generator. As shown in figure 2.16, this is then amplified to 31 dbm before being sent to the EOM. The switch allows the sidebands to be turned on and off quickly using Labview.

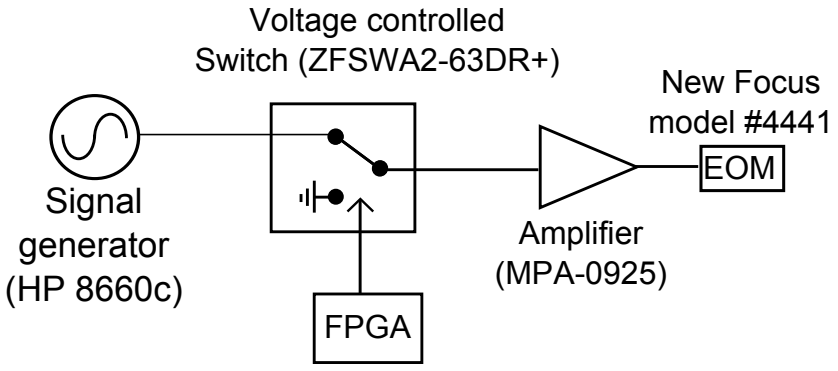

Figure 2.16: Electrical circuit used to power the EOM.

(b) AOM

The AOM is driven by a 200 MHz Voltage Controlled Oscillator (VCO) as shown in figure 2.17. The frequency of the VCO can be switched between a constant 200 MHz or a variable 0-200 MHz controlled using the FPGA. An amplifier is present to increase the 0-10 V output of the FPGA to the 0-15 V range of the VCO. A voltage variable attenuator allows the power of the signal and therefore the 369 nm beam power to be adjusted using the FPGA. The signal is amplified to 3 W before being sent to the AOM. The fixed attenuators prevent damage to the subsequent amplifiers.

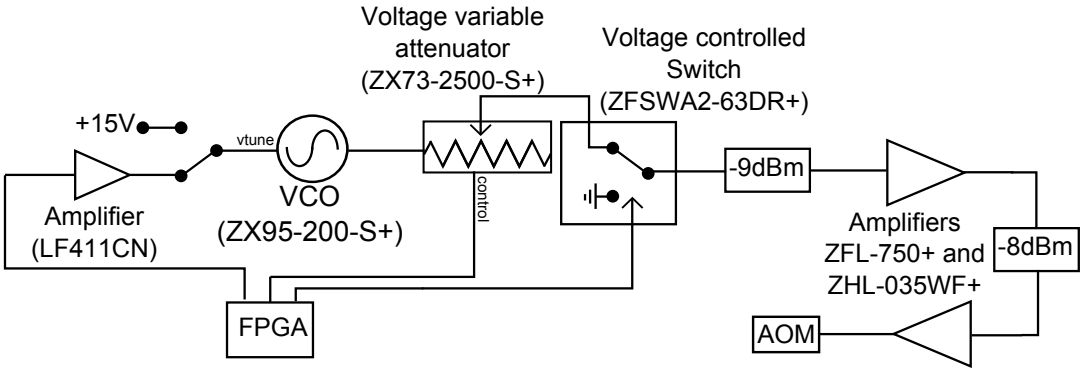

Figure 2.17: Electrical circuit used to power the AOM.

(c) Microwaves

The microwave horn is driven using a 12.6 GHz signal from a signal generator. This is amplified to ≈30 dbm before being sent to the horn via a FPGA controlled switch as shown in figure 2.18. This provides a single controllable microwave signal which is all that is required to trap and cool $^{171}Yb^{+}$. This microwave setup will be adjusted later in this thesis to provide phase control to measure ion coherence times (see chapter 3), to provide analogue signal control to produce STIRAP operations (see chapter 6) and to produce multiple signals to provide individual coherent control of two ions (see chapter 7).

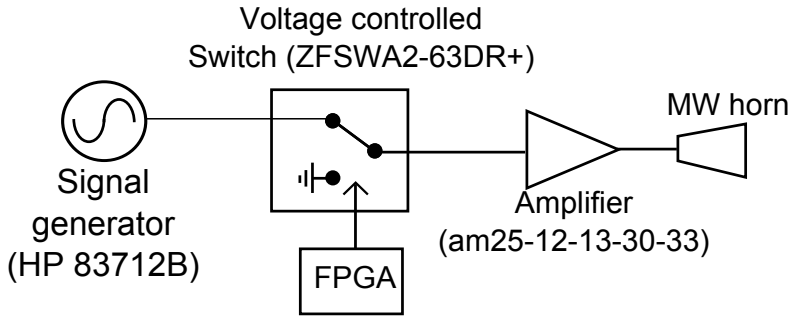

Figure 2.18: Electrical circuit used to power the MW horn.

2.6 Trapped ions

Figure 2.19 shows a chain of $^{174}Yb^{+}$ ions trapped using the apparatus described in this chapter. These ions were trapped with a drive frequency of $\Omega_{RF}/2\pi = 21.1\,\mathrm{MHz}$ at a vacuum pressure of 2×10^{-12} Torr.

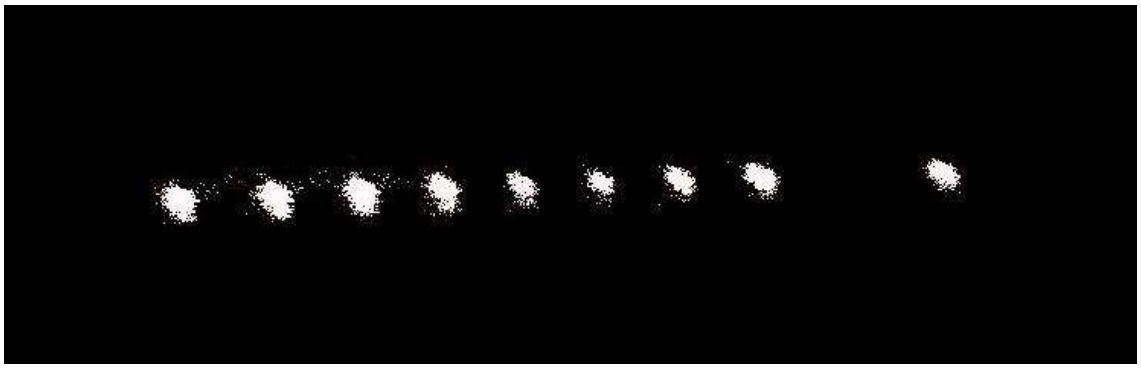

Figure 2.19: Trapped ytterbium ions. The gap is an ion of a different isotope which is being sympathetically cooled by the surrounding ions.

Chapter 3

Preparing and detecting quantum states

To perform quantum operations on trapped ytterbium ions we first need to define our qubit. The hyperfine structure of the ${}^2S_{\frac{1}{2}}$ level in ytterbium 171 is shown in figure 3.1. This consists of a lower F = 0 level and an upper F = 1 level which is split in frequency space into three m_F sublevels by the Zeeman effect caused by the magnetic field required for laser cooling (see section 2.3.2). These levels are ideal for use as qubits as they are well defined and have long lifetimes. Later, in chapter 6, I will describe how superpositions of these different levels and sublevels combined with incident microwave fields are used to produce a set of dressed qubit states. Initially, we shall simply define our $|0\rangle$ qubit state to be equal to the lower F = 0 level and our $|1\rangle$ qubit state to be equal to one of the upper F = 1 levels.

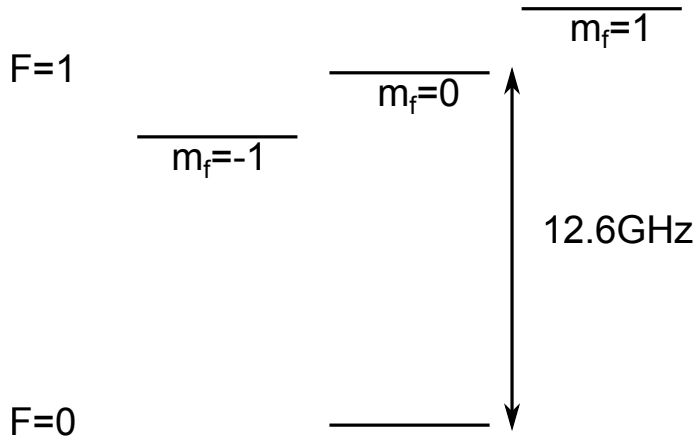

Figure 3.1: Hyperfine structure of the ${}^2S_{\frac{1}{2}}$ level of ytterbium 171.

This chapter will begin by explaining how the level populations in ytterbium 171 can be

modeled using rate equations. It will then go on to explain how the ion can be experimentally prepared in both the $|0\rangle$ and the $|1\rangle$ qubit states as well as how we can determine what state the ion is in. Finally, this chapter will introduce the Bloch sphere and explain how arbitrary quantum superposition states can be prepared and how the decoherence of these states can be measured.

3.1 Rate equations

The simplest way of modeling level populations is to use rate equations. These are a set of coupled differential equations formed by considering how the population of each level is effected by classical photon absorption and emission processes. This section will explain how these rate equations are formed and how they can then be used to determine level populations at a given time. It should be noted however that the rate equation model is an approximation and does not take into account quantum effects. This will be further discussed in section 3.1.3.

3.1.1 Forming the rate equations

In a two level system where the two levels are separated in frequency space by ω_{21}, electron population can be transferred between the levels by one of three processes as shown in figure 3.2. This is known as Einstein's model [44]. The three processes are as follows,

1. Spontaneous emission of a photon of energy, $\hbar\omega_{21}$ causing a transition from the upper level to the lower level.

2. Stimulated absorption from the lower level to the upper level caused by absorption of a photon of energy $\hbar\omega_{21}$.

3. Stimulated emission of two photons caused by the absorption of one photon of energy $\hbar\omega_{21}$. This causes a transition from the upper level to the lower level. The emitted photons will have a wavevector, $\mathbf{k}$, equal to that of the absorbed photon.

The total rate of change of population of the upper (n_2) and lower (n_1) levels is equal to the sum of the rate of population change from these three processes.

$$\frac{dn}{dt} = \frac{dn}{dt}(\text{stimulated absorption}) + \frac{dn}{dt}(\text{stimulated emission}) + \frac{dn}{dt}(\text{spontaneous emission}) \tag{3.1}$$

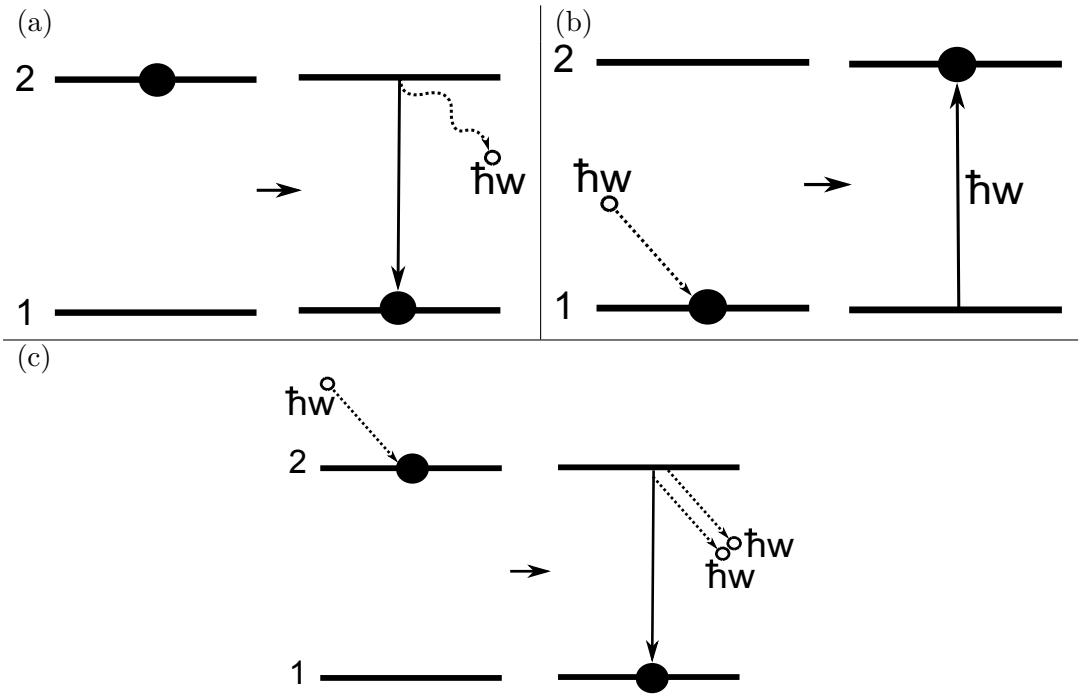

Figure 3.2: The three methods of population transfer between two levels as described by Einstein's model. (a) Spontaneous emission, (b) stimulated absorption and (c) stimulated emission.

These can be described using Einsteins A and B coefficients which respectively describe the probability of spontaneous and stimulated processes occurring. For the stimulated processes, the rate of population change is also dependent on the energy density of incident radiation, $\rho(\omega_l)$, given by [45]

$$\rho(\omega_l) = \frac{1}{2}\epsilon_0 E_0^2 g(\omega_l) \tag{3.2}$$

where E_0 is the electric field amplitude and $g(\omega)$ is the density of photon states with a frequency ω, as well as the linewidth of the transition, $\sigma_{ij}(\omega_l - \omega_0)$, where ω_0 and ω_l correspond to the resonant frequency and incident light frequency respectively. In real atoms, levels have a non zero linewidth which allows light which is slightly detuned from the resonant frequency to still excite the transition. Linewidth is defined as [45],

$$\sigma_{ij}(\omega_l - \omega_0) = \frac{\Gamma_j}{2\pi\left((\omega_l - \omega_0)^2 + \frac{\Gamma_j^2}{4}\right)} \tag{3.3}$$

Where $\Gamma_j = \frac{1}{\tau_j}$ is the rate of decay of level j where τ_j is the levels lifetime. For the two levels, equation 3.1 can therefore be expressed as [45],

$$\frac{dn_2}{dt} = B_{12}\rho(\omega_l)\sigma_{12}(\omega_l - \omega_0)n_1 - B_{21}\rho(\omega_l)\sigma_{21}(\omega_l - \omega_0)n_2 - An_2 \tag{3.4}$$

for the upper level and

$$\frac{dn_1}{dt} = -B_{12}\rho(\omega_l)\sigma_{12}(\omega_l - \omega_0)n_1 + B_{21}\rho(\omega_l)\sigma_{21}(\omega_l - \omega_0)n_2 + An_2 \tag{3.5}$$

for the lower level. Moving to a multi level system, the general form for the rate of change of population, n, for an energy level, j, is equal to the sum of transitions to and from each other level in the system,

$$\begin{array}{lll} \frac{dn_j}{dt} = \sum_k & +n_k B_{kj}\rho(\omega_l)\sigma(\omega_l - \omega_0) & \text{population gain due to stimulated processes} \\ & +n_k A_{kj} & \text{population gain due to spontaneous emission} \\ & -n_j B_{jk}\rho(\omega_l)\sigma(\omega_l - \omega_0) & \text{population loss due to stimulated processes} \\ & -n_j A_{jk} & \text{population loss due to spontaneous emission} \end{array} \tag{3.6}$$

Expressions for the A and B coefficients describing the respective spontaneous and stimulated processes within ytterbium 171 will now be derived.

Spontaneous emission

Einstein's A coefficient describing the rate of spontaneous emission from a level, i, causing a transition to level, j, is given by

$$A_{ij} = \frac{d_{ij}}{\tau_i} \tag{3.7}$$

where τ_i is the lifetime of level i and d_{ij} is the branching ratio of the transition from level i to j. The mean lifetimes of the main levels are given in table 3.1. The branching ratio of the transition i to j describes the probability that population leaving level i will enter level j. This will equal 0 for forbidden transitions. Transitions are allowed when the change in the total angular momentum quantum number, F is equal to 0 or ± 1 with the exception of transitions from F = 0 to F = 0. Additionally, the F level projection cannot change by more than 1 (i.e. allowed transitions must have $\Delta m_F = 0, \pm 1$.). For $^{171}Yb^+$ branching ratios can be found in [1, 37] and are given in table 3.2[1] .

[1]For simplicity, the m_F levels of the $^3D_{\frac{3}{2}}$ and $^3D[3/2]_{\frac{1}{2}}$ levels are assumed to be degenerate.

Level	Lifetime
$^2S_{\frac{1}{2}}$	1 year
$^2P_{\frac{1}{2}}$	8.12 ns
$^3D_{\frac{3}{2}}$	52.7 ms
$^3D[3/2]_{\frac{1}{2}}$	37.7 ns

Table 3.1: Table showing the average lifetimes of the main levels of $^{171}Yb^+$. Lifetimes sourced from [1].

			Upper level					
			$^2P_{\frac{1}{2}}$				$^3D[3/2]_{\frac{1}{2}}$	
			F = 0	F = 1			F = 0	F = 1
Lower level				$m_F = -1$	$m_F = 0$	$m_F = +1$		
$^2P_{\frac{1}{2}}$	F = 1	m_F = -1	0.332	0.332	0.332	0	0.327	0.246
		$m_F = 0$	0.332	0.332	0	0.332	0.327	0.246
		$m_F = +1$	0.332	0	0.332	0.332	0.327	0.246
	F = 0		0	0.332	0.332	0.332	0	0.246
$^3D_{\frac{3}{2}}$	F = 2		0	0.002	0.002	0.002	0	0.018
	F = 1		0.004	0.002	0.002	0.002	0.009	0.009

Table 3.2: Table showing branching ratios between the main levels within $^{171}Yb^+$. All numbers given to three significant figures.

Stimulated emission and absorption

The rate of stimulated emission/absorption from level i to level j, R_{ij}, is expressed in equations 3.4-3.6 as the following,

$$R_{ij} = B_{ij}\rho(\omega_l)\sigma(\omega_l - \omega_0). \tag{3.8}$$

This can also be represented by Fermi's golden rule which is given by [46],

$$R_{ij} = \frac{2\pi}{\hbar}|M_{ij}|^2 g(\hbar\omega)\sigma(\omega_l - \omega_0) \tag{3.9}$$

where $g(\hbar\omega)$ is the final density of photon states of the system and $M_{ij} = \langle i|\,\hat{H}'\,|j\rangle$ is the matrix element of the perturbation, $\hat{H}'$ which caused the transition.

Electromagnetic radiation incident on an electron in an atom results in a electric dipole interaction which is represented by the Hamiltonian

$$\hat{H}' = -\mathbf{p}\cdot\mathbf{E} \tag{3.10}$$

where $\mathbf{p} = -e\mathbf{r}$ and $\mathbf{E}$ is the electric field of the incident radiation. The amplitude of this

field is given by $|\mathbf{E}|^2 = \mathrm{E}_0$. M_{ij} can therefore be written as

$$M_{ij} = \boldsymbol{\zeta}_{\mathbf{ij}} \cdot \mathbf{E} \tag{3.11}$$

where ζ_{ij} is the electric dipole moment matrix element which is defined as,

$$\zeta_{ij} = e \begin{pmatrix} \langle i| r_x |j\rangle \\ \langle i| r_y |j\rangle \\ \langle i| r_z |j\rangle \end{pmatrix}. \tag{3.12}$$

Using equation 3.2 where $g(\omega) = \frac{dn}{d\omega} = \hbar\frac{dn}{dE} = \hbar g(E)$ and equations 3.8 and 3.9 results in an expression for Einsteins B coefficient given by,

$$B_{ij} = \frac{\pi|\zeta_{ij}|^2}{\epsilon_0\hbar^2}. \tag{3.13}$$

The rate of stimulated emission/absorption is therefore given by

$$R_{ij} = \frac{\pi|\zeta_{ij}|^2}{\epsilon_0\hbar^2}\rho(\omega_l)\sigma(\omega_l - \omega_0) \tag{3.14}$$

which can be written as

$$R_{ij} = \frac{\pi\Omega_{ij}^2}{2}\sigma(\omega_l - \omega_0), \tag{3.15}$$

where

$$\Omega_{ij} = \frac{|\zeta_{ij} \cdot E_0|}{\hbar} \tag{3.16}$$

is the Rabi frequency between levels i and j. This Rabi frequency can be written in terms of the intensity of incident radiation, I, and the decay rate of the level involved to give [2],

$$\Omega_{ij}^2 = \frac{\Gamma_j^2 d_{ij} I}{I_{sat}} \tag{3.17}$$

where I_{sat} is the saturation intensity given by,

$$I_{sat} = \frac{\hbar\omega_{ij}^3\Gamma_j}{6\pi c^2}. \tag{3.18}$$

3.1.2 Solutions to the rate equations

Applying equation 3.6 to $^{171}\mathrm{Yb}^+$ forms 12 equations describing the rate of change of population for each of the 12 main levels described in table 3.2. For time independent laser powers and frequencies, the population of each level will evolve over time tending

towards a steady state value. The total population of the system must always add up to 1, therefore by replacing one of the rate equations with the additional condition

$$\sum_{i}^{12} n_i = 1 \tag{3.19}$$

the steady state populations can be found by solving the 12 equations simultaneously.

The time dependent population of the levels as they evolve towards the steady state can be found by rewriting equation 3.6 as follows

$$\frac{d\mathbf{n}}{dt} = \mathbf{\Pi}\ \mathbf{n} \tag{3.20}$$

where Π is a matrix containing both the total spontaneous emission and stimulated absorption/emission rates between the levels. This equation can be solved by integration giving the following solution

$$\mathbf{n} = e^{\mathbf{\Pi} t} n_0 \tag{3.21}$$

where n_0 are the initial population values.

Both time dependent and steady state solutions are found using Mathematica. The code for this is shown in appendix A.

3.1.3 Limitations of rate equations

Einstein's rate equation model can be an extremely accurate method of describing population transfer between levels but it has its limitations. When the Rabi frequency between two levels Ω_{ij} becomes a lot greater than the upper level decay rate [47],

$$\Omega_{ij} >> \frac{1}{\tau_j}, \tag{3.22}$$

the system can no longer be treated classically and experiences rabi oscillations which are described by the Bloch equations (see section 3.5.1). The rate equations are a special case of these Bloch equations, where, when $\Omega \leq \frac{1}{\tau}$, population decays from the upper level before rabi oscillations can occur. Table 3.3 shows the main transitions in $^{171}Yb^{+}$ used within in the experiments shown in this thesis and the regimes in which they should be treated.

Transition	Wavelength/frequency	Intensity	$\Omega\tau$	Regime
$^2\mathrm{S}_{\frac{1}{2}} \longrightarrow {}^2\mathrm{P}_{\frac{1}{2}}$	369 nm	$0.1\,I_0$	0.18	Rate equations
$^3\mathrm{D}_{\frac{3}{2}} \longrightarrow {}^3\left[\frac{3}{2}\right]_{\frac{1}{2}}$	935 nm	$15\,I_0$	0.71	Rate equations
$^2S_{\frac{1}{2}}\,\mathrm{F}=0 \longrightarrow {}^2\mathrm{S}_{\frac{1}{2}}\,\mathrm{F}=1$	12.6 GHz	1 W	10^9	Bloch equations

Table 3.3: Table showing the main transitions used within $^{171}\mathrm{Yb}^+$, the required intensities and the regimes in which that should be modeled.

3.2 State detection

State detection is the ability to detect which qubit state the ion is in. State detection is achieved within $^{171}\mathrm{Yb}^+$ by applying a 369 nm cooling beam resonant with the $^2S_{\frac{1}{2}}$ F = 1 to $^2P_{\frac{1}{2}}$ F = 0 transition and a 935 nm repumper beam resonant with the $^3D_{\frac{3}{2}}$ F = 1 to $^3D[3/2]_{\frac{1}{2}}$ F = 0 transition. As shown in figure 3.3, this results in population from $|1\rangle$ following a closed cooling cycle and population in $|0\rangle$ remaining unaffected. Florescence from the system would therefore indicate that the ion is in $|1\rangle$.

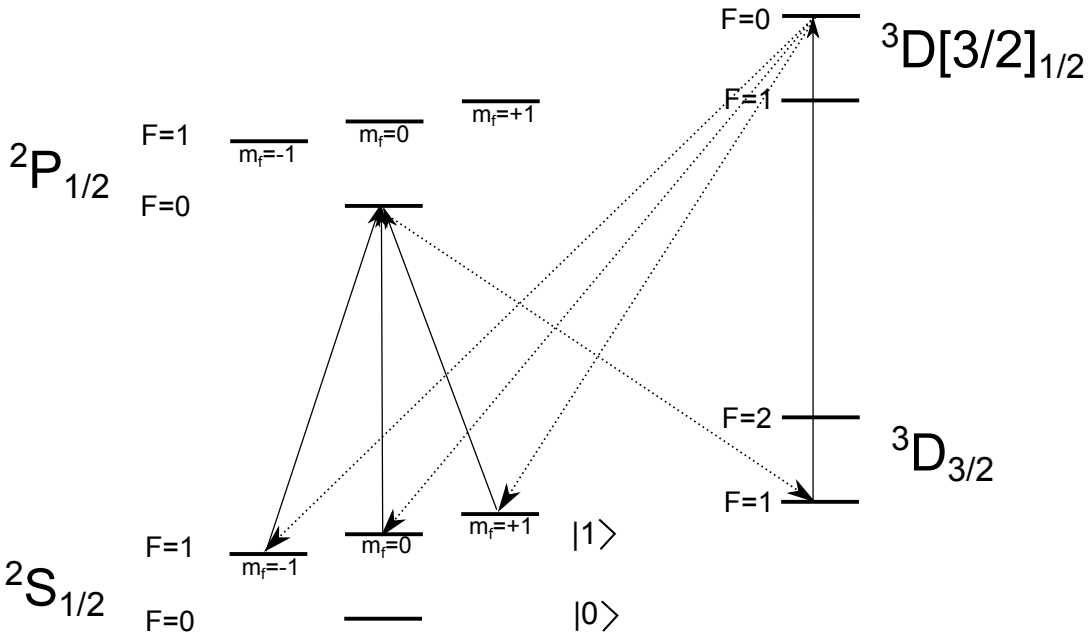

Figure 3.3: Closed cooling cycle used in state detection.

3.2.1 Off-resonant coupling

When the 369 nm cooling beam is applied there is a small probability that population from the $^2\mathrm{S}_{\frac{1}{2}}$ F = 1 level will be off-resonantly excited to the $^2\mathrm{P}_{\frac{1}{2}}$ F = 1 level which can decay into the $^2\mathrm{S}_{\frac{1}{2}}$ F = 0 level. Similarly, population in the $^2\mathrm{S}_{\frac{1}{2}}$ F = 0 level can be off-resonantly

excited by the 369 nm cooling light and make a transition into the pseudo-closed cooling cycle. This can be seen in figure 3.4 which shows the probability of finding the ion in the $^2S_{\frac{1}{2}}$ F = 0 (blue) and the $^2S_{\frac{1}{2}}$ F = 1 (red) levels at a time t during detection when the ion is initially in the $^2S_{\frac{1}{2}}$ F = 1, $m_F = 0$ level. These levels correspond to the $|0\rangle$ and $|1\rangle$ states of the qubit respectively. The population of these levels are converging towards their steady state populations. The exact time taken to reach steady state and the exact steady state populations depends on the intensities of the 369 nm and 935 nm light.

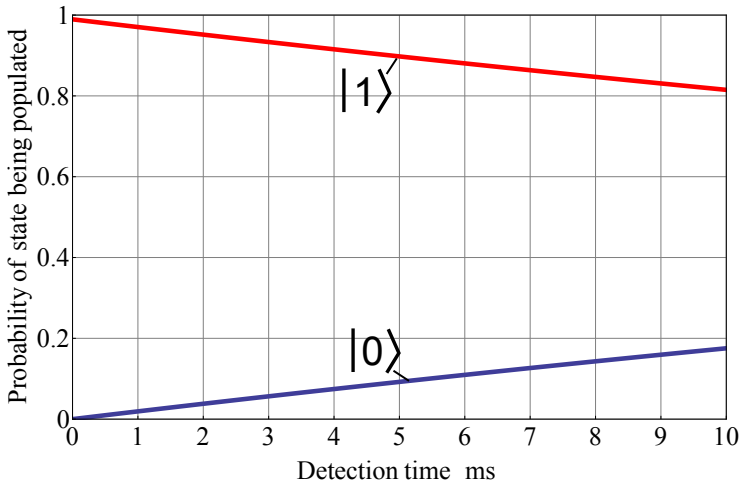

Figure 3.4: Probability of the population being in the $|0\rangle$ (blue) and $|1\rangle$ (red) states during detection as calculated using the rate equations. The population is initially in the $|1\rangle$ state and the 369 nm and 935 nm intensities are set to 0.1 I_{sat} and 10 I_{sat} respectively. The population of the other levels is negligible throughout and is therefore not shown.

The movement of population between the $|0\rangle$ and $|1\rangle$ states is unwanted during detection. Therefore, a detection time needs to be selected which is long enough to allow enough photons to be produced by the population initially in the $|1\rangle$ state while ensuring that off-resonant coupling is kept to a minimum.

The probability of detecting exactly n_D photons over a detection time, τ_D, from an ion initially in the $|0\rangle$ state is given by [24],

$$P(n) = e^{-\frac{\tau_D}{\tau_{(|0\rangle\rightarrow|1\rangle)}}} \times \left(\delta_{n_D} + \frac{\tau_D}{\tau_{(|0\rangle\rightarrow|1\rangle)}\lambda_0 \left(1 - \frac{\tau_D}{\tau_{(|0\rangle\rightarrow|1\rangle)}\lambda_0}\right)^{n+1}} \Gamma\left[n_D + 1, \left(\lambda_0 - \frac{\tau_D}{\tau_{(|0\rangle\rightarrow|1\rangle)}}\right)\right] \right) \quad (3.23)$$

where δ_{n_D} is the kronecker delta function, $\Gamma(i,j)$ is the incomplete gamma function, $\tau_{(|i\rangle\rightarrow|j\rangle)}$ is the average off-resonant pumping time from state i to j and λ_0 is the average number of photons collected from an ion in the $|1\rangle$ state over τ_D. Similarly the probability of detecting n_D photons over a detection time, τ_D, from an ion initially in the

$|1\rangle$ state is given by [24],

$$\begin{aligned} Q(n) =& \frac{\lambda^{n_D} e^{-\left(\lambda_0 + \frac{\tau_D}{\tau_{(|1\rangle\rightarrow|0\rangle)}}\right)}}{n_D!} \\ &+ \frac{\tau_D}{\tau_{(|1\rangle\rightarrow|0\rangle)}\lambda_0(1+\frac{\tau_D}{\tau_{(|1\rangle\rightarrow|0\rangle)}\lambda_0})^{n_D+1}}\Gamma\left[n_D+1, \left(\lambda_0 + \frac{\tau_D}{\tau_{(|1\rangle\rightarrow|0\rangle)}}\right)\right]. \end{aligned} \tag{3.24}$$

The parameters $\tau_{(|0\rangle\rightarrow|1\rangle)}$ and $\tau_{(|1\rangle\rightarrow|0\rangle)}$ are equal to the reciprocal of the total off-resonant pumping rate, given by,

$$\begin{aligned} \tau_{(|0\rangle\rightarrow|1\rangle)} &= \frac{1}{\Sigma_\beta R_{|0\rangle,\beta}} \\ &\approx 60\,\mathrm{Wm^{-2}s} \times I_c^{-1} \end{aligned} \tag{3.25}$$

and

$$\begin{aligned} \tau_{(|1\rangle\rightarrow|0\rangle)} &= \frac{1}{\Sigma_\alpha \Sigma_\beta R_{\alpha,\beta}} \\ &\approx 1.14\,\mathrm{Wm^{-2}s} \times I_c^{-1} \end{aligned} \tag{3.26}$$

where α represents all the Zeeman levels of the $|1\rangle$ state, β represents all Zeeman levels within the $^2\mathrm{P}_{\frac{1}{2}}$ F = 1 level, $R_{i,j}$ is given by equation 3.15 and I_c is the intensity of the 369 nm cooling laser.

The only photons detected from the ion are from the spontaneous decay of the $^2P_{\frac{1}{2}}$ levels. This is because the imaging optics is at an angle with respect to the lasers therefore photons emitted from the ion due to stimulated processes will not be detected. Additionally the imaging contains a 369 nm filter so 935 nm photons will be blocked. Not all photons from this spontaneous decay will be detected however due to inefficiencies in the imaging system. The average number of collected photons, λ_0, is therefore equal to the total number of photons released from spontaneous decay of the $^2P_{\frac{1}{2}}$ levels multiplied by the collection efficiency of the imaging optics, ρ_e. This can be expressed as

$$\lambda_0 = \rho_e \int_0^{\tau_D} (n_{p_1}(t)\Gamma_{p_1} + n_{p_2}(t)\Gamma_{p_2} + n_{p_3}(t)\Gamma_{p_3} + n_{p_4}(t)\Gamma_{p_4})dt \tag{3.27}$$

where $n_x(t)$ is the population of level x at time t given by the rate equation program where p_1, p_2, p_3 and p_4 represent the four $^2P_{\frac{1}{2}}$ sublevels. The photon collection efficiency, ρ_e, of the imaging setup used for all the experiments in this thesis is calculated by comparing the number of photons collected by the PMT during detection to the number of photons released by the spontaneous decay of the $^2\mathrm{P}_{\frac{1}{2}}$ level, (λ_0/ρ_e). Figure 3.5 shows λ_0/ρ_e vs detection time for 369 nm and 935 nm intensities equal to I_{sat} and $100\,\mathrm{I}_{sat}$ respectively. Using this, for a detection time of 1200 us, the total number of detectable photons released

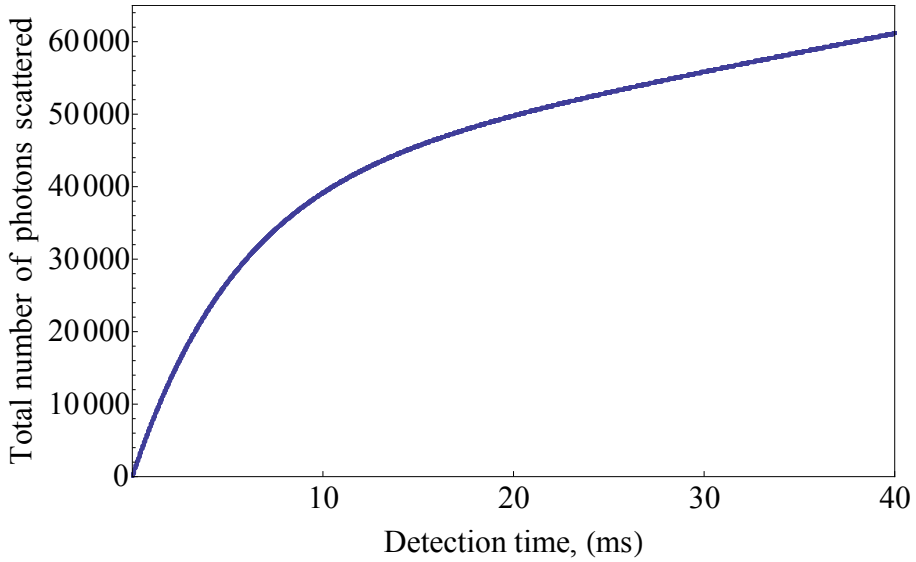

Figure 3.5: Number of photons released through spontaneous decay of the $^2P_{\frac{1}{2}}$ level of $^{171}Yb^+$ vs detection time. The 369 nm intensity was set to equal I_{sat} and the 935 nm Intensity was set to equal $100\,I_{sat}$.

from the ion, λ_0/ρ_e, will equal 8600. Experimentally, the PMT collects an average of 18 photons[2]. This gives a collection efficiency of approximately 0.0021.

Using equations 3.23-3.26, the probability of detecting n photons within a detection time, t_D, can be calculated for an ion initially in the $|0\rangle$ and the $|1\rangle$ states. To distinguish between these states, a photon number known as the discriminator is chosen. If the number of detected photons is equal or below this number, the ion is recorded as being in the $|0\rangle$ state, overwise the ion is recorded as being in the $|1\rangle$ state. For the ideal case, where there is no background scatter, the discriminator will equal 0. The state detection fidelity is determined by adding the probability of an ion in the $|0\rangle$ state producing a number of photons equal or below the discriminator and the probability of an ion in the $|1\rangle$ state producing a number of photons above the discriminator.

Figure 3.6 shows the state detection infidelity vs the detection time for a range of 369 nm intensities with ρ_e equal to 0.0021. For each 369 nm intensity, the fidelity initially increases as the detection time is increased, this occurs as more photons from an ion in the $|1\rangle$ state can be collected. A optimum detection time is reached where the detection fidelity is maximum. At detection times above this optimum, the detection fidelity decreases due to off-resonant coupling.

The maximum detection fidelity increases as 369 nm intensity decreases due to a reduction in the off resonant pumping rate. In addition, as the 369 nm intensity is decreased, less photons are produced by the ion, therefore the detection time required to reach the

[2]Averaged over 200 runs.

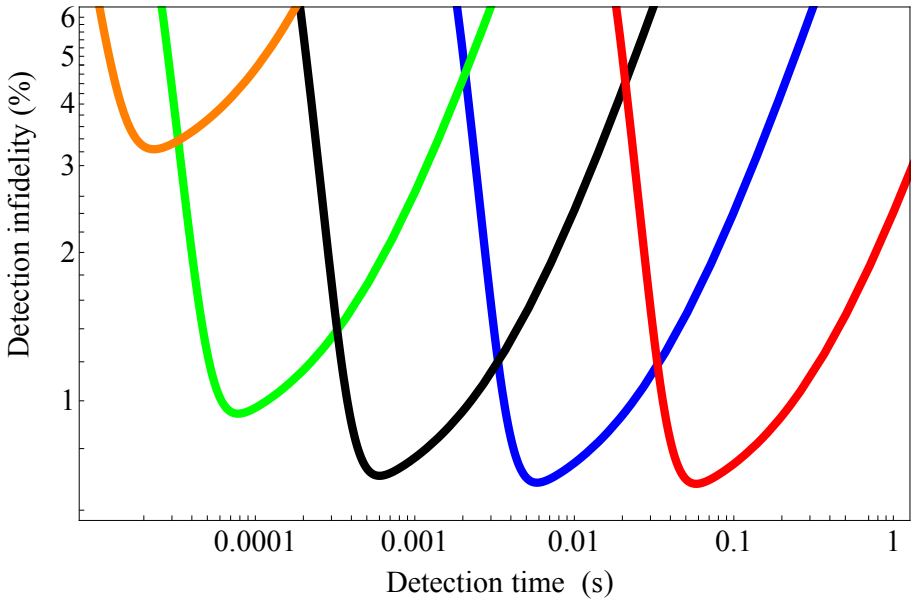

Figure 3.6: Graph showing the detection infidelity vs detection time for 369 nm intensities equal to 10 I_{sat} (orange), 1 I_{sat} (green), 0.1 I_{sat} (black), 0.01 I_{sat} (blue) and 0.001 I_{sat} (red). The graph was simulated using a collection efficiency equal to 0.0021 and a 935 nm intensity equal to 10 I_{sat}.

maximum fidelity increases. The maximum fidelity does however level out below 369 nm intensities of 0.01 I_{sat} at a maximum fidelity limit of 99.322 %. This maximum fidelity limit can be increased by increasing the systems collection efficiency. This is shown in figure 3.7 which shows the maximum state detection efficiency vs the detection time for a range of 369 nm intensities and collection efficiencies. Figure 3.7 shows that increasing the collection efficiency will both increase the maximum fidelity limit and decrease the detection time required to reach the limit. The calculated maximum detection fidelities are 98.598 %, 99.864 % and 99.985 % for collection efficiencies of 0.001, 0.01 and 0.1 respectively. The collection efficiency can be increased by improved collection optics as proposed in [48–51]. For example, detection efficiencies of up to 0.548 have been demonstrated by trapping within the focus of a parabolic mirror [52]. Using only optics external to the vacuum system, efficiencies of up to 0.1 have been achieved [53].

Within our current experimental setup, the optimum 369 nm intensity which provides a large fidelity within a relatively short time is 0.1 I_{sat} which should give a detection fidelity of > 99.3 % in approximately 1 ms as shown in figure 3.6.

3.2.2 935 nm power broadening

It is possible for off-resonant coupling to occur between the $^3D_{\frac{3}{2}}$ F = 1 and $^3D[3/2]_{\frac{1}{2}}$ F = 1 levels on the 935 nm transition. This is undesirable as the $^3D[3/2]_{\frac{1}{2}}$ F = 1 level can decay

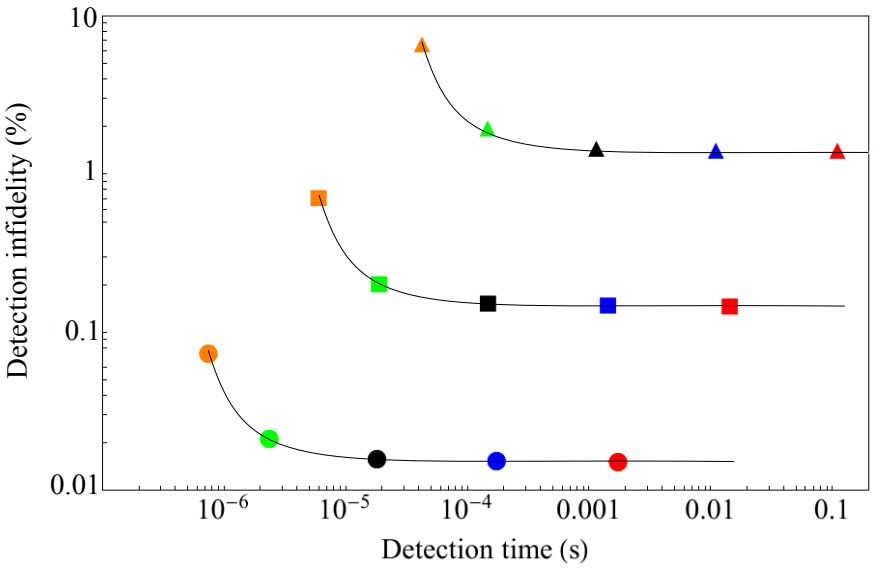

Figure 3.7: Graph showing the points of maximum detection fidelity for 369 nm intensities equal to 10 I_{sat} (orange), 1 I_{sat} (green), 0.1 I_{sat} (black), 0.01 I_{sat} (blue) and 0.001I_{sat} (red) with collection efficiencies equal to 0.1 (circles), 0.01 (squares) and 0.001 (triangles). The 935 nm intensity was set to equal 10 I_{sat}

into the $|0\rangle$ state as shown in table 3.2. The extent of which this effects the population is explored in figure 3.8 which shows the time taken for the population in $|0\rangle$ to reach 1% during detection when the initial population starts in $|1\rangle$. The graph shows that the 935 nm intensity has little observable effect until it reaches around 1000 I_{sat}. Above this, the power has significantly broadened the transition causing the effects of off-resonant coupling on the 935 nm transition to be dominant over the effects of the off-resonant coupling on the 369 nm transition which increases the rate at which population is added to the $|0\rangle$ state. The increase in preparation time shown on figure 3.8 at 935 nm intensities lower than 1 I_{sat} is due to population trapping in the $^3D_{\frac{3}{2}}$ F = 1 level.

3.3 State preparation

State preparation is the ability to prepare the ion into either the $|0\rangle$ state or the $|1\rangle$ state. State preparation into the $|0\rangle$ state is ideally achieved by the process shown in figure 3.9 where 2 GHz sidebands are added to the 369 nm cooling laser, usually resonant with the $^2S_{\frac{1}{2}}$ F = 1 to $^2P_{\frac{1}{2}}$ F = 0 transition, which allows the $^2P_{\frac{1}{2}}$ F = 1 levels to be populated from which population can decay into the $|0\rangle$ state. In addition, 3 GHz sidebands should be added to the 935 nm laser to stop population becoming trapped in the $^2D_{\frac{3}{2}}$ F = 2 level. Figure 3.10 shows the populations of all the levels vs time during preparation when all the population begins in the $^2S_{\frac{1}{2}}$ F = 1 $m_F = 0$ level. It shows that population is

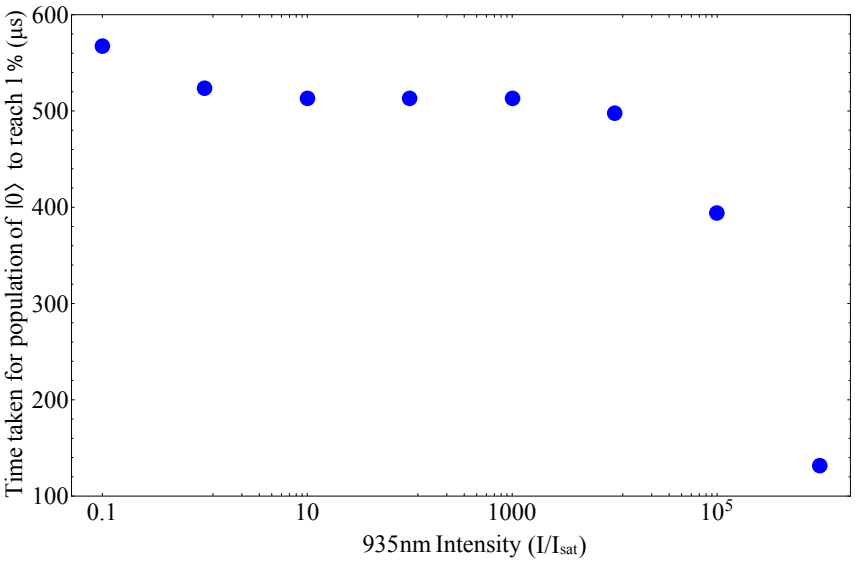

Figure 3.8: Time taken for population of the $|0\rangle$ state to reach 1 % during state detection as a function of 935 nm intensity. The 369 nm intensity is set to 0.1 I_{sat} and the population is initially in the $|1\rangle$ state.

quickly transferred between this and the $|0\rangle$ state via the other levels. To prepare the ion in the $|1\rangle$ state, the 369 nm laser is turned off and a microwave π pulse is applied at $\omega_{hf} = 2\pi \times 12.6\,\text{GHz}$.

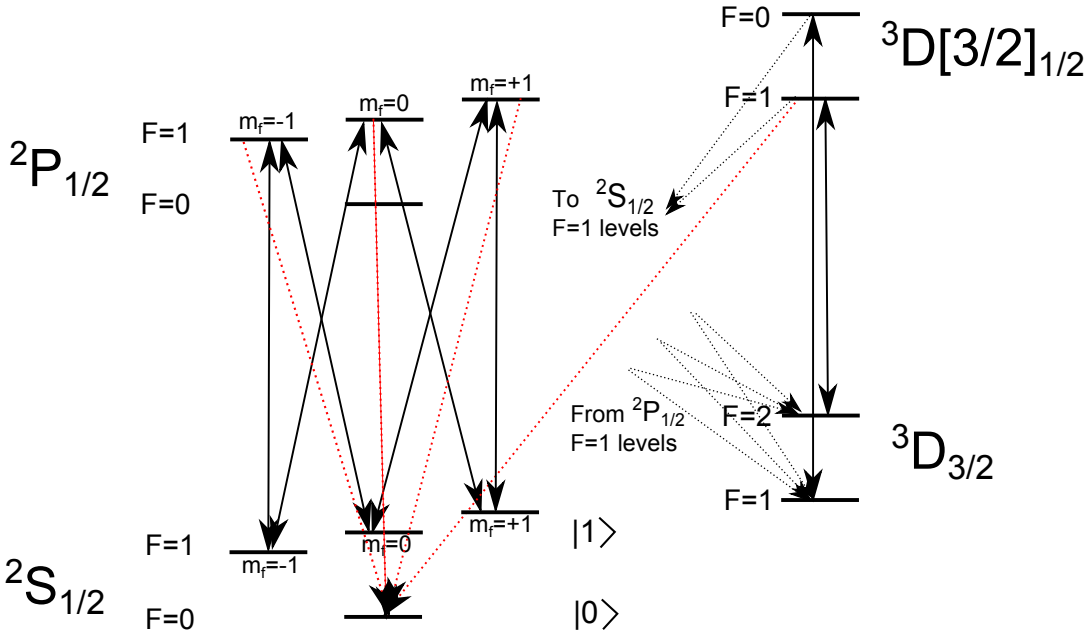

Figure 3.9: Transitions used to prepare ion into the $|0\rangle$ state.

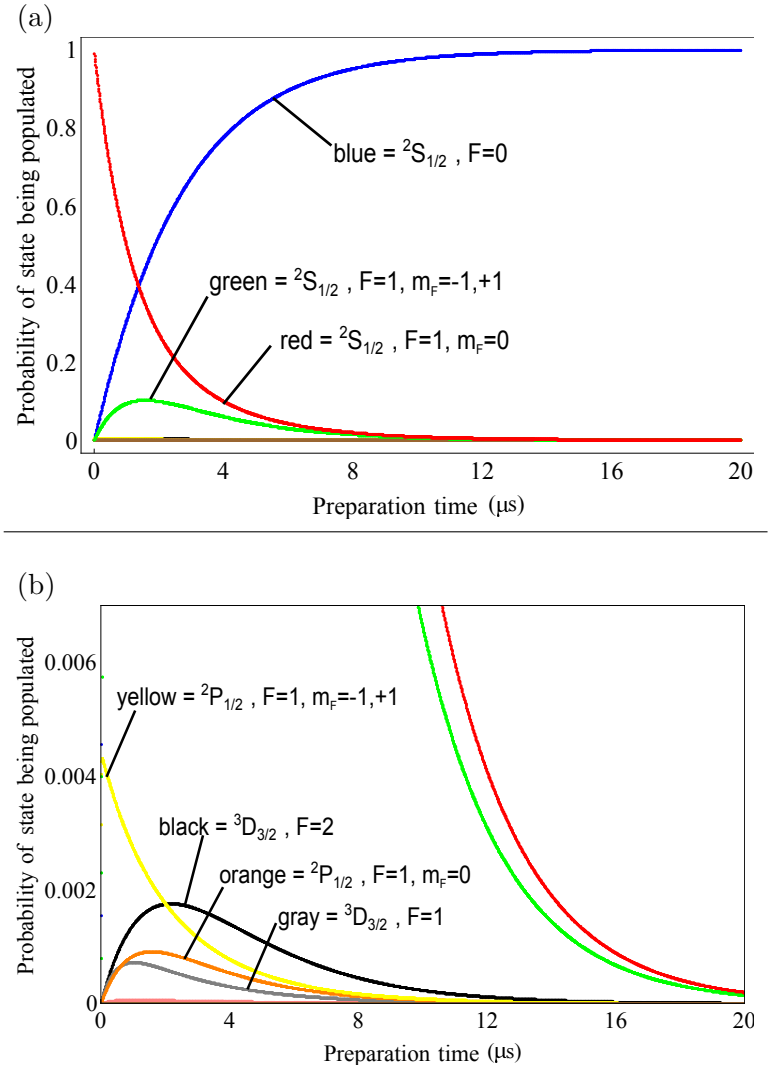

Figure 3.10: (a) Level populations during state preparation with population beginning in the $^2P_{\frac{1}{2}}$ F = 1 $m_F = 0$ level assuming no 369 nm carrier light is present and 50 % of the 935 nm light is within the 3 GHz sidebands. (b) is equivalent to (a) but with a different scale to distinguish the less populated levels. Data was found using the rate equation program with 369 nm and 935 nm intensity equal to 0.1 I_{sat} and 10 I_{sat} respectively. The probability of population being in the ^{3}D$[3/2]_{\frac{1}{2}}$ and ^{2}P$_{\frac{1}{2}}$ F = 0 levels is negligible and therefore not shown.

3.3.1 2 GHz 369 nm sidebands

Ideally, during state preparation, there would be no 369 nm light present resonant with the $^2S_{\frac{1}{2}}$ F = 1 to $^2P_{\frac{1}{2}}$ F = 0 transition as shown in figure 3.9. Light present at this frequency would result in an increased preparation time as population can be excited to the $^2P_{\frac{1}{2}}$ F = 0 level which is unable to decay into the $|0\rangle$ state. Complete suppression of the carrier frequency when adding sidebands can however be both difficult and expensive. Figure 3.11 shows the extent to which the ratio of 369 nm carrier intensity, I_c, to the 2 GHz side-

band intensity, I_{sb}, effects the preparation time at a range of different total intensities, ($I_t = I_c + I_{sb}$). As expected, the minimum preparation time is achieved when all the intensity is contained within the sidebands. The preparation time then rises exponentially as the power is moved into the carrier. In addition, figure 3.11 also shows that preparation time decreases with overall 369 nm intensity. For state preparation, higher intensities are therefore advantageous which is counter to detection where lower intensities are required to reduce off-resonant coupling. Experimentally, we add 2.1 GHz sidebands to the 369 nm

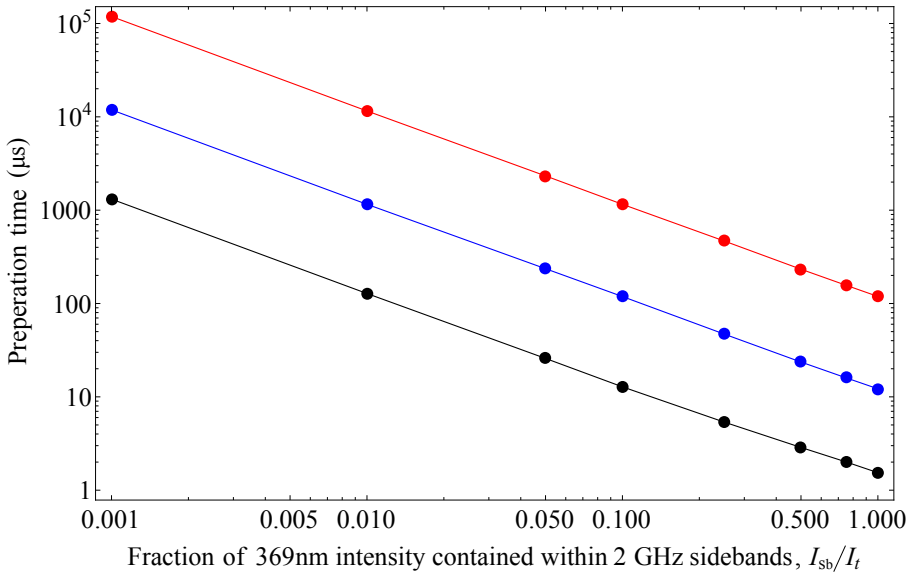

Figure 3.11: Effect the 2 GHz 369 nm sideband strength has on the preparation time of the $|0\rangle$ state, this data was collected using the rate equation program with the 935 nm intensity equal to 10 I_{sat} and the total 369 nm intensity, I_t equal to 0.01 I_{sat} (red), 0.1 I_{sat} (blue) and I_{sat} (black). The sideband intensity is distributed equally between the red and blue sidebands.

cooling beam by applying 1.05 GHz sidebands to a 739 nm laser beam which is then frequency doubled (see section 2.3.3). These 1.05 GHz sidebands can be added by one of two methods. Firstly, the current powering the laser diode of the 739 nm Toptica laser can be modulated at 1.05 GHz. This method is however limited as the carrier frequency of the laser changes significantly when sideband powers higher than a percent are applied which causes the doubling cavity to unlock. Figure 3.12 (a) shows the minimum preparation time achievable with this method is 900 μs. A more successful method is to put a 1.05 GHz EOM into the beam path of the 739 nm laser. This method allows at least 45 % of the light to be in the sidebands which gives a minimum preparation time of 15 μs as shown in figure 3.12 (b). The error bars in figure 3.12 represent a 70 % binomial confidence interval as discussed in appendix B. Unless overwise stated, all error bars within this thesis will be calculated in the same way.

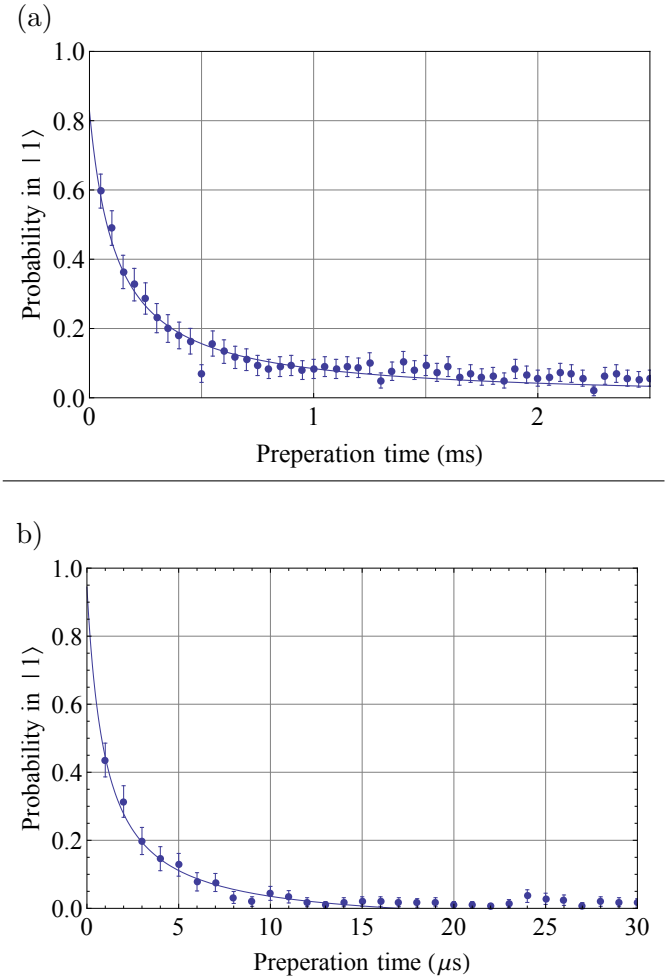

Figure 3.12: Population of the $|1\rangle$ state vs detection time with (a) approximately 1 % of the 369 nm intensity in the sidebands formed from modulation of the 739 nm Toptica diode. (b) Approximately 45 % of the 369 nm intensity in the sidebands formed using an EOM in the beam path of the 739 nm beam. Both graphs were taken with a 369 nm laser power of approximately 1.2 μW focused down to a 60 μm beam waist and a 935 nm laser power of approximately 6mW focused down to a beam waist of approximately 1 mm. This gives intensities at the ion equal to $\mathrm{I}_{369} \approx 0.4\,\mathrm{I}_{sat}$ and $\mathrm{I}_{935} \approx 500\,\mathrm{I}_{sat}$. The population at each point is calculated by averaging the results of 100 runs.

3.3.2 3 GHz 935 nm sidebands

During state preparation, as shown in figure 3.9, population within the $^2\mathrm{P}_{\frac{1}{2}}$ F = 1 levels can decay into the $^3\mathrm{D}_{\frac{3}{2}}$ F = 2 level. 3 GHz 935 nm sidebands can be added to the 935 nm laser resonant with the $^3\mathrm{D}_{\frac{3}{2}}$ F = 1 to $^3\mathrm{D}[3/2]_{\frac{1}{2}}$ F = 0 transition to avoid population becoming trapped within the $^2D_{\frac{3}{2}}$ F = 2 level. To remove any trapped population, as little as 1 % of the total 935 nm power is required to be within the sidebands. This can be achieved by modulating the current powering the 935 nm laser diode by combining 3 GHz with the DC current supply using a bias-tee[3]. This can however reduce the effectiveness of the 935 nm

[3]Mini-Circuit ZFBT-4R2G+

frequency locking. The amount of trapped population is however only on the order of 0.6 % as shown in figure 3.13, this is a negligible amount therefore for the majority of experiments outlined in this thesis, these sidebands were not be present.

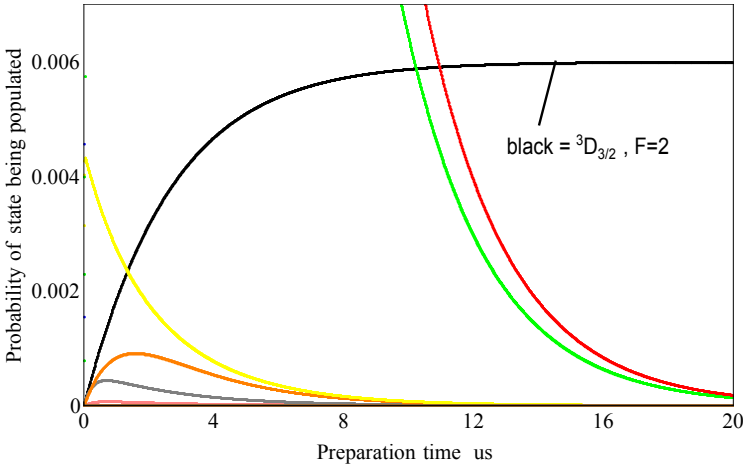

Figure 3.13: Figure showing the population of the levels during preparation with no 3 GHz sidebands on the 935 nm repumper light. Levels are coloured as shown in figure 3.10. The population becoming trapped in the $^3D_{\frac{3}{2}}$ F = 2 level increases and reaches a steady state value of approximately 0.6 %.

3.4 Experimental results

Figure 3.14 shows the probability certain numbers of photons will be detected during the detection time for an ion prepared in the $|0\rangle$ state (blue) and the $|1\rangle$ state (purple). To prepare the ion in the $|0\rangle$ state, a 369 nm beam with a intensity equal to 25 I_{sat} was applied for 50 μs with 45 % of the light within the 2 GHz sidebands. As shown in figure 3.11, these parameters should be adequate to prepare the state into the $|0\rangle$ state. More than zero photons are however still being counted with a probability of more than 20 %. This is due to back-ground scatter from for example, 369 nm photons scattering off the electrodes. This is currently the limiting factor of our state detection fidelity.

During detection, a 369 nm beam of approximately 0.4 I_{sat} was applied. This intensity is however an overestimate as the 369 nm beam power was measured just before the final lens and therefore does not take into account power loss from the final lens and the vacuum system window. The optimal state detection time, where the detection fidelity was found to be maximum was found to be around 1200 μs which suggests the the 369 nm intensity at the ion is slightly less than 0.1 I_{sat}.

Using figure 3.14 it can be concluded that if three or more photons are collected during detection the ion is most probably in the $|1\rangle$ state and if only zero, one or two photons

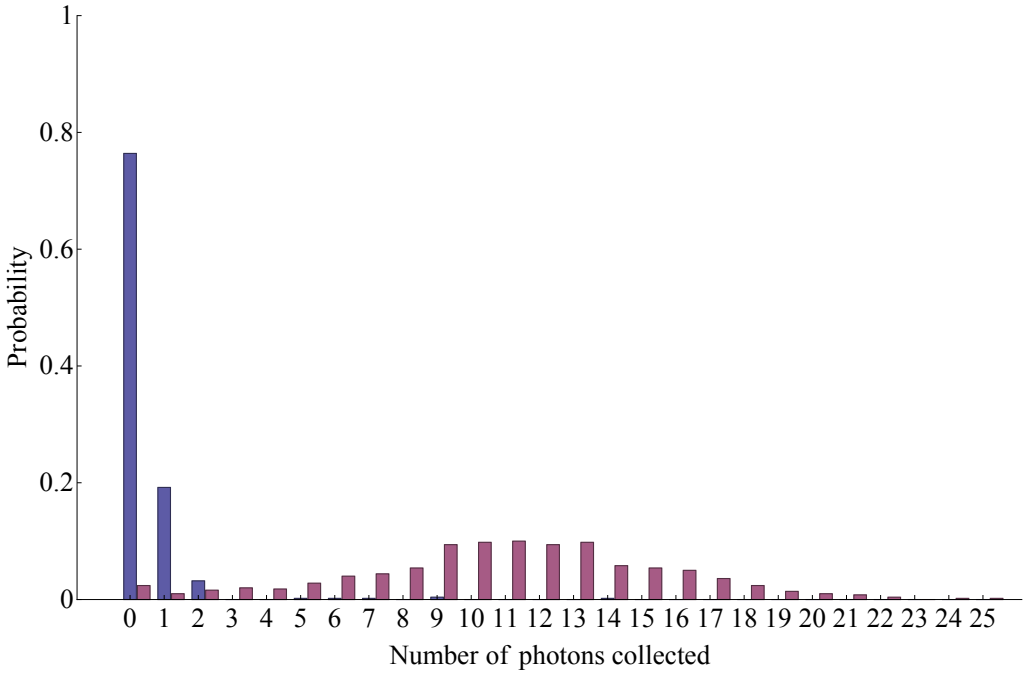

Figure 3.14: Probability of the detection of certain photon numbers from an ion prepared in the $|0\rangle$ state (blue) and the $|1\rangle$ state (purple). The $|0\rangle$ state was prepared with 60 μW of 369 nm light focused down to a beam waist of 60 μm with 45 % of this light contained within the 2 GHz sidebands. The $|1\rangle$ state was prepared by applying a microwave pulse to an ion in the $|0\rangle$ state. During detection, 1.2 μW of 369 nm light was focused down to a beam waist of 60 μm for 1.5 ms. The 935 nm beam intensity was equal to 500 I_{sat}. The graph is an average of 500 measurements. Using a discriminator of 3, the state detection fidelity is approximately 95%.

are collected the ion is most probably in the $|0\rangle$ state. This gives a state detection fidelity of approximately 95 %.

3.5 Preparation of superposition states

The fundamental difference between classical and quantum bits is that in addition to the $|0\rangle$ and $|1\rangle$ states, a quantum bit can also exist in a superposition state represented by the following equation,

$$|\psi\rangle = q_0 |0\rangle + q_1 |1\rangle \tag{3.28}$$

where q_0 and q_1 obey the relation $q_0^2 + q_1^2 = 1$. For simplicity, equation 3.28 can also be represented in matrix form as

$$|\psi\rangle = \begin{pmatrix} q_0 \\ q_1 \end{pmatrix}. \tag{3.29}$$

Upon measurement, the ion will collapse into the $|0\rangle$ or $|1\rangle$ state with a probability equal to q_0^2 or q_1^2 respectively. A useful way to visualise superposition states is to represent them

as a point on a diagram known as the Bloch sphere, as shown in figure 3.15. The $|0\rangle$ and $|1\rangle$ states are located on the z-axis of the Bloch sphere at the respective minimum and maximum points. Points on the equator of the Bloch sphere represent ideal superpositions where the ion is in $|0\rangle$ or $|1\rangle$ with equal probability ($q_0^2 = q_1^2 = \frac{1}{2}$). Section 3.3 described

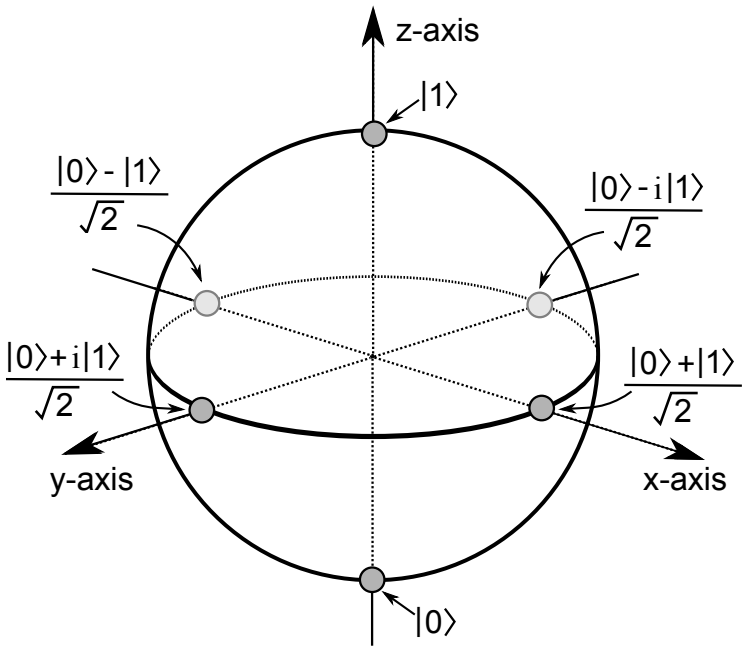

Figure 3.15: The Bloch sphere

how an ion can be prepared in the $|0\rangle$ and $|1\rangle$ state; here I will show how arbitrary superposition states of the form given in equation 3.28 can be realised by applying coherent radiation to the ion.

3.5.1 Optical Bloch equations

The Hamiltonian describing a two level system interacting with a electromagnetic field is given by

$$\hat{H} = \hat{H}_0 + \hat{H}' \tag{3.30}$$

where H_0 is the unperturbed Hamiltonian describing the system without the applied field and is given by the sum of the Hamiltonian of a two level system, H_a and the Hamiltonian of a trapped ion which can be modeled as a quantum harmonic oscillator, H_b [47],

$$\hat{H}_0 = \hat{H}_a + \hat{H}_b \tag{3.31}$$

where

$$\hat{H}_a = \frac{1}{2}\hbar\omega_{hf}\hat{\sigma}_z \tag{3.32}$$

and

$$\hat{H}_b = \hbar v \hat{a}^\dagger \hat{a}. \tag{3.33}$$

ω_{hf} is the resonant frequency of the two level system, v is the trap secular frequency, a and $a^\dagger$ are the quantum raising and lowering operators and σ_z is the Pauli-z operator which is given in matrix form as

$$\hat{\sigma}_z = \begin{pmatrix} 1 & 0 \\ 0 & -1 \end{pmatrix} \tag{3.34}$$

and acts by rotating the state of the system by 180 degrees around the z-axis of the Bloch sphere.

$\hat{H}'$ is the perturbation due to the field given by equation 3.10,

$$\hat{H}' = -\mathbf{p} \cdot \mathbf{E}. \tag{3.35}$$

Assuming the electromagnetic field is propagating along the -**z** direction, this can be expanded into the following form

$$\begin{aligned} \hat{H}' &= -p_z E_z cos(\omega_M t - kz + \phi) \\ &= -\frac{p_z E_z}{2}[e^{i(\omega_M t - kz + \phi)} + e^{-i(\omega_M t - kz + \phi)}] \end{aligned} \tag{3.36}$$

where w_M is the field frequency and ϕ is the fields phase. To express equation 3.36 in terms of the Rabi frequency, Ω, it can be multiplied on either side by the relation

$$\sum_u |u\rangle \langle u| = 1 \tag{3.37}$$

giving

$$\begin{aligned} \sum_{u,v} |u\rangle \langle u| \hat{H}' |v\rangle \langle v| &= \hat{H}' \\ &= -\sum_{u,v} |u\rangle \langle u| \frac{p_z E_z}{2} |v\rangle \langle v| [e^{i(\omega_M t - kz + \phi)} + e^{-i(\omega_M t - kz + \phi)}]. \end{aligned} \tag{3.38}$$

This can be simplified and written in terms of Ω using equations 3.12 and 3.16,

$$\hat{H}' = -\sum_{u,v} \frac{\hbar\Omega}{2} |u\rangle \langle v| [e^{i(\omega_M t - kz + \phi)} + e^{-i(\omega_M t - kz + \phi)}] \tag{3.39}$$

In a two level system, the perturbation Hamiltonian caused by an electromagnetic field is

therefore given by,

$$H' = -\frac{\hbar\Omega}{2}(\hat{\sigma}_+ + \hat{\sigma}_-)|[e^{i(\omega_M t - kz + \phi)} + e^{-i(\omega_M t - kz + \phi)}] \tag{3.40}$$

where $\sigma_+ = \begin{pmatrix} 0 & 1 \\ 0 & 0 \end{pmatrix}$ and $\sigma_- = \begin{pmatrix} 0 & 0 \\ 1 & 0 \end{pmatrix}$.

State evolution

The evolution of a state under the total Hamiltonian given by equation 3.30 is found using the time dependent Schrödinger equation

$$i\hbar\frac{d}{dt}|\Psi(t)\rangle = \hat{H}|\Psi(t)\rangle \tag{3.41}$$

where $|\Psi(t)\rangle$ is the wavefunction of the system which can be expressed as the complete set of the eigenstates of $\hat{H}_0$ [1],

$$|\Psi(t)\rangle = \sum_u q_u(t)e^{iE_u t/\hbar}|u\rangle \tag{3.42}$$

where $\hat{H}_0|u\rangle = E_u|u\rangle$. Combining equations 3.30, 3.41 and 3.42 gives

$$\sum_u \left(i\hbar\dot{q}_u e^{-iE_u t/\hbar} + q_u E_u e^{-iE_u t/\hbar}\right)|u\rangle = \sum_u q_u e^{-iE_u t/\hbar}(\hat{H}_0 + \hat{H}')|u\rangle\,. \tag{3.43}$$

This simplifies to

$$\sum_u i\hbar\dot{q}_u e^{-iE_u t/\hbar}|u\rangle = \sum_u q_u e^{-iE_u t/\hbar}\hat{H}'|u\rangle\,. \tag{3.44}$$

Taking the inner product of one of the coefficients, v gives

$$i\hbar\dot{q}_v e^{-iE_v t/\hbar} = \sum_u q_u e^{-iE_u t/\hbar}\langle v|\hat{H}'|u\rangle\,. \tag{3.45}$$

Using equation 3.40 and assuming the wavelength of light is a lot larger than the spatial extent of the ion ($kz \approx 0$), the expression $\langle v|\hat{H}'|u\rangle$ is equal to

$$\langle v|\hat{H}'|u\rangle = -\frac{\hbar\Omega}{2}\left(e^{i(\omega_M t + \phi)} + e^{-i(\omega_M t + \phi)}\right)(\langle v|\hat{\sigma}_+|u\rangle + \langle v|\hat{\sigma}_-|u\rangle) \tag{3.46}$$

Putting equation 3.46 into equation 3.45 and using the relations $\langle 0|\hat{\sigma}_{+/-}|0\rangle = \langle 1|\hat{\sigma}_{+/-}|1\rangle = \langle 1|\hat{\sigma}_+|0\rangle = \langle 0|\hat{\sigma}_-|1\rangle = 0$ and $\langle 0|\hat{\sigma}_+|1\rangle = \langle 1|\hat{\sigma}_-|0\rangle = 1$ gives the following simultaneous

equations for a two level system.

$$\dot{q}_0 = iq_1\frac{\Omega}{2}e^{-i\omega_{01}}\left(e^{i(\omega_M t+\phi)} + e^{-i(\omega_M t+\phi)}\right) \tag{3.47}$$

$$\dot{q}_1 = iq_0\frac{\Omega}{2}e^{i\omega_{01}}\left(e^{i(\omega_M t+\phi)} + e^{-i(\omega_M t+\phi)}\right) \tag{3.48}$$

where $\omega_{01} = \frac{E_1-E_0}{\hbar}$ is the frequency difference between the two levels. These equations can be simplified by noting that at on large timescales ($t >> \omega_{01}+\omega_M$), the fast oscillating terms $e^{\pm i(\omega_{01}+\omega_M t+\phi)}$ average to zero. This is known as the rotating wave approximation and allows equations 3.47 and 3.48 to be rewritten as

$$\dot{q}_0 = iq_1\frac{\Omega}{2}e^{i(\Delta t+\phi)} \tag{3.49}$$

$$\dot{q}_1 = iq_0\frac{\Omega}{2}e^{-i(\Delta t+\phi)} \tag{3.50}$$

where $\Delta = \omega_M - \omega_{01}$ is the detuning of the field from resonance. These are known as the optical Bloch equations for a two level system and describe the rate of probability transfer between the states. In matrix form equations 3.49 and 3.50 can be expressed together as

$$\begin{pmatrix} \dot{q}_0 \\ \dot{q}_1 \end{pmatrix} = i\frac{\Omega}{2}\begin{pmatrix} 0 & e^{i\Delta t+\phi} \\ e^{-i\Delta t+\phi} & 0 \end{pmatrix}\begin{pmatrix} q_0 \\ q_1 \end{pmatrix}. \tag{3.51}$$

It should be noted that in the derivation above, state changes due to spontaneous decay were assumed to be equal to zero. Our qubit states have a lifetime of ≈ 1 year [23] which is a lot longer than any experiment we plan on doing therefore this assumption remains valid.

3.5.2 Rabi flopping

The solution to the two level optical Bloch equations given in equations 3.49 and 3.50 can be found in appendix C. For the simple case where the detuning equals zero, the solution is equal to

$$\begin{aligned} q_0 &= \cos\frac{\Omega t}{2} \\ q_1 &= ie^{-i\phi}\sin\frac{\Omega t}{2} \end{aligned} \tag{3.52}$$

when the ion is initially in the $|0\rangle$ state ($q_0 = 1$, $q_1 = 0$ at t = 0) and

$$\begin{aligned} q_0 &= ie^{i\phi}\sin\frac{\Omega t}{2} \\ q_1 &= \cos\frac{\Omega t}{2} \end{aligned} \tag{3.53}$$

when the ion is initially in the $|1\rangle$ state ($q_0 = 0$, $q_1 = 1$ at t = 0). When the ion begins in a superposition of the states (ie, where $|\phi(0)\rangle = q_0(0)\,|0\rangle + q_1(0)\,|1\rangle$) the final state after time, t, is therefore given by the application of the following matrix on the initial state.

$$\Pi = \begin{pmatrix} \cos\frac{\Omega t}{2} & ie^{-i\phi}\sin\frac{\Omega t}{2} \\ ie^{i\phi}\sin\frac{\Omega t}{2} & \cos\frac{\Omega t}{2} \end{pmatrix} \tag{3.54}$$

The state will oscillate between $|0\rangle$ and $|1\rangle$ with a frequency equal to Ω, this is known as Rabi flopping. The exact path the population takes around the Bloch sphere is determined by the phase of the applied field, ϕ, as shown in figure 3.16. For example, when $\phi = 0$, the population rotates around the y-axis and when $\phi = \frac{\pi}{2}$, the population will rotate around the x-axis. It is therefore possible to reach any point on the Bloch sphere after time, t, by careful selection of ϕ and Ω.

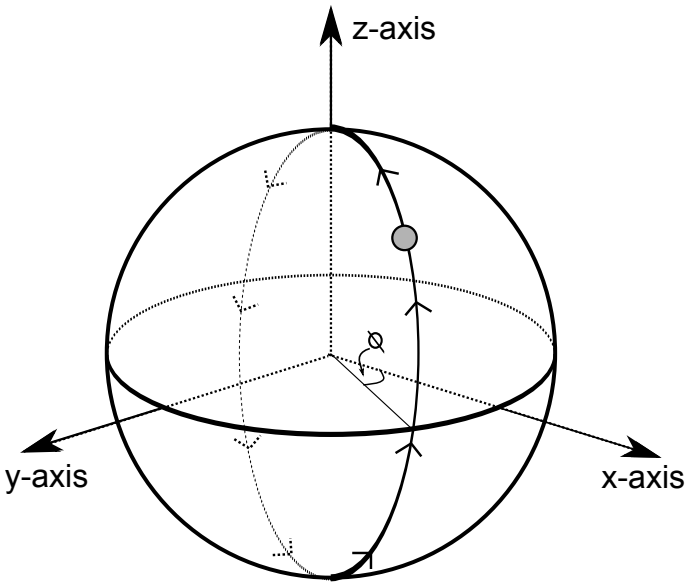

Figure 3.16: Figure showing the path the population takes around the Bloch sphere during Rabi flopping. The angle ϕ is set by the phase of the applied field.

Experimental realisation

To Rabi flop on a transition within the $^2\mathrm{S}_{\frac{1}{2}}$ level, microwave pulses at the frequency of that transition must be applied. As the three m_F states within the $^2S_{\frac{1}{2}}$ F = 1 level of $^{171}\mathrm{Yb}^+$ are split in frequency space due to the Zeeman effect, the exact frequencies of these states are hard to calculate theoretically. This is due to difficulty in measuring the exact magnetic field strength at the ion. The transition frequencies between these states and the $|0\rangle$ state are therefore determined experimentally by performing a microwave frequency scan.

A microwave frequency scan is preformed by first preparing the ion into the $|0\rangle$ state,

a microwave pulse of a set length is then applied before detection. The frequency of this pulse is then adjusted before the next experiment run. Figure 3.17 shows the pulse sequence and results of this experiment. Figure 3.17 (a) is a frequency scan over the whole qubit subspace, it shows three main peaks which represent the resonances of the transitions between the $|0\rangle$ state and the three m_F levels within the ${}^2S_{\frac{1}{2}}$ F = 1 level. Figure 3.17 (b) shows a more detailed frequency scan over the centre peak representing the $|0\rangle$ to ${}^2S_{\frac{1}{2}}$ F = 1 $m_F = 0$ transition. The data in figure 3.17 was taken with a microwave pulse time, t, equal to $t_\pi = \frac{\pi}{\Omega_0}$ where Ω_0 is the on-resonance Rabi frequency of the ${}^2S_{\frac{1}{2}}$ F = 1 $m_F = 0$ transition. This Rabi frequency is determined by performing a Rabi flop on the transition.

A Rabi flop is preformed in a similar way to a frequency scan, the only differences are that the frequency of the microwave pulse is held constant at the transition frequency and the pulse duration is adjusted between experiment runs. Figure 3.18 shows a Rabi flop between the $|0\rangle$ state and the ${}^2S_{\frac{1}{2}}$ F = 1 $m_F = 0$ (a) and $m_F = +1$ (c) levels. The Rabi frequency can be seen to be equal to $\approx 2\pi\times$ 1.9 kHz for the Rabi flop in figure 3.18 (a) and $\approx 2\pi\times$ 50 kHz for the Rabi flop in figure 3.18 (b). The Rabi flops slowly decay over time due to decoherence caused by, for example, frequency noise from the microwave setup and magnetic field noise which effects the level frequencies. The point at which the amplitude is $\frac{1}{e}$ of its initial value is known as the decoherence time and is smaller for the $|0\rangle$ to ${}^2S_{\frac{1}{2}}$ F = 1 $m_F = \pm 1$ transitions as these are more sensitive to magnetic field fluctuations. For these transitions, the decoherence time is found to be less than 500 μs. The decoherence time for the $|0\rangle$ to ${}^2S_{\frac{1}{2}}$ F = 1 $m_F = 0$ transition can be found using a technique known as Ramsey fringes and will be discussed in section 3.5.3.

3.5.3 Ramsey fringes

When the microwave frequency field is turned off, a two level system will evolve according to the Hamiltonian given in equation 3.31. Moving into the rotating frame with respect to the microwave field frequency, ω_M, results in the following Hamiltonian under the rotating wave approximation,

$$\hat{H}_0 = \frac{1}{2}\hbar\Delta\hat{\sigma}_z \tag{3.55}$$

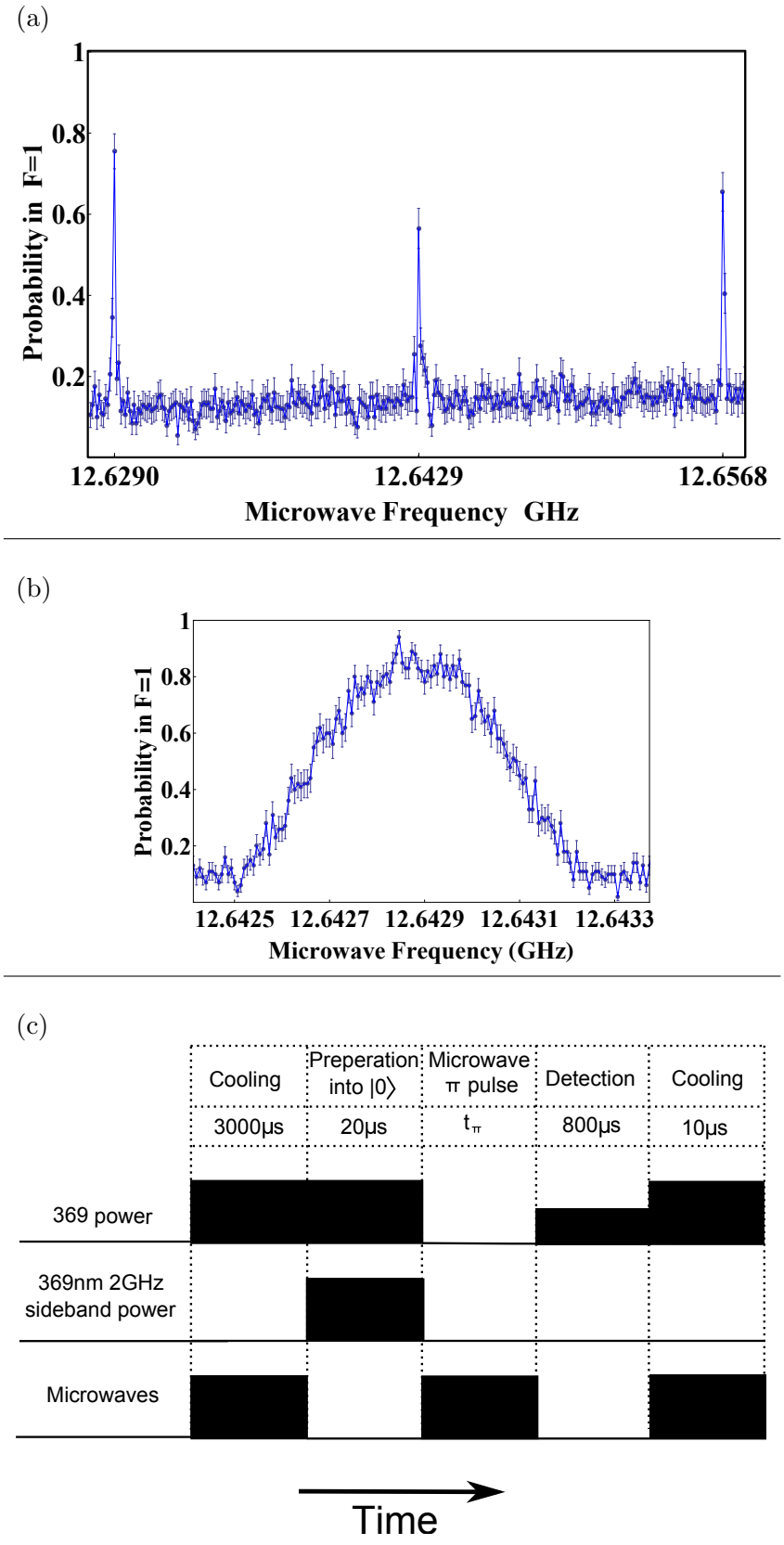

Figure 3.17: Microwave frequency sweep over the (a) whole qubit subspace and (b) $|0\rangle$ to ${}^2S_{\frac{1}{2}}$ $F=1$ $m_F=0$ transition. The pulse sequence for these sweeps is shown in (c). After preparation into $|0\rangle$, a π pulse is applied to the ion, this puts the ion into the $|1\rangle$ state for detection if the applied microwave frequency is resonant with a transition.

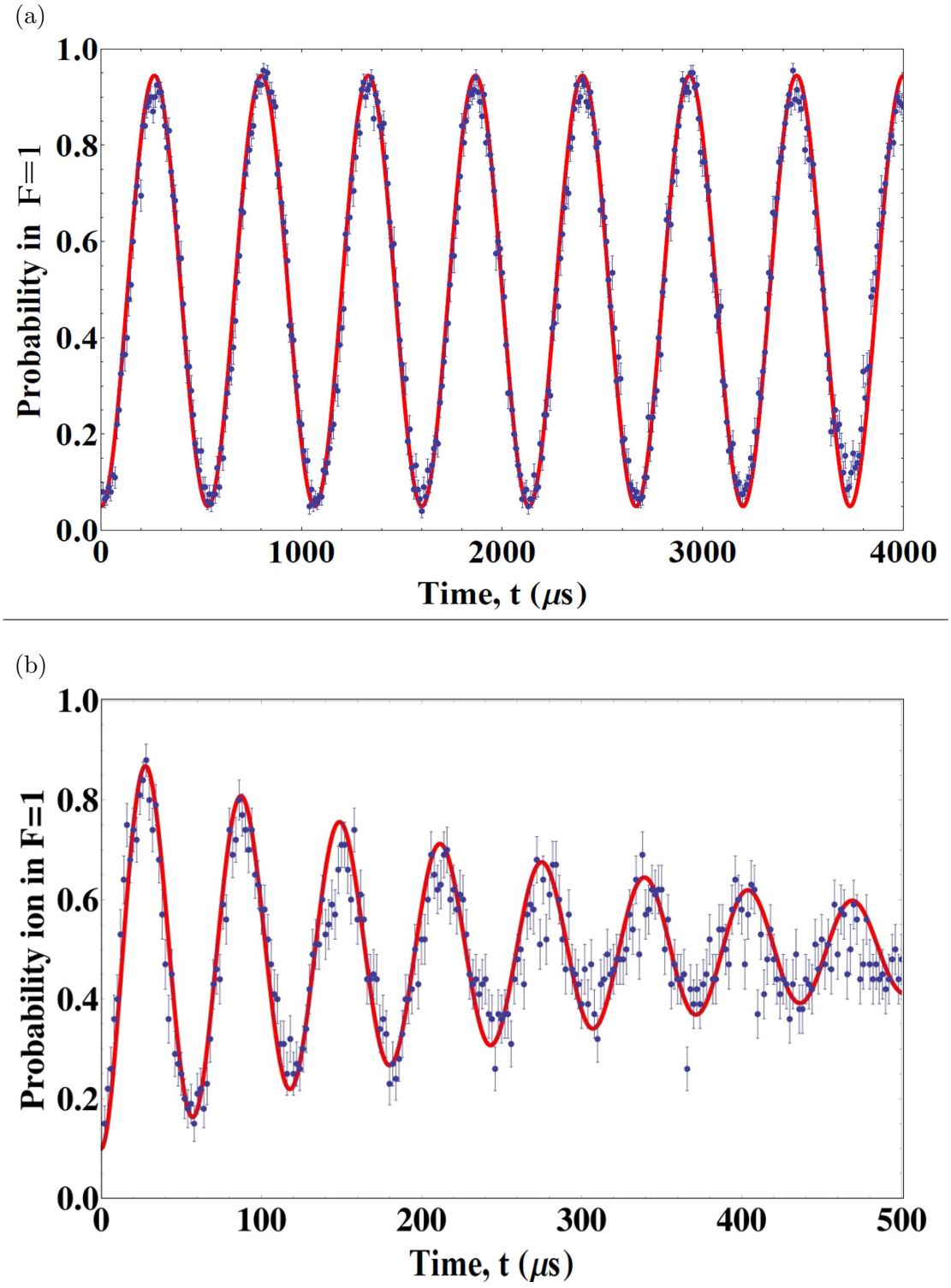

Figure 3.18: Rabi flops between the $|0\rangle$ and (a) $^2S_{\frac{1}{2}}$ $F=1$ $m_F=0$ and (b) $^2S_{\frac{1}{2}}$ $F=1$ $m_F=+1$ states. After preparation, a microwave pulse is applied, the length of this pulse is increased after each run. The Rabi frequency is equal to (a) $2\pi \times 1875\,\mathrm{kHz}$ and (b) $2\pi \times 18.5\,\mathrm{kHz}$.

where $\Delta = \omega_{hf} - \omega_M$. Evolution under this Hamiltonian is given by

$$\begin{aligned} U &= e^{\frac{-iH_0 t_p}{\hbar}} \\ &= e^{\frac{-i\hbar\Delta t_p \sigma_z}{2}} \\ &= \cos\tfrac{\Delta t_p}{2}\sigma_0 - i\sin\tfrac{\Delta t_p}{2}\sigma_z \end{aligned} \tag{3.56}$$

where t_p is the evolution time. In matrix form, this is equivalent to

$$U = \begin{pmatrix} \cos\frac{\Delta t_p}{2} - i\sin\frac{\Delta t_p}{2} & 0 \\ 0 & \cos\frac{\Delta t_p}{2} + i\sin\frac{\Delta t_p}{2} \end{pmatrix}. \tag{3.57}$$

When applied to an arbitrary initial state, this matrix leaves the state unchanged and adjusts the state's phase. This is equivalent to a rotation around the z-axis of the Bloch sphere at a frequency equal to Δ as shown in figure 3.19 (a).

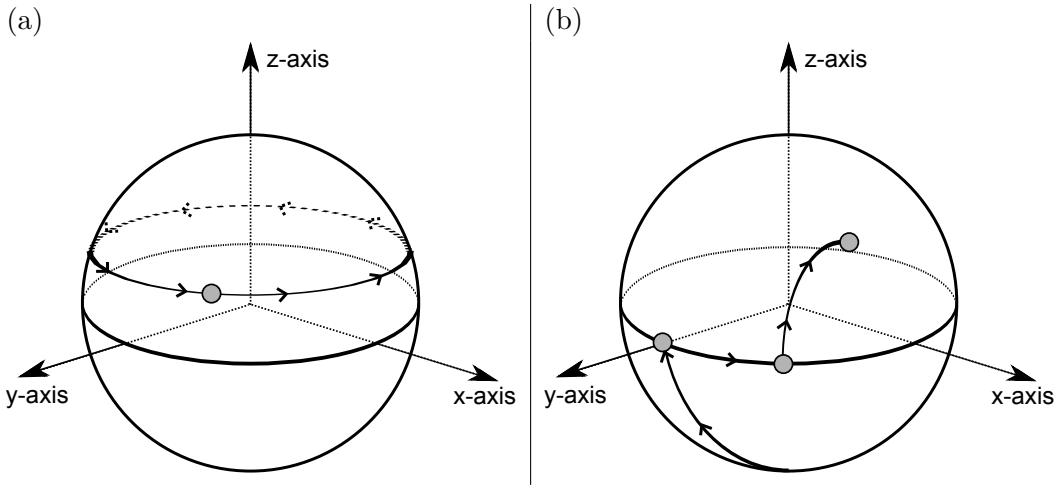

Figure 3.19: (a) Diagram showing movement around the Bloch sphere caused by the free evolution of a two-level system. (b) Diagram showing path along Bloch sphere and resulting Bloch sphere position when two $\frac{\pi}{2}$ pulses of a fixed phase, separated by an arbitrary time, t_p, are applied to the ion.

This rotation means that two $\frac{\pi}{2}$ pulses with equal phase, ϕ, separated in time, t_p, known as the free precession time will only produce a spin flip when $\Delta = 0$ or $\frac{\Delta t_p}{2} = 2\pi m$ where m is an integer. When these conditions are not met, the second pulse will move the ion along the same plane of the Bloch sphere as the first pulse as shown in figure 3.19 (b) and the resultant state will be a superposition of $|0\rangle$ and $|1\rangle$. The resultant population of the state as a function of t_p will therefore oscillate between $|0\rangle$ and $|1\rangle$. These oscillations are known as Ramsey fringes.

Experimental realisation

A Ramsey fringe on the $|0\rangle$ to $^2S_{\frac{1}{2}}$ F = 1 $m_F = 0$ transition with the accompanying pulse sequence is shown in figure 3.20. After preparation in $|0\rangle$, the ion is moved onto the equator of the Bloch sphere with a slightly detuned microwave pulse for a time, $t_{\frac{\pi}{2}} = \frac{\pi}{2\Omega_0}$. After a time, t_p, a second microwave pulse is applied for a time $t_{\frac{\pi}{2}}$. The final population is shown to oscillate as the precession time, t_p, is increased. This shows the ions movement around the Bloch sphere during t_p and therefore the frequency of these oscillations equals the detuning of the microwave pulses from resonance.

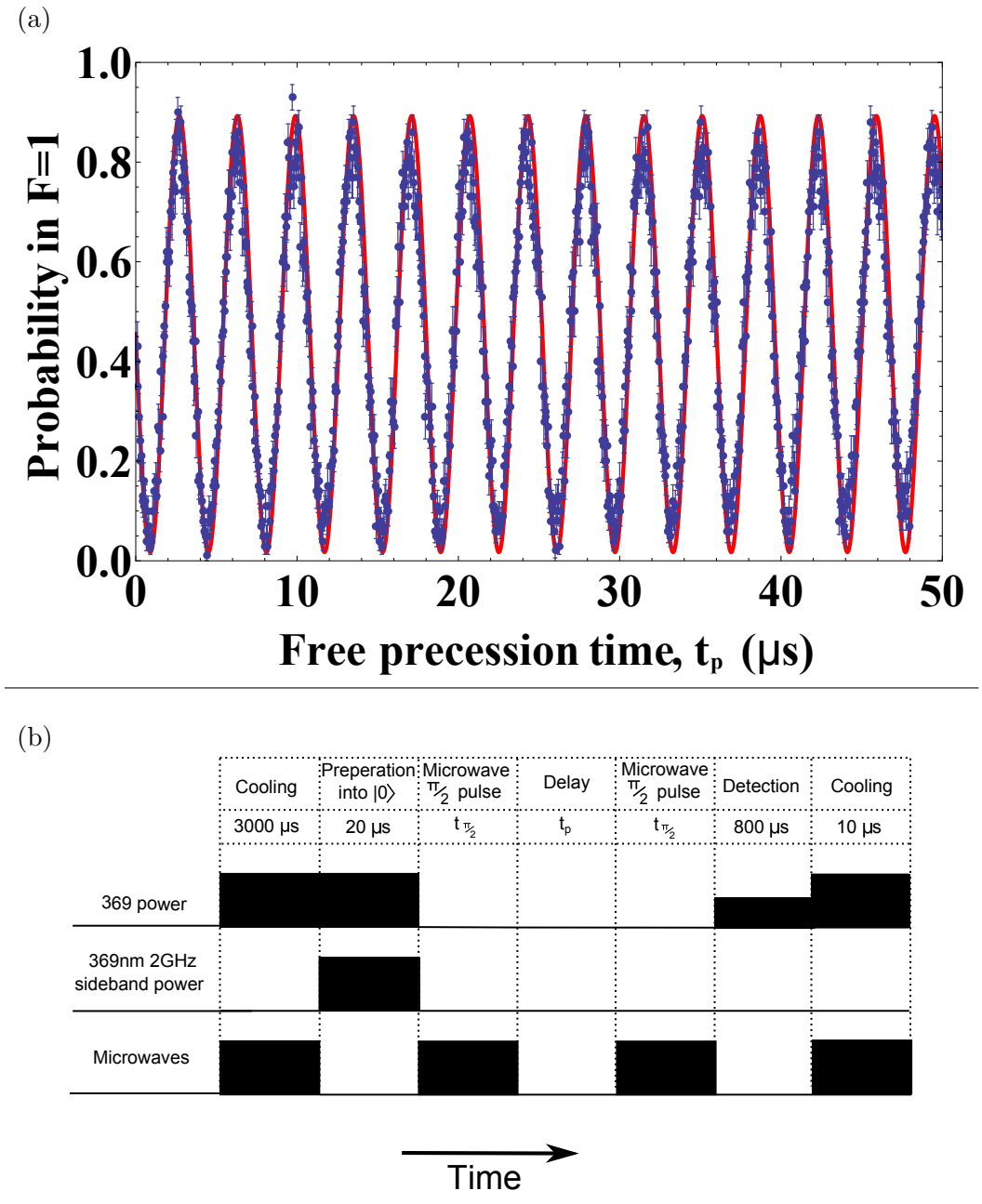

Figure 3.20: (a) Ramsey fringes on the $|0\rangle$ to $^2S_{\frac{1}{2}}$ F = 1 $m_F = 0$ transition. (b) Pulse sequence used to produce (a). Each point is an average of 100 measurements.

Measuring coherence time

A similar effect can be found with a fixed t_p by adjusting the phase of the second microwave pulse. The coherence time is found by measuring the contrast of these fringes at different values of t_p. This will decay exponentially over time as the state decoheres. This requires a change in the microwave setup, initially introduced in section 2.5.2 and shown in figure 2.18, as shown in figure 3.21 in order to have individual control of the parameters of each pulse.

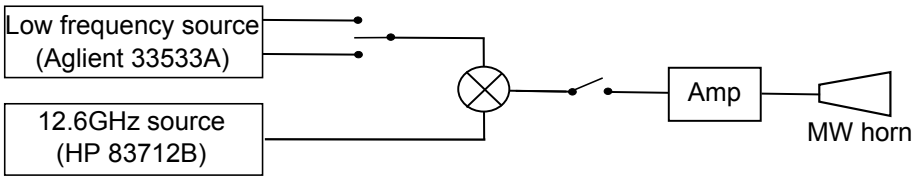

Figure 3.21: Modification of microwave setup to allow individual phase control of two microwave pulses. The 12.6 GHz frequency source is used to produce a signal several MHz away from resonance, this is then mixed using a high frequency mixer (Mini-Circuits ZX05-153LH-S+) with a signal from a second frequency source which brings the total frequency back to resonance. The signal from the second frequency sources can be switched between two separate channels each with independent phases.

An example of the resultant fringes for the $|0\rangle$ to $^2\mathrm{S}_{\frac{1}{2}}$ $\mathrm{F}=1$ $\mathrm{m}_F=0$ transition is given in figure 3.22 (a). The fringe contrast is measured to be the difference between the highest point and lowest point of the fringe. The contrast measured at different values of t_p is shown in figure 3.22 (b) which gives a coherence time of 1.5 seconds.

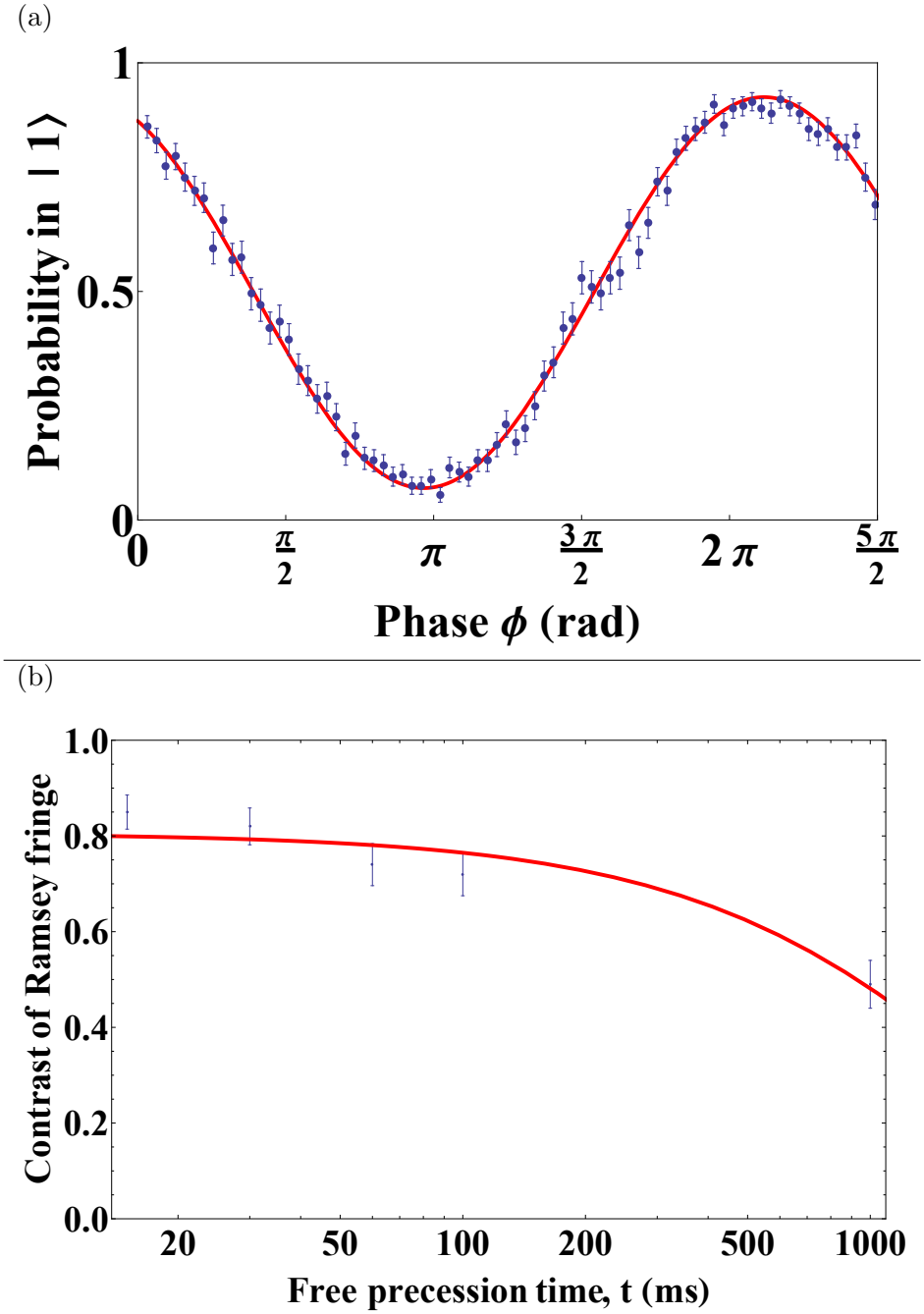

Figure 3.22: (a) Example of Ramsey fringe produced when phase of second $\frac{\pi}{2}$ pulse is adjusted with a fixed evolution time, $t_p = 15\,\text{ms}$. Each point is an average of 100 measurements. (b) Plot of the fringe contrast vs the evolution time. An exponential fit to these points is also shown and gives a coherence time of $\approx 1.5\,\text{s}$

Chapter 4

Frequency stability of the 369 nm cooling laser

This chapter will describe the method used to stabilise the frequency of the 369 nm cooling laser. The frequency at any point in time, t of a laser can be defined as [54]

$$f(t) = \frac{1}{2\pi}\frac{d\phi}{dt} \tag{4.1}$$

where ϕ is the phase of the laser oscillation and $f(t)$ is the laser frequency at time, t. Fluctuations in this frequency are known as frequency noise and are therefore directly related to fluctuations in the laser's phase. Laser phase fluctuations have three main origins:

1. **Mechanical**: such as vibrations of the lasers diffraction grating which can cause the cavity length to fluctuate.

2. **Electrical**: such as shot noise and thermal noise which can cause fluctuations in the current through the diode and the voltage applied to the piezo.

3. **Quantum**: caused by the addition of photons with random phase to the laser cavity due to spontaneous emission.

While it could be possible to minimise each of these sources individually (with the exception perhaps of quantum fluctuations), it's often easier and more practical to stabilise the laser frequency indirectly using a feedback circuit. This is the method employed within the stabilisation systems described in this chapter.

This chapter will begin by discussing how stability is measured and will go on to explore what frequency stability of the 369 nm light is required within the experiments described

in this thesis. This chapter will then describe how a reference frequency is produced by stabilising a 780 nm laser to an atomic transition in rubidium 87 and how, using this reference frequency, the 739 nm laser frequency is stabilised using a dual resonance method. As the 369 nm light is produced by frequency doubling the 739 nm laser this results in 369 nm frequency stability.

4.1 Measuring stability

The stability of the laser frequency is measured by passing the light through a Fabry-Perot cavity[1]. When the laser frequency is being scanned over time, peaks in the amount of light transmitted through the cavity are observed. These peaks are known as Fabry-Perot peaks and have a peak to peak distance in frequency space equal to the free spectral range of the cavity. This is given by [54]

$$\Delta f = \frac{c}{2nl_c} \tag{4.2}$$

where n is the refractive index of the cavity (=1.000277 for air) and l_c is the cavity length. Therefore, if the laser frequency was set at a point half way up a Fabry-Perot peak where the transmission through the cavity is 50 % of it maximum value, any frequency fluctuations can be detected by observing any changes in the transmission of light through the cavity. This is shown in figure 4.1, a decrease in transmission will indicate an increase in laser frequency and an increase in transmission will indicate a decrease in laser frequency. By knowing the peak height, peak width and peak to peak distance, this change transmission with frequency can be calibrated.

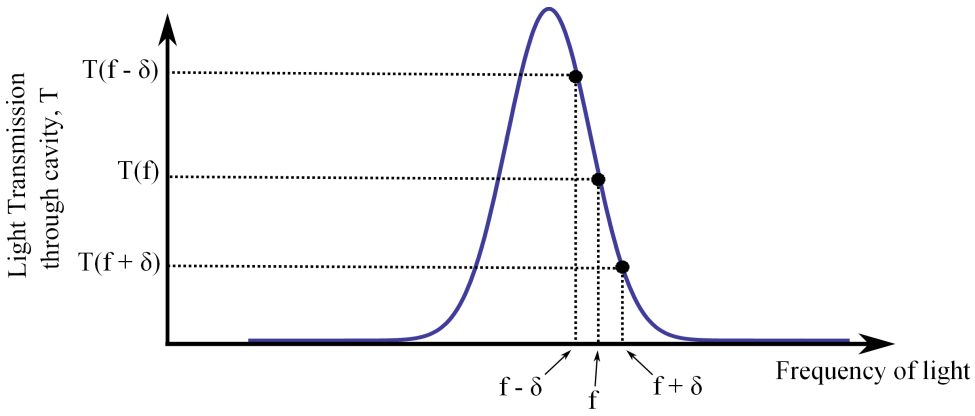

Figure 4.1: By setting the frequency of light to a point half way up the Fabry-Perot peak, the stability of that laser frequency can be measured. An increase in light transmission indicates a decrease in laser frequency and a decrease in light transmission indicates an increase in laser frequency.

[1] All cavities used within this chapter were built to the same design as those described within [55]

Using this method, the change in laser frequency of the 739 nm laser[2] over 1 ms was measured and shown in figure 4.2 (a). The light was coupled into a cavity and the transmission through the second cavity mirror was measured using a fast photodiode[3].

There are two main ways of analysing this data. Firstly the discrete Fourier transform of the data can be taken. The discrete Fourier transform of a set of data can be calculated using Mathematica. The Mathematica definition of a discrete Fourier transform is given by [56]

$$DFT(t) = \frac{1}{\sqrt{N}} \sum_{r=1}^{N} d_r \sin \frac{\pi}{N}(r - \frac{1}{2})t \tag{4.3}$$

where N is the total number of data points, d_r. This transforms the data into frequency space so the main frequency components of the noise can be observed, this helps to identify where the noise is coming from. Figure 4.2 (b) shows the Fourier transform of the data shown in figure 4.2 (a). This shows a main noise component is present at 85 kHz

A second method is to look at the Allan variance [57]. This is found by first splitting the time over which the data is measured into sets of a length t_s. The average of the data collected within each set is then taken. The variance between the averages across all the sets is known as the Allan variance. This is written mathematically as

$$\sigma^2(q_n) = \langle q_n - \langle q_n \rangle \rangle \tag{4.4}$$

where q_n is a set of indicies, where $0 \leq n < ss$ and ss is the set size, given by

$$q_n = \langle p_{i-j} \rangle \tag{4.5}$$

where p_{i-j} represents all the data points between (and including) i and j where $i = n \lfloor \frac{N}{ss} \rfloor + 1$ and $j = (n+1) \lfloor \frac{N}{ss} \rfloor$.

By varying the set size, t_s, different noise components can be observed. At long set times for example, high frequency noise averages to zero within each set meaning the only difference between sets is due to long term drifts. This method has the advantage over the Fourier transform as the stability in particular time regimes can be easily observed. Figure 4.2 (c) shows the Allan variance of the data shown in figure 4.2 (a). The highest Allan variance is present at small sample times and corresponds to quantum noise as well as shot noise from electrical components[4] The lowest Allan variance is present at a sample

[2]The 369 nm light required for experiments is formed through frequency doubling of a 739 nm laser.

[3]Thorlabs: DET36A/M

[4]It should be noted that this could be from the photodiode and oscilloscope and therefore doesn't necessarily correspond to laser noise.

time of around 30 μs. Above this, the variance is due to slower drifts from mechanical effects. A discontinuity in the Allen variance is present at 166 μs. The exact source of this is unknown but it is suspected to be a consequence of the use of a finite number of data points. At step sizes above 166 μs, the number of data points can only be split into a maximum of two sets. Any remaining data points above the number needed for the two sets is then ignored. This can cause a discontinuity in the Allan variance.

4.2 Stability requirements

The 369 nm cooling laser is used at three main points within a typical experiment:

- Cooling
- State preparation
- State detection

During cooling, for experiments where the ions mean vibrational quantum number, $\bar{n}$, (see appendix D) is not important[5], the 369 nm laser has the lowest stability requirements. Providing the laser frequency remains below the resonant frequency to prevent heating and remains close enough to the resonant frequency to provide efficient Doppler cooling, any frequency fluctuations are not an issue. This is because cooling pulses are applied for long periods of time and the resultant state is not important. For state preparation and detection however, frequency stability is more important.

4.2.1 State preparation

As shown in chapter 3, during state preparation, the 369 nm laser is applied for approximately 20 μs, which together with 2 GHz sidebands results in the population being optically pumped into the $^2\mathrm{S}_{\frac{1}{2}}$ $F = 0$ level. This is most efficient when the frequency of the 369 nm light with the addition of 2 GHz sidebands is resonant with the $^2\mathrm{S}_{\frac{1}{2}}$ $F = 1$ to $^2\mathrm{P}_{\frac{1}{2}}$ $F = 1$ transition. Detuning from this frequency will cause the transition probability to be smaller which will result in longer preparation times being needed as shown in figure 4.3. Detunings caused by laser instability during a pulse sequence with a fixed preparation time will therefore cause a random infidelity in state preparation.

[5]This is the case for the majority of experiments within this thesis

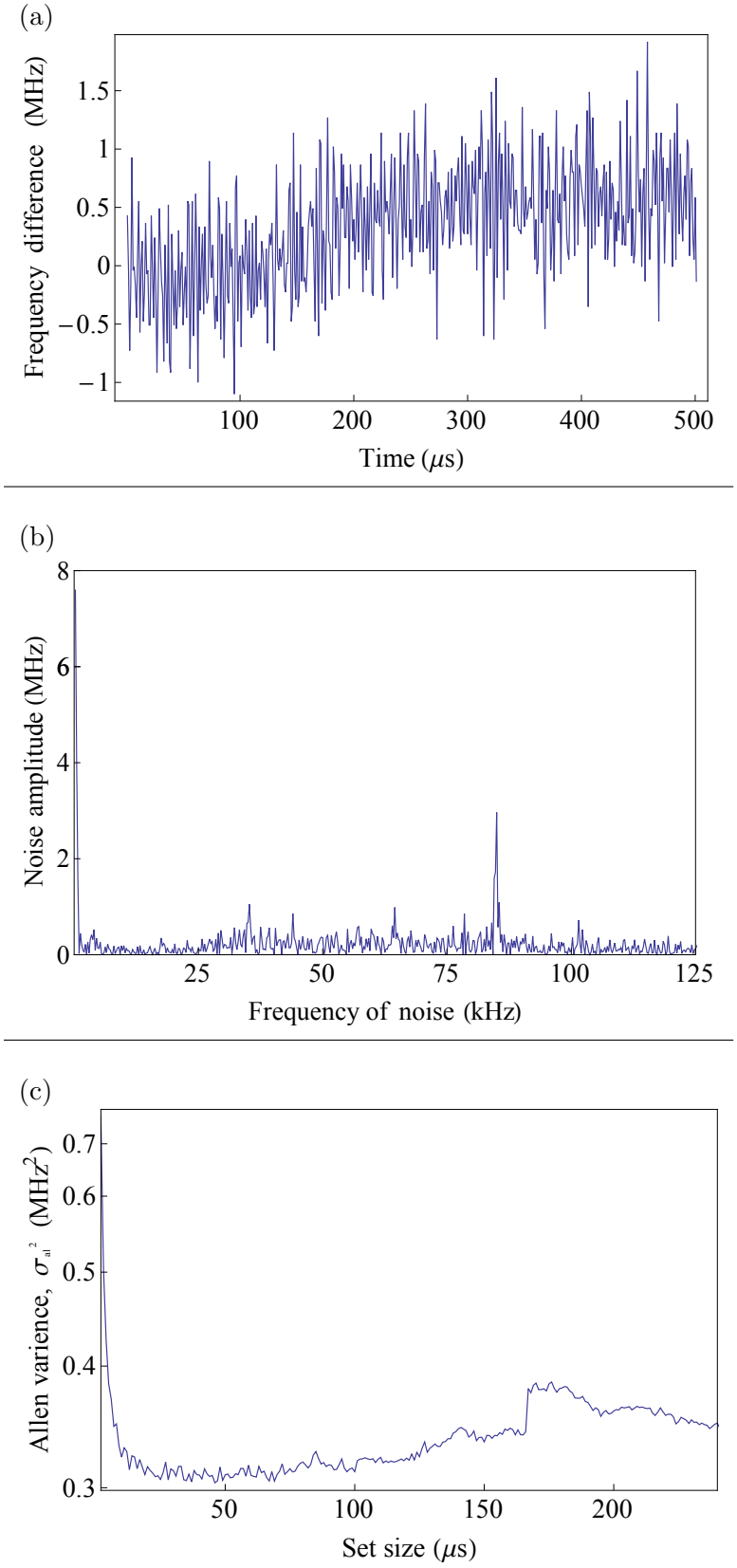

Figure 4.2: (a) The change in frequency over time of the 739 nm laser signal. The data was taken by observing the transmission through a Fabry-Perot cavity around the half way point of a Fabry-Perot peak using a fast photodiode. (b) A Fourier transform of the data shown in (a). (c) A plot of the Allan variance of the data shown in (a).

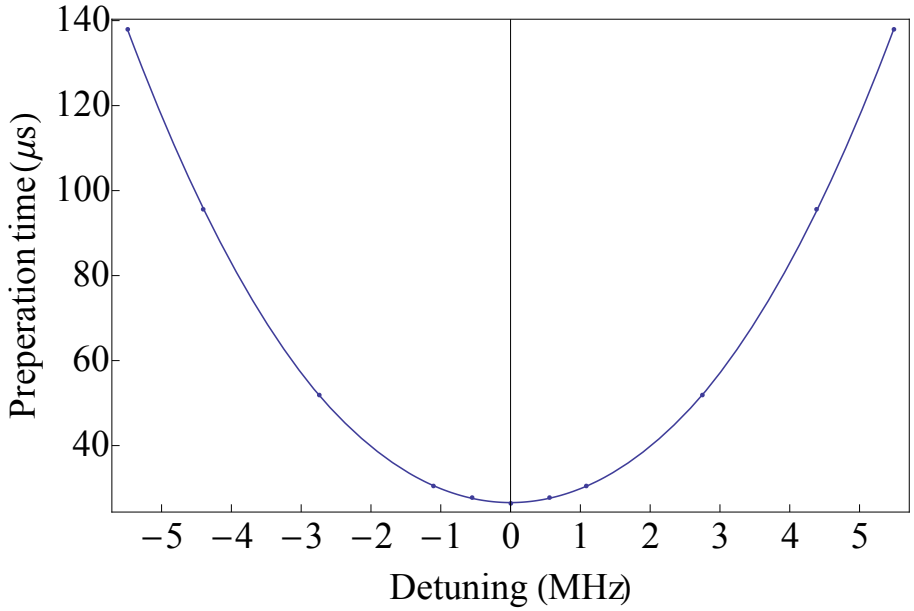

Figure 4.3: Figure showing the time taken to prepare 99.9 % of the population into the $^2S_{\frac{1}{2}}$ $F = 0$ level vs the frequency of the 369 nm laser in terms of detuning from the resonant frequency. This was simulated using the rate equation program discussed in chapter 3 with 66 % of the 369 nm light within the 2 GHz sidebands and using 369 nm and 935 nm intensities equal to 0.1 I_{sat} and 10 I_{sat} respectively.

4.2.2 State Detection

During state detection, a 369 nm laser resonant with the $^2S_{\frac{1}{2}}$ $F = 1$ to $^2P_{\frac{1}{2}}$ $F = 0$ transition is applied for approximately 800 μs, during which any population present within the $^2S_{\frac{1}{2}}$ $F = 1$ level will undergo a closed cooling cycle and the emitted photons will be collected. Figure 4.4 shows the effect the 369 nm frequency has on the number of collected photons. Figure 4.4 shows that if, due to laser frequency instabilities, the laser becomes detuned from resonance during detection, the number of photons collected during detection will be reduced. This will have a significant effect on the state detection fidelity.

4.2.3 Stability regimes

The Allan variance needs to be minimised for 20 us and 800 us to minimise errors in state preparation and state detection respectively. In addition, during an experiment, the frequency needs to be stable between repeat applications of a pulse sequence as well as throughout the whole experiment which corresponds to times of between 0.1 and 1 s and 10 and 60 minutes respectively, therefore, errors due to DC drift also need to be minimised.

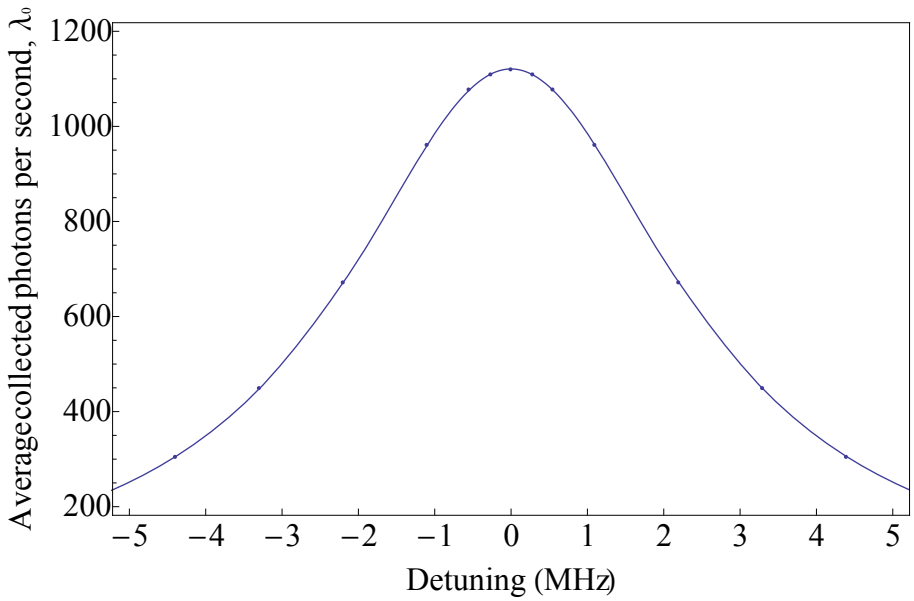

Figure 4.4: Figure showing the average number of collected photons from an ion prepared in the $^2S_{\frac{1}{2}}$ $F = 1$ level vs the frequency detuning of the 369 nm laser from resonance. This was simulated using the rate equation program discussed in chapter 3 using 369 nm and 935 nm intensities equal to 0.1 I_{sat} and 10 I_{sat} respectively.

4.3 Feedback mechanisms

The basis behind all the stabilisation methods used within this chapter is known as the feedback mechanism. The basic idea behind a feedback mechanism is shown in figure 4.5. The parameter to be stabilised is first measured and amplified, which is then used to form an error signal. This is simply a voltage which is proportional to the change in the parameter from its required value. The error signal is then sent into a proportional-integral (PI) controller. This creates a feedback signal which, when applied to the experiment, will correct for the fluctuation in the parameters value.

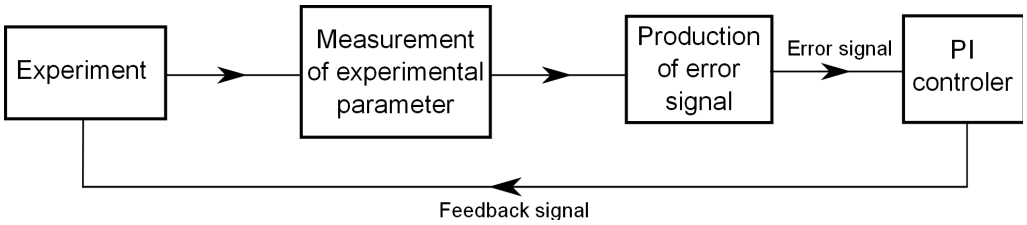

Figure 4.5: General schematic of a feedback system.

The remainder of this chapter will describe several different feedback mechanisms used for the stabilisation of the 739 nm laser. These are outlined in section 4.4. The method of parameter measurement and error signal production will vary between the different mechanisms and will therefore be described individually as each mechanism is discussed. The method by which the feedback signal is produced using a PI controller is however the

same for all the different mechanisms and will therefore now be described.

4.3.1 Producing feedback signals: the PI controller

As previously mentioned, a PI controller converts an error signal, which is a voltage proportional to the difference in a measured parameter from its ideal value, to a feedback signal which, when applied to the experiment, corrects for this difference. A PI controller consists of a proportional and an integrating amplifier. The proportional amplifier produces a signal $s_P(t)$ which is proportional to the error signal, $D(t)$, with a proportionality constant K_P [58],

$$s_P(t) = K_P D(t). \tag{4.6}$$

K_P is known as the proportional gain and controls the size of the feedback signal and therefore the speed at which the parameter will move back towards its initial value. If the gain is too high, the response will occur faster than the time taken for the change in the error signal to reach the PI controller therefore the parameter will overshoot its ideal value. This will result in the parameter oscillating around the ideal value.

While the proportional term can be very effective at correcting for fast oscillations, alone it is ineffective at compensating for slow long term drifts. These are corrected for by the integrating amplifier. The integrating amplifier produces a signal $s_I(t)$ equal to the integral of the error signal over a predetermined time constant, $\int_0^t D(t)$, times by a proportionality constant known as the integral gain K_I [58],

$$s_I(t) = K_I \int_0^t D(t')dt'. \tag{4.7}$$

As with the proportional gain, high integral gain increases the speed of the feedbacks response. However, too high a gain and the parameter will overshoot and oscillate around it ideal value.

The schematic for the home-built PI controllers used within the locking setup is shown in figure 4.6. The amplifier gains, K_P and K_I are adjusted using variable resistors.

4.4 Stabilising the 739 nm laser

To stabilise the frequency of a laser, a reference frequency is first required. This is a frequency which is constant and well known, such as an atomic transition frequency. The difference between the laser frequency and the reference frequency can then be calculated and compared to the difference between the reference frequency and the ideal laser

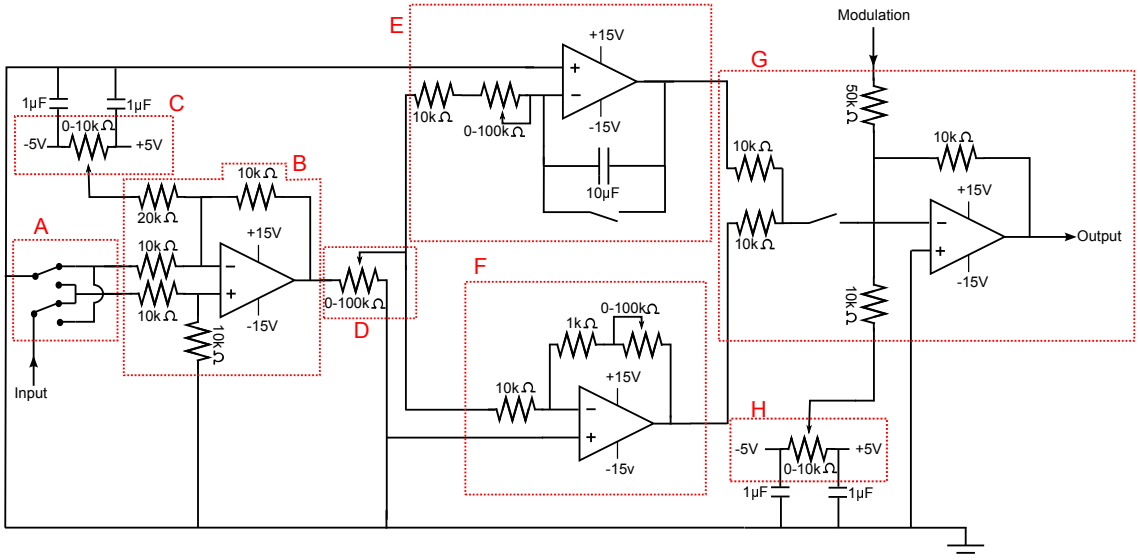

Figure 4.6: Schematic for the homebuilt PI controllers used within the locking setup. The controller consists of eight parts. **A** controls the polarity of the error signal. **B** is a summing amplifier which adds the error signal to a input offset generated by **C**. **D** controls the input amplitude of the signal into the device. The signal is then split and sent through an integrating amplifier **E** and a proportional amplifier **F** in parallel before being recombined using a second summing amplifier **G**. **G** also combines an output offset produced by **H**.

frequency.

For the lock described in this chapter, the reference used will be an atomic hyperfine transition within rubidium 87. A 780 nm laser is locked to this transition using saturated absorption spectroscopy. This will be explained in section 4.4.1. Two methods of comparing this stable 780 nm laser to the 739 nm laser will then be discussed. Section 4.4.2 will discuss a scanning cavity lock, which compares the peak positions of the two lasers within a scanning Fabry-Perot cavity. Section 4.4.3 will then discuss a dual resonant lock, which uses the stable 780 nm laser to stabilise the length of a Fabry-Perot cavity. The 739 nm laser is then stabilised to this cavity.

4.4.1 Stabilising the 780 nm laser to rubidium

To stabilise the 780 nm laser to a hyperfine transition in rubidium 87, a method of measuring the transition frequency is required. An ideal method would be to scan the frequency of a 780 nm laser incident on a group of perfectly stationary rubidium atoms. The atoms would absorb photons when the laser frequency is equal to the hyperfine transition frequencies of rubidium resulting in dips in the intensity of the laser light which could be detected using a photodiode. Unfortunately, however, rubidium atoms within a vapor cell are not stationary. The frequency of the photons absorbed by each atom therefore depend

on the atoms velocity as a result of the Doppler effect. Due to the large range of velocities present in a gas at room temperature, the resultant frequencies of laser light absorbed for a transition become broadened over all transitions. As a result, the individual hyperfine transition frequencies cannot be distinguished. To find these frequencies a method known as saturated absorption spectroscopy is used.

Saturated absorption spectroscopy

To detect the hyperfine transition frequencies of rubidium atoms within a vapor cell, the 780 nm light needs to be split into two beams, these are sent counter-propagating through the vapor cell. The first laser beam is known as the pump beam. An atom will absorb photons from this pump beam and become saturated when the following equation is satisfied [59],

$$v_r = \frac{\lambda(\omega_l - \omega_0)}{2\pi} \tag{4.8}$$

where v_r is the speed of the atom in the direction parallel to the laser beams, ω_l is the frequency of the 780 nm light, ω_0 is the resonant frequency of a transition within the rubidium and λ_l is the wavelength of the laser.

The second beam is known as the probe beam. An atom will be resonant with this beam if the following relation is obeyed,

$$v_r = \frac{\lambda(\omega_0 - \omega_l)}{2\pi}. \tag{4.9}$$

An atom cannot however absorb photons from the probe beam if it has already been saturated by the pump beam. By equating equations 4.8 and 4.9, it can be concluded that this will occur when ω_l equals ω_0. When the laser frequency is equal to a hyperfine transition frequency, photons from the probe beam will therefore not be absorbed by the rubidium and as a result, a peak will be seen in the probe beams intensity.

Peaks will also be present when the velocity of an atom is such that the pump beam is resonant with a different transition to the probe beam. These are known as crossover peaks.

The signal from a photodiode measuring the intensity of the probe beam during a frequency scan of the 780 nm laser over the main hyperfine transitions in rubidium is shown in figure 4.7(a). The structure on the left is due to the isotope rubidium 87 and the structure on the right is due to the isotope rubidium 85. The 87 isotope has the most well defined peaks, therefore this is the isotope which we use to stabilise the 780 nm laser.

The inset is a zoomed in image of these peaks. Figure 4.7(b) shows the energy spectrum of rubidium 87.

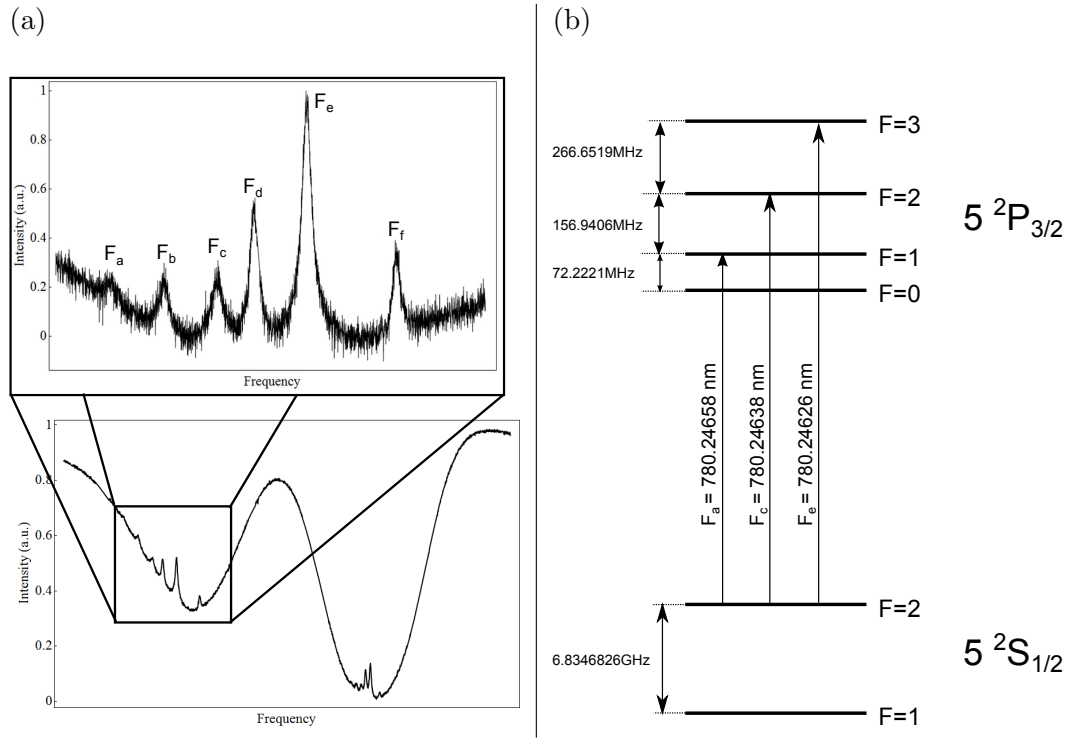

Figure 4.7: (a) Saturation absorption spectrum of a rubidium vapor cell with an inset showing the main peaks of rubidium 87. (b) Energy level structure of rubidium 87 giving the transitions represented by peaks F_a, F_c and F_e. Peaks F_b and F_d are crossover peaks caused by the pump and the probe beam each exciting different transitions within an atom. F_b and F_d correspond to crossovers of the F_a and F_c peaks and the F_c and F_e peaks respectively.

Before an error signal is created, the absorption of 780 nm light by rubidium without the presence of a pump beam, known as the background Doppler signal, is first subtracted from the probe photodiode signal. This eliminates the background 'curve' and the resultant signal, when the 780 nm laser frequency is scanned, is simply a row of peaks each at frequencies corresponding to transition resonant frequencies or crossovers.

Creating an error signal

As previously described, an error signal is a voltage proportional to the difference in the measured frequency from its ideal value. The peaks present in the absorption signal of the 780 nm rubidium probe beam when the laser frequency is scanned can be turned into an error signal by differentiating them with respect to frequency as shown in figure 4.8.

To experimentally differentiate these peaks, a lock-in amplifier method is used[6]. This

[6] Also known as the Pound-Drever-Hall technique.

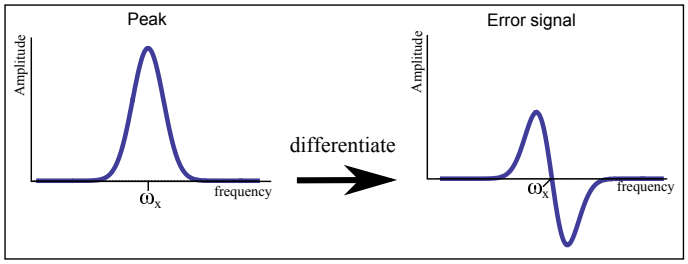

Figure 4.8: When a peak is differentiated with respect to frequency it forms an error signal. Close to the resonant frequency, ω_x, the amplitude of the error signal is proportional to the distance in frequency from ω_x.

method is explained briefly here, for more details on how lock-in amplifiers work, please refer to [60].

The 780 nm laser current is first modulated at a reference frequency, f_r, of 100 kHz. As a result, the intensity of the laser as a function of laser frequency is given by

$$I(\omega) = I\left(\omega_0 + \alpha \sin(f_r t + \phi_1)\right) \tag{4.10}$$

$$= I(\omega_0) + \alpha \sin(f_r t + \phi_1)\frac{dI(\omega_0)}{d\omega} + \alpha^2 \sin^2(f_r t + \phi_1)\frac{d^2 I(\omega_0)}{d\omega^2} + ... \tag{4.11}$$

where $I(\omega_0)$ is the lasers intensity at a frequency ω_0, ϕ_1 is the phase of the modulation signal and α is the modulation amplitude. This intensity will be converted into a voltage using a photodiode. This voltage will be linearly proportional to the intensity and will therefore, to first order, be equal to

$$V(\omega) \approx V(\omega_0) + \alpha \sin(f_r t + \phi_1)\frac{dV(\omega_0)}{d\omega}. \tag{4.12}$$

This voltage is then sent into a lock-in amplifier. The lock-in amplifier multiplies this signal by an oscillating voltage, $V(t)$, of the same frequency as the 780 nm current modulation, $V(t) = \sin(f_r t + \phi_2)$. This results in the following voltage,

$$V_\times = \sin(f_r t + \phi_2)V(\omega_0) + \alpha \sin(f_r t + \phi_1)\sin(f_r t + \phi_2)\frac{dV(\omega_0)}{d\omega} \tag{4.13}$$

$$= \sin(f_r t + \phi_2)V(\omega_0) + \frac{\alpha}{2}(\cos(\phi_1 - \phi_2) - \cos(2f_r t + \phi_1 + \phi_2))\frac{dV(\omega_0)}{d\omega}. \tag{4.14}$$

This voltage is then averaged over one modulation period to give the output voltage of the lock-in amplifier,

$$V_{out} = \int_0^{2\pi} V_\times dt = \pi\alpha \cos(\phi_1 - \phi_2)\frac{dV(\omega_0)}{d\omega}. \tag{4.15}$$

The output voltage is therefore proportional to the differential of the input with respect to frequency. This error signal is then sent to a PI controller to form a feedback signal which, when sent to the 780 nm laser grating piezo, stabilises the laser to the center of a transition peak.

4.4.2 Scanning cavity lock

One method of stabilising the 739 nm laser frequency using the stable 780 nm laser is a scanning cavity lock. The method behind the lock is summarised here. For a more detailed description please refer to the thesis of Robin Sterling [55].

The 739 nm and 780 nm laser beams are first combined using a polarising beam splitter (PBS) and sent into a Fabry-Perot cavity. The transmission of these beams through the cavity is then split back into the two separate 780 nm and 739 nm beams by another PBS and detected using separate photodiodes whose signals are sent to the Labview realtime machine. The length of the cavity is then scanned by modulating a piezo attached to one of the cavity mirrors. As a result, peaks in time are observed in the transmission of the laser beams through the cavity. The position in time of these peaks will be dependent on the frequency of the lasers and can therefore be used to stabilise the 739 nm laser frequency. As the 780 nm laser has been stabilised, the relative position of the 739 nm peaks to the 780 nm peaks will determine the stability of the 739 nm laser. This relative position can therefore be used as an error signal. An inbuilt Labview PI controller is used to send feedback from this error signal to the 739 nm laser grating piezo which locks the 739 nm peak position and therefore its frequency.

This method of stabilisation is limited by the speed of Labview realtime which runs at 500 Hz [37]. This proved to not be stable enough for our main cooling laser and so a dual resonance lock is used (see section 4.4.3). The scanning cavity lock is however used to stabilise the frequency of the 935 nm repumper laser as this laser is operated at a high power to induce power broadening on the 935 nm transition, as described in chapter 3, and therefore does not require the same level of stability.

4.4.3 Dual resonant lock

A faster method of stabilising the frequency of the 739 nm laser using the stable 780 nm laser is a dual resonance lock. The basic principle is to first stabilise the length of a Fabry-Perot cavity to the 780 nm laser frequency. The 739 nm laser frequency is then stabilised to the length of the stable Fabry-Perot cavity. How these two processes are performed will

now be described in more detail.

Locking the cavity length to the 780 nm laser frequency

When the cavity length is scanned, peaks will be present in the transmission of 780 nm light through the cavity. These peaks describe the cavity lengths where the 780 nm laser is resonant with the cavity. Using the lock-in amplifier method described in section 4.4.1, the transmission of the 780 nm laser through the cavity can therefore used to form an error signal. When sent through a PI controller this produces feedback which is applied to the cavity mirror piezo to stabilise the cavity length to a point where the 780 nm laser is resonant.

Locking the 739 nm laser frequency to the cavity length

Due to bugetary constraints, to lock the 739 nm laser to the stabilised cavity, a side of fringe method is used. The side of fringe method is a simple and cheap method of error signal production as it uses the photodiode signal directly as the error signal. When the 739 nm laser frequency is scanned, peaks will be observed. These peaks will be centered around the frequencies at which the 739 nm laser is resonant with the cavity. By adding an offset voltage to these peaks equal to half the peak height, the side of these Fabry-Perot peak become equivalent to the required error signal as shown in figure 4.9. Therefore, sending

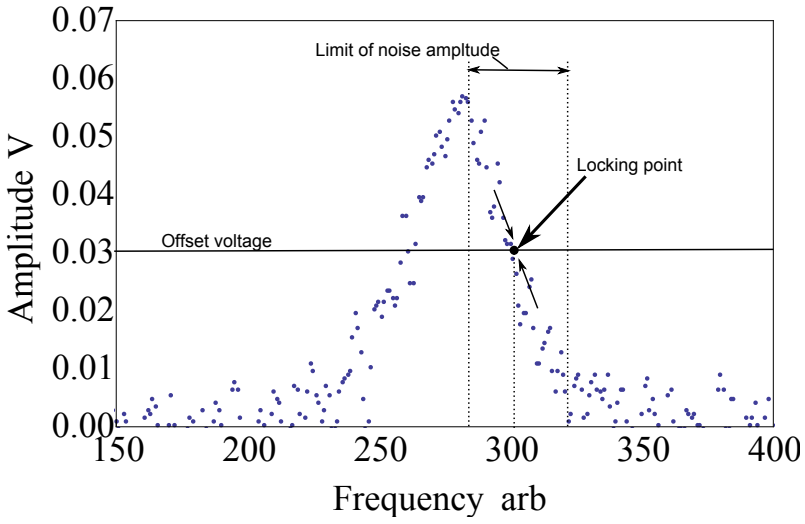

Figure 4.9: Diagram showing how a Fabry-Perot peak can be used to stabilise laser frequency. The addition of an offset voltage results in the side of the peak resembling an error signal as the voltage varies linearly from the locking point. This can then be sent directly to a PI controller to produce the stabilising feedback signal.

the offset photodiode signal through a PI controller results in a feedback signal. Applying this feedback signal to the 739 nm laser piezo results in the 739 nm frequency becoming

stabilised to a frequency slightly higher than the resonant frequency of the laser with the cavity. This side of fringe method does however have several disadvantages. Firstly, the amplitude of noise which can be corrected for is limited by half the width of the peak and secondly, the lock is sensitive to any amplitude fluctuations as these will effect the peak height. Despite these disadvantages, this method provided sufficient stability of the 739 nm frequency for the experiments described within this thesis. If a greater degree of stability is needed in the future this should be upgraded to the lock-in amplifier method.

4.5 Experimental setup

This section will explain the experimental equipment setup used to perform a rubidium lock on the 780 nm laser and a dual resonance lock of the 739 nm laser. Section 4.5.3 will then describe how the photodiodes are shielded from environmental noise using a box and finally section 4.5.4 will give a step by step guide of how to operate the equipment to produce an effective lock.

Figure 4.10 and 4.11 show the respective electronics and optics setup developed to perform a rubidium lock on the 780 nm laser and a dual resonance lock of the 739 nm laser[7]. The red numbers and letters are labels which allow the various optics and equipment to be identified with ease for the remainder of the chapter.

4.5.1 780 nm rubidium lock

As shown in figure 4.11, upon exiting the 780 nm laser box, a small percentage of the beam ($\approx 10\,\%$) is reflected by a glass plate (g). This passes through a half waveplate (d) which allows the ratio of light reflected and transmitted through the subsequent PBS (h) to be adjusted. The transmitted beam passes through a rubidium vapor cell and onto the 780 nm Rb photodiode. The reflected beam is sent through the rubidium vapor cell in the opposite direction where it overlaps with the transmitted beam. These two light beams form the required probe and pump beams for saturated absorption spectroscopy. The optimum power ratio of these beams was found to be equal to 3:1. Another small percentage of the main 780 nm beam ($\approx 5\,\%$) is reflected by another glass plate (b). This is also sent through the rubidium vapor cell and detected by a separate photodiode. This forms the background absorption signal.

[7]Note: The optics setup to perform a scanning cavity lock of the 935 nm laser is also shown. Please see the thesis by Robin Sterling [55] for details of this.

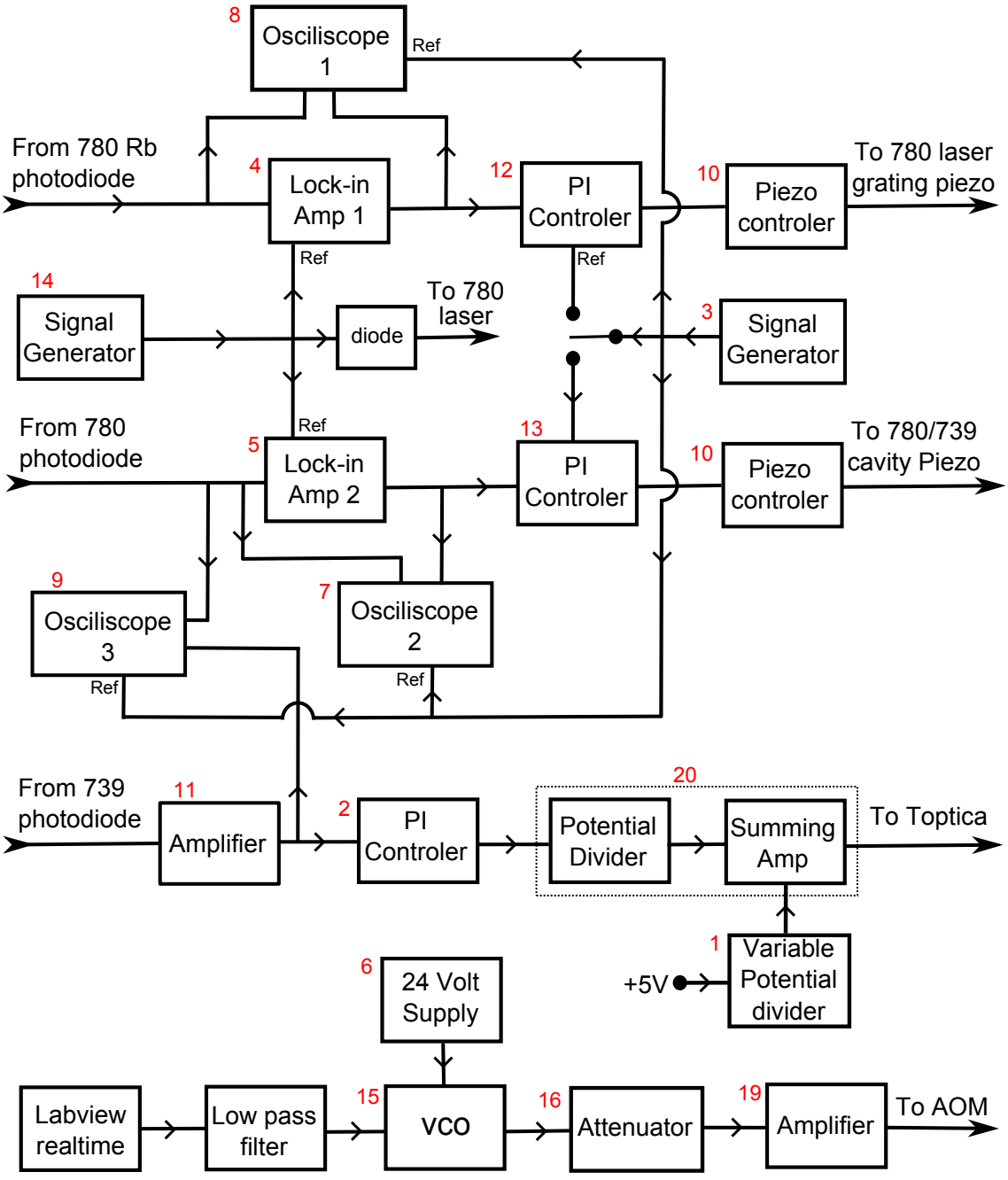

Figure 4.10: Diagram showing electrical schematic of electronics used to lock the 739 nm laser.

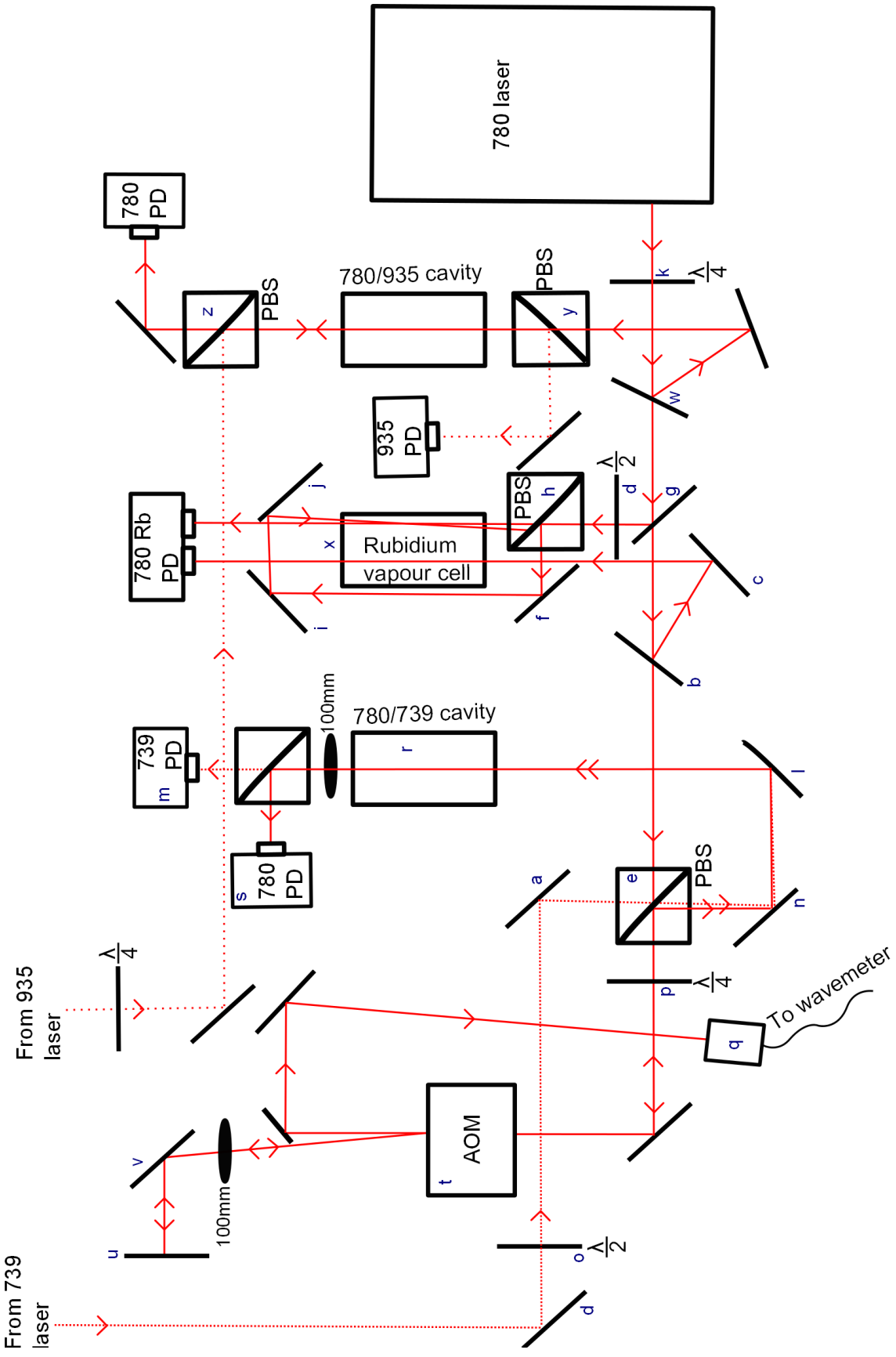

Figure 4.11: Diagram showing the on table optical setup used to lock the 739 nm and 935 nm lasers.

4.5.2 Dual resonant lock

The 780 nm beam polarisation is adjusted to vertical immediately after it exits the laser using a quarter waveplate (k). This allows it to pass straight through a PBS (e) to an AOM[8]. The AOM is set up in a double pass configuration to allow the frequency of the light to be adjusted without affecting the beam path. Additionally, this doubles the available scan range when adjusting the AOM frequency. A double pass through a quarter waveplate (p) adjusts the polarisation of the beam to horizontal which allows it to be reflected by the beam splitter (e) and sent into a Fabry-Perot cavity (r). When the light is at a frequency resonant with the cavity it will exit the cavity and be detected by a photodiode (s). The 739 nm laser is shown in figure 4.11 by the dotted red line. The beam is vertically polarised by the half waveplate (o) which allows it to pass straight through the beam splitter (e) and be overlapped with the 780 nm beam before passing through the Fabry-Perot cavity (r). The 739 nm light resonant with the cavity is then detected by a photodiode (m).

To maximise the beam power available for the experiment, the beam power taken from the main 739 nm beam for locking is quite weak ($\approx 200\,\mu$W). The current produced by the photodiode is therefore passed through a transimpedance amplifier (11) to produce a large enough error signal amplitude.

A 3:1 potential divider (20) and summing amp are present between the PI controller and the Toptica system. This prevents damage to the Toptica piezo which is only specified to receive a 0-5 V modulation input whereas the PI controller can produce up to 12 V as well as allowing the addition of an offset voltage. This offset voltage is used to adjust the 739 nm frequency while it is unlocked.

Wavelength adjustment

As previously mentioned, when unlocked, the 739 nm wavelength can be adjusted using the variable potential divider (1) which changes the magnitude of a DC offset which is being sent to the Toptica laser grating piezo.

When locked, this will have no effect as the PI controller will produce an equal and opposite voltage to keep the 739 nm frequency equal to a point where the transmission through the cavity is half its maximum value. The 739 nm frequency can however be adjusted by changing the frequency of the 780 nm light which the cavity length is stabilised to. This will cause the cavity length to change which results in the 739 nm frequency

[8] Interaction corp 2001A2.78

where the laser transmission through the cavity is half its maximum value changing. As previously mentioned, the 780 nm frequency going into the transfer cavity can be adjusted by changing the frequency sent to an AOM within the 780 nm beam path. This AOM is setup in a double path configuration so a change in frequency doesn't effect the spatial position of the beam. The AOM is powered by a voltage controlled oscillator (VCO) (15) and can provide a single path frequency shift of between 0 and 300 MHz determined by applying a variable voltage (0-18 V) to the VCO[9]. This is produced by Labview realtime and sent through a low pass filter to minimise noise. The signal from the VCO is sent through an attenuator (16) and a +30 db amplifier (19) which together provide a power which gives optimum AOM efficiency[10]. Changing the AOM frequency will also have an effect on the amplitude of 780 nm light passing through the AOM. This will not effect the lock stability as the lock-in amplifier method used to form the error signal is, to first order, unaffected by peak height.

4.5.3 Optics containment box

The whole on table optics setup shown in figure 4.11 is contained within a box to shield the photodiodes from environmental noise. The box contains several layers as shown in figure 4.12 and includes rubber and foam to shield from acoustic vibrations and a layer of aluminum to act as a Faraday cage to shield from electromagnetic noise. Figure 4.13 shows the effect this box has on the Fourier transform of the locked 369 nm laser. Figure 4.13 shows that when the lid of the box is removed, a significant amount of 50 Hz noise is present.

4.5.4 How to lock users guide

This section will provide a step by step guide of how to use the equipment shown in figures 4.11 and 4.10 to stabilise the 739 nm laser.

Firstly the 780 nm wavelength needs to be stabilised to an atomic transition in rubidium.

- Adjust the 780 nm laser current and grating piezo voltage (10) until the wavelength of an atomic transition is reached. Transition wavelengths are given in figure 4.7.

[9] An adjustment of the AOM frequency without reoptimising the beam path does however result in a reduction in the efficiency of light passing through the AOM. As a result, the maximum frequency shift during operation is only on the order of 40 MHz

[10] The attenuator is needed to ensure the signal power does not exceed the maximum input power of the amplifier.

(a)

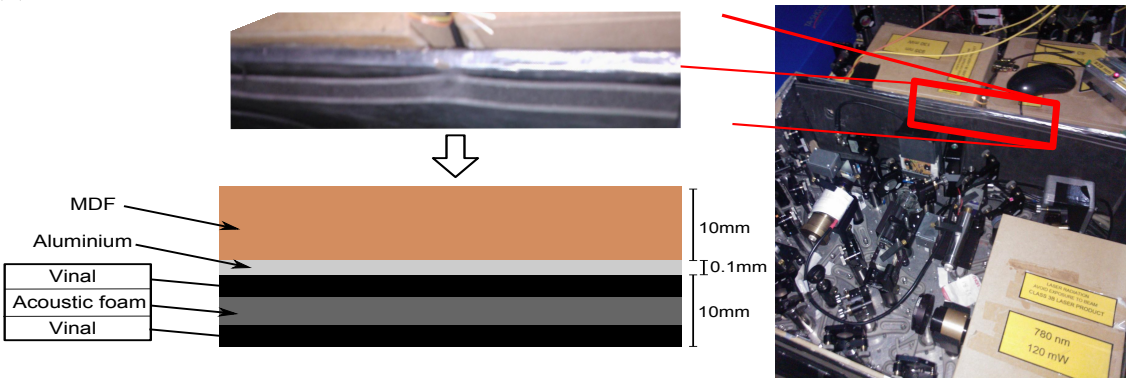

(b)

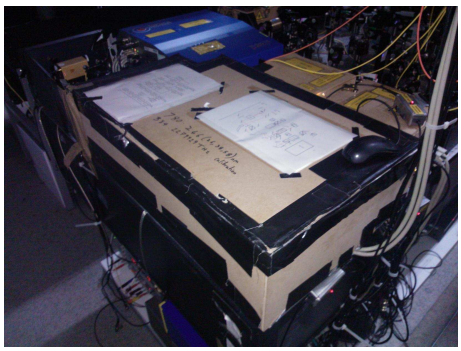

Figure 4.12: (a) Picture showing the layering of the box used to insulate the locking optics from environmental noise. The bottom three layers are formed from an acoustic underlay (The Sound Solution NSSF7). This is attached using duct tape to an aluminum layer, created using aluminum foil, and a rigid MDF layer. The box encloses four sides of the optics with a lid consisting of MDF covered with aluminum on the top as shown in (b).

Ensure there is roughly a 50 pm scan range both above and below this wavelength before the laser goes multimode.

- If the wavelength cannot be found it may be necessary to adjust the laser diode temperature. Ensure that you wait 5-10 minutes after doing this to allow the laser temperature to stabilise.

- Turn on the modulation signal generator (3) ensuring the switch is switched to the "780" position. This causes the laser piezo voltage to oscillate from 0 to 5 V at 100 Hz. On channel one of oscilloscope 1 (8) you should now see the saturated absorption spectrum of rubidium as shown in figure 4.7.

- If the signal is not present, the optical setup may need realigning. First ensure the light from mirror (g) is hitting the photodiode. Then, use mirrors (f) and (i) to overlap the pump beam with the probe beam within the Rb cell. (note: This can sometimes be easier to do by first removing the Rb vapour cell.)

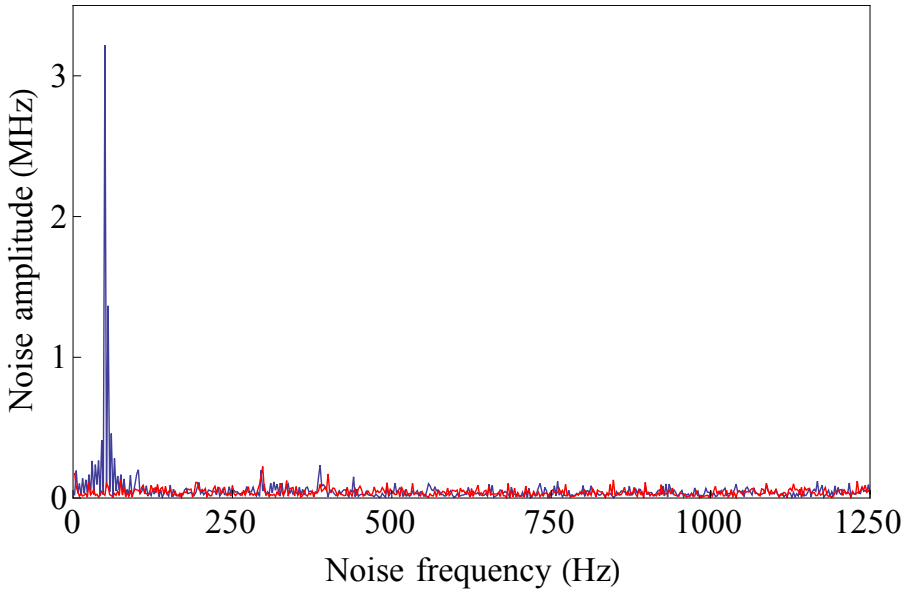

Figure 4.13: Graphs showing the Fourier transform of the transmission of locked 739 nm light through a locked Fabry-Perot cavity when the lid of the box is removed (blue) and present (red). A large peak in noise is present at 50 Hz only when the lid is removed.

- If there is still no signal, ensure the photodiode isn't being saturated by misaligning the setup slightly using mirror (g).

- Once the spectrum has been found, use mirrors (f-j) to optimise the absorption peaks and mirrors (b) and (c) to optimise the background cancellation.

- Channel two of oscilloscope 1 (8) should also show the error signal produced from this spectrum. This should be optimised using the sensitivity, phase and time constant settings on the lock-in amp (4) to produce the steepest signal with the least noise.

- Adjust the offset on the lock-in amp (4) to equal ground as this is the steepest point in the error signal.

- Turn the switch after the modulation signal generator (3) to "cavity" and turn the output of the signal generator off.

- If the wavelength has drifted in this time find the transition wavelength again using the 780 nm grating piezo controller (10).

- On the 780 nm PI controller box (12) switch on the P switch followed by the I switch.

- If the error signal shown on oscilloscope 1 (8) starts to oscillate, increase the time constant on the lock in amplifier (4).

Next the Fabry-Perot cavity length needs to be stabilised to the 780 nm wavelength and then the 739 nm wavelength needs to be stabilised to the cavity length. These have to be done together as once the cavity is locked it cannot be scanned.

- Find the 739 nm wavelength by adjusting the DC offset being sent to the Toptica grating piezo using the variable potential divider (1).
- If the wavelength is out of range of the potential divider, the grating piezo voltage and diode current on the Toptica system should be adjusted.
- Turn on the signal generator (3). This causes the cavity piezo voltage to oscillate from 0-5 V at 100 Hz. On oscilloscope 3 (9) you should now see Fabry-Perot peaks from the 780 nm and the 739 nm beams.
- The peak sizes should be greater than 0.25 V for the 780 nm and greater than 0.2 V for the 739 nm. If not, optimise the peaks by first using mirrors (n) and (l) to optimise the 739 nm peaks followed by mirrors (a) and (d) to optimise the 739 nm peaks.
- If the 780 nm peaks are still below 0.25 V, the beam position may have drifted and the AOM angle (t) may need to be adjusting to compensate.
- On oscilloscope 2 (7) you should see the Fabry-Perot peaks from the 780 nm beam as well as the corresponding error signal. This error signal should be optimised using the sensitivity, phase and time constant settings on the lock in amplifier (5) to produce the steepest signal with the least noise. (note: The signal can be made clearer by reducing the scan frequency on the signal generator (3).)
- Adjust the offset on the lock-in amp (5) to equal ground as this is the steepest point in the error signal.
- Turn off modulation (3).
- Flip the P switch and then the I switch on the cavity PI controller box (13). The signal on oscilloscope 2 (7) should jump up to the top of the peak. If nothing happens flip the I switch and then the P switch back, flip the polarity and retry. If there are large oscillations of the error signal on oscilloscope 2 (7) increase the time constant of the lock in amp (5) until the oscillations become flat.
- Adjust the 739 nm wavelength using the potential divider (1) until the signal on oscilloscope 3 (9) moves up the peak.

- Flip the P switch and then the I switch on the 739 nm PI controller box. The 739 nm peak signal should lock half way up the peak.
- If the locked wavelength is more than $\pm 5 \times 10^{-5}$ nm from the desired wavelength, unlock both the 739 nm and cavity PI controller boxes. Adjust the cavity length using the cavity piezo controller (10) and repeat the last three steps. Note: If the wavelength is less/more than required, the cavity length should be decreased/increased respectively.
- To adjust the wavelength of the 739 nm wavelength while locked, slowly adjust the voltage being sent to the AOM by the Labview realtime.

If the 739 nm laser doesn't stabilise, the offsets which cause the PI controllers to lock to the side of the fringe should be checked. This is done using the following procedure:

- Disconnect the feedback going to the summing amp (20) and plug it into a spare DC coupled oscilloscope.
- Turn on the modulation signal generator (3) ensuring the switch is in the "cavity" position.
- With the P and I switches of the 739 nm PI controller (2) turned off, adjust the controllers output offset so the output signal on the oscilloscope is equal to ground.
- Switch on the P switch of the PI controller (2). The scope should now show the 739 nm Fabry-Perot peaks.
- By adjusting the input offset of the PI controller (2), move the signal so that ground is positioned half way up the peak.
- Reconnect the feedback to the Toptica and relock.

4.6 Results

Figure 4.14 shows the Allan variance of the frequency of the 739 nm light found by measuring the transmission of the 739 nm beam through the stable Fabry-Perot cavity measured at the side of a Fabry-Perot peak as described in section 4.1. The 739 nm is measured when it is both, locked (red) and unlocked (blue), to the cavity. The graph shows that with a sample time of 20-300 μs, the locked variance is several times smaller than the unlocked variance. The locked Allan variance of 0.1 MHz^2 corresponds to a standard deviation of

approximately 0.32 MHz. Using figure 4.3, the required preparation time should therefore change by less than 90 ns between measurements. Above a sample time of 200 μs the lock gets more efficient and the Allen variance drops to below 0.01 MHz^2 which is more than two orders of magnitude smaller than the unlocked variance. 0.01 MHz^2 is equivalent to a standard deviation of 100 kHz. Therefore, using figure 4.4, with a state detection time of 800 μs, the average number of photons collected should therefore change by less than 0.05 between measurements.

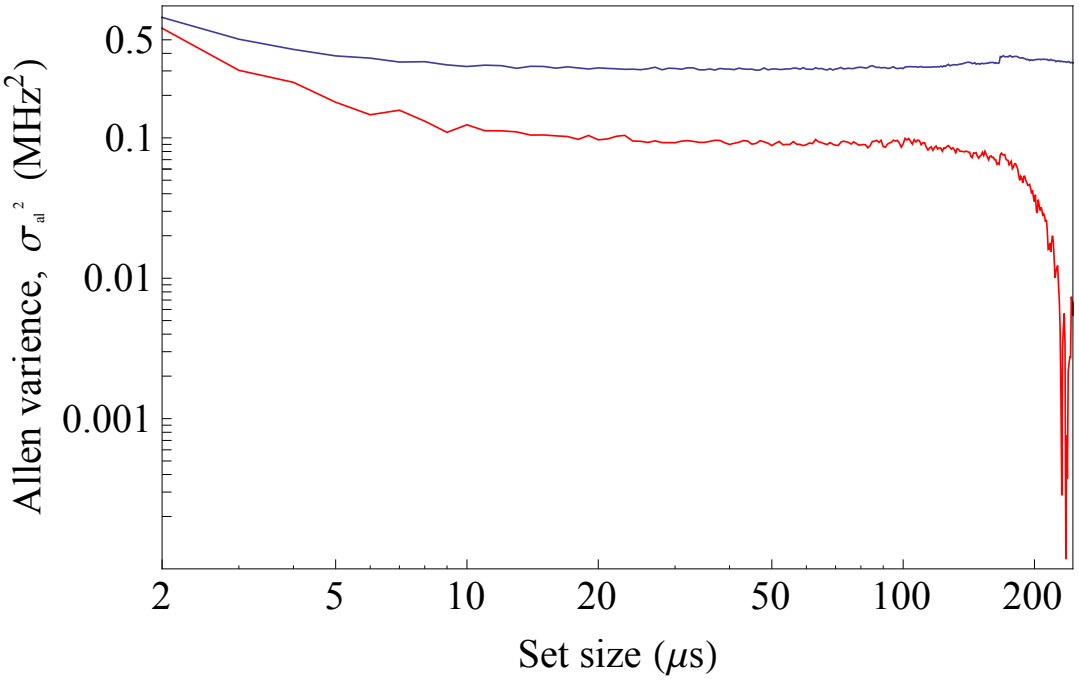

Figure 4.14: Allan variance of the photodiode signal measuring the transmission of 739 nm light through a stable Fabry-Perot cavity. The cavity length is set to around the half way point of a Fabry-Perot peak and is shown both locked (red) and unlocked (blue).

The long term frequency stability can be measured directly using the wavemeter and is given in figure 4.15. The locked signal (blue) is seen to be significantly more stable, with a standard deviation of the 10 second moving average of 6.515×10^{-7} nm, than the unlocked signal (red), which has a standard deviation of the 20 second moving average of 3.3×10^{-6} nm. Figure 4.15 also shows the effect of locking the 739 nm laser to a free cavity which has not been externally stabilised. The signal shows a slow drift in frequency caused by thermal changes in the cavity. Instead of locking the cavity to a stable 780 nm laser as presented here, this could have been minimised by constructing the cavity out of a thermally stable material such as Invar.

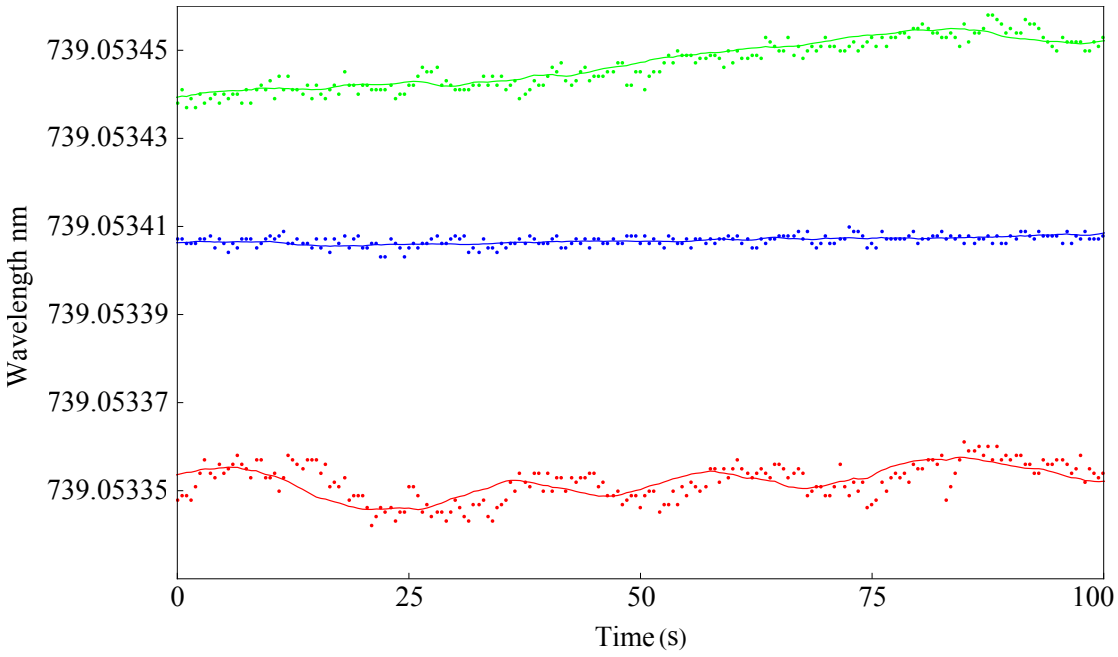

Figure 4.15: Long term frequency measurement of the 739 nm laser taken using the wavemeter when the laser is locked to a stable cavity (blue), locked to a unstable cavity (green) and unlocked (red). The bold lines show moving averages over 10 points.

Chapter 5

Review and comparison of entanglement schemes

An ion trap quantum computer will work by implementing quantum algorithms to a set of ionic qubits. It can be shown [18] that any quantum algorithm can be produced using a combination of single qubit rotations such as those shown in chapter 3 and a two qubit entangling gate such as a controlled-not gate (CNOT) or controlled-phase gate (CZ). Three different methods of producing such two qubit gates are the Cirac and Zoller gate [61], the geometric phase gate [27, 62, 63] and the ultrafast pushing gate [64]. This chapter will begin by introducing single qubit gates and will go on to discuss entanglement and how CNOT and CZ logic gates affect a set of qubits. The three methods of implementing entangling gates mentioned above will be explained and ways by which they can be realised experimentally will be explored. Finally the chapter will compare all the methods to find a suitable entanglement solution for our lab.

It should be noted that this chapter will make frequent reference to an ions motional state. Motional states are the quantised energy levels describing a trapped ions motion and are discussed in appendix D.

5.1 Quantum logic

As discussed in chapter 3, a qubit state is represented in matrix form by

$$|\psi\rangle = \begin{pmatrix} q_0 \\ q_1 \end{pmatrix}. \tag{5.1}$$

where q_0 and q_1 obey the relation $q_0^2 + q_1^2 = 1$ and determine the qubits position on the Bloch sphere. Quantum logic gates are processes which transform one set of qubit states to another. Unlike classical logic gates, which are preformed using electric components which dissipate heat, quantum logic gates rely on the evolution of Hamiltonians using the Schrödinger equation which makes them reversible and unitary.

5.1.1 Single qubit gates

Single qubit gates are formed using Pauli rotations such as the σ_z rotation discussed in chapter 3 to rotate the qubit around the Bloch sphere. Three important single qubit gates are known as the σ_x, σ_x and σ_x gates and act on the qubit state to produce 180° rotations around the x, y and z axes of the Bloch sphere respectively. The matrixes associated with these gates are as follows,

$$\sigma_x = \begin{pmatrix} 0 & 1 \\ 1 & 0 \end{pmatrix} \ , \quad \sigma_y = \begin{pmatrix} 0 & -i \\ i & 0 \end{pmatrix} \ , \quad \sigma_z = \begin{pmatrix} 1 & 0 \\ 0 & -1 \end{pmatrix} . \tag{5.2}$$

The σ_x gate is the quantum equivalent of a classical NOT gate and acts to translate $|0\rangle$ into $|1\rangle$ and $|1\rangle$ into $|0\rangle$. The σ_y gate is similar to a NOT gate but also introduces a phase to the qubit states by translating $|0\rangle$ into $i\,|1\rangle$ and $|1\rangle$ into $-i\,|0\rangle$. The σ_z gate leaves the $|0\rangle$ state unchanged and adds a phase of -1 to the $|1\rangle$ state.

Another commonly seen single qubit gate is the Hadamard gate which is the result of a rotation around the x axis of the Bloch sphere by 90°, given by

$$H_d = \frac{1}{\sqrt{2}} \begin{pmatrix} 1 & 1 \\ 1 & -1 \end{pmatrix} \tag{5.3}$$

This gate maps the qubit computational basis states ($|0\rangle$ and $|1\rangle$) to equal superposition qubit states where the population is shared equally between $|0\rangle$ and $|1\rangle$ as follows,

$$\begin{aligned} |0\rangle &\xrightarrow{H_d} \tfrac{1}{\sqrt{2}} \left(|0\rangle + |1\rangle\right) \equiv |+\rangle \\ |1\rangle &\xrightarrow{H_d} \tfrac{1}{\sqrt{2}} \left(|0\rangle - |1\rangle\right) \equiv |-\rangle . \end{aligned} \tag{5.4}$$

5.1.2 Two qubit gates

Gates applied to two qubits can be either separable or inseparable. Separable gates can be split into separate single qubit gates in a tensor product. An example of a separable gate is the $H_d^{(2)}$ gate. This gate is the application of Hadamard gates to two separate qubits

simultaneously, given by

$$H_d^{(2)} = H_d \otimes H_d = \frac{1}{\sqrt{2}} \begin{pmatrix} 1 & 1 \\ 1 & -1 \end{pmatrix} \otimes \frac{1}{\sqrt{2}} \begin{pmatrix} 1 & 1 \\ 1 & -1 \end{pmatrix} = \frac{1}{\sqrt{2}} \begin{pmatrix} 1 & 1 & 1 & 1 \\ 1 & -1 & 1 & -1 \\ 1 & 1 & -1 & -1 \\ 1 & -1 & -1 & 1 \end{pmatrix}. \tag{5.5}$$

Gates which are inseparable, i.e. cannot be split using a tensor product into two single qubit gates, result in the gate outcome for each qubit depending on the input values of both qubits. These are known as entangling gates. The controlled-not (CNOT) gate is a key example of this, performing a σ_x gate on the second qubit only when the input state of the first qubit is equal to $|1\rangle$. This is represented by the following matrix and truth table

$$\text{CNOT} = \begin{pmatrix} 1 & 0 & 0 & 0 \\ 0 & 1 & 0 & 0 \\ 0 & 0 & 0 & 1 \\ 0 & 0 & 1 & 0 \end{pmatrix} \qquad \begin{aligned} |00\rangle &\Rightarrow |00\rangle \\ |01\rangle &\Rightarrow |01\rangle \\ |10\rangle &\Rightarrow |11\rangle \\ |11\rangle &\Rightarrow |10\rangle. \end{aligned} \tag{5.6}$$

When a CNOT gate is applied to a pair of qubits where the first qubit is in a superposition state, an entangled state is formed, for example,

$$|+0\rangle = \frac{1}{\sqrt{2}} \left(|00\rangle + |10\rangle\right) \overset{CNOT}{\longrightarrow} \frac{1}{\sqrt{2}} \left(|00\rangle + |11\rangle\right). \tag{5.7}$$

Both qubits have an equal probability of being in the $|0\rangle$ or $|1\rangle$ state, but by measuring the state of the first qubit in the computational basis, the state of the second qubit collapses and is known with 100 percent probability.

5.1.3 The Cirac and Zoller gate scheme

A method of producing a CNOT gate with trapped ions was proposed in 1995 by Cirac and Zoller [65]. The scheme requires the ions to be cooled to their ground state of motion then uses a laser, focused down onto the first ion, to excite a combined motional mode of the two ions, conditional on the first ion being in the $|1\rangle$ state[1]. A second laser is then focused down onto the second ion which will, as a result, experience a spin flip if the combined motional mode is excited. The application of this scheme can be quite challenging as the ions need to be in the ground state and, as the scheme requires individual addressing, the

[1] Coupling spin to motion will be explained further in section 5.3.6

lasers need to be tightly focused onto each ion. Nevertheless, fidelities of up to 95 percent have been achieved using the method described in [66].

5.1.4 Controlled-phase gates

Another example of an entanglement gate is the controlled-phase (CZ) gate. This has the effect of applying a σ_z gate to the second qubit if the state of the first qubit is equal to $|1\rangle$. The matrix and truth table for this gate are given by

$$\mathrm{CZ} = \begin{pmatrix} 1 & 0 & 0 & 0 \\ 0 & 1 & 0 & 0 \\ 0 & 0 & 1 & 0 \\ 0 & 0 & 0 & -1 \end{pmatrix} \qquad \begin{aligned} |00\rangle &\Rightarrow |00\rangle \\ |01\rangle &\Rightarrow |01\rangle \\ |10\rangle &\Rightarrow |10\rangle \\ |11\rangle &\Rightarrow -|11\rangle . \end{aligned} \tag{5.8}$$

A CZ gate can be turned into a CNOT gate by the application of Hadamard gates to qubit number two before and after the gate operation as shown in figure 5.1

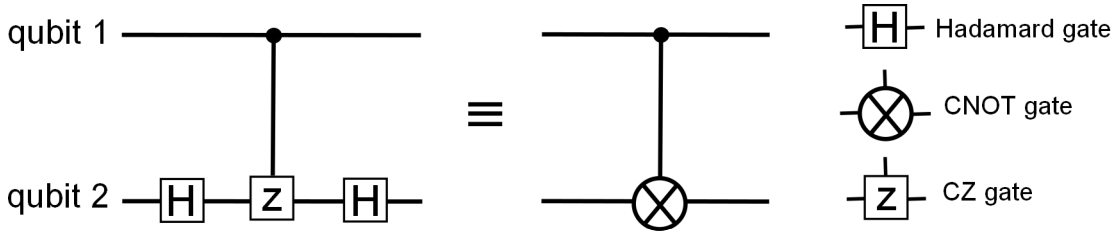

Figure 5.1: Creation of a CNOT gate from a CZ gate.

The remainder of this chapter will focus on the realisation of a CZ gate with trapped ions.

A CZ gate can be performed in a similar way to the Cirac and Zoller gate explained in the previous section, an example of a method by which this is carried out is explained in [67].

5.2 The Mølmer and Sørenson gate scheme

One of the main challenges of the Cirac and Zoller gate scheme is the requirement for ground state cooling. In 1999, a scheme to produce a CZ gate on "hot" ions was proposed by Mølmer and Sørenson [63]. The scheme was shown to be insensitive to the ion's motional state providing the ion stayed within the Lamb-Dicke regime, that is where

$$\eta^2(2\bar{n}+1) << 1 \tag{5.9}$$

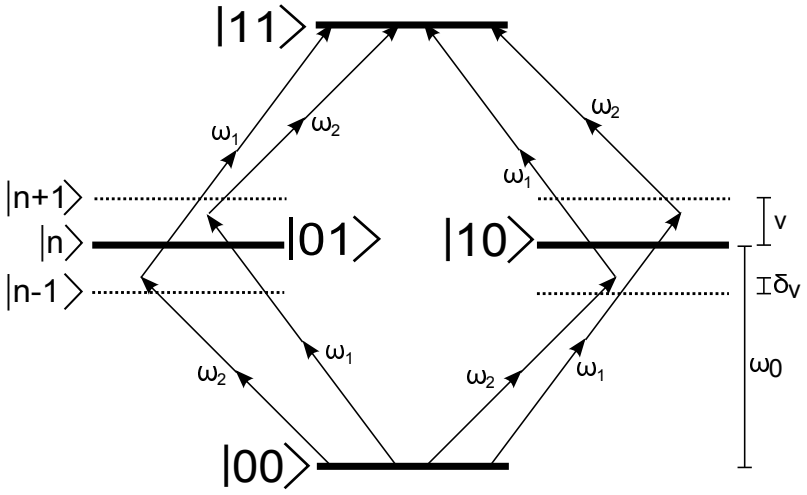

Figure 5.2: Rabi oscillation routes during the Mølmer and Sørenson gate

where $\bar{n}$ is the ions average motional quantum number (see appendix D) and η is the Lamb-Dicke parameter, given by

$$\eta = \frac{2\pi x_0}{\lambda} \tag{5.10}$$

where λ is the wavelength of the incident radiation and x_0 is the spatial extent of the ions ground state wavefunction, $x_0 = \sqrt{\frac{\hbar}{2mv}}$.

The scheme involves applying two electromagnetic fields to the two ions with frequencies slightly detuned by δ_v from the resonant frequency plus and minus a motional frequency, $\omega_1 = \omega_0 + v - \delta_v$ and $\omega_2 = \omega_0 - v + \delta_v$. Assuming the single ion Rabi frequency, Ω, induced by these fields obeys the relation $\eta\Omega << \delta_v$, known as the weak coupling regime, the ions will undergo collective Rabi oscillations via the routes shown in figure 5.2. The Rabi frequency of these oscillations is independent of the motional quanta n, and is given by [63],

$$\tilde{\Omega} = \frac{(\Omega\eta)^2}{2\delta_v} \tag{5.11}$$

The truth table for this is given by [68],

$$\begin{aligned}
|00\rangle &\Rightarrow \cos\tfrac{\tilde{\Omega}t}{2}\,|00\rangle + i\sin\tfrac{\tilde{\Omega}t}{2}\,|11\rangle & |\phi_0\phi_0\rangle &\Rightarrow e^{-i\frac{\tilde{\Omega}t}{2}}\,|\phi_0\phi_0\rangle \\
|01\rangle &\Rightarrow \cos\tfrac{\tilde{\Omega}t}{2}\,|01\rangle - i\sin\tfrac{\tilde{\Omega}t}{2}\,|10\rangle & |\phi_0\phi_1\rangle &\Rightarrow e^{i\frac{\tilde{\Omega}t}{2}}\,|\phi_0\phi_1\rangle \\
|10\rangle &\Rightarrow \cos\tfrac{\tilde{\Omega}t}{2}\,|10\rangle - i\sin\tfrac{\tilde{\Omega}t}{2}\,|01\rangle & |\phi_1\phi_0\rangle &\Rightarrow e^{i\frac{\tilde{\Omega}t}{2}}\,|\phi_1\phi_0\rangle \\
|11\rangle &\Rightarrow \cos\tfrac{\tilde{\Omega}t}{2}\,|11\rangle + i\sin\tfrac{\tilde{\Omega}t}{2}\,|00\rangle & |\phi_1\phi_1\rangle &\Rightarrow e^{-i\frac{\tilde{\Omega}t}{2}}\,|\phi_1\phi_1\rangle.
\end{aligned} \tag{5.12}$$

The second truth table shows the transformation of the states in the σ_ϕ basis, where $|\phi_{0,1}\rangle = (|0\rangle \pm e^{i\phi}\,|1\rangle)/\sqrt{2})$, with $\phi = \pi/2$. After a time $t = \pi/\tilde{\Omega}$, only the $|\phi_0\phi_0\rangle$ and

$|\phi_1\phi_1\rangle$ states have gained a phase[2] of -1.

The Mølmer and Sørenson gate was later discovered to be a special case of a gate known as the geometric phase gate [62]. The geometric phase gate will be described in the following section.

5.3 Geometric phase gates

A highly successful method of producing a CZ gate is to use a geometric phase gate. This method avoids the main issues associated with the Cirac and Zoller scheme, namely, ground state cooling and the need for tightly focused laser beams, by the application of a oscillating state dependent force to a pair of ions. This will result in the state dependent movement of the ions' motional states resulting in an overall phase change which depends on the initial state of both the ions. To explain this process in more detail, I will begin by looking at the effect an oscillating state dependent force has on a single ion before looking at how this translates to two ions.

5.3.1 Oscillating force on a single ion

A single ion qubit trapped in a harmonic well can be modeled as a quantum harmonic oscillator whose motion is described in equation 3.31 of chapter 3 as

$$\hat{H}_b = \hbar v \left(\hat{a}^\dagger \hat{a} + \frac{1}{2} \right) \tag{5.13}$$

where v is the trap secular frequency and $\hat{a}$ and $\hat{a}^\dagger$ are the respective state lowering and raising operators. The addition of an external time dependent force, $f(t)$, to such a system will result in the following addition to this Hamiltonian [69]

$$H' = x_0(\hat{a} + \hat{a}^\dagger) f(t) \tag{5.14}$$

It will be assumed that $f(t)$ is spatially uniform and oscillates at a frequency slightly detuned from v,

$$f(t) = F \cos\left((v - \delta)t\right) \tag{5.15}$$

where δ is the detuning. Combining equations 5.14 and 5.15 and moving into the interaction picture with respect to H_b gives the interaction Hamiltonian, $\hat{H}_I$ where $\hat{H}_I =$

[2] Ignoring the global phase, i.

$e^{\frac{i\hat{H}_b t}{\hbar}}\hat{H}'e^{-\frac{i\hat{H}_b t}{\hbar}}$,

$$\hat{H}_I = x_0\left(\hat{a}e^{-ivt} + \hat{a}^\dagger e^{ivt}\right)F\cos\left((v-\delta)t\right) \tag{5.16}$$

This can be simplified by writing $\cos(x)$ in terms of exponentials and applying the rotating wave approximation to eliminate the fast rotating terms [70],

$$\hat{H}_I(t) = \frac{Fx_0\hat{a}}{2}e^{-i\delta t} + \frac{Fx_0\hat{a}^\dagger}{2}e^{i\delta t} \tag{5.17}$$

The evolution of a state, $|\psi\rangle$, being acted on by this Hamiltonian is found by solving the Schrödinger equation, $i\hbar d/dt\,|\psi\rangle = \hat{H}\,|\psi\rangle$.

The solution to the Schrödinger equation for a time dependent Hamiltonian is given by the Mangus expression which to the first order is given by [71],

$$|\psi(t)\rangle = e^{\hat{A}(t)}e^{\hat{B}(t)}\,|\psi(0)\rangle \tag{5.18}$$

where

$$\hat{A}(t) = \frac{1}{i\hbar}\int_0^t dt'\hat{H}(t') \tag{5.19}$$

and

$$\begin{aligned}\hat{B}(t) &= -\frac{1}{2}\left(\frac{1}{i\hbar}\right)^2\int_0^t dt''\int_0^{t''}dt'[\hat{H}(t'),\hat{H}(t'')].\\ &= -\frac{1}{2}\left(\frac{1}{i\hbar}\right)\int_0^t dt''[\hat{A}(t''),\hat{H}(t'')].\end{aligned} \tag{5.20}$$

For the interaction Hamiltonian given by equation 5.17, $A(t)$ is equal to,

$$\hat{A}(t) = \frac{Fx_0}{2\delta\hbar}\left((1-e^{i\delta t})\hat{a}^\dagger + (e^{-i\delta t}-1)\hat{a}\right). \tag{5.21}$$

As a result, the first term in equation 5.17 has the exact form of the displacement operator (see appendix D)

$$e^{A(t)} = D(\alpha) \tag{5.22}$$

$$= e^{\alpha\hat{a}^\dagger - \alpha^*\hat{a}} \tag{5.23}$$

where α is given by

$$\alpha = \frac{Fx_0}{\delta\hbar}(1-e^{i\delta t}). \tag{5.24}$$

The application of the Hamiltonian 5.17 to an initial motional state will therefore result

in the formation of a coherent motional state, $|\alpha\rangle$. When the ion is initially in the ground state

$$|\alpha\rangle = e^{\frac{-|\alpha|^2}{2}} \sum_{n=0}^{\infty} \frac{\alpha^n}{\sqrt{n!}} |n\rangle \,, \tag{5.25}$$

which will follow a trajectory in phase space described by α. The real and imaginary parts of α describe the expectation values of the position and momentum of the motional state[3],

$$\langle x \rangle = Re[\alpha] \tag{5.26}$$

$$= \frac{Fx_0}{\delta\hbar}(1 - \cos(\delta t)) \tag{5.27}$$

$$\langle p \rangle = Im[\alpha] \tag{5.28}$$

$$= -\frac{Fx_0}{\delta\hbar}(\sin(\delta t)). \tag{5.29}$$

This trajectory is plotted in figure 5.3.

In addition to the displacement operator, equation 5.18 also contains a second term, $e^{B(t)}$. Using equation 5.20, $B(t)$ is equal to

$$B(t) = \frac{Fx_0}{4i\hbar} \int_0^t dt' \left[(\alpha\hat{a}^\dagger + \alpha^*\hat{a}), (e^{-i\delta t}\hat{a} + e^{i\delta t}\hat{a}^\dagger) \right] \tag{5.30}$$

$$= \frac{Fx_0}{4i\hbar} \int_0^t dt' \left(\alpha^* e^{i\delta t'} + \alpha e^{-i\delta t'} \right) \tag{5.31}$$

$$= \frac{F^2 x_0^2}{2i\delta\hbar^2} \left(\frac{\sin(\delta t)}{\delta} - t \right) \tag{5.32}$$

for the interaction Hamiltonian. This second term therefore represents the addition of a time dependent phase, $\Phi(t)$, to the motional state

$$e^{B(t)} = e^{i\Phi(t)} \tag{5.33}$$

where $\Phi(t)$ is given by

$$\Phi(t) = \frac{F^2 x_0^2}{2\delta\hbar^2} \left(t - \frac{\sin(\delta t)}{\delta} \right). \tag{5.34}$$

This phase corresponds to the area sweeped out by the coherent motional state and the Re(α) axis of phase space as it cycles in time as shown in figure 5.3 [68] and is therefore known as a geometric phase.

The coherent motional state has performed a full rotation in phase space after at time $t = \frac{2\pi}{\delta}$. At this time α equals zero and the motional state has returned to its initial state.

[3]It should be noted that this is within the rotating frame with respect to the ions secular motion

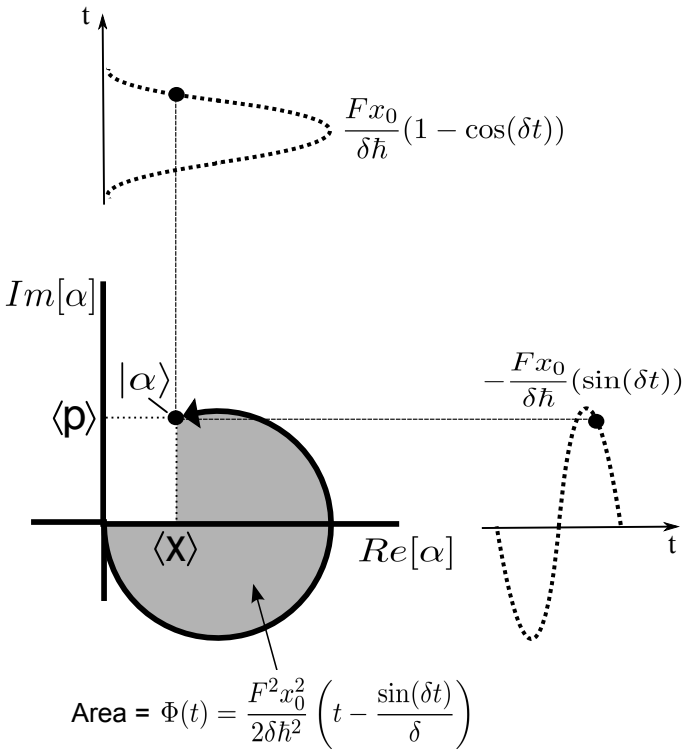

Figure 5.3: The main graph shows the movement of an ion's motional state in phase space when acted on by an oscillating force. The dotted graphs show the time evolution of the expectation values of position and momentum of the motional state.

The state has however picked up a geometric phase equal to

$$\Phi_T = \Phi(2\pi/\delta) = \pi\left(\frac{Fx_0}{\delta\hbar}\right)^2. \tag{5.35}$$

5.3.2 State dependent oscillating force on a single ion

If the applied force, F, is state dependent (ie, two orthogonal states, $|m_1\rangle$ and $|m_2\rangle$, experience different forces, F_{m_1} and F_{m_2}) the phase given by equation 5.35 will depend on the internal state of the ion. This state dependent phase is the key to producing a CZ gate.

Two orthogonal qubit states represent a state basis therefore, using equation 5.17, the Hamiltonian describing this system is given by [62]

$$\hat{H}_I = \sum_{m_1,m_2}\left(\frac{F_m x_0 \hat{a}}{2}e^{-i\delta t} + \frac{F_m x_0 \hat{a}^\dagger}{2}e^{i\delta t}\right)|m\rangle\langle m| \tag{5.36}$$

$$= \frac{x_0}{2}\left(\hat{a}e^{-i\delta t} + \hat{a}^\dagger e^{i\delta t}\right)\left(F_{m_1}|m_1\rangle\langle m_1| + F_{m_2}|m_2\rangle\langle m_2|\right). \tag{5.37}$$

This can be rearranged to give

$$\hat{H}_I = \frac{x_0}{2}\left(\hat{a}e^{-i\delta t} + \hat{a}^\dagger e^{i\delta t}\right)\left(F_+\hat{I} + F_-(|m_1\rangle\langle m_1| - |m_2\rangle\langle m_2|)\right) \tag{5.38}$$

where $F_+ = \frac{F_{m_1}+F_{m_2}}{2}$ and $F_- = \frac{F_{m_1}-F_{m_2}}{2}$. The identity term is global and can therefore be ignored leaving

$$\hat{H}_I = \frac{F_- x_0}{2}\left(\hat{a}e^{-i\delta t} + \hat{a}^\dagger e^{i\delta t}\right)(|m_1\rangle\langle m_1| - |m_2\rangle\langle m_2|). \tag{5.39}$$

Using equation 5.18, the application of this Hamiltonian will result in time dependent evolution equal to

$$|\psi(t)\rangle = D(\alpha)e^{i\Phi(t)}|m_1\rangle \tag{5.40}$$

$$= e^{i\Phi(t)}|\alpha\rangle|m_1\rangle \tag{5.41}$$

for an ion initially in the $|m_1\rangle$ state and

$$|\psi(t)\rangle = D(-\alpha)e^{i\Phi(t)}|m_2\rangle \tag{5.42}$$

$$e^{i\Phi(t)}|-\alpha\rangle|m_2\rangle \tag{5.43}$$

for an ion initially in the $|m_2\rangle$ state where $D(\alpha)$, α and $\Phi(t)$ are given by equations 5.23, 5.24 and 5.34 with the substitution $F = F_-$.

It follows that the expectation values within the interaction picture of the position and momentum of an ion's motional coherent states under this Hamiltonian are given by

$$\begin{aligned}\langle x\rangle &= \frac{F_- x_0}{\delta\hbar}(1-\cos(\delta t))\\ \langle p\rangle &= -\frac{F_- x_0}{\delta\hbar}\sin(\delta t)\end{aligned} \tag{5.44}$$

and

$$\begin{aligned}\langle x\rangle &= -\frac{F_- x_0}{\delta\hbar}(1-\cos(\delta t))\\ \langle p\rangle &= \frac{F_- x_0}{\delta\hbar}\sin(\delta t)\end{aligned} \tag{5.45}$$

for an ion in the $|m_1\rangle$ and $|m_2\rangle$ states respectively. This is shown in figure 5.4. The time taken to perform a complete rotation in phase space and the total geometric phase after one full rotation, Φ_T, will be equal for both states.

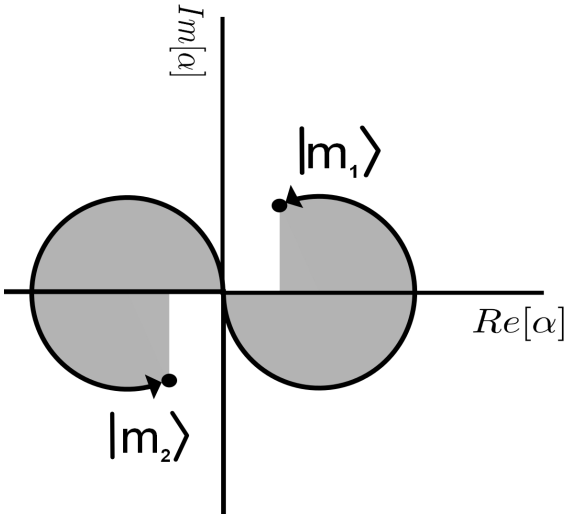

Figure 5.4: Movement in phase space of an ion in the $|m_1\rangle$ and $|m_2\rangle$ states when acted on by a state dependent oscillating force.

5.3.3 State dependent oscillating force on two ions

Two ions in the same potential well will share motional modes mediated by the Coulomb interaction. When applied to two ions, a state dependent oscillating force will therefore create common coherent motional states which rotate in phase space analogously to the coherent motional states of a single ion. After a full rotation of these states in phase space, the total accumulated phase of the coherent state, $\Phi(t)$, will be shared by both ions.

The axial modes of two trapped ions are the center of mass mode (COM) and the stretch mode (SM), these have frequencies equal to v_C and v_S where $v_S = \sqrt{3}v_C$ and coordinates in space equal to [62],

$$z_C = \frac{z_1 + z_2}{\sqrt{2}} \tag{5.46}$$

and

$$z_S = \frac{z_1 - z_2}{\sqrt{2}} \tag{5.47}$$

respectively where z_1 and z_2 are the axial positions of the two ions. The total force experienced by the two modes in terms of the forces experienced by the individual ions is therefore given by,

$$F_C = \frac{F_{1,m} + F_{2,n}}{\sqrt{2}} \tag{5.48}$$

when acting on the center of mass mode and

$$F_S = \frac{F_{1,m} - F_{2,n}}{\sqrt{2}} \tag{5.49}$$

when acting on the stretch mode, where $F_{1,m}$ and $F_{2,m}$ are the forces experienced by ions 1 and 2 in the $|m\rangle$ and $|n\rangle$ states respectively.

The Hamiltonian acting on the COM mode of the two ions equals the sum of equation 5.17 acting on the basis states for each ion.

$$\hat{H}_I = \sum_{m=m_1,m_2} \sum_{n=m_1,m_2} (\frac{F_C x_0 \hat{a}}{2} e^{-i\delta t} + \frac{F_C x_0 \hat{a}^\dagger}{2} e^{i\delta t}) \left|m,n\right\rangle \left\langle m,n\right| \tag{5.50}$$

Using equation 5.48 and assuming the forces experienced by both ions in state $|m\rangle$ are equal and of the same phase, $(F_{1,m} = F_{2,m})$,

$$\begin{aligned}
\hat{H}_I =& \frac{x_0}{2\sqrt{2}} \left(\hat{a}e^{-i\delta t} + \hat{a}^\dagger e^{i\delta t}\right) \times \\
& \Big((F_{m_1} + F_{m_2}) \left(|m_1 m_2\rangle \left\langle m_1 m_2\right| + |m_2 m_1\rangle \left\langle m_2 m_1\right|\right) && (5.51) \\
& + 2F_{m_1} |m_1 m_1\rangle \left\langle m_1 m_1\right| + 2F_{m_2} |m_2 m_2\rangle \left\langle m_2 m_2\right| \Big) && (5.52) \\
=& \frac{x_0}{2\sqrt{2}} \left(\hat{a}e^{-i\delta t} + \hat{a}^\dagger e^{i\delta t}\right) \left(F_+ \hat{I} + F_- \left(|m_1 m_1\rangle \left\langle m_1 m_1\right| - |m_2 m_2\rangle \left\langle m_2 m_2\right|\right)\right). && (5.53)
\end{aligned}$$

As before, the identity term is global and can therefore be ignored. Similarly, when coupled to the SM, Hamiltonian 5.50 equals

$$\hat{H}_I = \frac{x_0}{2\sqrt{2}} \left(\hat{a}e^{-i\delta t} + \hat{a}^\dagger e^{i\delta t}\right) F_- \left(|m_1 m_2\rangle \left\langle m_1 m_2\right| - |m_2 m_1\rangle \left\langle m_2 m_1\right|\right). \tag{5.54}$$

Under these Hamiltonians, the modes will evolve in phase space with trajectories dependent on the internal states of the two ions. As before, the exact trajectories can be found using the solution to the Schrödinger equation given in equation 5.18. Table 5.1 shows the evolution of the x and p expectation values of the COM and SM coherent motional states and the total phase accumulated after a full rotation of the coherent states in phase space for the initial states $|m_1 m_1\rangle$, $|m_1 m_2\rangle$, $|m_2 m_1\rangle$ and $|m_2 m_2\rangle$.

A truth table and transformation matrix for the resultant state after an integer number of rotations, n_r is given below for state dependent forces coupled to the stretch mode of motion.

$$\begin{aligned}
&|m_1 m_1\rangle \Rightarrow |m_1 m_1\rangle \\
&|m_1 m_2\rangle \Rightarrow e^{in_r\Phi_T} |m_1 m_2\rangle \\
&|m_2 m_1\rangle \Rightarrow e^{in_r\Phi_T} |m_2 m_1\rangle \\
&|m_2 m_2\rangle \Rightarrow |m_2 m_2\rangle
\end{aligned} \qquad \begin{pmatrix} 1 & 0 & 0 & 0 \\ 0 & e^{in_r\Phi_T} & 0 & 0 \\ 0 & 0 & e^{in_r\Phi_T} & 0 \\ 0 & 0 & 0 & 1 \end{pmatrix}. \tag{5.55}$$

initial state	COM mode evolution			SM evolution		
	$\langle x \rangle$	$\langle p \rangle$	$\Phi(\frac{2\pi}{\delta})$	$\langle x \rangle$	$\langle p \rangle$	$\Phi(\frac{2\pi}{\delta})$
$\|m_1 m_1\rangle$	$x(t)$	$-p(t)$	Φ_T	0	0	0
$\|m_1 m_2\rangle$	0	0	0	$x(t)$	$-p(t)$	Φ_T
$\|m_2 m_1\rangle$	0	0	0	$-x(t)$	$p(t)$	Φ_T
$\|m_2 m_2\rangle$	$-x(t)$	$p(t)$	Φ_T	0	0	0

Table 5.1: Evolution of the expectation values of the position and momentum of the coherent COM and SM motional states of two ions and the phase accumulated after one rotation of the states in phase space when acted on by a state dependent oscillating force. $x(t) = \frac{F_- x_0}{\delta\hbar}(1 - \cos(\delta t))$, $p(t) = \frac{F_- x_0}{\delta\hbar}\sin(\delta t)$ and $\Phi_T = \pi\left(\frac{F x_0}{\delta\hbar}\right)$.

By ensuring $n_r \Phi_T = \frac{\pi}{2}$ the transformation matrix takes the form

$$M_1 = \begin{pmatrix} 1 & 0 & 0 & 0 \\ 0 & i & 0 & 0 \\ 0 & 0 & i & 0 \\ 0 & 0 & 0 & 1 \end{pmatrix}, \tag{5.56}$$

which cannot be separated by the tensor product.

This transformation can be turned into a CZ gate by applying the single qubit rotation S to both ions as shown in figure 5.5. where S is equivalent to a rotation of 90° anticlockwise around the z-axis of the Bloch sphere and is given by the matrix

$$S = \begin{pmatrix} 1 & 0 \\ 0 & -i \end{pmatrix}. \tag{5.57}$$

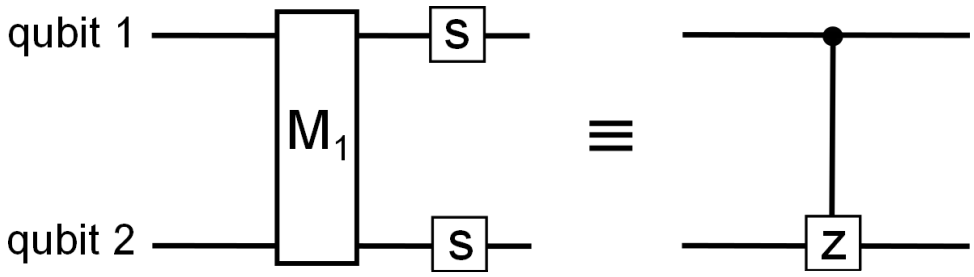

Figure 5.5: Formation of a CZ gate from the gate operation given by M_1.

This section has so far shown how the application of an oscillating state dependent force to a pair of ions can be used to produce a CZ gate due to the geometric phases aquired by the ions' motional states traversing circles in phase space. The remainder of

this section will describe the main methods known to produce the required state dependent force. Section 5.3.4 will describe the production of a state dependent force between the $|m_1\rangle = |0\rangle$ and $|m_2\rangle = |1\rangle$ states (known as the σ_z basis) and section 5.3.5 will describe the production of a state dependent force between the $|m_1\rangle = |\phi_0\rangle$ and $|m_2\rangle = |\phi_1\rangle$ basis states (known as the σ_ϕ basis) where $|\phi_0\rangle$ and $|\phi_1\rangle$ describe points on opposite ends of the equator of the Bloch sphere and are given by

$$|\phi_0\rangle = \frac{1}{\sqrt{2}}\left(|0\rangle + e^{i\phi}\,|1\rangle\right) \tag{5.58}$$

and

$$|\phi_1\rangle = \frac{1}{\sqrt{2}}\left(|0\rangle - e^{i\phi}\,|1\rangle\right). \tag{5.59}$$

where ϕ is the angle of rotation of the $|\phi_0\rangle$ state from the x-axis of the Bloch sphere as shown in figure 5.6.

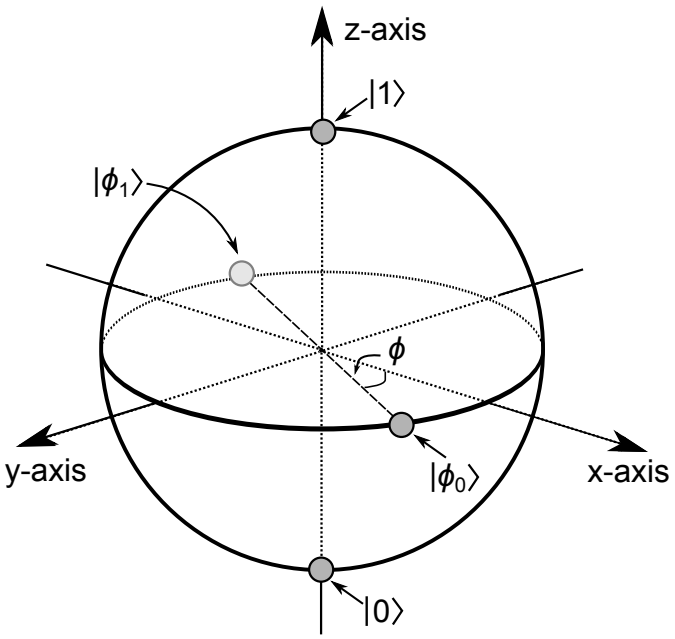

Figure 5.6: Figure showing the location of the $|0\rangle$, $|1\rangle$, $|\phi_0\rangle$ and $|\phi_1\rangle$ states on the Bloch sphere.

5.3.4 Experimental production of an oscillating state dependent force in the σ_z basis

The most common method of producing a state dependent force between the $|0\rangle$ and $|1\rangle$ states is to use the optical dipole force felt by the ions in a moving standing wave [27, 62]. This is produced when two lasers whose frequencies ω_1 and ω_2 obey the relation, $\Delta\omega = \omega_1 - \omega_2 = \upsilon - \delta$, are applied at right angles along the trap axis as shown in figure

5.7.

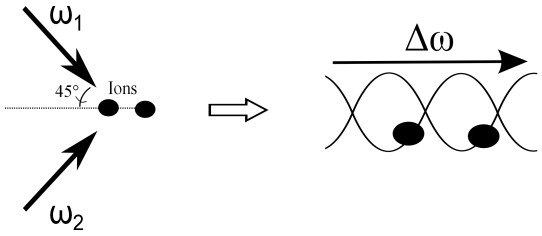

Figure 5.7: Production of a moving standing wave at the ions by the application of two lasers at right angles along the trap axis.

The two fields interfere, producing a standing wave which moves along the trap axis at a frequency equal to the difference in frequency of the two fields, Δw. The ions experience a state dependent Stark shift potential which, due to the standing wave, results in a periodic force. The direction of this force will be state dependent resulting in the system having the Hamiltonian given by equation 5.38 [62].

By ensuring the ion-ion separation is an integer value of the wavelength of this standing wave, the phase of the force will be equal for both ions.

A disadvantage of this method is that it requires the optical path of the two beams to be interferometrically stable to maintain the phase difference between the two co-propagating fields. In addition, the use of lasers introduces the probability of decoherence from off resonant scattering. The performance of this gate has however produced fidelities of up to 97 percent [27].

5.3.5 Experimental production of an oscillating state dependent force in the σ_ϕ basis.

A scheme to produce a state dependent force between the $|\phi_0\rangle$ and $|\phi_1\rangle$ states was proposed initially by Mølmer and Sørensen [72]. As described in section 5.2, this scheme involves applying electromagnetic fields at frequencies close to the first order motional sidebands of the ions. The effect of applying radiation to a single ion at a frequency slightly detuned from the first red motional sideband $\omega_1 = \omega_0 - v + \delta_v$ is given by the Jaynes-Cummings interaction Hamiltonian [73],

$$\hat{H}_I = \frac{i\hbar\eta\Omega}{2}(\hat{a}e^{-i\delta_v}\hat{\sigma}_+ - \hat{a}^\dagger e^{+i\delta_v}\hat{\sigma}_-) \tag{5.60}$$

where $\hat{\sigma_-} = |0\rangle\langle 1|$ and $\hat{\sigma_+} = |1\rangle\langle 0|$. Similarly the effect of applying radiation with a frequency slightly detuned from the first blue sideband, $\omega_2 = \omega_0 + v - \delta_v$, to a single ion

is given by the anti-Jaynes-Cummings interaction Hamiltonian [73],

$$\hat{H}_I = \frac{i\hbar\eta\Omega}{2}(\hat{a}^\dagger e^{+i\delta_v}\hat{\sigma}_+ - \hat{a}e^{-i\delta_v}\hat{\sigma_-}) \tag{5.61}$$

Applying the red and the blue motional sideband fields to the ion simultaneously gives the following Hamiltonian which is the sum of equations 5.60 and 5.61.

$$\hat{H}_I = \frac{\hbar\eta\Omega}{2}(\hat{a}^\dagger e^{+i\delta_v} + \hat{a}e^{-i\delta_v})\hat{\sigma}_y \tag{5.62}$$

where $\hat{\sigma}_y = i(\hat{\sigma}_+ - \hat{\sigma}_-)$. Using equations 5.58 and 5.59 this can be written in the σ_ϕ basis as

$$\hat{H}_I = \frac{\hbar\eta\Omega}{2}(\hat{a}^\dagger e^{+i\delta_v} + \hat{a}e^{-i\delta_v})\left(|\phi_0\rangle\langle\phi_0| - |\phi_1\rangle\langle\phi_1|\right) \tag{5.63}$$

with $\phi = \pi/2$ which is equivalent to equation 5.39 with $F_- = \frac{\hbar\eta\Omega}{x_0}$.

The scheme showed in section 5.2 is a special case of the geometric phase gate where the two ions are in the weak coupling regime ($\eta\Omega << -\delta_v$). In this regime, the total phase after each rotation in phase space, given by equation 5.35,

$$\Phi_T = \pi\left(\frac{F_- x_0}{\hbar\delta_v}\right)^2 \tag{5.64}$$

$$= \pi\left(\frac{\eta\hat{\Omega}}{\delta_v}\right)^2 \tag{5.65}$$

is very small therefore the gate consists of lots of small cycles in phase space to make up the $\frac{\pi}{2}$ phase required for a phase gate. This makes the gate very slow.

To minimise gate time, ideally the modes should only make one rotation in phase space giving $\Phi(t) = \frac{\pi}{2}$. This can be done outside of the weak regime where the following required relation can be satisfied,

$$\hat{\Omega} = \frac{-\delta_v}{\sqrt{2}\eta}, \tag{5.66}$$

This results in a gate time of $T = \frac{\sqrt{2}\pi}{\eta\Omega}$. In this regime however the internal state will become dependent on n during the gate time making it more susceptible to heating [68].

5.3.6 Motional coupling strength

The electromagnetic fields used to create the state dependent force must have sufficiently strong coupling to the motional modes of the ions. If the coupling is too weak, the ions would decohere before traversing the required path in phase space. The strength of the

coupling is described by the Lamb-Dicke parameter which is given by equation 5.10,

$$\eta = \frac{2\pi x_0}{\lambda}, \tag{5.67}$$

where λ is the wavelength of the incident radiation and x_0 is the spatial extent of the ions ground state wavefunction. The qubit splitting within ytterbium 171 has a frequency approximately equal to 12.6 GHz and with a typical trap frequency of $2\pi \times 200$ kHz this gives a Lamb-Dicke parameter of the order of 3×10^{-6} which is far too small for significant coupling. Two main solutions to this problem are as follows:

- Use optical Raman fields with a frequency difference equal to the qubit splitting.
- Introduce a magnetic field gradient [34], which when combined with magnetic field dependent qubit states produces a new effective Lamb-Dicke parameter.

Both these methods are explored in the following sections.

5.3.7 Motional coupling using Raman transitions

A Raman transition is a method by which the ion is excited from an initial state, $|i\rangle$ to a final state $|f\rangle$ via an intermediate state, $|e\rangle$. Two fields incident on the ion excite the states $|i\rangle$ and $|f\rangle$ to $|e\rangle$ respectively. If these fields are detuned significantly from $|e\rangle$ then the population entering $|e\rangle$ becomes negligible. Using Raman beams, coupling strengths on the order of $\eta = 0.5$ can be achieved [74]. While to first order this system is analogous to the application of one field equal at ω_0, it is also subject to off-resonant scattering effects which can limit the overall fidelity of the gate. Nevertheless Raman transitions have been used to produce gate fidelities higher than 99.3% [75] which is an acceptable level for fault tolerant quantum computing.

To simultaneously apply the red and blue sidebands required for gate operations, three fields are needed as shown in figure 5.8 [62]. These fields can be produced from a single laser along with a system of AOMs and EOMs to produce the required frequency differences. An example setup is shown in figure 5.9. The offset frequencies need to be carefully chosen in order to avoid unwanted excitations by the additional frequency orders from the modulators. Alternatively, two lasers can be used as shown in figure 5.9 which eliminates the extra frequency orders present as a result of the EOM. This method also allows for more power and therefore higher Rabi frequencies which can lead to faster gate times, it should be noted however that to ensure the frequency difference between the two lasers

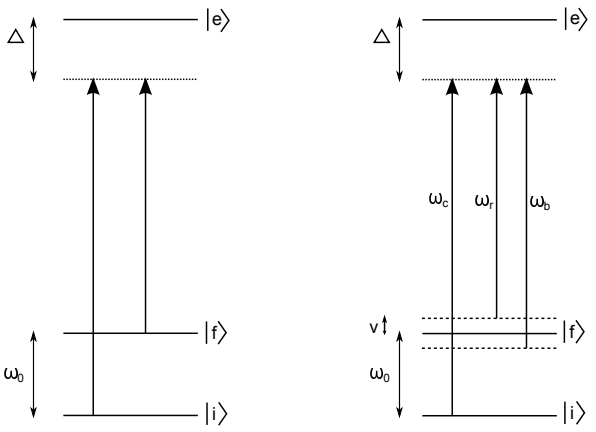

Figure 5.8: (a) Diagram showing how a Raman transition is performed. Population is excited from $|i\rangle$ to $|f\rangle$ via an excited state $|e\rangle$ which remains unpopulated. This requires two laser fields detuned from the $|i\rangle$ and $|f\rangle$ to $|e\rangle$ transitions by Δ where Δ is greater than the Rabi frequency of the two fields [2]. (b) Diagram showing the three frequencies required to simultaneously drive the red and blue motional sidebands using Raman transitions.

remains constant, phase-locking is required. Phase-locking can be technically demanding and is performed using methods such as those shown in [76–78].

Raman transitions using a pulsed laser.

Another method of producing the Raman transitions required for gate operations is presented in [4] and [79]. The scheme uses the interference from chains of large bandwidth laser pulses to produce the required transitions. A train of these pulses in the frequency domain can be represented as a frequency comb as shown in figure 5.10 (a). The comb teeth are separated in frequency by the repetition rate of the laser and the width of each tooth corresponds to the repetition rate/N where N is the number of pulses in the pulse train [4]. When two counterpropagating pulse chains, formed for example, from one pulse chain split into two using a beamsplitter, are incident on an ion, the ion can absorb a photon from one of the comb teeth in the first chain, then undergo stimulated emission as a result of a comb tooth in the second chain. When the two chains are separated in frequency space by the hyperfine splitting, ω_0, this will result in many small Raman transitions as shown in figure 5.10 (b) (Note: if ω_0 divided by the repetition rate is an integer, these Raman transitions can be driven using only one chain.). Each of these small Raman transitions will result in a small population transfer between states. To perform a full spin flip, many of these small transitions are needed[4]. Motional sidebands can be addressed in a similar way to before by introducing an AOM into each beam path to create the required frequency combs as shown in figure 5.10 (a).

[4]For example in [79], a spin flip was made up of 260 small Raman transitions

(a)

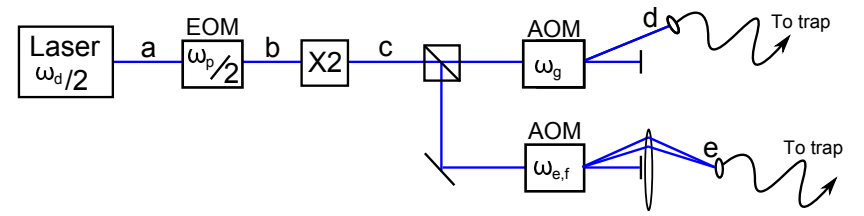

(b)

a	$\frac{w_d}{2}$
b	$\frac{w_d}{2} \pm \frac{w_p}{2}$
c	w_d $w_d \pm w_p$
d	$w_d - w_g$ $w_d \pm w_p - w_g$
e	$w_d - w_e$ $w_d - w_f$ $w_d \pm w_p - w_e$ $w_d \pm w_p - w_f$

(c)

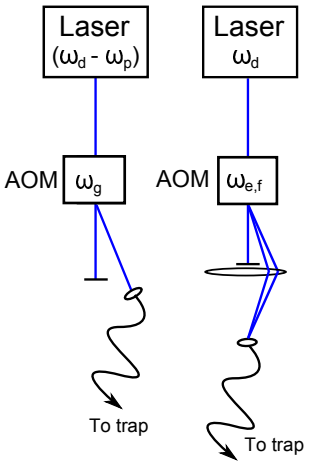

Figure 5.9: Example experimental setup for addressing the motional sidebands using one (a) and two (c) lasers, where $\omega_d - \omega_p + \omega_g$ equals the carrier frequency, ω_c, $\omega_d - \omega_e$ equals the blue sideband frequency, ω_b and $\omega_d + \omega_f$ is the red sideband frequency, ω_r. (b) shows a table of the main frequency components present at the given points in the beam path of the single laser setup. At e there are many extra frequencies present as a result of the EOM, the modulation frequencies therefore need to be carefully chosen to avoid unwanted excitations as a result of these frequencies.

An advantage of this method is that while the frequency difference between the comb teeth, determined by the lasers repetition rate, is important, the overall frequency is not important, and therefore this method does not require the laser to be frequency locked.

5.3.8 Motional coupling using a magnetic field gradient

In a magnetic field, the F = 1 hyperfine level within the $^2S_{\frac{1}{2}}$ level of $^{171}Yb^+$ is split via the Zeeman effect into three separate levels with different energies determined by the magnetic field strength. Within a magnetic field gradient, these energies therefore become dependent on the ion's position in space and are given by

$$E(z) = \hbar\omega_{m_F}(z) = \hbar\omega_{m_F}(0) + \hbar\partial_z\omega_{m_F}(0)z + \hbar\frac{\partial_z^2\omega_{m_F}(0)z^2}{2!} + ... \tag{5.68}$$

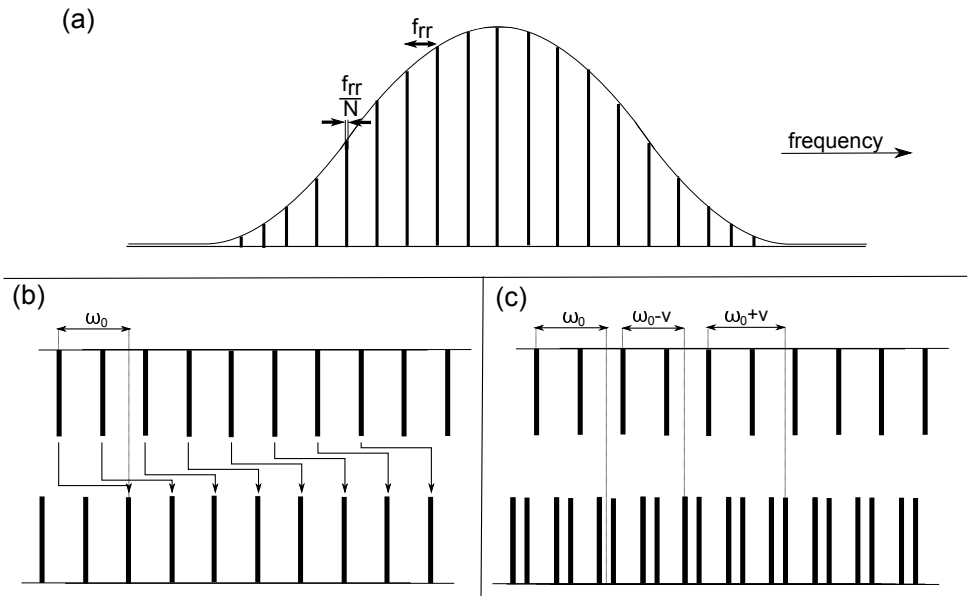

Figure 5.10: (a) In frequency space a series of laser pulses gives a frequency comb. (b) Two of these combs can be used to drive Raman transitions if the frequency difference between comb teeth is equal to the qubit splitting, ω_0. The ion absorbs a photon from the first comb then emits a photon into the second comb via the routes shown effectively producing lots of small Raman transitions. (c) To perform two qubit gates, the combs must contain components with frequency differences equal to the red and blue motional sidebands

where $m_F = -1, 0, 1$ is the projection of the total angular momentum quantum number of the state, z is the distance in space from the ions equilibrium position, which has been defined to be at the origin. $\partial_z \omega_{m_F}(0)$ is the frequency gradient at the ions equilibrium position due to the magnetic field gradient, $\partial_z B(0)$, and is given to first order by [80],

$$\partial_z \omega_{m_F}(0) = \frac{g_F m_F \mu_B \partial_z B(0)}{\hbar}. \tag{5.69}$$

where μ_B is the Bohr magnetron and g_F is the states g-factor. Assuming a linear gradient, high order terms in equation 5.68 equal zero allowing the energy to be rewritten using equation 5.69 as

$$E(z) = \hbar\omega_{m_F}(z) = \hbar\omega_{m_F}(0) + g_F m_F \mu_B \partial_z B(0) z \tag{5.70}$$

The following derivation closely follows that given in [34] and will show how this energy gradient results in an increased motional coupling strength.

The Hamiltonian describing the unperturbed ion's system is given by equation 3.31 and repeated here,

$$\hat{H}_0 = \frac{1}{2}\hbar\omega_{m_F}\hat{\sigma}_z + \hbar v \hat{a}^\dagger \hat{a}, \tag{5.71}$$

where ω_{m_F} is the resonant frequency of the qubit transition and v is the secular frequency. Using equation 5.70 and rewriting z in terms of the creation and annihilation operators,

$$z = \sqrt{\frac{\hbar}{2mv}}(\hat{a} + \hat{a}^\dagger), \tag{5.72}$$

H_0 can be rewritten as

$$\hat{H}_0' = \frac{1}{2}\hbar\omega_{m_F}(0)\hat{\sigma}_z + \frac{1}{2}\hbar v\epsilon(\hat{a}^\dagger + \hat{a})\hat{\sigma}_z + \hbar v\hat{a}^\dagger\hat{a} \tag{5.73}$$

where ϵ is a constant given by

$$\epsilon = \frac{g_F m_F \mu_B \partial_z B(0)}{\hbar}\sqrt{\frac{\hbar}{2mv^3}}. \tag{5.74}$$

When a microwave field of frequency ω_m is applied to the ion, the total Hamiltonian for the system is the sum of equation 5.73 and the Hamiltonian describing the ions interaction with an electromagnetic field, $\hat{H}_M$. $\hat{H}_M$ is given by equation 3.40 in chapter 3 and repeated here where kz has been replaced by $\eta(\hat{a} + \hat{a}^\dagger)$ using equations 5.67 and 5.72,

$$\hat{H}_M = \frac{1}{2}\hbar\Omega(\hat{\sigma}_+ + \hat{\sigma}_-)(e^{i(\omega_M t - \eta(\hat{a}+\hat{a}^\dagger))} + e^{-i(\omega_M t - \eta(\hat{a}+\hat{a}^\dagger))}). \tag{5.75}$$

To see the effect of the magnetic field gradient on the microwave coupling, a unitary Schrieffer-Wolff transformation [81] is performed,

$$\widetilde{H} = e^{\hat{U}}\hat{H}e^{-\hat{U}}, \tag{5.76}$$

where $\hat{U} = \frac{1}{2}\epsilon(\hat{a}^\dagger - \hat{a})\hat{\sigma}_z$. Under this transformation, ignoring constant terms, the vibrational coupling Hamiltonian, $\hat{H}_0'$, reverts back to the expression given before the field gradient was added, $\widetilde{H}_0' = \hat{H}_0$. The transformation $\hat{U}$ therefore moves the effect of the gradient into the Hamiltonian $\hat{H}_M$ which becomes

$$\widetilde{H}_M = \frac{1}{2}\hbar\Omega(\hat{\sigma}_+ e^{\epsilon(\hat{a}^\dagger - \hat{a})} + \hat{\sigma}_- e^{-\epsilon(\hat{a}^\dagger - \hat{a}_)})(e^{i(\eta(\hat{a}^\dagger + \hat{a} - \epsilon\hat{\sigma}_z) - \omega_M t)} + e^{-i(\eta(\hat{a}^\dagger + \hat{a} - \epsilon\hat{\sigma}_z) - \omega_M t)}). \tag{5.77}$$

Moving into the interaction picture with respect to $\hat{H}_0$ gives the following results for the

transformed and untransformed versions of the Hamiltonian $\hat{H}_M$,

$$\hat{H}_I = e^{\frac{i\hat{H}_0 t}{\hbar}} \hat{H}_M e^{-\frac{i\hat{H}_0 t}{\hbar}} \tag{5.78}$$

$$= \frac{1}{2}\hbar\Omega(\hat{\sigma}_+ e^{i(\eta(\hat{a}+\hat{a}^\dagger)-(\omega_M-\omega_{m_F}(0))t)} + \hat{\sigma}_- e^{-i(\eta(\hat{a}+\hat{a}^\dagger)-(\omega_M-\omega_{m_F}(0))t)}) \tag{5.79}$$

for the untransformed Hamiltonian and

$$\widetilde{H}_I = e^{\frac{i\hat{H}_0 t}{\hbar}} \widetilde{H}_M e^{-\frac{i\hat{H}_0 t}{\hbar}} \tag{5.80}$$

$$= \frac{1}{2}\hbar\Omega(\hat{\sigma}_+ e^{i(\eta_+\hat{a}+\eta_-\hat{a}^\dagger-(\omega_M-\omega_{m_F}(0))t-2\eta\epsilon)} + \hat{\sigma}_- e^{-i(\eta_+\hat{a}+\eta_-\hat{a}^\dagger-(\omega_M-\omega_{m_F}(0))t-2\eta\epsilon)}) \tag{5.81}$$

for the transformed Hamiltonian where fast rotating terms have been ignored using the rotating wave approximation and $\eta_\pm = \eta \pm i\epsilon$. $\eta_\pm$ can be rewritten in terms of exponentials as

$$\eta_\pm = \sqrt{\eta^2+\epsilon^2} e^{\pm \tan^{-1}(\frac{\epsilon}{\eta})}. \tag{5.82}$$

By absorbing the exponential term in equation 5.82 into the interaction transformation and by ignoring the globel phase $e^{2i\eta\epsilon}$, $\widetilde{H}_I$ and $\hat{H}_I$ become analogous with the substitution

$$\eta \Rightarrow \sqrt{\eta^2+\epsilon^2}. \tag{5.83}$$

With a magnetic field gradient, the coupling to motion is therefore higher and characterised by a new effective Lamb-Dicke parameter, $\eta_{eff} = \sqrt{\eta^2+\epsilon^2}$. A visual conceptual representation of this coupling is given in figure 5.11. For the F = 0 to F = 1 transition within the $^2S_{\frac{1}{2}}$ level of $^{171}Yb^+$, microwave fields give $\eta_{eff} \approx 0.1$ for the field sensitive $m_F = \pm 1$ states with a field gradient of $50\,\mathrm{Tm}^{-1}$ and a typical trap frequency of $2\pi \times 200\,\mathrm{kHz}$. This is almost five orders of magnitude higher than the value of η achievable using microwaves without a magnetic field gradient. To increase the value of ϵ, therefore increase the value of η_{eff}, the magnetic field gradient should be increased or the trap frequency lowered. Experimentally a magnetic field gradient can be formed using static permanent magnets or electromagnets. Electromagnets can be formed using current carrying wires on microfabricated surface traps which can form gradients at the ion of up to $150\,\mathrm{Tm}^{-1}$ [82].

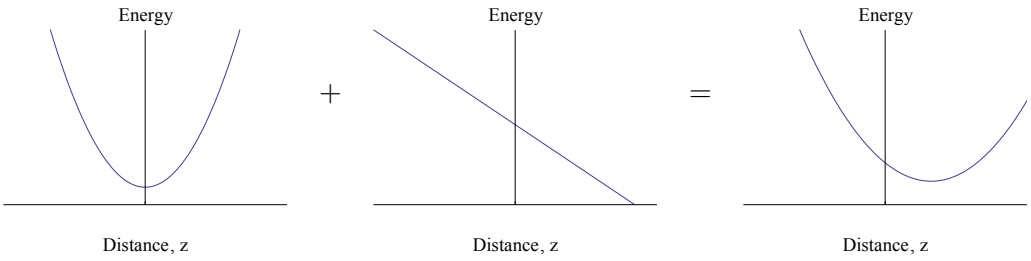

Figure 5.11: The harmonic trapping potential of the $m_F = \pm 1$ states is shifted in space when a magnetic field gradient is added. A transition from a magnetic field insensitive state such as $|0\rangle$ would therefore cause the ion to move in space and hence the internal state is coupled to the motion.

5.4 Ultrafast gates

In 2003, a new method of producing a phase gate was proposed by Garcia-Ripoll et al [64]. As opposed to the spectral methods involving coupling an ions state to its motional state as detailed in the previous sections, this proposal involves mechanical pushing the ions using state dependent 'kicking' forces. As a result motional sidebands are not required which therefore makes the gate independent of ion temperature, allowing it to be performed outside of the Lamb-Dicke regime [83]. A similar gate proposal was also proposed in 2004 by L. M. Duan [84].

Section 5.4.1 will describe how the use of kicking forces can result in the addition of the state dependent phase required for a CZ gate. Section 5.4.2 will describe how kicking forces can be created using pulsed lasers and will compare the suitability of several lasers currently[5] on the market for this purpose.

5.4.1 Gate description

To visualise the gate process, the phase space picture of the ions motion will be used. In contrast to the phase space picture used in the previous section, here, the ion will not be put into the rotating frame with respect to the ions secular motion. As a result, an unperturbed ion will traverse circles in phase space at a frequency equal to the secular frequency as shown in figure 5.12 (a). The application of an instantaneous kicking force to an ion will cause a transfer of momentum which will result in a straight line in phase space as shown in figure 5.12 (b).

A carefully selected sequence of state dependent kicking forces and periods of free evolution will result in the ion retuning to its initial motional state with the addition of a

[5] As of June 2011

state dependent phase. An example of the phase space evolution of one spin state under such a sequence is shown in figure 5.12 (c). The procedure for producing a pulse sequence to accomplish this with the pulsed laser kicks outlined in the following section is presented in [64].

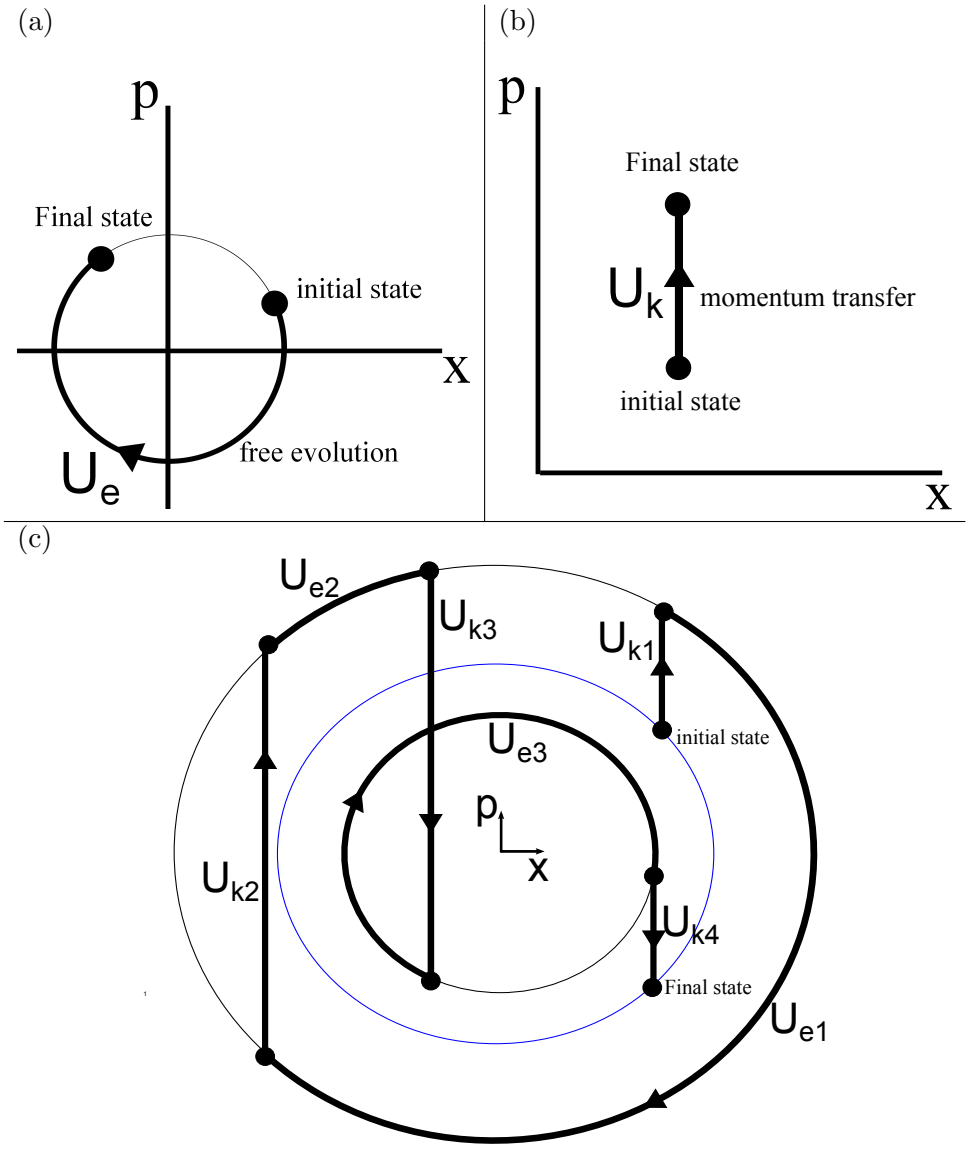

Figure 5.12: Movement in x-p phase space of an ion undergoing (a) free evolution and (b) an instantaneous momentum kick. (c) A combination of free evolution and state dependent momentum kicks can be used to move an ion to a different point on its initial free evolution motional circle with the addition of a state dependent phase.

5.4.2 Producing 'kicking' forces with a pulsed laser

A method of producing a fast kicking force on an ion is to use the momentum transfer caused by the absorption of a photons during a fast spin flip. Here I will present a conceptual summary, for a detailed mathematical treatment please see the thesis by Mizrahi [85].

As shown in [3], a single high power pulse with a bandwidth greater than the qubit splitting, ω_0, can produce population transfer between $|0\rangle$ and $|1\rangle$. Assuming the pulse power is such that the Rabi frequency of the transition is a lot greater than the trap secular frequency, a regime known as the strong regime, the probability of making a transition using a pulse of an arbitrary pulseshape $f(t)$ and width τ is given by [86, 87],

$$P = \sin^2(A)\left[FT_t\left(\frac{1}{\tau}f(t)\right)\right]^2 \tag{5.84}$$

where $FT_t(x)$ is the Fourier transform of x with respect to time and A is a constant known as the pulse area. The pulse area is defined as [87]

$$A = \frac{1}{2}\mu E_0 \int_{-\infty}^{\infty} f(t')dt' = \frac{1}{2}\mu E_0 \tau. \tag{5.85}$$

Using equation 3.17 this can be simplified to

$$A = \frac{\Omega_{max}\tau}{2} \tag{5.86}$$

where Ω_{max} equals the Rabi frequency at the maximum pulse amplitude. The two main pulse shapes available from commercial pulsed laser systems are Gaussian and sech. The pulse shape function and respective Fourier transforms for both Gaussian and sech shaped pulses are given by [87]

$$\begin{array}{cc} f_s(t) = \mathrm{sech}\left(\frac{\pi t}{\tau}\right) & FT_s\left(\frac{1}{\tau}f(t)\right) = \mathrm{sech}\left(\frac{1}{2}\omega_0\tau\right) \\ f_g(t) = e^{-\frac{\pi t^2}{\tau^2}} & FT_g\left(\frac{1}{\tau}f(t)\right) = e^{-\frac{\omega_0^2\tau^2}{2\pi}}. \end{array} \tag{5.87}$$

The transition probability is therefore highly dependent on the properties of the laser system used such as repetition rate, laser power and pulse width. The solution to equation 5.84 and thereby the capability of a variety of commercially available laser systems in producing a spin flip with a single pulse will now be explored.

Transition probabilities of laser systems

The laser systems we will investigate will have wavelengths equal to 355 nm. A wavelength of 355 nm corresponds to a transition between the $|1\rangle$ state and a point 33 THz above the $^2P_{\frac{1}{2}}$ level of $^{171}Yb^+$. This is about a third of the distance between the $^2P_{\frac{1}{2}}$ level and the higher $^2P_{\frac{3}{2}}$ level as shown in figure 5.13 (b). This point is close to local minimas in the total spontaneous emission rate from the $^2P_{\frac{1}{2}}$ and $^2P_{\frac{3}{2}}$ levels, the total stark shift of the

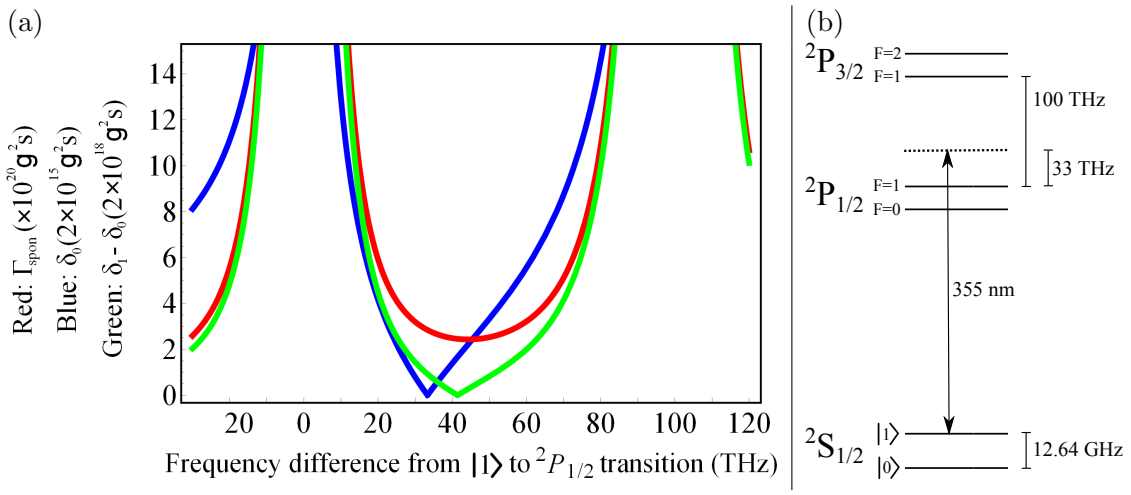

Figure 5.13: (a) Graph showing the total spontaneous emission rate of the ^{2}P levels (red), Γ_{spon}, the AC stark shift of the $|0\rangle$ state (Blue), δ_0, and the differential AC stark shift between the $|0\rangle$ and $|1\rangle$ states (green), $\delta_1 - \delta_0$ as a function of the difference in frequency of the applied light from resonance with the $|1\rangle$ to $^2\mathrm{P}_{\frac{1}{2}}$ transition. These are calculated using equations (1), (2) and (3) from [3] where Ω_{D2} is the single photon Rabi frequency of the $|1\rangle$ to $^2\mathrm{S}_{\frac{3}{2}}$ F = 2 transition given by equation 3.16. $\Omega_{(D2)} = \frac{|\zeta_{D2} \cdot E_0|}{\hbar}$. (b) Energy level diagram of $^{171}\mathrm{Yb}^+$ showing the transition with a frequency which gives a close to minimum AC stark shift, differential stark shift and spontaneous emission rate as shown in (a).

$|0\rangle$ and $|1\rangle$ states as well as the total differential stark shift of the two levels [3] as shown in figure 5.13 (a).

Three examples of pulsed laser systems on the market at 355 nm[6] and their specifications[7] are given in table5.2. They are all based around a frequency tripled 1064 nm laser. All the systems form laser pulses using a process known as modelocking. This is briefly described in figure 5.14.

The average intensity of a pulsed laser is given by the integral of the intensity of a single pulse over time divided by the time between pulses

$$I_{av} = f_{rep} \int I(t)dt \tag{5.88}$$

where f_{rep} is the lasers repetition rate. The integral is approximately equal to the peak intensity multiplied by the pulse width, τ, divided by a constant, K, which depends on the pulse shape. This leads to the following expression for the peak intensity of a pulsed laser

$$I_p \approx K \frac{I_{av}}{f_{rep}\tau} \tag{5.89}$$

[6]Information correct as of June 2011
[7]information obtained through private communications with the respective companies

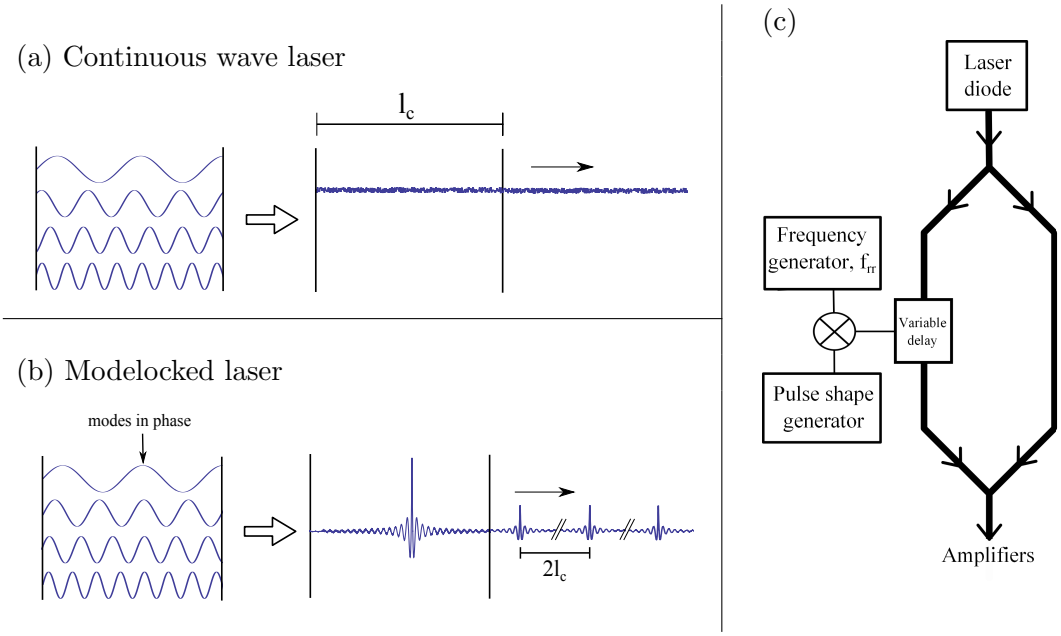

Figure 5.14: Within a laser, the light propagates backwards and forwards within the laser cavity. This forms standing waves known as longitudinal modes. When the different longitudinal modes have a random relative phase relationship, the constructive and destructive interference of the modes within the cavity results in a constant continuous intensity. This results in a continuous wave laser as shown in (a). When the longitudinal modes have a fixed phase relationship, at one point within an oscillation cycle the modes are all in phase and constructively interfere to produce a laser pulse. This is known as modelocking and is shown in (b). Lasers can be modelocked actively, by introducing a shutter or AOM into the cavity or passively by the introduction of a saturate absorber which absorbs low power light and amplifies high power light initially formed from random power fluctuations. These methods are discussed in detail within [45]. A different method of producing a pulsed laser is to use a Mach-Zender interferometer [88] as showed in (c). The desired pulse shape is sent to a variable delay within one arm. the interference from the interferometer then forms the laser pulses.

where K is a constant approximately equal to $\frac{1}{1.06}$ for Gaussian shaped pulses and $\frac{1}{1.14}$ for Sech shaped pulses [54].

The maximum Rabi frequency, Ω_{max}, achieved using light at 355 nm in $^{171}Yb^{+}$ is found in [4] and is equal to

$$\Omega_{max} = 1.76 \times 10^{-2} I_p W^{-1} s^{-1} \tag{5.90}$$

which can be rewritten in terms of the parameters given in table 5.2 using equation 5.89

$$\Omega_{max} = 1.76 \times 10^{-2} K \frac{I_{av}}{f_{rep}\tau} W^{-1} s^{-1}. \tag{5.91}$$

Using this, the transfer probability given by equation 5.84 is calculated for all the lasers given in table 5.2 and is plotted in figure 5.15 for a beam waist of 20 μm. Each graph contains two plots which correspond to the probability achieved by the maximum and

Company	Laser 2000	High Q	Coherent
Laser type	MOPA fibre	modelocked diode	modelocked diode
wavelength (nm)	355	355	355
Repetition rate (MHz)	150 variable* $\pm$ 0.0045	80.145$\pm$ 0.02	120 $\pm$ 2** .
Average power (W)	8 $\pm$ 2% RMS	4 $\pm$ 2% RMS	8 $\pm$ 2% RMS
Pulse shape	Gaussian	Sech	Gaussian
Pulse width, τ (ps)	10-15	4.5-5.5	10-15
Approx cost (x £1000)	107	142	65

Table 5.2: Summary of the main high power pulsed lasers available and their specifications. The error ranges given for repetition rate and pulse width are due to the characteristics of each individual laser. The laser we would receive would therefore have specifications which were constant but within the range given. In addition to a pulsed laser system, a pulse picker would be required. This would provide us with the ability to extract single pulses from the pulse chain which would help us to perform specific pulse sequences. Pulse pickers can cost up to £30 k but can be cheaper if brought as a package with the laser. It should also be noted that the third harmonic generation systems within the above lasers contain non-linear crystals of finite lifetimes of several thousand hours with the laser powers involved. These come with a replacement cost of roughly £7000.

*The system used a fibre based Mach-Zender interferometer which allows the repetition rate to be varied by the user.

** while this may seem quite large, Coherent have offered to measure the exact repetition rate of each of their lasers until they find one which fits within our specifications

minimum possible pulse durations of the laser. As shown in figure 5.15, the laser from High Q could achieve the greatest transition probability of approximately 0.97 which is due to its small pulse duration. This is however only reachable if 2.5 W of the lasers 4 W available reaches the ion.

Figure 5.15 shows that a full spin flip cannot be produced using a single pulse from any of the lasers given in table 5.2. To produce a transition probability of 1, the pulse duration will need to be effectively zero which is not experimentally possible. A method of overcoming this problem was shown in [3], where two pulses, formed by splitting a single pulse into two, were applied to the ion separated by a time, t. The power of each pulse was set to give a transfer probability equal to 0.5. The result is similar to Ramsey experiment. By modifying the delay between the pulses, a full spin flip can therefore be produced.

Splitting the pulse into two will half the amount of laser power within each pulse. The experimental setup must therefore be carefully designed to minimise the total power loss and beam waist to ensure the intensity of each pulse at the ion is high enough to give a transfer probability of 0.5. To illustrate this, figure 5.16 shows a contour plot of the transfer probability of one of these pulses for the Laser 2000 pulsed laser system, with a pulse duration of 10 ps, as a function of beam waist and total percentage power loss. The green area represents the points where a transfer probability of 0.5 is obtainable by the

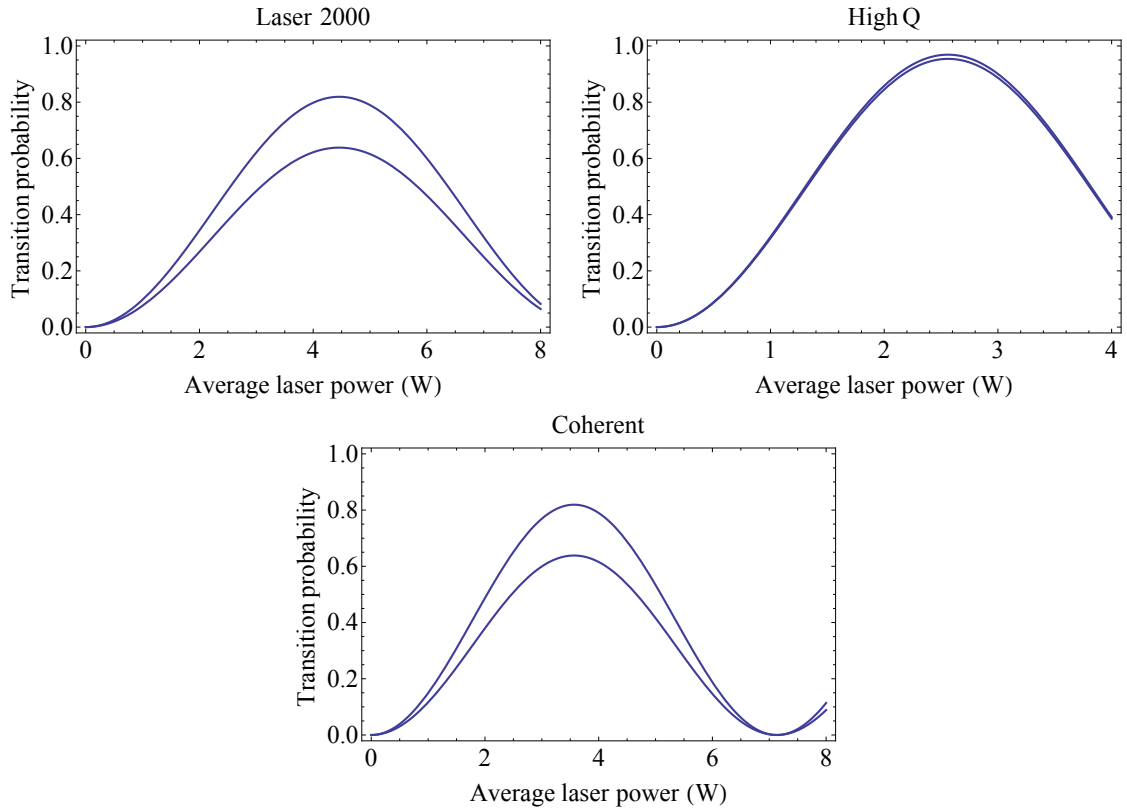

Figure 5.15: The transition probability from a pulse of laser light for the three different laser systems given in table 5.2 assuming a beam waist of 20 μm.

pulse and therefore a spin flip can be produced. Figure 5.16 shows that a spin flip could not be produced with a beam waist greater than approximately 18 μm. This maximum beam waist reduces as the total power loss increases. Reaching such small beam waists while maintaining low power losses can be technically challenging and may require the use of specialist optics.

The spin flip produced using this method will provide a momentum transfer to the ion of $\frac{4\pi\hbar}{\lambda}$ which will occur regardless of the ions state. To produce a CZ gate the momentum transfer needs to be state dependent. A method of making the momentum transfer from a pulse state dependent is explained in [85] and summarised in the following section.

5.4.3 Production of state dependent kicking forces with a pulsed laser

As described in [4], to make the momentum transfer state dependent, the experimental setup shown in figure 5.17 is used. First a single pulse would be isolated using a pulse picker. This pulse would then travel trough a series of beamsplitters and delay lines to produce a chain of pulses. This pulse chain would then be split into two pulse chains which are sent counter propagating to the ion. These are separated in frequency by ω_0 using an

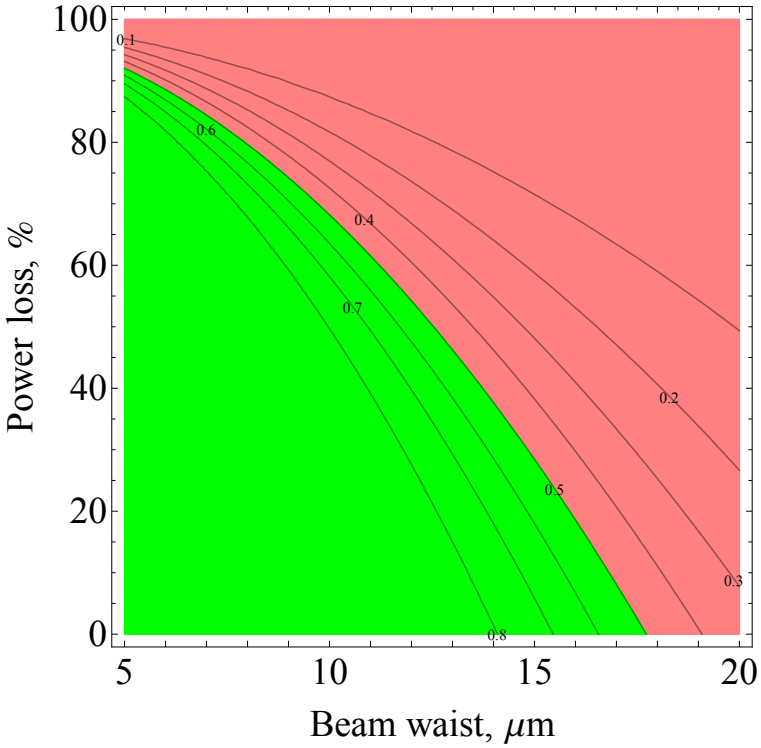

Figure 5.16: Contour plot showing the transfer probability of the Laser 2000 pulsed laser system, with a pulse duration of 10 ps, as a function of beam waist and total percentage power loss. The green area represents the points where a transfer probability of 0.5 is obtainable.

AOM in one of the beam paths. Assuming ω_0 divided by the ions repetition rate does not equal an integer[8], the ion will then make the spin flip in several steps by performing Raman transitions through absorption of photons from one pulse chain and emission into the other (similar to the method described in section 5.3.7). Assuming ω_0 divided by the ions repetition rate also does not equal half an integer, the $|0\rangle$ and $|1\rangle$ states will only be able to absorb and emit photons from opposite pulse chains resulting the ion in each state having equal and opposite momentum transfers.

5.4.4 Experimental gate production

While state dependent fast momentum kicks have been experimentally realised [4], the production of an ultrafast entanglement gate has yet to be performed. This could be due to the fact that the pulse shapes and timings required need to be "perfect" as small systematic errors can result in exponential increases in gate infidelity. For full details please refer to [83].

[8]This would result in Raman transitions being driven by one chain alone

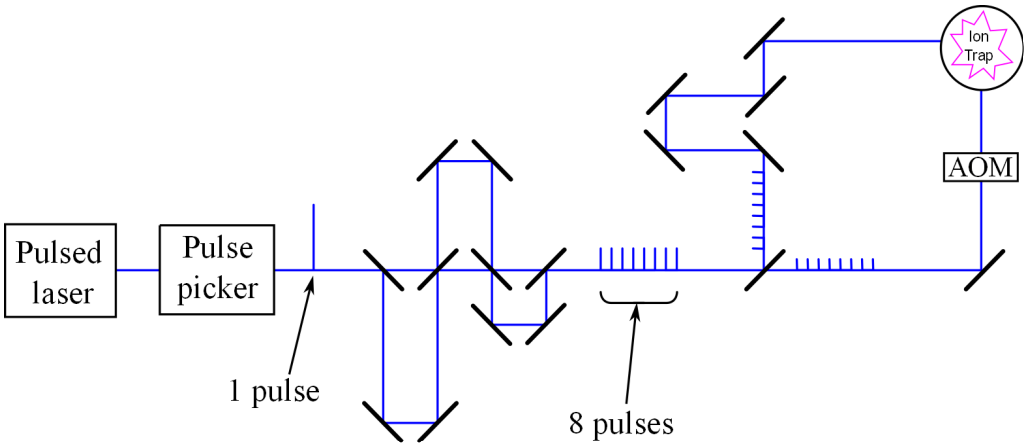

Figure 5.17: Experimental setup required to produce a state dependent kicking force with a pulsed laser. This diagram was replicated from [4].

5.5 Summary and choosing a suitable entanglement method for the lab

Ideally, the lab requires an entanglement method which can be performed with high fidelity, is scalable and is financially low risk. These points will be explored below. Table 5.3 gives an overview of the main entanglement methods presented in this chapter along with their main sources of decoherence and the equipment/capabilities the lab will need to gain in order to perform them.

5.5.1 Scalability

Any quantum algorithm can be performed with a combination of single qubit and two qubit entanglement gates [18]. For > 3 qubit algorithms performed on a single ion chain, this requires the selective entanglement of two arbitrary ions within the chain. This requires the capability to individually address single ions which is already a requirement of the Cirac and Zoller gate scheme. The main method of individual addressing using lasers is to use tightly focus laser beams [89] which due to the typical ion-ion distance being close to the diffraction limit of light can be technically challenging. In addition this would limit the trap frequency and therefore limit the possible gate speed [90]. Methods of overcoming this by utilising the ions' micromotion have been proposed [91,92] but encounter different technical challenges at large ion numbers due to large required trap voltages. It should be noted however that the inability to individually address does not mean a method is not scalable. Trap architectures have been proposed which utilise ion shuttling in order to bring specific ions together for entanglement [93].

The magnetic field gradient entanglement method does not require lasers therefore all

the above challenges are avoided. The scheme can easily produce individual addressing as each ion along the chain will have a different microwave resonant frequency on its magnetic field sensitive states due to the magnetic field gradient.

5.5.2 High fidelity

To produce a high fidelity gate operation, the decoherence sources need to be minimised during the gate time.

The use of lasers for entanglement results in potential decoherence from off resonant coupling and laser fluctuations. While overcoming these decoherence sources can be challenging, gate fidelities of 99.3% can been performed using amplitude modulation techniques [94].

An ultrafast gate using a pulsed laser would benefit from increased gate speeds which could lead to higher fidelities as decoherence sources have less time to act. The scheme does however require 'perfect' pulses, any deviation from which would cause an exponentially increasing errors which would quickly counter the advantages gained by having a faster gate.

The magnetic field gradient method uses microwaves and therefore the decoherence sources associated with lasers are avoided. The use of magnetic field sensitive states does however make the method highly sensitive to magnetic field fluctuations. Decoherence from magnetic field fluctuations can compensated for using dynamical decoupling [95], which has successfully been performed to give fidelities of $> 99\%$ [25]. Alternitivly magnetic field sensitive qubits can be shielded from magnetic field fluctuations by the use of microwave dressed states as first described by Timoney et al [96]. This method is explored further in chapter 6 and is shown to reduce the decoherence caused by magnetic field fluctuations by two orders of magnitude.

5.5.3 Financial risk

The lab already has a 369 nm Toptica laser and using this laser it is, in principle, possible to do an entanglement gate using moving standing waves or Raman transitions with little extra expenditure.

The microwave field gradient entanglement method requires the building of a microwave frequency setup which will require new frequency sources to provide the microwave horn with the required frequencies. In addition, while the magnets required to produce a static magnetic field gradient are relatively cheap, these will need to be placed within

the vacuum system. This would take some time to perform and carries the risk that due to human error or magnet movement during the baking process, the gradient center may become displaced from the trap center causing a high offset field to be present potentially making the trap unusable.

The costs required for the ultrafast scheme are very high and in addition to a high powered laser system, expensive additions are required such as a pulse picker and high power optics. This scheme is also high risk because of the large number of potential decoherence sources mentioned previously.

With all the above considerations taken into account, the use of microwaves with a magnetic field gradient using microwave dressed states is determined to be an ideal way forward for the lab.

		Moving standing wave	Raman transitions		Magnetic field gradient	Momentum kicks using ultrafast pulsed laser
			CW	Pulsed		
Scheme	Cirac and Zoller gate	Geometric phase gate, σ_z basis	Geometric phase gate, σ_ϕ basis	Geometric phase gate, σ_ϕ basis	Geometric phase gate, σ_ϕ basis	Ultrafast gate
Required ion temperature	Ground state	Lamb-Dicke regime	Lamb-Dicke regime	Lamb-Dicke regime	Lamb-Dicke regime	None
Main sources of decoherence	• Crosstalk • Pulse power, phase, spacial and frequency fluctuations • Deviation from $n = 0$	• Interformetric instability • Laser power, phase, spacial and frequency fluctuations • heating	• Off resonant coupling • Laser power, phase, spacial and frequency fluctuations • heating	• Off resonant coupling • Pulse power and spacial fluctuations • heating	• Magnetic field fluctuations • heating	• Pulse imperfections (eg. dispersion) • Pulse power, phase, spacial and frequency fluctuations • heating
Additional lab requirements	• Ground state cooling	• Interferometer	• AOM's and/or • Additional 369 nm laser	• Pulsed laser • AOM's	• Magnetic field gradient • Microwave frequency setup	• High power pulsed laser • Pulse picker • High power optics
Estimated cost	Low	Low	Low	Medium	Medium	High

Table 5.3: Comparison of main entanglement methods

Chapter 6

Microwave dressed states

The use of the magnetic field gradient entanglement scheme outlined in the previous chapter requires the use of magnetic field sensitive states such as the $m_F = \pm 1$ sublevels of the $^2S_{\frac{1}{2}}$ $F = 1$ level in Ytterbium 171. Use of these levels as qubits however leads to fast decoherence due to magnetic field fluctuations. This can be seen in figure 3.18 in chapter 3 which shows that a Rabi flop performed between the $^2S_{\frac{1}{2}}$ $F = 0$ level and the magnetic field sensitive $^2S_{\frac{1}{2}}$ $F = 1$ $m_F = +1$ level has a decoherence time of less than 500 μs.

This chapter begins by explaining how this decoherence can be avoided by dressing the magnetic field sensitive states with microwaves to produce a dressed qubit which is insensitive to magnetic field fluctuations as first proposed by Timoney et al [96]. A method of preparing the ion into the dressed qubit states by the use of STImulated Raman Adiabatic Passage (STIRAP) is then described and optimised in section 6.2. Methods by which coherent manipulation can be performed with this dressed qubit using both the original method proposed in [96] and an improved method which allows for arbitrary qubit rotation is described and performed in section 6.3. Finally, section 6.4 confirms that the magnetic field gradient entanglement scheme described in the previous chapter is still applicable within the dressed state basis.

6.1 Dressed states of $^{171}Yb^+$

A dressed state is a superposition state between an ion's unperturbed levels and incident electromagnetic radiation. For a multi-level system, the unperturbed Hamiltonian is

$$\hat{H}_A = \sum_n \hbar\omega_n |n\rangle \langle n| \tag{6.1}$$

where ω_n is the angular position in frequency space of level n. For the $^2S_{\frac{1}{2}}$ levels in $^{171}Yb^+$ as shown in figure 6.1, this Hamiltonian is equal to

$$\hat{H}_A = -\hbar\omega_0 \left|0\right\rangle \left\langle 0\right| + \hbar\omega_{r1} \left|+1\right\rangle \left\langle +1\right| - \hbar\omega_{r2} \left|-1\right\rangle \left\langle -1\right| \tag{6.2}$$

where the $|-1\rangle$, $|0'\rangle$ and $|+1\rangle$ states represent the $^2S_{\frac{1}{2}}$ F$=$ 1 m$_F$ =-1, 0 and +1 levels respectively and the zero point in energy has been defined as at the $|0'\rangle$ level.

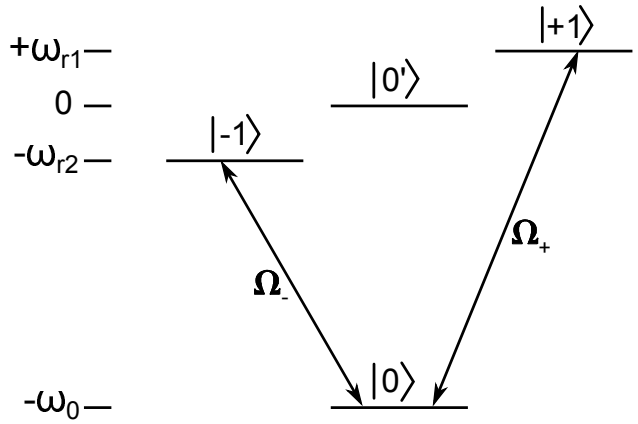

Figure 6.1: Frequency space diagram of the $^2S_{\frac{1}{2}}$ levels within ytterbium 171. The $^2S_{\frac{1}{2}}$ F$=$1 m$_F$ =-1, 0 and +1 levels are defined as the $|-1\rangle$, $|0'\rangle$ and $|+1\rangle$ states respectively.

The perturbation caused by the addition of electromagnetic fields is derived in chapter 3 and is equal to

$$\hat{H}' = \sum_{i,j} \hbar\Omega_{i-j} \cos(\omega t + \phi) \left|i\right\rangle \left\langle j\right| \tag{6.3}$$

where Ω_{i-j} is the Rabi frequency of the transition between states i and j when illuminated with an electromagnetic field of frequency ω and phase ϕ and it is assumed that the wavelength of the fields is a lot larger than the spatial extent of the ion. Adding two microwave fields, resonant with the $|0\rangle$ to $|-1\rangle$ transition and the $|0\rangle$ to $|+1\rangle$ transition, results in the following perturbation Hamiltonian

$$\begin{aligned} \hat{H}' = {} & \hbar\Omega_- \cos\left(\omega_- t + \phi_-\right) \left(\left|0\right\rangle \left\langle -1\right| + \left|-1\right\rangle \left\langle 0\right|\right) \\ & + \hbar\Omega_+ \cos\left(\omega_+ t + \phi_+\right) \left(\left|0\right\rangle \left\langle +1\right| + \left|+1\right\rangle \left\langle 0\right|\right) \end{aligned} \tag{6.4}$$

where $\omega_+ = \omega_0 + \omega_{r1}$ and $\omega_- = \omega_0 - \omega_{r2}$. Setting the phase of the two fields, $\phi_\pm$ to zero and by making the Rabi frequencies of the two fields equal, $\Omega_{ds} = \Omega_\pm$, this can be simplified to

$$\begin{aligned} \hat{H}' = {} & \hbar\Omega_{ds} \left[\cos\left(\omega_- t\right)\left(\left|0\right\rangle \left\langle -1\right| + \left|-1\right\rangle \left\langle 0\right|\right)\right. \\ & \left. + \cos\left(\omega_+ t\right)\left(\left|0\right\rangle \left\langle +1\right| + \left|+1\right\rangle \left\langle 0\right|\right)\right] \end{aligned} \tag{6.5}$$

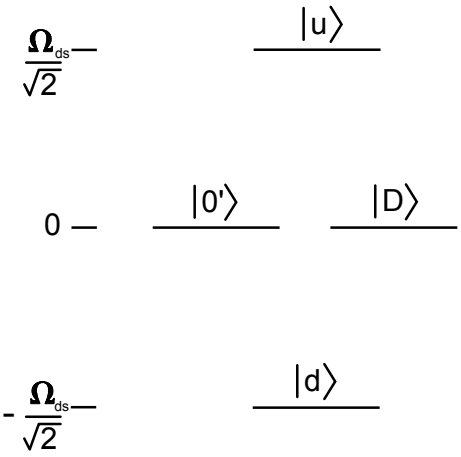

Figure 6.2: Frequency space diagram of the dressed state basis.

Moving into the interaction picture with respect to H_A gives the interaction Hamiltonian, $\hat{H}'_I$, where $\hat{H}'_I = e^{\frac{i\hat{H}_A t}{\hbar}} \hat{H}' e^{-\frac{i\hat{H}_A t}{\hbar}}$ which is equal to

$$\begin{aligned} \hat{H}'_I = \frac{\hbar\Omega_{ds}}{2} [&\cos\omega_- t \left(e^{-i\omega_- t} |0\rangle \langle -1| + e^{i\omega_- t} |-1\rangle \langle 0| \right) \\ &+ \cos\omega_+ t \left(e^{-i\omega_+ t} |0\rangle \langle +1| + e^{i\omega_+ t} |+1\rangle \langle 0| \right)] \end{aligned} \tag{6.6}$$

By writing $\cos(x)$ in terms of exponential's and applying the rotating wave approximation to eliminate the fast rotating terms, this Hamiltonian simplifies to

$$\hat{H}'_I = \frac{\hbar\Omega_{ds}}{2} \left(|0\rangle \langle -1| + |-1\rangle \langle 0| + |0\rangle \langle +1| + |+1\rangle \langle 0| \right). \tag{6.7}$$

The eigenstates of this Hamiltonian are as follows,

$$\begin{aligned} |u\rangle &= \frac{1}{2}(|+1\rangle + |-1\rangle + \sqrt{2}\,|0\rangle) \\ |d\rangle &= \frac{1}{2}(|+1\rangle + |-1\rangle - \sqrt{2}\,|0\rangle) \\ |D\rangle &= \frac{1}{\sqrt{2}}(|+1\rangle - |-1\rangle) \end{aligned} \tag{6.8}$$

These form a new state basis known as the dressed state basis. Rewriting equation 6.7 in the dressed state basis gives

$$\hat{H}'_I = \frac{\hbar\Omega_{ds}}{\sqrt{2}} \left(|u\rangle \langle u| - |d\rangle \langle d| \right). \tag{6.9}$$

Figure 6.2 shows the dressed state basis in frequency space. The following subsections will show how a qubit formed from the $|0'\rangle$ and $|D\rangle$ states is insensitive to both magnetic field fluctuations and fluctuations in the amplitude of the microwave dressing fields.

6.1.1 Magnetic field fluctuations

Magnetic field fluctuations in the bare state basis cause the $|-1\rangle$ and $|+1\rangle$ states to shift in frequency by equal and opposite amounts given by $\omega_\Delta(t)$. This creates the following perturbation to the Hamiltonian

$$\hat{H}'_f = \hbar\omega_\Delta(t)\left(|+1\rangle\langle+1| - |-1\rangle\langle-1|\right). \tag{6.10}$$

This Hamiltonian commutes with $\hat{H}_A$ and therefore it remains unchanged when moved into the interaction picture with respect to $\hat{H}_A$. Rewriting this Hamiltonian in the dressed state basis gives

$$\hat{H}'_{I,f} = \frac{\hbar\omega_\Delta(t)}{\sqrt{2}}\left(|D\rangle\langle u| + |D\rangle\langle d| + |u\rangle\langle D| + |d\rangle\langle D|\right). \tag{6.11}$$

Field fluctuations therefore only couple population from $|D\rangle$ to $|u\rangle$ and $|d\rangle$. As shown in figure 6.2 this coupling however involves crossing an energy gap of $\frac{\hbar\Omega_{ds}}{\sqrt{2}}$. It follows that any field fluctuations of a frequency far from Ω_{ds} will not be able to cross the energy gap and therefore have no effect [96].

By using the $|0'\rangle$ and $|D\rangle$ states as our qubit, we therefore heavily suppress decoherence due to magnetic field fluctuations. As discussed in chapter 5, magnetic field fluctuations are the main source of decoherence associated with the magnetic field gradient entanglement scheme using the bare state qubit. By eliminating this source of decoherence, the dressed qubit therefore has the potential to produce high fidelity gate operations.

6.1.2 Microwave amplitude fluctuations

A fluctuation in the amplitude of one of the microwave dressing fields will cause a change in the Rabi frequency of that field given by δ_Ω. This results in the following addition to the Hamiltonian given in equation 6.5, where the fluctuation was on the Ω_- field.

$$H'_{\delta_\Omega} = \hbar\delta_\Omega\cos(\omega_- t)(|0\rangle\langle-1| + |-1\rangle\langle0|). \tag{6.12}$$

Rewriting this within the interaction picture with respect to $\hat{H}_A$ gives

$$H'_{I,\delta_\Omega} = \frac{\hbar\delta_\Omega}{2}\cos(\omega_- t)(e^{-\omega_- t}|0\rangle\langle-1| + e^{\omega_- t}|-1\rangle\langle0|) \tag{6.13}$$

which after rewriting $\cos(x)$ in terms of exponentials and applying the rotating wave approximation gives

$$H'_{I,\delta_\Omega} = \frac{\hbar\delta_\Omega}{2}(|0\rangle\langle -1| + |-1\rangle\langle 0|). \tag{6.14}$$

This is rewritten in the dressed state basis as

$$H'_{I,\delta_\Omega} = \frac{\hbar\delta_\Omega}{\sqrt{2}}(|u\rangle\langle u| - \langle d|\langle d|) + \frac{1}{2}(|d\rangle\langle D| + \langle D|\langle d| - |u\rangle\langle D| - \langle D|\langle u|). \tag{6.15}$$

Amplitude fluctuations will therefore only cause coupling of population from $|D\rangle$ to $|u\rangle$ and $|d\rangle$ which as previously discussed, involves crossing an energy gap of $\frac{\hbar\Omega_{ds}}{\sqrt{2}}$, therefore the effect of amplitude fluctuations will be negligible unless they are at a frequency close to $\sqrt{2}\Omega_{ds}$. In addition, the energy of the $|u\rangle$ and $|d\rangle$ states will become shifted by equal and opposite amounts, $\frac{\hbar\delta_\Omega}{\sqrt{2}}$. Assuming $\delta_\Omega << \Omega_{ds}$, the energy gap will remain large and this will have a negligible effect on the qubit.

6.2 Preparing the dressed state qubit

To initalise an ion in the $|D\rangle$ state, the first half of a STIRAP (STImulated Raman Adiabatic Passage) pulse sequence is used. STIRAP is a method of moving population between two states, $|a\rangle$ to $|b\rangle$, via a third intermediate state, $|c\rangle$, which remains unpopulated. The mechanism behind STIRAP is explained briefly here, for a more detailed explanation, please refer to [97] or [98].

If two fields, a and b, resonant with the $|a\rangle$ to $|c\rangle$ and $|b\rangle$ to $|c\rangle$ transitions are applied to the system with Rabi frequencies equal to Ω_a and Ω_b respectively, a 'dark' eigenstate of the system will exist which is a superposition of the $|a\rangle$ and $|b\rangle$ states [99],

$$|Dark\rangle = \frac{\Omega_b|a\rangle - \Omega_a|b\rangle}{\sqrt{\Omega_a^2 + \Omega_b^2}}. \tag{6.16}$$

To move population between $|a\rangle$ and $|b\rangle$ without populating $|c\rangle$, Ω_a and Ω_b need to be adjusted adiabatically so the population is always within this dark state [97]. This is done using a counter-intuitive pulse sequence, where field a is applied before field b. For example, in the $^2S_{\frac{1}{2}}$ level of $^{171}Yb^+$ as shown in figure 6.1, population transfer between the $|-1\rangle$ state and the $|+1\rangle$ state is achieved via the $|0\rangle$ state by application of the counter-intuitive pulse sequence shown in figure 6.3. A Gaussian pulse resonant with the $|0\rangle$ to $|+1\rangle$ transition is applied slightly before a Gaussian pulse resonant with the $|0\rangle$ to $|-1\rangle$ transition, this results in population transfer while ensuring the $|0\rangle$ state remains

unpopulated. At the half way point of this STIRAP operation (where the orange and purple line cross on figure 6.3 (a), the Rabi frequencies of both fields are equal and the dark state, $|Dark\rangle$, is the $|D\rangle$ state mentioned in the previous section.

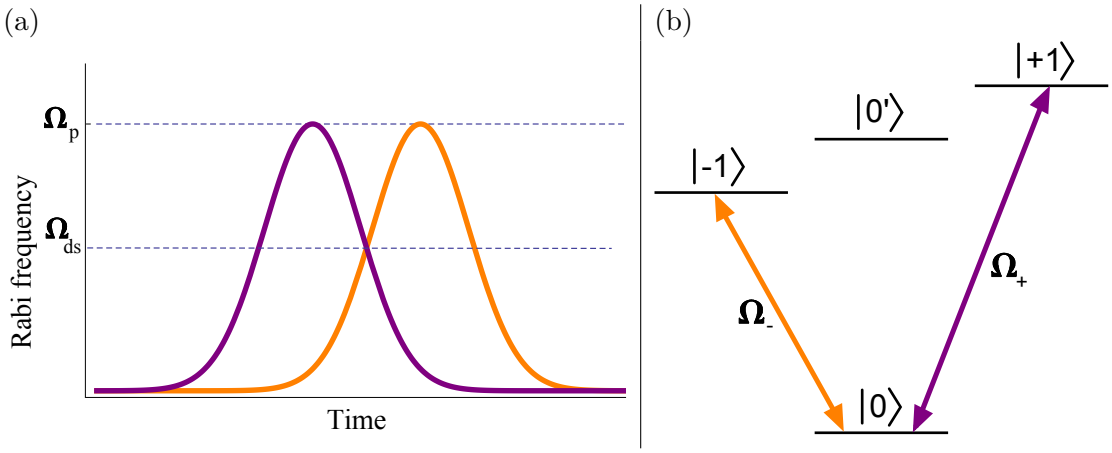

Figure 6.3: (a) STIRAP pulse sequence used to transfer population from the $|-1\rangle$ state to the $|+1\rangle$ state. The transition frequencies are shown in (b), Orange represents the $|0\rangle$ to $|-1\rangle$ transition and purple represents the $|0\rangle$ to $|+1\rangle$ transition. Unless overwise stated, the results in this chapter are performed using a peak STIRAP Rabi frequency, Ω_p, of $2\pi \times 23\,\text{kHZ}$ which corresponds to a dressing field Rabi frequency, Ω_{ds} of $2\pi \times 16\,\text{kHz}$.

6.2.1 Experimental setup

In order to perform STIRAP, the microwave setup shown in chapter 2 is modified to allow for two separate controllable microwave fields as shown in figure 6.4. The STIRAP pulse envelopes given in figure 6.3 (a) are designed in Labview which allows for easy adjustment of pulse parameters such as pulse width and pulse-pulse separation. This is then sent to the experiment using two FPGA channels[1] which output voltages proportional to the two respective STIRAP pulses. Switches are present to allow the user to switch from these STIRAP channels to channels set to a constant voltage. (This allows the setup to produce microwaves at a constant Rabi frequency for cooling.) Two low frequency signals, ω_{l1} and ω_{l2} are produced at a constant amplitude from separate channels of the signal generator. These are then convoluted with the FPGA signals using low frequency mixers[2] and then combined using a power splitter/combiner[3]. This is then mixed using a high frequency mixer[4] with a high frequency signal, ω_{hf} before being amplified and sent to the microwave horn.

The frequencies, ω_{l1}, ω_{l2} and ω_{hf} are selected so that when mixed together in the above

[1] see section 2.5
[2] Mini-Circuit ZX05-iL-S+
[3] Mini-Circuit ZMSC-2-2
[4] Mini-Circuit ZX05-153LH-S+

setup they produce the required transition frequencies, for example,

$$\begin{aligned} \omega_- &= \omega_{hf} + \omega_{l1} \\ \omega_+ &= \omega_{hf} + \omega_{l2} \end{aligned} \tag{6.17}$$

In addition, to prevent any unwanted population transfer, we must ensure the selected frequencies and any other modulation products formed during mixing are far away from the transition frequencies ω_0 and $\omega_\pm$ which were found in chapter 3 to equal $\omega_- = 12.6290$, $\omega_0 = 12.6429$ and $\omega_+ = 12.6568$ (see figure 3.17 (a)). The set of frequencies used which fulfill these conditions were $\omega_{l1} \approx 29.64\,\text{MHz}$, $\omega_{l2} \approx 2.21\,\text{MHz}$ and $\omega_{hf} \approx \omega_0 - 15.94\,\text{MHz}$ $= 12.63\,\text{GHz}$.

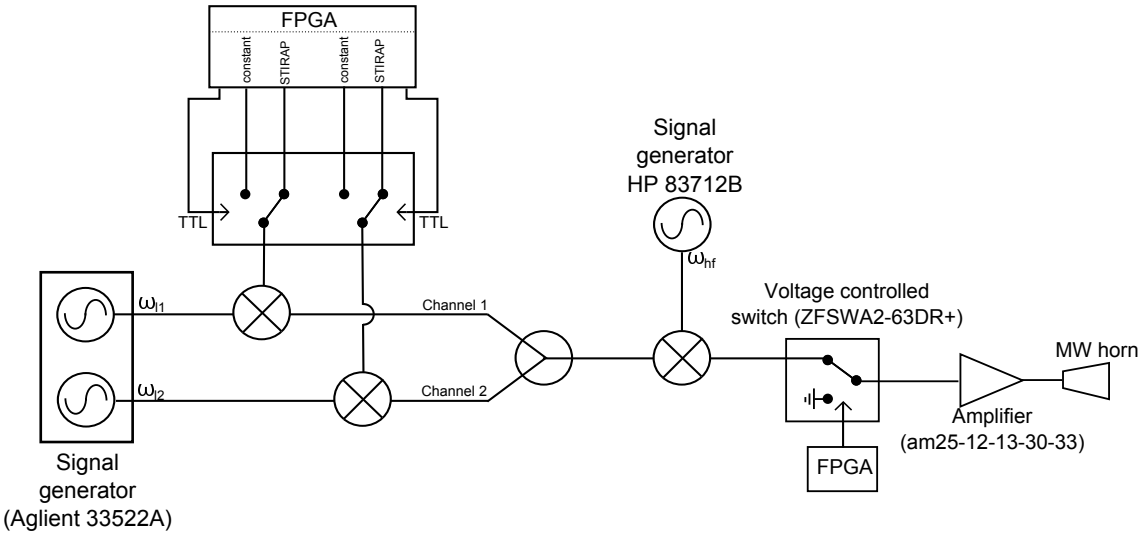

Figure 6.4: Microwave setup used with two separate controllable channels required for STIRAP operation.

6.2.2 Results and optimization

The pulse sequence used to move population from the $|-1\rangle$ state to the $|+1\rangle$ state using a STIRAP operation and then detect the final state is shown in figure 6.5.

After the state is prepared in the $|0\rangle$ state by optical pumping, the population is moved to $|-1\rangle$ using a π pulse applied on the $|0\rangle$ to $|-1\rangle$ transition. The STIRAP pulse envelopes are then activated which moves the population into the $|+1\rangle$ state. To determine if the population transfer has been successful, a π pulse is applied on the $|0\rangle$ to $|+1\rangle$ state transition. This moves population successfully transferred into the $|0\rangle$ state where it remains dark during state detection. Population from an unsuccessful STIRAP would have remained in the $|-1\rangle$ state and would therefore be bright during state detection.

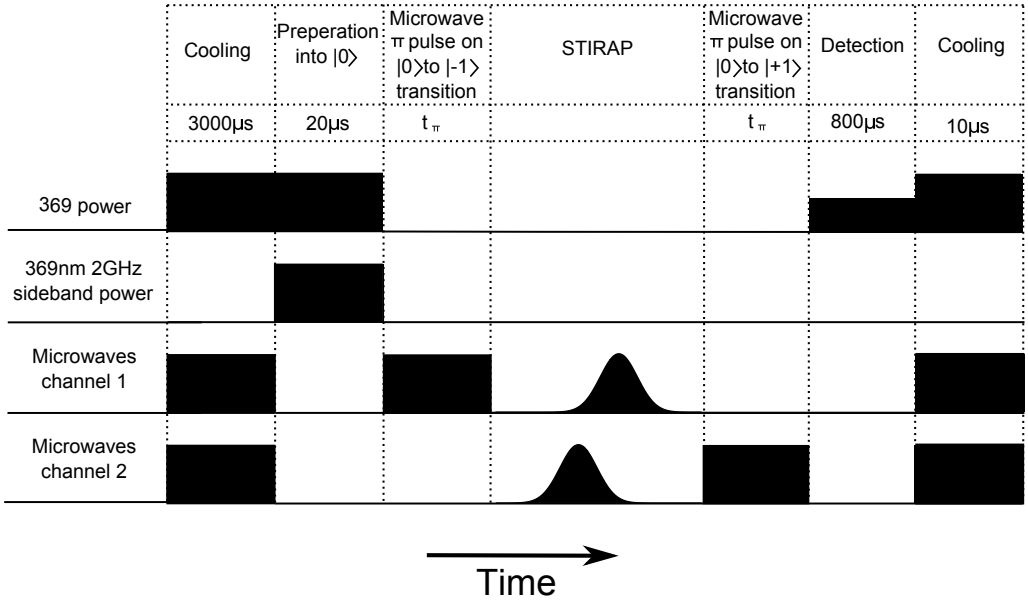

Figure 6.5: Pulse sequence used to perform a STIRAP operation between the $|-1\rangle$ state and the $|+1\rangle$ state.

In order to maximize the population transfer, the parameters of the STIRAP pulse envelopes need to be optimized. The main parameters are the width of the Gaussian pulses (pulse width), the separation between the two STIRAP pulses (pulse separation) and the FPGA step size (sample spacing). The FPGA step size refers to the time between the sequential changes in FPGA output voltage required to form the analogue pulse shape as shown in figure 6.6.

The effect of changing the STIRAP pulse parameters are shown in figures 6.7, 6.8 and 6.9 respectively for a Ω_p equal to $2\pi \times 25\,\mathrm{kHz}$. The STIRAP sequence was found to be quite robust and large ranges in each parameter were found where the population transfer was optimum. The range of optimum pulse separation was found to equal 120-485 μs for a pulse width of 300 μs, the range of optimum pulse width was found to equal 150-650 μs for a pulse separation of 400 μs and the maximum sample spacing was found to equal 20 μs. In addition, the relative phase of the pulses was shown to have no effect. Taking points roughly in the center of each of these ranges, the results in the remainder of this chapter were performed with a sample spacing of 10 μs, a pulse width of 450 μs and a pulse separation of 356 μs unless overwise stated.

Maximum transfer efficiency

The overall maximum population transfer efficiency, T, was found to be approximately 80%. This is limited as the population transfer is not completely adiabatic. The adiabatic condition for STIRAP is fulfilled when the area of the STIRAP pulses is a lot greater than

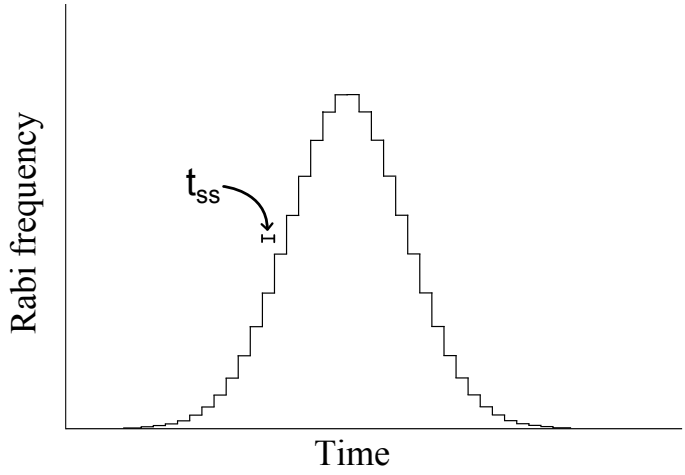

Figure 6.6: The FPGA produces the analogue pulse shape by changing the output voltage in a series of steps separated in time by the sample spacing, t_{ss}.

one [100],

$$A_{+,-} = \int_{-\infty}^{\infty} \Omega_{+,-}(t)dt >> 1. \tag{6.18}$$

The maximum transfer efficiency of the STIRAP operation is then given by [100]

$$T \approx 1 - \frac{1}{A_{+,-}^2}. \tag{6.19}$$

To increase T, the maximum Rabi frequency achievable using the setup shown in figure 6.4 therefore needs to be increased. This can be achieved by, for example, inserting a second amplifier or reducing losses by using more efficient components.

6.2.3 Lifetime

At the half way point of a STIRAP pulse sequence when the Rabi frequency of the two transitions are equal, the ion is in the $|D\rangle$ state. To remain in the $|D\rangle$ state, the amplitude modulation of the pulses is paused and the Rabi frequency of the two microwave fields is held constant as shown in figure 6.10 (a). All coherent manipulation of the dressed state qubit is then performed during this hold time. The maximum hold time is determined by the lifetime of the $|D\rangle$ state. As discussed in section 6.1, population can decay from the $|D\rangle$ state into the $|u\rangle$ and $|d\rangle$ states as a result of field fluctuations present at $\Omega_{ds}/\sqrt{2}$.

The $|D\rangle$ state lifetime is determined using the pulse sequence described in section 6.2.2 with the addition of a hold into the STIRAP pulse envelopes. During this hold if the $|D\rangle$ state decays, the amount of population transferred to $|+1\rangle$ during the final part of the STIRAP will decrease. The decayed population will become equally distributed between the $|0\rangle$, $|-1\rangle$ and $|+1\rangle$ states therefore if the $|D\rangle$ state has completely decayed during

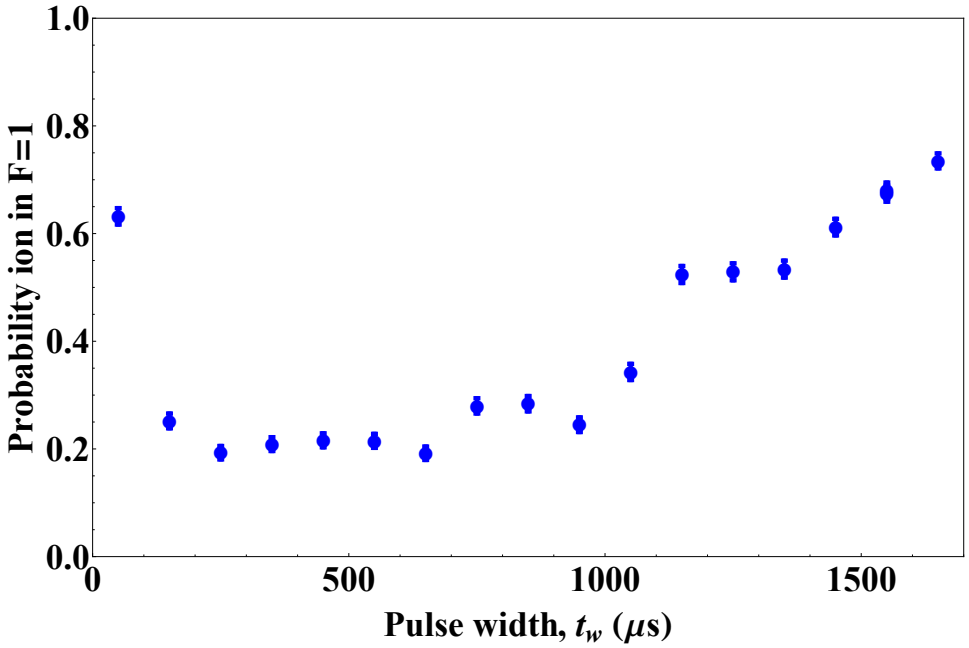

Figure 6.7: Graph showing how varying the pulse width effects the population transfer efficiency of a STIRAP pulse sequence. Population transferred effectively will end up in the $|0\rangle$ state. The data was taken with a pulse separation of 400 μs and a sample spacing of 10 μs. Each point is an average of 1000 measurements.

the hold, the probability of the resultant state of the ion being $|+1\rangle$ will become $\frac{1}{3}$. The duration of the hold, t_h is gradually increased and the results after a final π pulse on the $|0\rangle$ to $|+1\rangle$ state transition are shown in figure 6.10 (b). The lifetime is calculated using an exponential fit to this data with a baseline of $\frac{1}{3}$ and is found to equal 550 ms.

6.3 Coherent manipulation

Coherent manipulation of the dressed state qubit is achieved by applying RF radiation resonant with the $|0'\rangle$ to $|\pm1\rangle$ transitions as shown in figure 6.11. Due to the sensitivity of the $|0'\rangle$ state to the second order Zeeman effect, the exact transitions involved will depend on the strength of the magnetic field present.

The difference in frequency between the $|0'\rangle$ to $|+1\rangle$ transition and the $|0'\rangle$ to $|-1\rangle$ transition due to the second order Zeeman effect is [101, 102],

$$\begin{aligned} \omega_{r2} - \omega_{r1} &= -\frac{1}{2\hbar^2\omega_0}\left(\frac{2g_j\mu_B B}{(2I+1)}\right)^2 \\ &= 2\pi \times 0.31 B^2 kHz/G^2. \end{aligned} \tag{6.20}$$

Where B is the magnetic field applied to the system. At low magnetic fields, when $\Omega_{RF} >> (\omega_{r2} - \omega_{r1})$, the second order Zeeman effect is negligible and the $|0'\rangle$ to $|\pm1\rangle$ transition

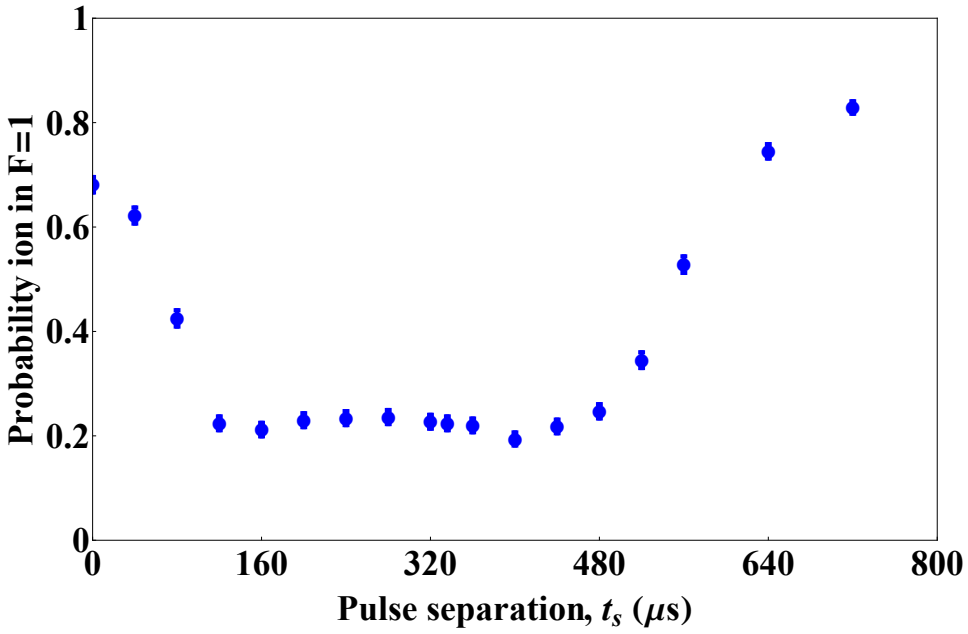

Figure 6.8: Graph showing how varying the pulse separation effects the population transfer efficiency of a STIRAP pulse sequence. Population transferred effectively will end up in the $|0\rangle$ state. The data was taken with a pulse width of 300 μs and a sample spacing of 10 μs. Each point is an average of 1000 measurements.

frequencies are equal. This will be referred to as the low field regime. At high magnetic fields, when $\Omega_{RF} \leq (\omega_{RF2} - \omega_{RF1})$, the difference between the $|0'\rangle$ to $|\pm 1\rangle$ transition frequencies becomes significant. This will be referred to as the high field regime. This section will show how coherent manipulation can be performed in both regimes.

6.3.1 Low field regime

In this regime, the method given in the original paper by Timoney et al [96] applies. In low magnetic fields, second order Zeeman shifts can be ignored and the resonant frequency of the $|0'\rangle$ to $|+1\rangle$ and $|0'\rangle$ to $|-1\rangle$ transitions are equal and given by ω_r. The perturbation to the Hamiltonian caused by applying an RF field of frequency, ω_r, and phase, Φ_{RF}, is found using equation 6.3 and is equal to

$$\hat{H}' = \hbar\Omega_{RF}\cos(\omega_r + \phi_r)\left[|0'\rangle\langle -1| + |-1\rangle\langle 0| + |0'\rangle\langle +1| + |+1\rangle\langle 0'|\right] \tag{6.21}$$

As in section 6.1 this Hamiltonian is moved into the interaction picture with respect to $\hat{H}_0$ becoming

$$\begin{aligned}\hat{H}'_{RF,I} = \hbar\Omega_{RF}\cos(\omega_r + \phi_r)\times \\ \left[e^{i\omega_r t}|0'\rangle\langle -1| + e^{-i\omega_r t}|-1\rangle\langle 0| + e^{-i\omega_r t}|0'\rangle\langle +1| + e^{i\omega_r t}|+1\rangle\langle 0'|\right]\end{aligned} \tag{6.22}$$

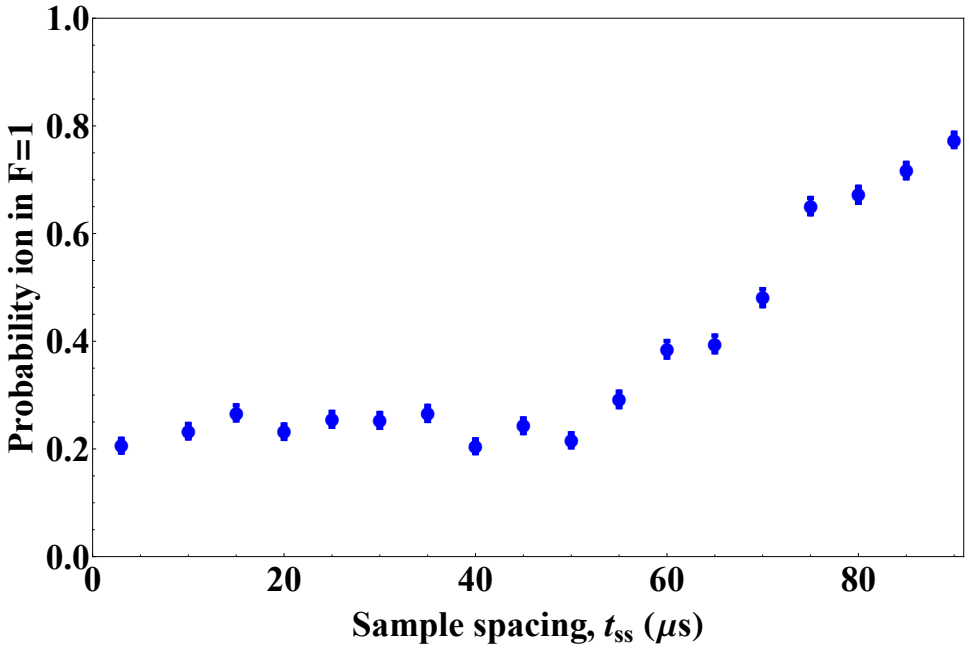

Figure 6.9: Graph showing how varying the FPGA's sample spacing effects the population transfer efficiency of a STIRAP pulse sequence. Population transferred effectively will end up in the $|0\rangle$ state. The data was taken with a pulse separation of 400 μs and a pulse width of 300 μs. Each point is an average of 1000 measurements.

By writing $\cos(x)$ in terms of exponentials and using the rotating wave approximation to eliminate fast rotating terms, this becomes,

$$\hat{H}'_{RF,I} = \frac{\hbar\Omega_{RF}}{2}\left[e^{-i\phi_r}\left|0'\right\rangle\langle -1| + e^{i\phi_r}\left|-1\right\rangle\left\langle 0'\right| + e^{i\phi_r}\left|0'\right\rangle\langle +1| + e^{-i\phi_r}\left|+1\right\rangle\left\langle 0'\right|\right]. \quad (6.23)$$

Which can be written in the dressed state basis as

$$\begin{aligned}\hat{H}'_{RF,I} = \frac{\hbar\Omega_{RF}}{2}[\cos(\phi_r)\left(|u\rangle\left\langle 0'\right| + |d\rangle\left\langle 0'\right| + \left|0'\right\rangle\langle u| + \left|0'\right\rangle\langle d|\right) \\ - \sqrt{2}i\sin(\phi_r)\left(|D\rangle\left\langle 0'\right| - \left|0'\right\rangle\langle D|\right)].\end{aligned} \quad (6.24)$$

When ϕ_r is set to equal $\frac{\pi}{2}$, the terms coupling population to $|u\rangle$ and $|d\rangle$ disappear and the following Hamiltonian remains

$$\hat{H}'_{RF,I} = \frac{\hbar\Omega_{RF}}{2}i\left(\left|0'\right\rangle\langle D| - |D\rangle\left\langle 0'\right|\right) \quad (6.25)$$

By treating $|0'\rangle$ and $|D\rangle$ as a two level system, equation 6.25 can be rewritten in matrix form as

$$\hat{H}'_{RF,I} = \frac{\hbar\Omega_{RF}}{2}\hat{\sigma}_y \quad (6.26)$$

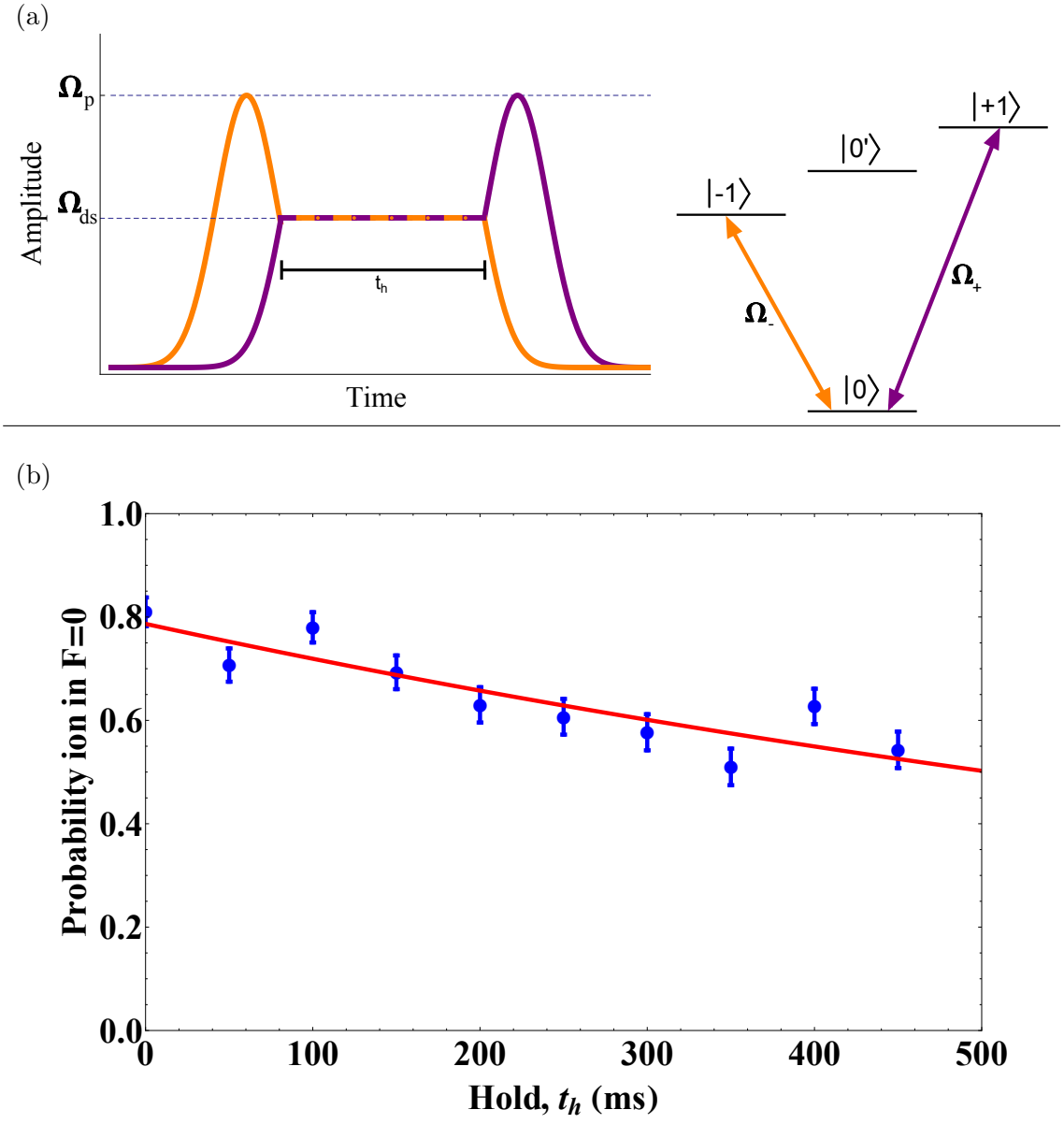

Figure 6.10: (a) STIRAP pulse envelopes showing hold time, t_h where $|D\rangle$ state is present. (b) Lifetime measurement of $|D\rangle$ state. Population is transferred from the $|-1\rangle$ state to the $|D\rangle$ state using half a STIRAP operation. The population is then held in this state for a time, t_h before being transferred to the $|+1\rangle$ state with the remainder of the STIRAP operation. A final π pulse on the $|0\rangle$ to $|+1\rangle$ transition is applied to move the successfully transferred population into the $|0\rangle$ state before detection. The solid line is an exponential fit to the data which gives a lifetime of 550 ms. Each point is an average of 200 measurements.

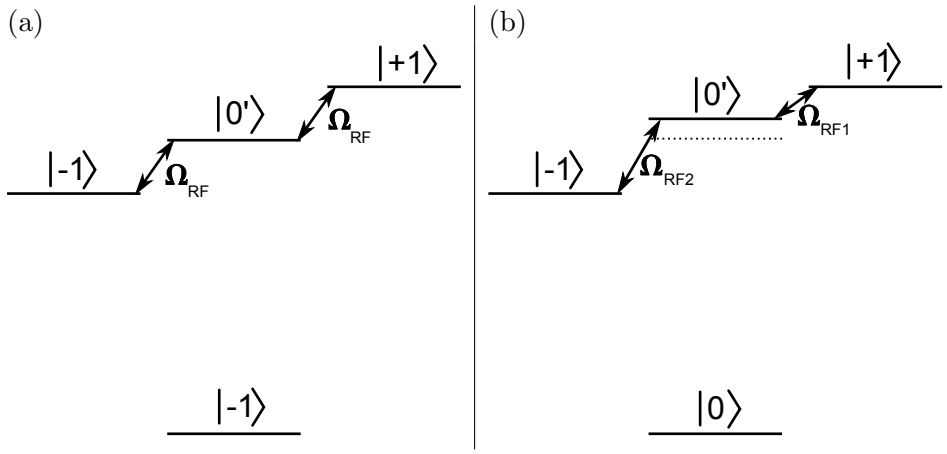

Figure 6.11: Transitions used for coherent manipulation between the $|0'\rangle$ and $|D\rangle$ states within the dressed state basis at (a) low and (b) high magnetic fields. At high magnetic fields, the $|0'\rangle$ state is shifted due to the second order Zeeman effect. This results in the transition frequency of the $|0'\rangle$ to $|-1\rangle$ state transition being different to the transition frequency of the $|0'\rangle$ to $|-1\rangle$ state transition.

which is equivalent to a rotation around the y axis of the Bloch sphere. Rotations around arbitrary axes cannot be realized as changing the RF phase ϕ_{RF} results in population coupling to the $|u\rangle$ and $|d\rangle$ states rather than changing the axis of rotation.

6.3.2 High B-field

In this regime, the second order Zeeman shifts are no longer negligible and the resonant frequency of the $|0'\rangle$ to $|+1\rangle$ and $|0'\rangle$ to $|-1\rangle$ transitions are no longer equal. This is the case for the magnetic field strengths typically found within ion trap experiments $\approx$ 10 Gauss. The method described in section 6.3.1 can still be realized in this regime by the application of two RF fields of equal phase with frequencies equal to ω_{r1} and ω_{r2} respectively.

An alternate method of coherent manipulation involves applying only one of these RF fields [102]. If for example, the field resonant with the $|0'\rangle$ to $|+1\rangle$ transition was used, the Hamiltonian of the system would be similar to equation 6.23 but without the terms coupling to the $|-1\rangle$ state

$$\hat{H}'_{RF,I} = \frac{\hbar\Omega_{RF}}{2}\left[e^{i\phi_{r1}}\left|0'\right\rangle\left\langle+1\right| + e^{-i\phi_{r1}}\left|+1\right\rangle\left\langle 0'\right|\right] \tag{6.27}$$

Moving into the dressed state basis using equations 6.8 gives the following Hamiltonian,

$$\begin{aligned}\hat{H}'_{RF,I} =& \frac{\hbar\Omega_{RF}}{2\sqrt{2}}\Big[e^{-i\phi_{r1}}\left|D\right\rangle\left\langle 0'\right| + e^{i\phi_{r1}}\left|0'\right\rangle\left\langle D\right| + \\ & \frac{1}{2}\left(e^{-i\phi_{r1}}(\left|u\right\rangle\left\langle 0'\right| + \left|0'\right\rangle\left\langle u\right|) + e^{i\phi_{r1}}(\left|0'\right\rangle\left\langle d\right| + \left|d\right\rangle\left\langle 0'\right|)\right)\Big]\end{aligned} \tag{6.28}$$

By ensuring that $\Omega_{RF} << \Omega_{ds}$, the terms in equation 6.28 which couple population from the $|0'\rangle$ state to the $|u\rangle$ and $|d\rangle$ states are suppressed by the energy gap shown in figure 6.2. This results in $\hat{H}'_{RF,I}$ only containing terms which couple population between the qubit states, $|0\rangle$ and $|D\rangle$. $\hat{H}'_{RF,I}$ can then be written in matrix form as

$$\hat{H}'_{RF,I} = \frac{\hbar\Omega_{RF}}{2\sqrt{2}} \begin{pmatrix} 0 & e^{-i\phi_{r1}} \\ e^{i\phi_{r1}} & 0 \end{pmatrix} \tag{6.29}$$

which corresponds to arbitrary rotations around the σ_ϕ axis of the Bloch sphere where the exact axis of rotation is given by the RF phase, ϕ_{r1}. This method is therefore preferable to the previous method as it allows for full manipulation of the Bloch sphere. In addition, within typical ion trap magnetic field strengths, this method requires half as many frequencies for coherent manipulation than the previous method which makes it technically simpler. The disadvantages of this method are however that the use of only one transition causes a reduction of a factor of $\sqrt{2}$ in Rabi frequency with respect to the previous method and that the RF Rabi frequency will be limited by the strength of the microwaves due to the $\Omega_{RF} << \Omega_{ds}$ approximation.

6.3.3 Experimental realisation

The magnetic field at the centre of our trap was determined using the frequencies of the $|0\rangle$ to $|\pm1\rangle$ transitions to be approximately 9.8 Gauss. Using equation 6.20, this results in a $|0'\rangle$ to $|\pm1\rangle$ transition frequency difference of $\omega_{RF2} - \omega_{RF1} \approx 2\pi \times 30\,\text{kHz}$ which puts us in the high field regime. Due to its ability to perform arbitrary rotations around the Bloch sphere, we will use the second method described in section 6.3.2.

RF setup

The RF field is generated by a coil which is attached to a RF signal generator in series with a capacitor and in parallel with a resistor for impedance matching as shown in figure 6.12. This forms a LCR circuit.

Such a circuit is resonant when the reactance of the inductor, $X_L = 2\pi f_{RF} L$ is equal to the reactance of the capacitor, $X_C = 1/(2\pi f_{RF} C)$. This occurs when

$$f_{RF} = \frac{1}{2\pi\sqrt{LC}}. \tag{6.30}$$

The inductor then acts as an antenna and radiates this frequency. To ensure the ion re-

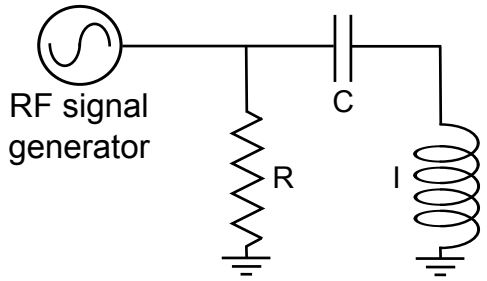

Figure 6.12: Diagram of an LCR circuit where a resistor or resistance R is in parallel with a capacitor of capacitance C and an inductor of inductance L.

ceives the maximum possible intensity of RF radiation, the inductor used is a coil designed to fit within the indentation formed by the front viewport of the vacuum system as shown in figure 6.13. In this position, the ion is less than 10 mm from the inductor coils axis. The inductor coils radius is therefore set to $r \approx 2.5$ cm. The inductance of the coil is given by [5]

$$L = \frac{\mu N^2 \pi r^2}{d} \tag{6.31}$$

where N is the number of turns, d is the diameter of the wire and μ is the magnetic permeability which equals 1.257×10^{-6} Hm^{-1} for air.

It was found that the efficiency of the resonant circuit, that is, where for a set RF input voltage, the inductor radiates the highest power, increased with the inductance [103]. An upper limit on this inductance is set by the circuits capacitance. In order to adjust the resonant frequency, the capacitance should be variable and high enough to be dominant over stray capacitances, resulting in a minimum capacitance of approximately 10 pF. The frequency splitting of the Zeeman states will be around 10 MHz based on a typical magnetic field of 10 Gauss. To achieve this the inductor has $N = 3$ turns and uses $d = 6.1$ mm wire. This gives an inductance of 5.8×10^{-6}H. A variable ceramic capacitor[6] is used with a capacitance of between 10 and 120 pF. This results in a variable resonant frequency of between ≈ 6 and 14 MHz. The resistor has a resistance equal to 50 Ω and is required to impedance match the circuit with the frequency generator to maximise the transmitted signal power and to avoid damage due to reflections.

In addition a digital switch[7] controlled via the FPGA is placed between the signal generator and the capacitor to allow the RF to be switched on and off quickly and efficiently.

[5] It should be noted that this is only an approximation due to the proximity of the coil to the Aluminum vacuum chamber.

[6] Murata Ltd: TZ03R121F169B00

[7] Minicircuits ZFSWA2-63DR+

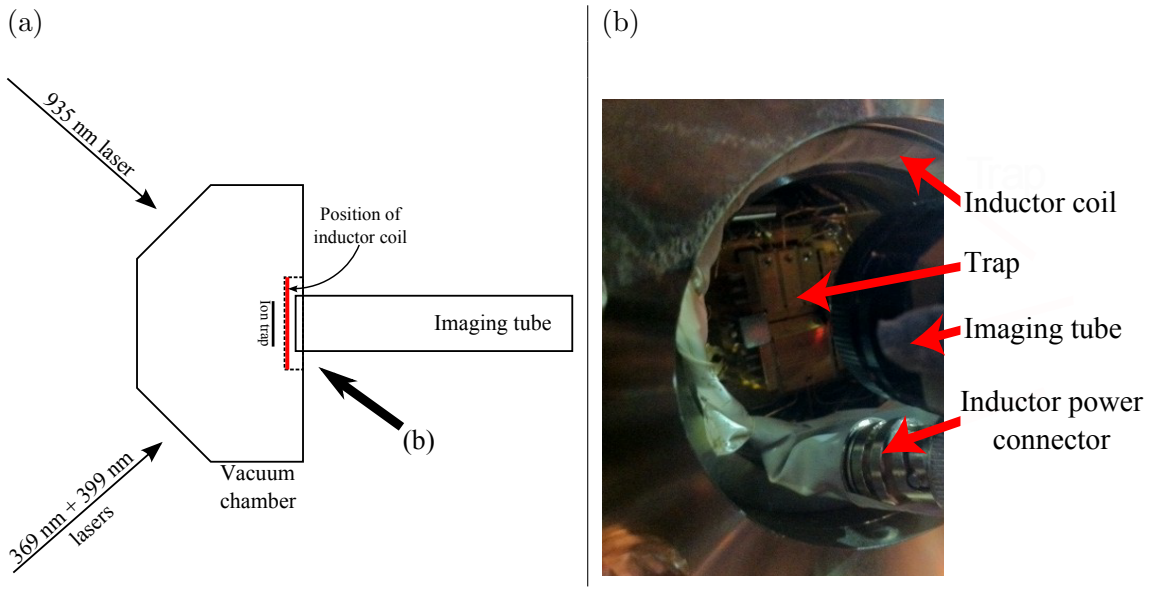

Figure 6.13: The inductor from the RF circuit is positioned within the alcove formed by the front imaging viewport. (a) shows an experimental schematic showing the location of the inductor coil with relation to the trap. (b) shows a photograph of the inductor coil in position.

RF setup testing

In order to test the RF setup, it was used to drive the $|0'\rangle$ to $|+1\rangle$ transition, without the dressing fields. The frequencies of these states were determined by measuring the $|0\rangle$ to $|0'\rangle$ and $|0\rangle$ to $|+1\rangle$ transition frequencies and taking the frequency difference. The RF frequency generator was then set to output this frequency and the circuits resonant frequency was set to this by adjusting the variable capacitor.

Following preparation in the $|0\rangle$ state, a π pulse on the $|0\rangle$ to $|+1\rangle$ transition places the population into the $|+1\rangle$ state. The RF is then switched on for a set time, t_{RF}. A second π pulse on the $|0\rangle$ to $|+1\rangle$ transition then places any population remaining in the $|+1\rangle$ state back into the $|0\rangle$ state before detection. Any population present in the bright state during detection has therefore been transferred to the $|0'\rangle$ state by the RF. Figure 6.14 shows the resultant population in the bright state and shows Rabi oscillations with a Rabi frequency equal to $2\pi\times18\,\mathrm{kHz}$.

To test the setup on the dressed state qubit, a frequency sweep was performed over the frequencies of the $|0'\rangle$ to $|\pm1\rangle$ transitions while the ion was being dressed. The RF Rabi frequency measured in the bare states is close to the second order Zeeman splitting therefore the RF power is turned down to reduce crosstalk between the $|0'\rangle$ to $|\pm1\rangle$ transitions. This allows exact transition frequencies to be determined.

The pulse sequence for this RF frequency sweep is shown in figure 6.15 (a). The $|D\rangle$

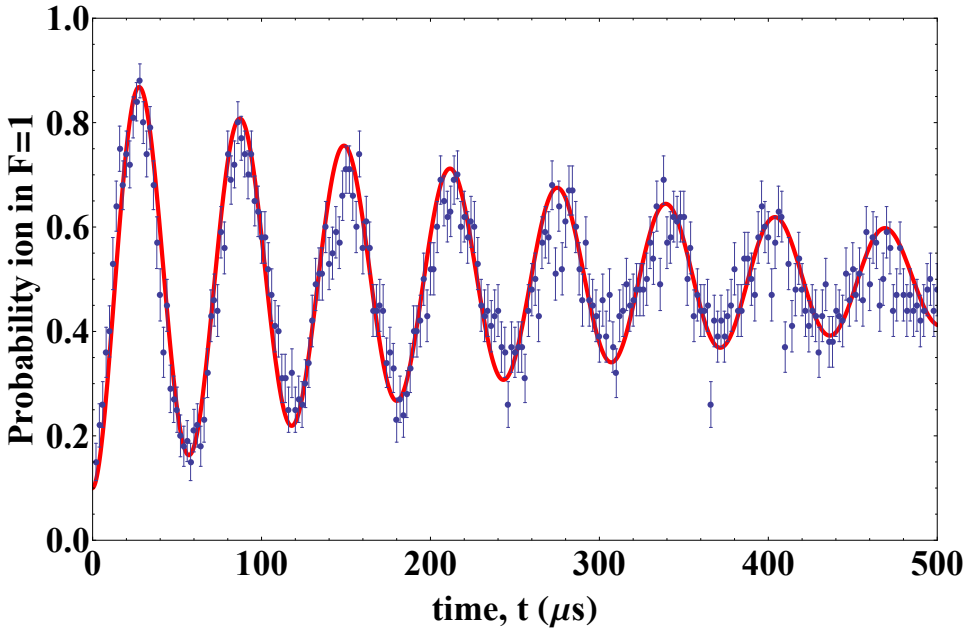

Figure 6.14: Graph showing Rabi oscillations between the $|0'\rangle$ and $|+1\rangle$ states performed using the RF setup. Each point is an average of 100 measurements.

state is prepared as described in section 6.2.3. During the hold time, an RF π pulse is applied. After the remainder of the STIRAP process, the standard π pulse on the $|+1\rangle$ to $|0\rangle$ transition is applied to prepare the ion for detection. The frequency of the RF pulse is varied over a range which includes the two transitions and the resultant population in the bright state with respect to this frequency is plotted in figure 6.15 (b).

Rabi flopping

By setting the RF frequency generator and RF resonant circuit to one of the resonant frequencies from the RF frequency sweep shown in figure 6.15, Rabi oscillations between the $|0'\rangle$ state and the $|D\rangle$ state can be observed. After preparation of the $|D\rangle$ state, the RF field is applied for increasing times. State detection is achieved in the same way as before and the results are shown in figure 6.16 (a) for times up to 2 ms. The Rabi frequency is measured to equal $2\pi \times 1.9$ kHz. Figure 6.16 (b) shows Rabi oscillations for times between 100 and 101 ms. The apparent change in Rabi frequency is due to slow drifts of the RF signal amplitude cause by for example, heating of components within the LCR circuit.

The decrease in oscillation amplitude at the different Rabi flopping times is used to calculate the minimum T_2 time of the qubit. This is found to equal ≈ 500 ms which is approximately equal to the lifetime of the $|D\rangle$ state. This is more than three orders of magnitude larger than the coherence time of the bare state qubit which shows that a significant amount of the decoherence due to magnetic field fluctuations has been suppressed.

(a)

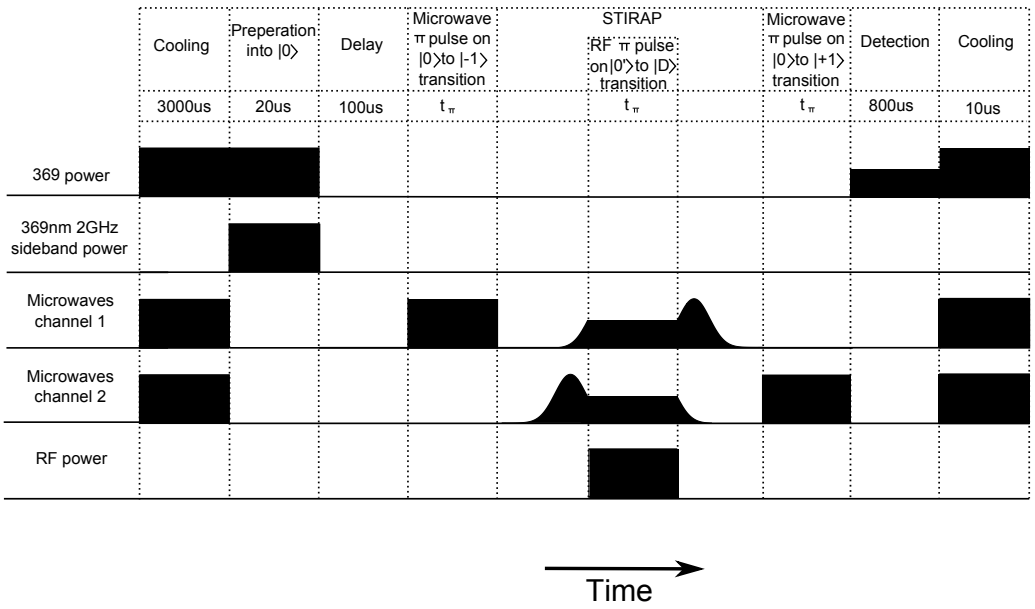

(b)

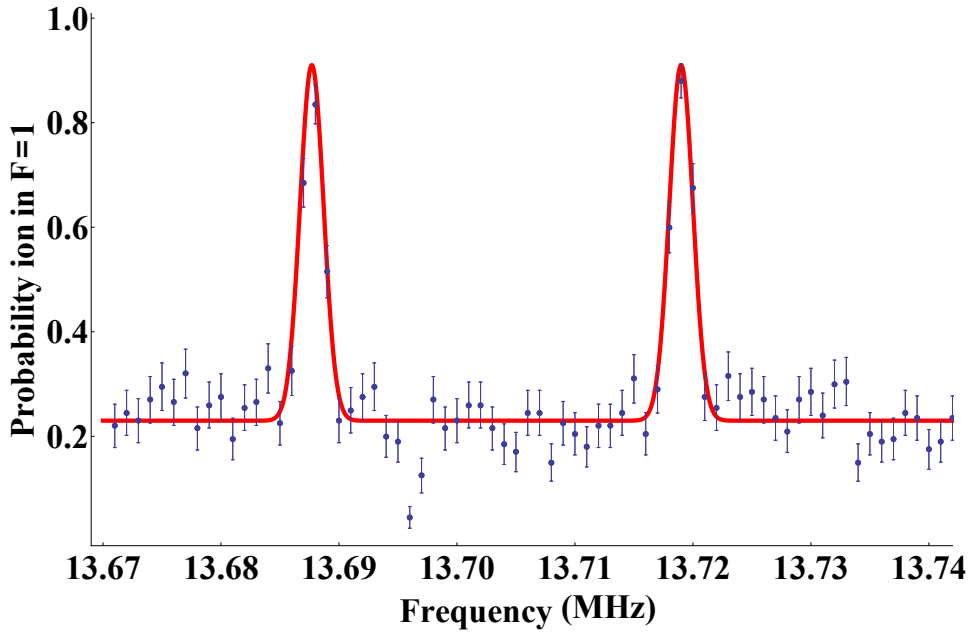

Figure 6.15: Pulse sequence (a) and results (b) of a frequency sweep over the $|0'\rangle$ to $|D\rangle$ state transition using the RF setup with a RF Rabi frequency approximately equal to $2\pi \times 4\,\mathrm{kHz}$. Two peaks are present representing the two available transition routes, from $|0'\rangle$ to $|-1\rangle$ and from $|0'\rangle$ to $|+1\rangle$. Each point is an average of 200 measurements.

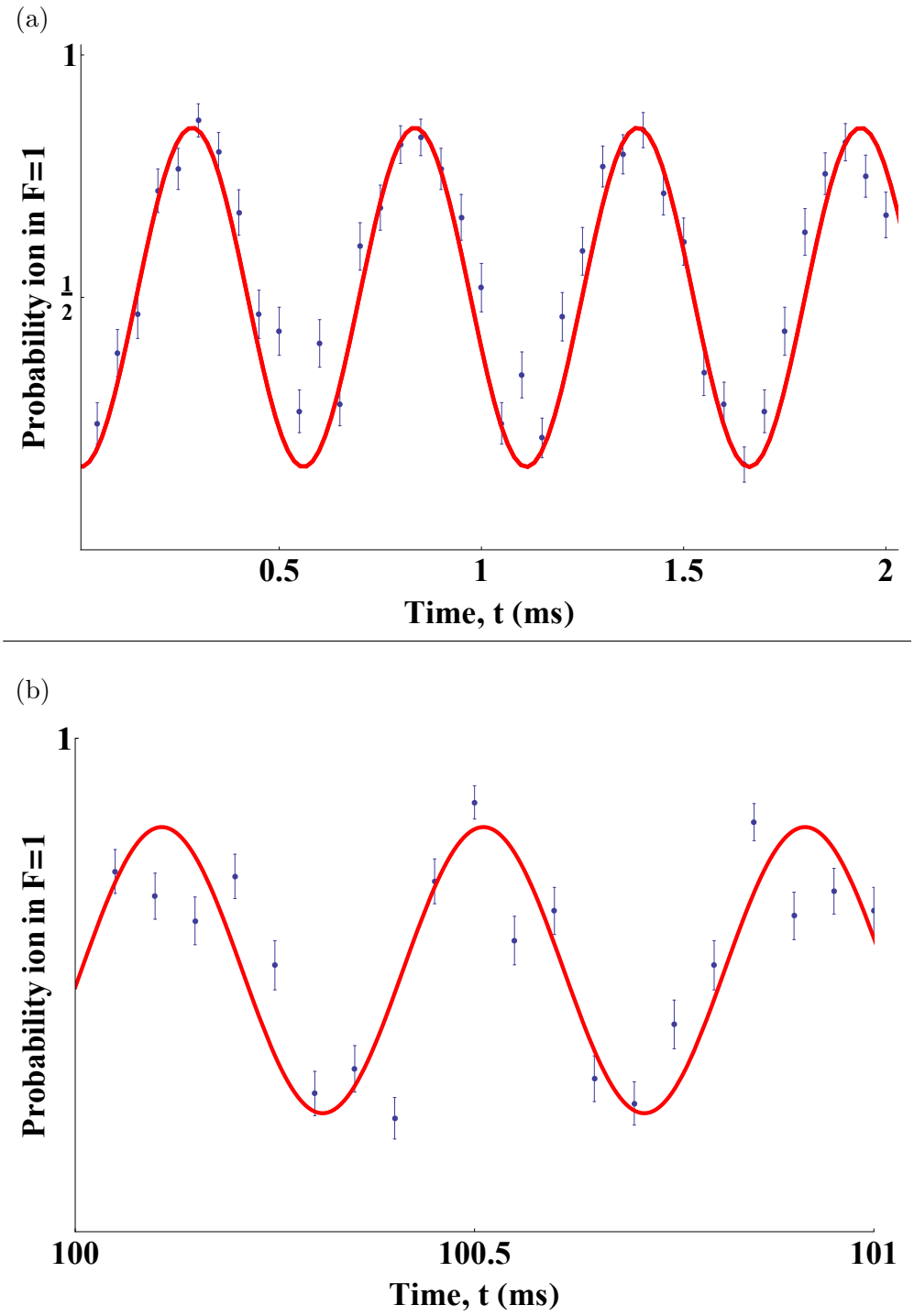

Figure 6.16: Graph showing Rabi oscillations on the $|0'\rangle$ to $|D\rangle$ transition between (a) 0-2 ms and (b) 100-101 ms. Each point is an average of (a) 100 and (b) 50 measurements.

The low contrast of the Rabi flop shown in figure 6.16 (a) is due to the low transfer efficiency of the STIRAP operation as described in section 6.2. This could potentially be increased by increasing the Rabi frequency of the dressing fields, Ω_{ds}.

An alternative method would be to initially prepare the ion in the $|0'\rangle$ state. During the Rabi flop, the dressing microwaves resonant with the $|0\rangle$ to $|-1\rangle$ and $|+1\rangle$ transitions should be turned on and kept at a constant power then turned off quickly so as to not affect the state population. The final state would then be determined by a π pulse on the $|0\rangle$ to $|0'\rangle$ transition, fluorescence during state detection would then indicate the ion is in the $|D\rangle$ state. This method would eliminate the need for a STIRAP operation which would result in a greater contrast. The disadvantage of this method is however that a third frequency resonant with the $|0\rangle$ to $|0'\rangle$ state transition would need to be added to the combiner in the microwave setup shown in figure 6.4 which would result in a more complicated microwave setup.

Ramsey fringes

To show the ability of the coherent manipulation method to perform arbitrary rotations of the Bloch sphere, Ramsey fringes are also produced. As described in chapter 3, Ramsey fringes are produced by applying two detuned $\pi/2$ pulses which are separated by a variable free precession time, t. During this time, the ion precesses around the equator of the Bloch sphere at a frequency equal to the detuning. The timing of the second pulse therefore determines the state the population ends up in.

This Ramsey experiment was carried out on the $|0'\rangle$ to $|D\rangle$ transition. The $|D\rangle$ state was prepared and detected using the same method as before and the results are shown in figure 6.17 for a free precession time of between 0 and 8 ms. The RF pulse detuning was inferred from the fringe frequency to be approximately equal to 160 Hz.

6.4 Magnetic field gradient entanglement within the dressed state basis

The magnetic field gradient entanglement scheme described in the previous chapter, requires the use of magnetic field sensitive states. This section will show how the states in the dressed basis are affected by a magnetic field gradient and will show how this allows entanglement to be performed within the this basis despite the suppression of the effects of magnetic field fluctuations.

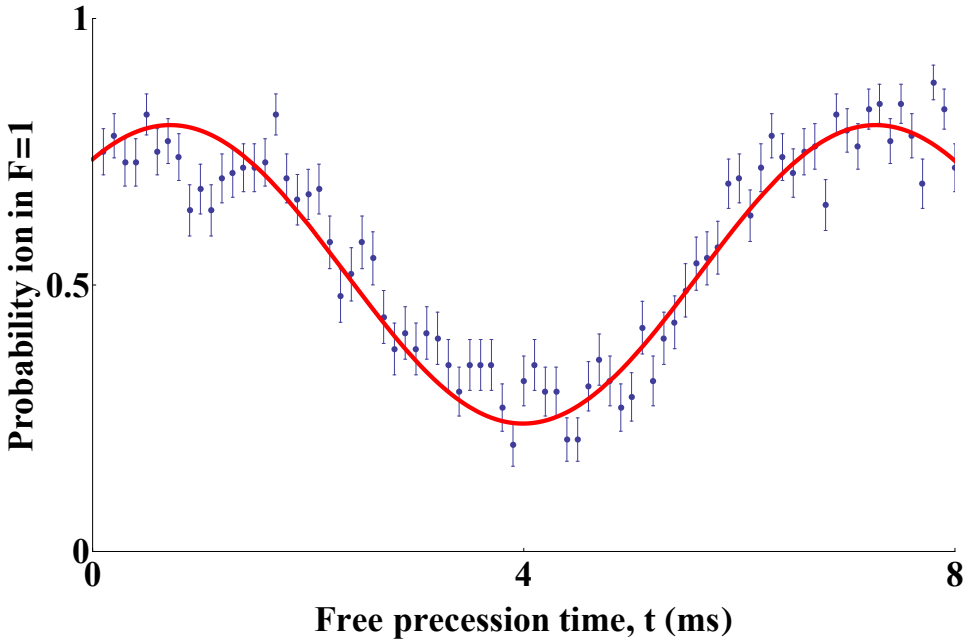

Figure 6.17: Graph showing Ramsey fringe on the $|0'\rangle$ to $|D\rangle$ transition with a pulse detuning of 160 Hz. Each point is an average of 100 measurements.

The Hamiltonian describing the unperturbed ion is given by the sum of the level Hamiltonian given by equation 6.2 and the Hamiltonian from a simple Harmonic oscillator given by $\hat{H}_b$ in equation 3.31. This gives

$$\hat{H}_0 = -\hbar\omega_0 |0\rangle\langle 0| + \hbar\omega_{r1} |+1\rangle\langle +1| - \hbar\omega_{r2} |-1\rangle\langle -1| + \hbar v \hat{a}^\dagger \hat{a} \tag{6.32}$$

where v is the secular frequency and $\hat{a}$ and $\hat{a}^\dagger$ are the state raising and lowering operators respectively. Within a magnetic field gradient, ω_{r1} and ω_{r2} will become dependent on the ions position as shown by equation 5.68 in chapter 5. Using the same processes used to obtain equation 5.73, equation 6.32 can be rewritten within a magnetic field gradient as

$$\begin{aligned}\hat{H}_0' = -\hbar\omega_0 |0\rangle\langle 0| + \hbar\omega_{r1}(0) |+1\rangle\langle +1| - \omega_{r2}(0) |-1\rangle\langle -1| \\ +\hbar v\epsilon(|+1\rangle\langle +1| - |-1\rangle\langle -1|) + \hbar v \hat{a}^\dagger \hat{a}\end{aligned} \tag{6.33}$$

where ϵ is a constant given by equation 5.74,

$$\epsilon = \frac{g_F m_F \mu_B \partial_z B(0)}{\hbar} \sqrt{\frac{\hbar}{2mv^3}}. \tag{6.34}$$

Within the magnetic field gradient entanglement formulation given in chapter 5, a polaron transformation was applied to move the effect of the magnetic field gradient into the Hamiltonian of the interacting fields. The same technique will be used here with a

transformation which, ignoring constant terms reverts $\hat{H}_0'$ back to $\hat{H}_0$, $\widetilde{H}_0' = \hat{H}_0$. This transformation is given by

$$\widetilde{H} = e^{\hat{V}} \hat{H} e^{-\hat{V}} \tag{6.35}$$

where $\hat{V} = \epsilon(|+1\rangle\langle+1| - |-1\rangle\langle-1|)(\hat{a}^\dagger - \hat{a})$. This transformation will now be applied to the Hamiltonian given by equation 6.5,

$$\begin{aligned}\hat{H}'_{MW} = \hbar\Omega_{ds} [&\cos(\omega_- t)(|0\rangle\langle-1| + |-1\rangle\langle0|) \\ &+ \cos(\omega_+ t)(|0\rangle\langle+1| + |+1\rangle\langle0|)],\end{aligned} \tag{6.36}$$

which describes the perturbation to the system caused by the application of the two microwave dressing fields. Under the transformation given by equation 6.35, this Hamiltonian becomes

$$\begin{aligned}\widetilde{H}'_{MW} = \hbar\Omega_{ds} [&\cos(\omega_- t)(e^{\epsilon(\hat{a}^\dagger - \hat{a})}|0\rangle\langle-1| + e^{-\epsilon(\hat{a}^\dagger - \hat{a})}|-1\rangle\langle0|) \\ &+ \cos(\omega_+ t)(e^{-\epsilon(\hat{a}^\dagger - \hat{a})}|0\rangle\langle+1| + e^{\epsilon(\hat{a}^\dagger - \hat{a})}|+1\rangle\langle0|)].\end{aligned} \tag{6.37}$$

Within the interaction picture with respect to $\hat{H}_0$, this Hamiltonian can be rewritten as

$$\begin{aligned}\widetilde{H}'_{MW,I} = \frac{\hbar\Omega_{ds}}{2} [&\cos(\omega_- t)(e^{\epsilon(\hat{a}^\dagger - \hat{a}) - i\omega_- t}|0\rangle\langle-1| + e^{-\epsilon(\hat{a}^\dagger - \hat{a}) + i\omega_- t}|-1\rangle\langle0|) \\ &+ \cos(\omega_+ t)(e^{-\epsilon(\hat{a}^\dagger - \hat{a}) - i\omega_+ t}|0\rangle\langle+1| + e^{\epsilon(\hat{a}^\dagger - \hat{a}) + i\omega_+ t}|+1\rangle\langle0|)].\end{aligned} \tag{6.38}$$

By writing $\cos(x)$ in terms of exponentials and applying the rotating wave approximation to eliminate the fast rotating terms, this Hamiltonian simplifies to

$$\begin{aligned}\widetilde{H}'_{MW,I} = \frac{\hbar\Omega_{ds}}{2} [&(e^{\epsilon(\hat{a}^\dagger - \hat{a})}|0\rangle\langle-1| + e^{-\epsilon(\hat{a}^\dagger - \hat{a})}|-1\rangle\langle0|) \\ &+ (e^{-\epsilon(\hat{a}^\dagger - \hat{a})}|0\rangle\langle+1| + e^{\epsilon(\hat{a}^\dagger - \hat{a})}|+1\rangle\langle0|)].\end{aligned} \tag{6.39}$$

The eigenstates of this Hamiltonian represent a new gradient transformed dressed state basis and are given by

$$\begin{aligned}|\widetilde{u}\rangle &= \frac{1}{2}(e^{2\epsilon(\hat{a}^\dagger - \hat{a})}|+1\rangle + |-1\rangle + \sqrt{2}e^{\epsilon(\hat{a}^\dagger - \hat{a})}|0\rangle) \\ |\widetilde{d}\rangle &= \frac{1}{2}(e^{2\epsilon(\hat{a}^\dagger - \hat{a})}|+1\rangle + |-1\rangle - \sqrt{2}e^{\epsilon(\hat{a}^\dagger - \hat{a})}|0\rangle) \\ |\widetilde{D}\rangle &= \frac{1}{\sqrt{2}}(e^{2\epsilon(\hat{a}^\dagger - \hat{a})}|+1\rangle - |-1\rangle).\end{aligned} \tag{6.40}$$

This transformed dressed state basis is analogous to the untransformed dressed state basis given by equation 6.8 with the addition of a factor A^2 to the contributions from the

$|+1\rangle$ state and a factor A to contributions from the $|0\rangle$ state where $A = e^{\epsilon(\hat{a}^\dagger - \hat{a})}$ and is dependent on the strength of the magnetic field gradient.

In order to excite the motion of an ion between the $|0'\rangle$ and the $|D\rangle$ states, a RF field resonant with a motional sideband of one of the $|0'\rangle$ to $|\pm 1\rangle$ state transitions should be applied. For the first red sideband of the $|0'\rangle$ to $|+1\rangle$ state transition, this gives the following perturbation Hamiltonian

$$\hat{H}_{rsb} = \hbar\Omega_{RF}\cos((\omega_{r1} - v_s)t)(|+1\rangle\langle 0'| + |0'\rangle\langle +1|). \tag{6.41}$$

Under the transformation given by equation 6.35 this Hamiltonian becomes

$$\widetilde{H}_{rsb} = \hbar\Omega_{RF}\cos((\omega_{r1} - v_s)t)(e^{\epsilon(\hat{a}^\dagger - \hat{a})}|+1\rangle\langle 0'| + e^{-\epsilon(\hat{a}^\dagger - \hat{a})}|0'\rangle\langle +1|). \tag{6.42}$$

Within the interaction picture with respect to $\hat{H}_0$, this Hamiltonian is rewritten as

$$\widetilde{H}_{rsb,I} = \hbar\Omega_{RF}\cos((\omega_{r1} - v_s)t)(e^{\epsilon(\hat{a}^\dagger - \hat{a}) + i\omega_{r1}t}|+1\rangle\langle 0'| + e^{-\epsilon(\hat{a}^\dagger - \hat{a}) - i\omega_{r1}t}|0'\rangle\langle +1|). \tag{6.43}$$

By writing $\cos(x)$ in terms of exponentials and applying the rotating wave approximation to eliminate the fast rotating terms, this Hamiltonian simplifies to

$$\widetilde{H}_{rsb,I} = \frac{\hbar\Omega_{RF}}{2}(e^{\epsilon(\hat{a}^\dagger - \hat{a}) + iv_s t}|+1\rangle\langle 0'| + e^{-\epsilon(\hat{a}^\dagger - \hat{a}) - iv_s t}|0'\rangle\langle +1|). \tag{6.44}$$

Writing this Hamiltonian in terms of the new transformed dressed state basis given by equation 6.40 gives

$$\begin{aligned}\widetilde{H}_{rsb,I} = \frac{\hbar\Omega_{RF}}{4}[&e^{-\epsilon(\hat{a}^\dagger - \hat{a}) + iv_s t}(|\widetilde{u}\rangle\langle 0'| + |\widetilde{d}\rangle\langle 0'| + \sqrt{2}|\widetilde{D}\rangle\langle 0'|) \\ &+e^{\epsilon(\hat{a}^\dagger - \hat{a}) - iv_s t}(|0'\rangle\langle\widetilde{u}| + |0'\rangle\langle\widetilde{d}| + \sqrt{2}|0'\rangle\langle\widetilde{D}|).\end{aligned} \tag{6.45}$$

Assuming $\Omega_{RF} << \Omega_{ds}$, the terms coupling population from the $|0'\rangle$ state to the $|\widetilde{u}\rangle$ and $|\tilde{d}\rangle$ states are suppressed by the energy gap shown in figure 6.2 which allows equation 6.45 to be rewritten as

$$\widetilde{H}_{rsb,I} = \frac{\hbar\Omega_{RF}}{2\sqrt{2}}\left(e^{-\epsilon(\hat{a}^\dagger - \hat{a}) + iv_s t}|\widetilde{D}\rangle\langle 0'| + e^{\epsilon(\hat{a}^\dagger - \hat{a}) - iv_s t}|0'\rangle\langle\widetilde{D}|\right). \tag{6.46}$$

By making the substitution $\eta_{eff} = \sqrt{\eta^2 + \epsilon^2}$ where $\eta = kz$ has been assumed to be negligible, equation 6.46 becomes analogous to equation 5.81 for the transformed dressed state qubit represented by $|0'\rangle$ and $|\tilde{D}\rangle$. Motional coupling and quantum logic operations

can be therefore performed as described by chapter 5 within the dressed state basis by simply applying RF fields resonant with the motional sidebands of one of the $|0'\rangle$ to $|\pm 1\rangle$ state transitions.

Chapter 7

Motional coupling using a magnetic field gradient

As discussed in chapter 5, an entanglement gate between ion qubits can be produced by the application of electromagnetic fields, providing they have a strong coupling to the motional modes of the ions. These fields create a state dependent force, which results in the movement of an ion's motional states in phase space leading to the addition of a state dependent geometric phase.

This chapter will detail the progress towards the production of such an entanglement gate using microwave fields. As discussed in section 5.3.6, due to the low frequency of the required microwaves, a magnetic field gradient is needed to provide sufficient coupling of these microwaves to the motional modes of the ions. The gradient provides a spatially dependent frequency shift of the magnetic field sensitive states which results in an effective Lamb-Dicke parameter when making a transition to these states

Section 7.1 describes how a gradient of $24\,\mathrm{Tm}^{-1}$ is created at the ion's position using in-vacuum permanent magnets. As a result of this gradient, adjacent ions have different transition frequencies between their $^2\mathrm{S}_{\frac{1}{2}}$ $\mathrm{F}=0$ and $^2\mathrm{S}_{\frac{1}{2}}$ $\mathrm{F}=1$ $\mathrm{m}_F=\pm1$ levels. This allows for individual addressing of adjacent ions which is described in section 7.2

Section 7.3.1 demonstrates that, within this gradient, microwaves can couple to the motional states of both a single ion and two adjacent ions. This is shown in the form of motional sidebands, that is, population transfer between states when the applied microwaves are at a frequency equal to the resonant frequency plus and minus the ions secular frequency.

This coupling is then used to produce a state dependent force in the σ_ϕ basis. Section 7.3.4 demonstrates this force by observing the movement of a single ions motional state

in phase space.

The use of magnetic field sensitive states does however leave the qubit open to decoherence from magnetic field fluctuations. As described in chapter 6 this decoherence can be avoided by dressing the ions with microwaves and using a new dressed state qubit which is shielded from this decoherence. It was also shown in section 6.4 that the effective Lamb-Dicke parameter present due to a magnetic field gradient is still present for the dressed state qubit. Section 7.3.5 demonstrates this, showing the observation of the motional sidebands of the dressed state qubit.

Finally section 7.4 describes how this work can be expanded to produce a two ion entanglement gate using microwave dressed states.

7.1 Creating a magnetic field gradient

A brief summary of the setup used to produce a high magnetic field gradient at the ion is shown here, for more details please refer to the MRes thesis by Joe Randall [104]. A high magnetic field gradient at the ion is produced using four permanent magnets. These were designed to fit inside the vacuum system on the chip bracket around the existing trap as shown in figure 7.1. The magnets are made of Samarium Cobalt (SmCo). This material was chosen due to its high residual magnetic flux density[1] of 11.5 kG [105] and its high Curie temperature[2] of 800 degrees [105] which is four times higher than the maximum baking temperature. The magnets are coated in Nickel Copper Nickel (NiCuNi) which is UHV compatible and provides corrosion resistance.

As shown in figure 7.1, two of the magnets were designed to fit between the trap electrodes (yellow) and the compensation electrode holder (green). The magnets contain six machined holes for the compensation electrodes. The compensation electrodes then hold the magnets in place. In addition, the friction between the magnets and the stainless steel cage, intensified by the magnetic repulsion, provides extra stability. The two larger magnets were designed to fit at either end of the chip bracket and are attached via two screws which fit through machined holes in the magnet. The magnets were supplied and machined to a precision of 0.05 mm by e-Magnets UK.

The magnets are positioned so they all have their north poles pointing towards the trap centre. Figure 7.2 shows the trap after the magnets have been added. This setup was then baked and put under vacuum.

[1] Residual magnetic flux density is the maximum magnetic flux density as measured on the surface of the magnet.

[2] Curie temperature is the temperature at which the magnetic properties of the magnet are destroyed.

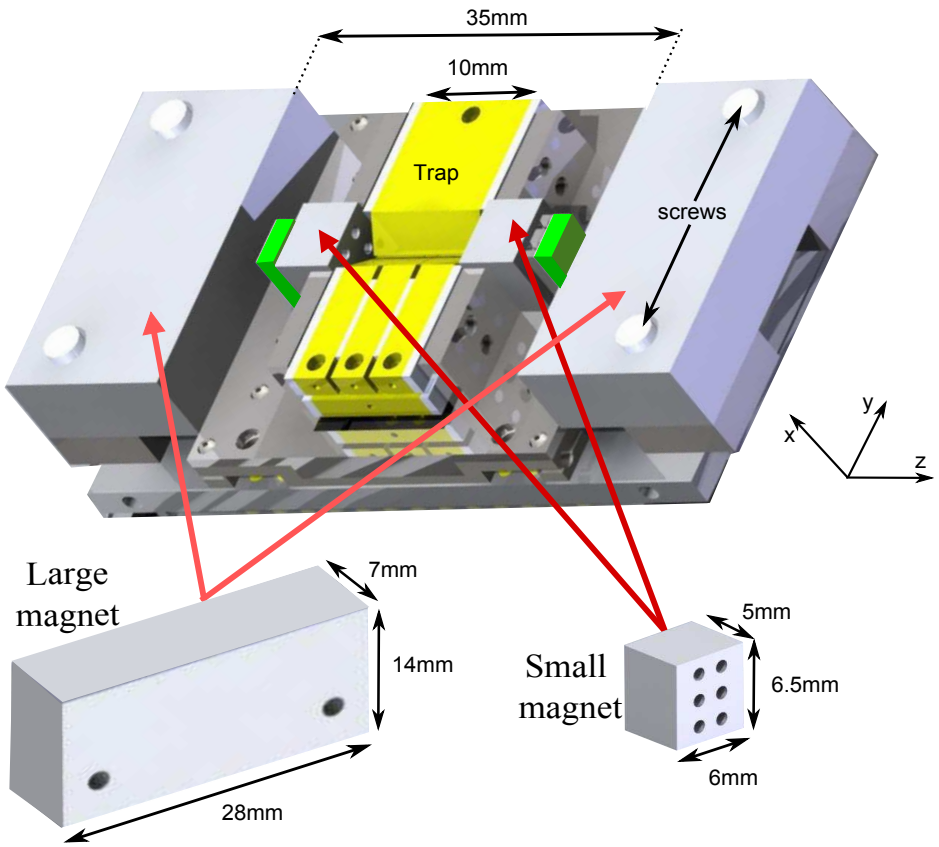

Figure 7.1: SolidWorks diagram showing how the magnets fit on the chip carrier. The large magnets are screwed onto either end of the chip bracket. The two smaller magnets fit between the trap electrodes (yellow) and the compensation electrode holder (green) and are held in place by the compensation electrodes. The insets show the dimensions of the magnets.

The magnetic field strength given by this magnet setup within the trap was simulated[3] and the results are shown in figure 7.3 [74]. The simulated magnetic field gradient at the trap centre was found to equal $42\,\mathrm{Tm}^{-1}$ along the trap axis and between 20 and $22\,\mathrm{Tm}^{-1}$ in the radial directions.

As shown in figure 7.3, the magnet setup was designed to give a magnetic field strength minimum as well as a high magnetic field gradient at the trap centre. This low magnetic field strength is required for efficient cooling and detection of the ion. As the magnitude of the magnetic field at a $^{171}\mathrm{Yb}^{+}$ ion increases, the Zeeman splitting of the m_F levels within the $^2\mathrm{S}_{\frac{1}{2}}$ $\mathrm{F}=1$ level increases. This reduces the rate at which 369 nm light resonant with the $^2\mathrm{S}_{\frac{1}{2}}$ $\mathrm{F}=1$ $\mathrm{m}_F=0$ to $^2\mathrm{P}_{\frac{1}{2}}$ $\mathrm{F}=0$ transition can off-resonantly pump ions out of the $^2\mathrm{S}_{\frac{1}{2}}$ $\mathrm{F}=1$ $\mathrm{m}_F=\pm1$ levels which consequently reduces the rate of cooling. This is investigated further using the rate equation program from chapter 3. Figure 7.4 shows the effect a magnetic field has on the number of detectable photons[4] produced during

[3]Simulation performed using Computer Simulation Technology (CST)

[4]Detectable photons are photons produced by spontaneous emission of the $^2\mathrm{P}_{\frac{1}{2}}$ levels of the ytterbium

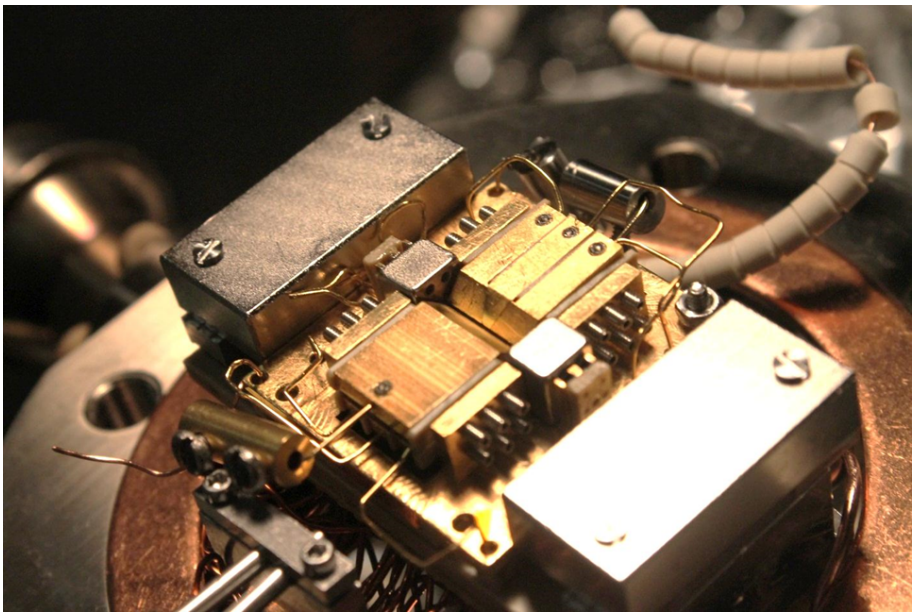

Figure 7.2: Photograph of the trap with the magnets in place.

Doppler cooling using 369 nm light with an intensity equal to I_{sat} (green), $10\,I_{sat}$(orange) and $100\,I_{sat}$(pink). Figure 7.4 shows that below 1 mT, the effect of the magnetic field strength on the number of detectable photons is negligible. Above 1 mT the Zeeman shift of the magnetic field sensitive levels becomes significant and, due to population trapping, the number of photons drops and approaches negligible levels at approximately 100 mT. The exact magnetic field strength at which this drop off occurs increases slightly as the 369 nm intensity is increased due to power broadening.

Experimentally, when the 369 nm intensity is above approximately $100\,I_{sat}$ the ion begins to become indistinguishable from the background scatter from the trap electrodes. Using figure 7.4, assuming this upper limit in 369 nm intensity, the maximum magnetic field where detection of the ion during Doppler cooling is possible is approximately 30 mT. To maximise the chances of detection however, ideally the magnetic field should be kept below 1 mT.

The magnetic field strength will also have an effect on the state detection fidelity. The optimum state detection fidelity for our experiment was found in chapter 3 to be present with a 369 nm intensity equal to $0.1\,I_{sat}$ and a detection time of 1 ms. Figure 7.5 shows the effect the magnetic field strength has on this maximum detection fidelity. From figure 7.5 it becomes clear that to optimise the fidelity of state detection, the magnetic field strength should be kept below approximately 0.1 mT.

It should be noted that while figures 7.4 and 7.5 both suggest that the ideal B-field is

ion.

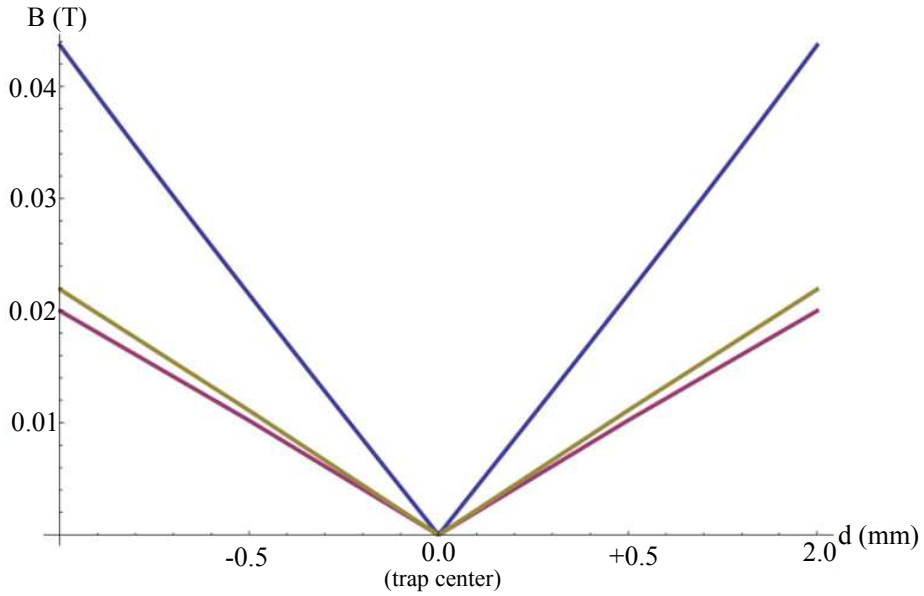

Figure 7.3: Simulation of the magnet setup showing the magnetic field strength within the centre 2 mm of the trap in the x axis (Yellow), y axis (Red) and z axis (Blue).

zero. A small offset field ($\approx 10^{-4}$ T) is required to avoid population trapping in the $^2S_{\frac{1}{2}}$ F = 1 $m_F = \pm 1$ levels as a result of limited polarisation components, this was discussed in detail within section 2.3.

A method to counter the effects on cooling and state detection caused by a high offset magnetic field is to apply sidebands with a frequency equal to the frequency difference between the $^2S_{\frac{1}{2}}$ F = 1 $m_F = 0$ and $m_F = \pm 1$ levels to the 369 nm laser using an EOM. Alternatively, the field can be compensated using external field coils.

7.1.1 Compensation coils

Experimentally, the magnetic field minimum was however not expected to coincide exactly with the trap centre. This shift in the magnetic field minimum would be due to unpredictable errors such as machining errors, human errors in placing the magnets or movement of the magnets and/or the trap electrodes during the baking process. In order to shift the magnetic field minimum to the trap centre and thereby allow the most efficient cooling, state detection and maximum possible magnetic field gradient, external magnetic field coils were built [104]. These consist of three pairs of Helmholtz coils made with 200 turns of 1 mm diameter copper wire. The coil pairs have radii equal to 150 mm, 90 mm and 120 mm, and coil separations of 95 mm, 30 mm and 65 mm, for the x, y and z axis coil sets respectively. These provide constant magnetic fields in all three dimensions and, based on the aforementioned dimensions, are capable of moving the magnetic field minimum within the trap by 42 μm, 92 μm and 66 μm per amp in the x, y and z axes respectively [74]. A

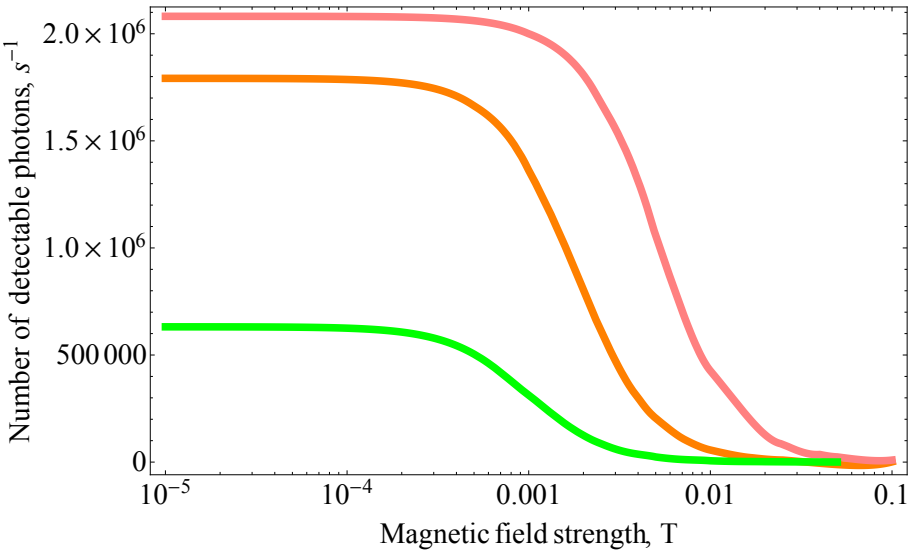

Figure 7.4: Graph showing the number of detectable photons released after an ion initially in the $^2S_{\frac{1}{2}}$ F = 1 $m_F = 0$ level is Doppler cooled for 1 second vs the magnetic field strength. This graph was formed using the rate equation program with 369 nm light resonant with the $^2S_{\frac{1}{2}}$ F = 1 $m_F = 0$ to $^2P_{\frac{1}{2}}$ F = 0 transition with an intensity equal to 1 I_{sat} (green), 10 I_{sat} (orange) and 100 I_{sat} (pink) and microwaves resonant with the $^2S_{\frac{1}{2}}$ F = 0 to $^2S_{\frac{1}{2}}$ F = 1 $m_F = 0$ transition to move population which decays into the $^2S_{\frac{1}{2}}$ F = 1 $m_F = 0$ level back into the cooling cycle. The 935 nm intensity was set to equal 1000 I_{sat}. The slight jaggedness of the curves is a consequence of the finite step size used by the rate equation program.

photograph of these coils is shown in figure 7.6.

When new ions were trapped, the frequency of the $^2S_{\frac{1}{2}}$ F = 0 to F = 1 $m_F = +1$ transition of a single ion before compensation was found to equal 12.79633 GHz which corresponds to a magnetic field of approximately 0.011 T. While this is low enough for us to cool and observe the ions with a high intensity 369 nm laser beam as shown in figure 7.4, it is too high for efficient state detection as shown in figure 7.5.

Setting the offset magnetic field

To find the compensation coil currents which give the magnetic field minimum at the trap centre, the frequency of the $^2S_{\frac{1}{2}}$ F = 0 to F = 1 $m_F = +1$ transition of a single ion was measured (as explained in section 3.5.2) for a range of compensation coil currents on the x axis coils. The coil current was then set to the value which gave the minimum transition frequency. This was then repeated using both the y and z axis coils. Due to potential coupling of the magnetic field between axes, caused by, for example, the coils not being perfectly perpendicular, this process was iterated several times until the coil currents at which the minimum transmission frequency occurs did not change. The current on the z

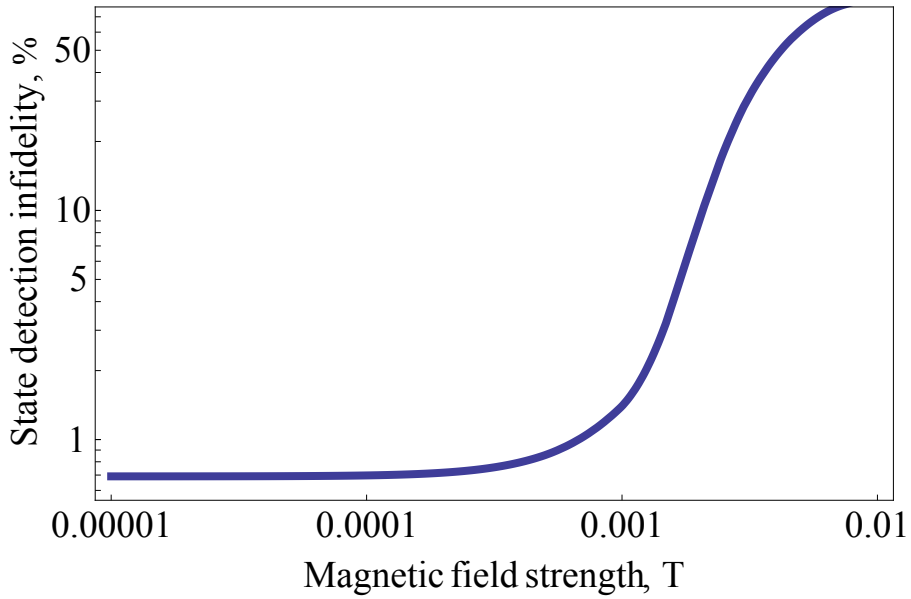

Figure 7.5: Graph showing the detection fidelity vs magnetic field strength. This graph was simulated using the rate equation program and equations 3.24 and 3.24 with a collection efficiency equal to 0.0021, a detection time of 1 ms and 369 nm and 935 nm intensities equal to 0.1 I_{sat} and 100I_{sat} respectively.

axis coil was then increased to give a large enough Zeeman shift of the $^2S_{\frac{1}{2}}$ $F=1$ levels to allow full manipulation of the Bloch sphere of a dressed state qubit to be performed (This requires the ability to individually address the $^2S_{\frac{1}{2}}$ $F=1$ $m_F=0$ to $m_F=\pm1$ transitions (see section 6.3.2), which requires a significant second order Zeeman shift of the $^2S_{\frac{1}{2}}$ $m_F=0$ level). To accomplish this, the z axis coil current was increased to give the shift between the $^2S_{\frac{1}{2}}$ $F=1$ $m_F=0$ and $m_F=\pm1$ level of approximately 9 MHz, equivalent to 0.64 mT. This gives a frequency on the $^2S_{\frac{1}{2}}$ $F=0$ to $F=1$ $m_F=+1$ transition equal to 12.655182 GHz. Using figure 7.5, the maximum state detection fidelity achievable with a 0.64 mT offset field is $\approx 99.5\,\%$.

Initially, it was found that the minimum magnetic field strength coincided with the trap centre with a current of roughly 5.75 A on the x axis compensation coil. As a result the coil dissipated around 350 W and needed to be water cooled to avoid melting the wire insulation. Water cooling however is not ideal as it can cause vibrations as well as temperature fluctuations in the coils which could cause experimental errors. To remove the need for water cooling, two sets of four N42 cylindrical permanent magnets[5] were stacked together and placed above the vacuum system at a distance of approximately 120 mm from the ion to provide the majority of the required magnetic field compensation. With this addition, the compensation coil currents found to align the minimum magnetic

[5]Magnet Expert Ltd, F666

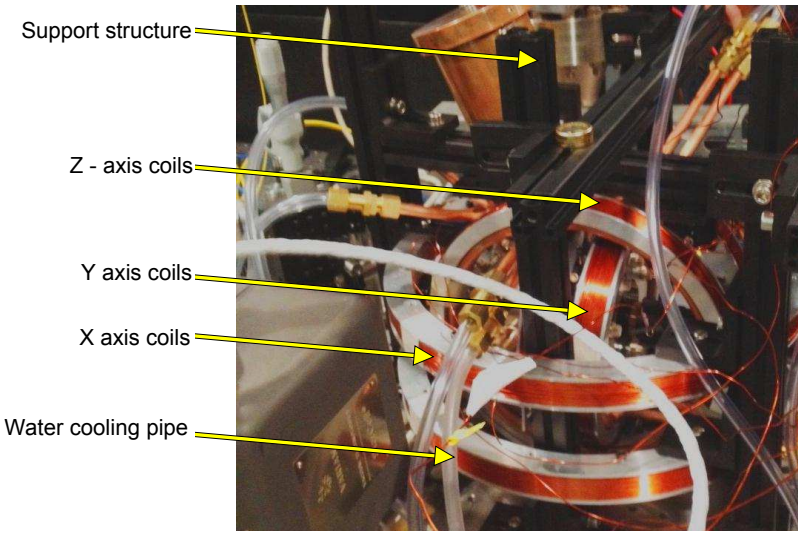

Figure 7.6: Photograph of the compensation coils used to insure the magnetic field magnitude minimum is at the trap centre. The coils are held in place using a black aluminum support structure. The coils are connected to a water cooling system to allow the use of high currents.

field in the x and y axes to the trap centre and apply a 0.64 mT magnetic field in the z axis are 1.63 A, 1.52 A and 1.94 A for the x, y and z axes respectively. This corresponds to a shift of the magnetic field minimum by 68 μm, 140 μm and 128 μm respectively.

7.1.2 Measuring the magnetic field gradient

The magnetic field gradient at the trap centre was measured by finding the resonant frequency of a magnetic field sensitive transition with the ion at different axial positions close to the trap centre. The ion was moved along the trap axis by adjusting the voltage of the endcap electrodes as described in chapter 2. The ion's distance from the trap centre was measured by observing the ion's image position on the CCD array.

The CCD array pixel size was first calibrated as follows. The axial secular frequency, v of two trapped ions is measured[6] and used to calculate the actual ion-ion separation, Δz, given by [106]

$$\Delta z = \left(\frac{e^2}{2\pi\epsilon_0 m v^2} \right)^{\frac{1}{3}} \tag{7.1}$$

where m is the mass of a $^{171}Yb^+$ ion. This is then compared to the measured ion-ion separation on the CCD array.

Figure 7.7 shows the change in resonant frequency of the $^2S_{\frac{1}{2}}$ F = 0 to F = 1 $m_F = 1$ transition as a function of axial distance along the trap. A fit to this data gives a magnetic

[6] To measure the ions secular frequency, an AC 'tickle' voltage is applied to the trap electrode. When the frequency of this voltage is equal to the secular frequency, the ion resonates.

field gradient of $24.4\,\mathrm{Tm}^{-1}$. This is approximately 60 % of the gradient simulated in the previous section. The difference is most likely due to in house adjustments of the smaller magnets[7] which may have reduced their magnetisation. Other potential error sources include magnet placement errors, impurities within the magnet or reductions in magnet strength resulting from the vacuum system bake.

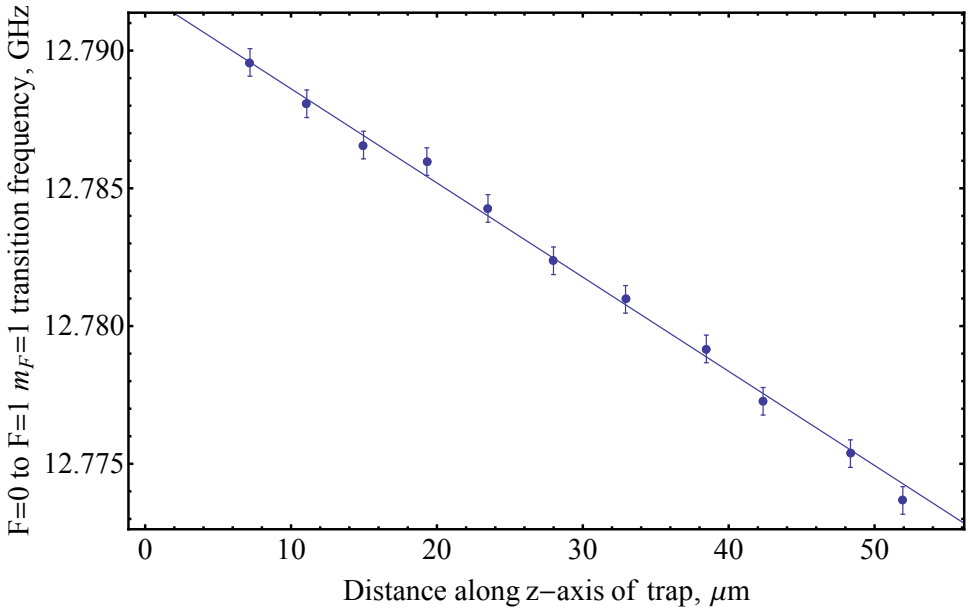

Figure 7.7: Change in the resonant frequency of the $^2\mathrm{S}_{\frac{1}{2}}$ $\mathrm{F}=0$ to $\mathrm{F}=1$ $\mathrm{m}_F=1$ transition vs axial distance along the trap. The solid line is a fit to the data and gives a field gradient of $24.4\,\mathrm{Tm}^{-1}$.

7.2 Individual addressing

A high magnetic field gradient allows separate ions within an ion chain to be individually addressed using microwaves by simply tuning the frequency of the microwave pulse to be resonant with one of the magnetic field sensitive transitions of a particular ion. As an example, figure 7.8 shows a frequency sweep, performed by adjusting the frequency of a microwave π pulse on the $^2\mathrm{S}_{\frac{1}{2}}$ $\mathrm{F}=0$ to $\mathrm{F}=1$ $\mathrm{m}_F=-1$ transition when two ions are present within the trap. The two peaks correspond to the resonant frequency of the transition for each ion. With a measured axial secular frequency equal to $2\pi \times 268\,\mathrm{kHz}$, these are separated by 2.8 MHz which is consistent with the magnetic field gradient measured in the previous section.

The probability that an adjacent ion to the one being addressed will become excited is given by the addressing error, P_{ia}. This is equal to the square of the amplitude of detuned

[7]The magnets were slightly too big and had to be filed down by a few hundred microns in order to fit in position next to the trap.

Rabi oscillations, $\frac{\Omega}{\sqrt{\Delta^2+\Omega^2}}$, derived in appendix C and is therefore given by

$$P_{ia} = \frac{\Omega^2}{(\Delta\omega)^2 + \Omega^2} \tag{7.2}$$

where $\Delta\omega$ is the difference in the resonant frequency of the two ions. For the data shown within figure 7.7, this equals 0.024 %. By comparison, the lowest addressing error achievable by the use of focused laser beams is only 2.5 % [89] which is two orders of magnitude larger. The use of a magnetic field gradient is therefore a very accurate method of individually addressing ions.

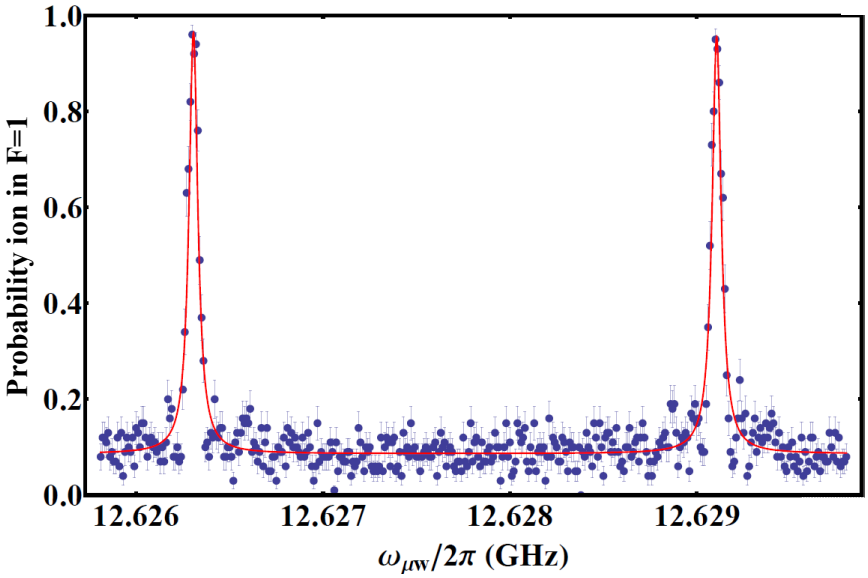

Figure 7.8: Frequency sweep over $^2S_{\frac{1}{2}}$ F = 0 to F = 1 $m_F = -1$ transition with two adjacent ions in a magnetic field gradient of 24.4 Tm^{-1}. Two peaks are present, each of which represent the transition frequency of a single ion. The difference in frequency of this transition for the two ions allows for individual addressing. The ions' axial secular frequency was measured to equal $2\pi \times 268$ kHz. Each point is an average of 200 measurements.

7.3 Coupling to the motional states of a single ion using microwaves

Within a magnetic field gradient, the effective Lamb-Dicke parameter allows microwaves to couple the internal states with the motional levels of the magnetic field sensitive states.

Subsection 7.3.1 will demonstrate this coupling by showing the resolved motional sidebands of a single ion. The size of the sidebands give an indication of the ions temperature

which determines whether the ion is within the required Lamb-Dicke regime. This is further explored in subsection 7.3.2. Subsection 7.3.3 will then show the motional sidebands of two ions.

By applying two microwave fields near resonant with the sideband frequencies of a single ion, a σ_ϕ force is felt by the ion whose motional states resultantly traverse in phase space as described in section 5.3. This is shown experimentally in subsection 7.3.4. To reduce decoherence due to magnetic field fluctuations, the dressed state qubit can be used as described in chapter 6. Subsection 7.3.5 shows the resolved motional sidebands of the microwave dressed state qubit thereby confirming that the magnetic field gradient and therefore the effective Lamb-Dicke parameter is felt by the dressed state qubit.

7.3.1 Motional sidebands

The magnetic field gradient of $24.4\,\mathrm{Tm}^{-1}$ combined with a typical secular frequency, v, of $2\pi \times 267\,\mathrm{kHz}$, gives an effective Lamb-Dicke parameter, η_{eff}, equal to 0.009. This is large enough to allow sufficient coupling of the microwave field to the motional states of the ion on the magnetic field sensitive transitions (see section 5.3.6).

A frequency scan over the $|0\rangle$ to $|\pm 1\rangle$ state transitions therefore shows peaks either side of the resonant frequencies, $\omega_\pm$, separated by the secular frequency, v. For example, a frequency scan over the $|0\rangle$ to $|+1\rangle$ transition is shown in figure 7.9. This was performed by adjusting the frequency of a microwave pulse with a length corresponding to a π pulse on one of the sideband transitions.

These peaks are known as motional sidebands and correspond to transitions between the motional states of the ion as shown in figure 7.10. As discussed in chapter 5, the motional sideband peaks below and above the resonant frequency are known as red and blue sidebands respectively. Applying a microwave field at a frequency resonant with the first red sideband will result in a loss of a motional quanta and applying a microwave field at a frequency resonant with the first blue sideband will result in a gain of a motional quanta.

The relative height of the sidebands can be used to find the average motional state, $\bar{n}$, of the ion. The ratio of the probability of excitation by applying the first red sideband, P_r to the probability of excitation by applying the first blue sideband, P_b is is related to $\bar{n}$ by [2]

$$\frac{P_r}{P_b} = \frac{\bar{n}}{\bar{n}+1}. \tag{7.3}$$

The ratio of the sideband heights in figure 7.9 is difficult to determine. While the first red

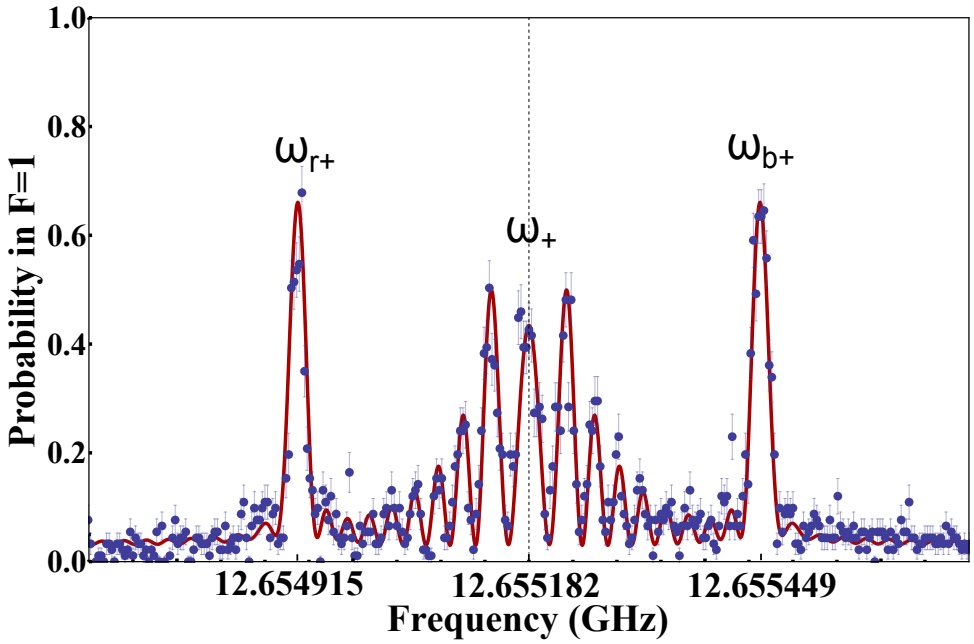

Figure 7.9: Frequency sweep over the $|0\rangle$ to $|+1\rangle$ transition showing the resolved motional sidebands. The peaks correspond to the transitions shown in figure 7.10. The peaks are separated in frequency from the carrier by the secular frequency, $\upsilon \approx 2\pi \times 267\,\text{kHz}$. The Rabi frequency of the carrier and sidebands were found to equal $2\pi \times 50\,\text{kHz}$ and $2\pi \times 8\,\text{kHz}$ respectively. The apparent oscillation on the carrier is due to the carrier having a different Rabi frequency than the sideband, the oscillation peaks correspond to detuned carrier frequencies where $62\,\mu\text{s}$ equals $\frac{n+1}{2\sqrt{\Delta^2+\Omega^2}}$ where n is an integer (see appendix C). Each point is an average of 200 measurements.

sideband height does appear to be slightly smaller than the first blue sideband height, the ratio is very close to one and the difference in height of the sidebands is within the error bars. This suggests the average motional state of the ion is very high. Another method of estimating the ions motional quantum number is to compare the Rabi frequency of either the red, Ω_r, or the blue, Ω_b, sideband to the carrier Rabi frequency, Ω_0. Ω_r and Ω_b are given by[8] [70]

$$\Omega_r = \eta e^{\frac{-eta^2}{2}} \left(\frac{(n-1)!}{n!}\right)^{\frac{1}{2}} L^1_{n-1}(\eta^2)\Omega_0 \tag{7.4}$$

and

$$\Omega_b = \eta e^{\frac{-eta^2}{2}} \left(\frac{n!}{(n+1)!}\right)^{\frac{1}{2}} L^1_{n}(\eta^2)\Omega_0 \tag{7.5}$$

respectively where $L^b_a(c)$ is the generalised Laguerre polynomial given by [38]

$$L^b_a(c) = \sum_m^\infty = 0(-1)^m \begin{pmatrix} a+b \\ b-m \end{pmatrix} \frac{c^m}{m!}. \tag{7.6}$$

[8]For a full derivation of this equation please refer to [70]

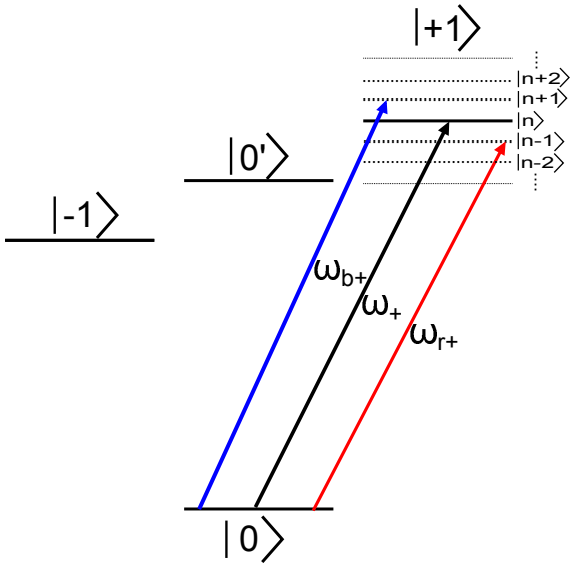

Figure 7.10: Motional sidebands on the $|0\rangle$ to $|+1\rangle$ transition. ω_{b+} represents a transition with the addition of a motional quanta, known as the first blue sideband and ω_{r+} represents a transition minus a motional quanta, known as the first red sideband.

At low $\bar{n}$, equations 7.4 and 7.5 are often approximated as [70]

$$\Omega_r = \eta\sqrt{\bar{n}}\Omega_0 \tag{7.7}$$

and

$$\Omega_b = \eta\sqrt{\bar{n}+1}\Omega_0. \tag{7.8}$$

Figure 7.11 shows the solution to equations 7.4 (blue) and 7.7 (red) for $\bar{n}$ between 0 and 10000 for our $\eta = \eta_{eff} = 0.009$. The graph shows that in our case the approximation given equation 7.7 only holds below $\bar{n} \approx 1000$. Using figure 7.11, the ratio of Ω_r to Ω_0 can be used to find $\bar{n}$.

As $\bar{n}$ increases, the ratio of Ω_r to Ω_0 will approach just under 0.6. As a result the π time of all three transitions will be similar and all three peaks can be observed in one scan. To illustrate this, figure 7.12 shows a frequency scan over the motional sidebands on the $|0\rangle$ to $|+1\rangle$ transition when a large amount of noise was present on the DC trap electrodes which increased the ions temperature to $\bar{n} \approx 10000$.

The Rabi frequency of the carrier and the sidebands from figure 7.10 was found to equal $2\pi \times 50\,\text{kHz}$ and $8\pi \times 50\,\text{kHz}$ respectively. Using figure 7.11 this gives $\bar{n} \approx 310$.

To produce a high fidelity entanglement gate within the magnetic field gradient entanglement scheme, the ion must be within the Lamb-Dicke regime. The Lamb-Dicke regime is defined as $\eta_{eff}^2(2\bar{n}+1) << 1$ (see section 5.2). With an $\bar{n} \approx 310$ and an $\eta_{eff} = 0.009$,

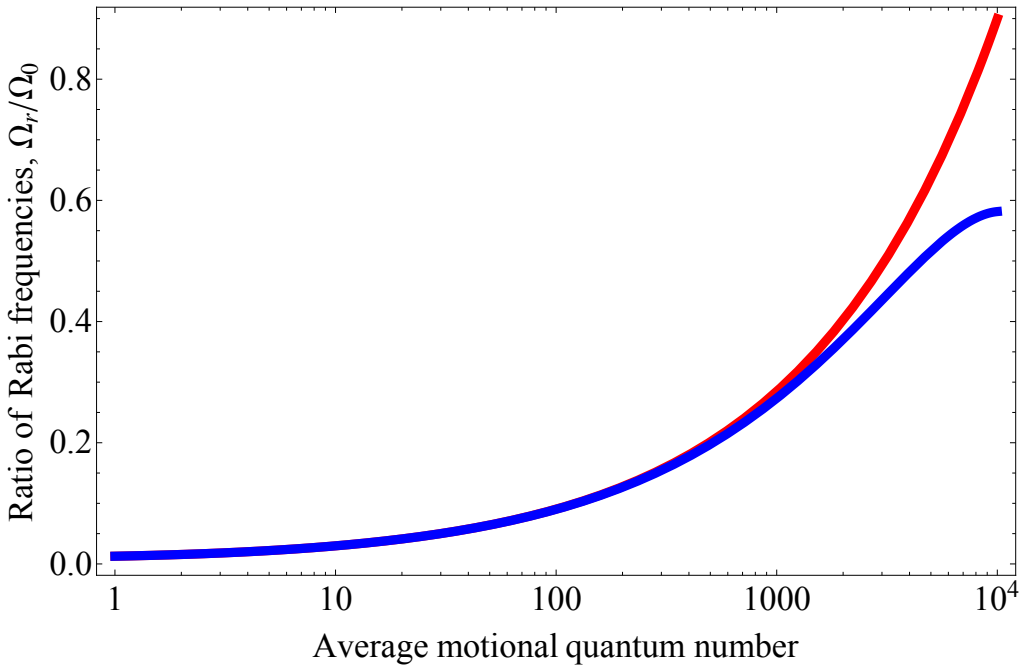

Figure 7.11: Graph showing how the ratio of the red sideband Rabi frequency to the carrier Rabi frequency changes with ion temperature. The blue curve shows the exact solution of equation 7.4 while the red curve shows the approximation given by equation 7.7 for low $\bar{n}$. Both curved were calculated using a $\eta_{eff} = 0.009$.

$\eta_{eff}^2(2\bar{n}+1) = 0.05$. While 0.05 is less than one, it is debatable as to whether it is 'a lot less' than 1. The following subsection will show how being outside the Lamb-Dicke regime effects the fidelity of a quantum gate and will explore how high $\bar{n}$ can be while still producing a gate of high fidelity.

7.3.2 Infidelity outside of the Lamb-Dicke regime

The fidelity of the production of the entangled $\frac{1}{\sqrt{2}}(|00\rangle - i\,|11\rangle)$ state using the Mølmer and Sørenson entanglement scheme[9] is given by [63]

$$F = \frac{1}{2}\left(1 + \sum_{n=0}^{\infty} P_n \sin(\tilde{\Omega}_n t)\right) \tag{7.9}$$

where P_n is the initial probability of state n being occupied, t is time the state dependent force has been applied and $\tilde{\Omega}_n$ is the Rabi frequency of the $|00\rangle$ to $|11\rangle$ transition given by [63]

$$\tilde{\Omega}_n = \tilde{\Omega}\left(1 - \eta^2(2n+1) + \eta^4(\frac{5}{4}n^2 + \frac{5}{4}n + \frac{1}{2} + ...\right) \tag{7.10}$$

[9] While, as discussed in chapter 5, the Mølmer and Sørensen gate is only a special case of the a geometric phase gate we will be using, the effect of high $\bar{n}$ is the same.

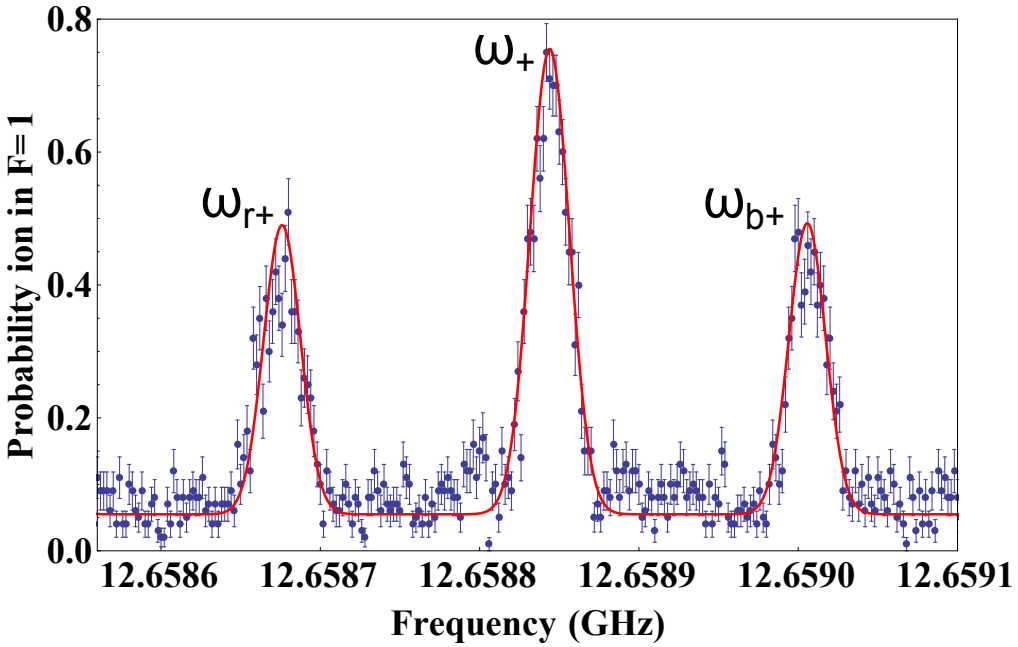

Figure 7.12: Frequency sweep over the $|0\rangle$ to $|+1\rangle$ transition showing the resolved motional sidebands for an ion with an $\bar{n} \approx 10000$. The peaks correspond to the transitions shown in figure 7.10. The secular frequency $v \approx 2\pi \times 168\,\text{kHz}$. Each point is an average of 200 measurements.

where $\tilde{\Omega}$ is given by equation 5.11. Within the Lamb-Dicke regime, $\tilde{\Omega}_n \approx \tilde{\Omega}$ resulting in $F = 1$. As $\bar{n}$ increases, The range of Ω_n begins to spread out. The time taken to reach maximum fidelity therefore become significantly different for all the different modes occupied. As a result, the ion becomes entangled with n and the fidelity decreases [63]. To investigate this effect further, it will first be assumed that the ion is within thermal equilibrium and can therefore P_n be given by a Boltzmann distribution

$$P_n = Ae^{-\frac{n}{\bar{n}}} \tag{7.11}$$

where A is a constant which can be determined by equating the total probability over all n to one

$$\sum_{n=0}^{\infty} Ae^{-\frac{n}{\bar{n}}} = \frac{A}{1 - e^{-\frac{1}{\bar{n}}}} = 1 \tag{7.12}$$

giving $A = 1 - e^{-\frac{1}{\bar{n}}}$.

Using equations 7.9, 7.10 and 7.11, the minimum infidelity of an entanglement gate is shown in figure 7.13 for an $\bar{n}$ between 10 and 10000 using $\eta = 0.009$.

Using figure 7.13, an $\bar{n} \approx 310$ will therefore result in a maximum gate fidelity of approximately 99.9 %. This is very high and therefore the ion, when the data in figure 7.9 was taken, is within the Lamb-Dicke regime. In contrast, when the data in figure 7.12

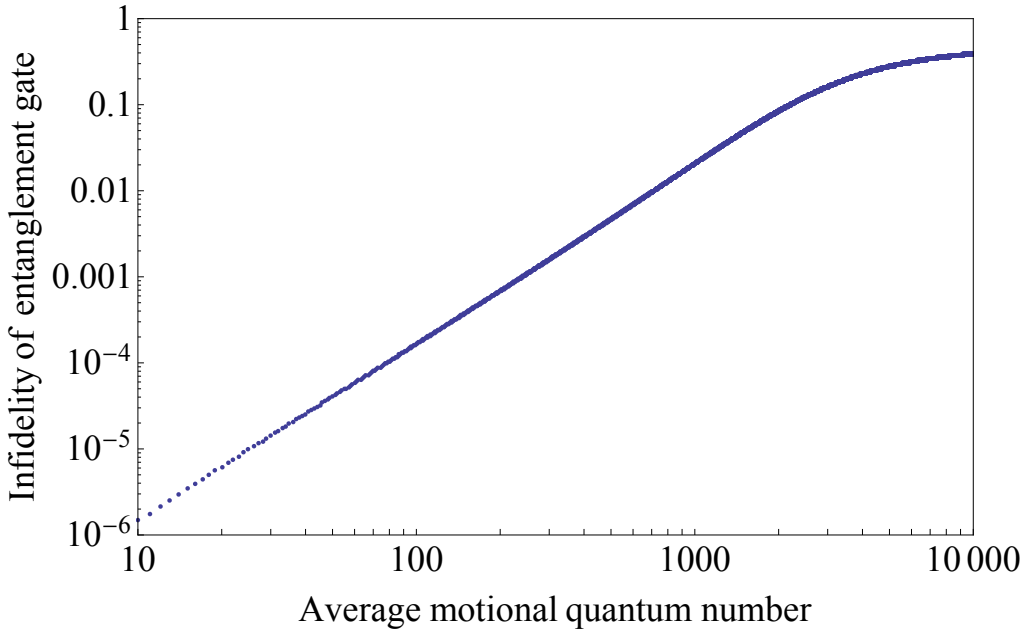

Figure 7.13: Infidelity of the production of the entangled $\frac{1}{\sqrt{2}}(|00\rangle - i\,|11\rangle)$ state vs the average motional state, $\bar{n}$, of the ion. This curve was simulated using equations 7.9, 7.10 and 7.11 with an $\eta = 0.009$. The curve is broken at low $\bar{n}$ due to the limited step size of the simulation.

was taken with a $\bar{n} \approx 10000$, the maximum fidelity would only have been approximately 60 %. The following subsection will discuss how $\bar{n}$ can be reduced in the future to allow for higher fidelities.

Methods of reducing $\bar{n}$

The only method of laser cooling used within this thesis is Doppler cooling. Using Doppler cooling, the lowest possible ion temperature, T_D, reachable is attained when [107]

$$\frac{\Delta}{\Gamma} = -\frac{1}{2} \tag{7.13}$$

where Δ is the detuning of the 369 nm cooling laser from resonance and $\Gamma = 2\pi \times 19.6\,\text{MHz}$ is the linewidth of the $^2\text{S}_{\frac{1}{2}}$ to $^2\text{P}_{\frac{1}{2}}$ transition. T_D is given by [107]

$$T_D = \frac{\hbar\Gamma}{2k_B} \tag{7.14}$$

where k_B is the Boltzmann constant. Using the expression for the average energy of the ion,

$$\bar{E} = k_B T = \bar{n}\hbar v, \tag{7.15}$$

this corresponds to an average motional state of approximately $\bar{n} = 37$ for a secular frequency equal to $2\pi \times 267\,\text{kHz}$. To reach this $\bar{n}$ requires perfect cooling. To achieve this within our experiment effects such as power fluctuations and micromotion need to be minimised.

Once the Doppler limit has been reached, to reduce $\bar{n}$ further, the ion could also be sideband cooled[10].

A different method of reducing $\eta^2(2n+1)$ and thereby move further into the Lamb-Dicke regime is to increase the secular frequency. This would have the dual effect of reducing both η_{eff} and $\bar{n}$ as $\eta_{eff} \propto \frac{1}{v^{\frac{3}{2}}}$ and $\bar{n} \propto \frac{1}{v}$ giving $\eta_{eff}^2(2\bar{n}+1) \propto \frac{1}{v^4}$.

7.3.3 Motional sidebands of two ions

As discussed in section 5.3.3, there are two axial modes present for two ions known as the centre of mass and stretch modes. Figure 7.14 shows a frequency sweep over the $|0\rangle$ to $|-1\rangle$ transition with two ions present in the trap. Four different sideband peaks are present which correspond to the red and blue sidebands of the stretch and centre of mass modes. As expected, the centre of mass mode sidebands are separated in frequency from the carrier peak by a secular frequency, in this case $\omega_{-,C} = \omega_- \pm 2\pi \times 263\,\text{kHz}$, and the stretch mode sidebands are separated by $\sqrt{3}$ times the secular frequency, in this case $\omega_{-,C} = \pm\sqrt{3}\omega_{-,C} = \omega_- \pm 2\pi \times 455\,\text{kHz}$.

7.3.4 Generation of a σ_ϕ state dependent force

As described in section 5.3, the application of two radiation fields with frequencies slightly detuned from the red and blue motional sidebands of a transition, ($\omega_{b+} = \omega_+ + v - \delta$ and $\omega_{r+} = \omega_+ - v + \delta$ or $\omega_{b-} = \omega_- + v - \delta$ and $\omega_{r-} = \omega_- - v + \delta$ where δ is the detuning from the secular frequency, v), to a trapped ion will result in a state dependent force in the σ_ϕ basis where $\phi = \frac{\pi}{2}$, that is, where an ion in the state $|\phi_0\rangle = \frac{1}{\sqrt{2}}(|0\rangle + i\,|1\rangle)$ experiences a different force to an ion in the state $|\phi_1\rangle = \frac{1}{\sqrt{2}}(|0\rangle - i\,|1\rangle)$.

The Hamiltonian of an ion under these fields is given by (see chapter 5)

$$\hat{H}_I = \frac{\hbar\eta_{eff}\Omega}{2}(\hat{a}^\dagger e^{i(-v+\delta)} + \hat{a}e^{i(v-\delta)})\left(|\phi_0\rangle\langle\phi_0| - |\phi_1\rangle\langle\phi_1|\right) \tag{7.16}$$

which, assuming the ion is initially in the motional ground state, results in the following

[10] For details on sideband cooling, please refer to the thesis by James McLoughlin [37]

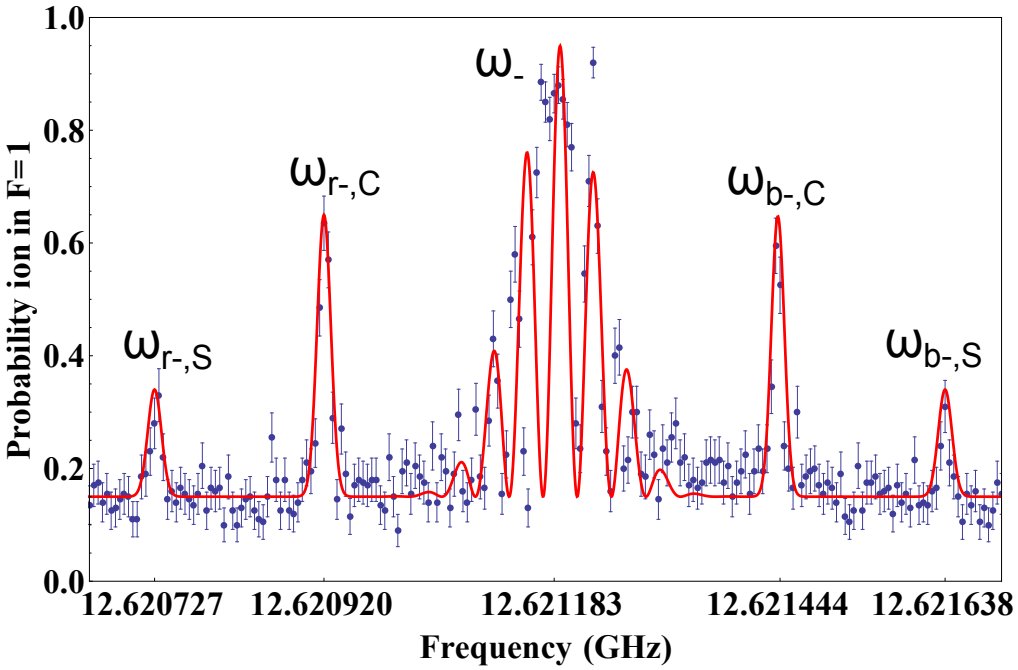

Figure 7.14: Frequency sweep over the $|0\rangle$ to $|-1\rangle$ transition showing the resolved motional sidebands of the centre of mass and stretch modes. The centre of mass mode and stretch mode peaks are separated in frequency from the carrier by v and $\sqrt{3}v$ respectively where $v \approx 2\pi \times 263\,\text{kHz}$. The Rabi frequency of the carrier and sidebands were found to equal $2\pi \times 50\,\text{kHz}$ and $2\pi \times 8\,\text{kHz}$ respectively. Each point is an average of 200 measurements.

evolution of the $|\phi_0\rangle$ and $|\phi_1\rangle$ states

$$|\phi_0(t)\rangle = D(\alpha(t))e^{i\Phi(t)}|\phi_0\rangle \tag{7.17}$$

$$= e^{i\Phi(t)}|\alpha(t)\rangle|\phi_0\rangle\,, \tag{7.18}$$

$$|\phi_1(t)\rangle = D(-\alpha(t))e^{i\Phi(t)}|\phi_1\rangle \tag{7.19}$$

$$= e^{i\Phi(t)}|-\alpha(t)\rangle|\phi_1\rangle \tag{7.20}$$

where $|\alpha(t)\rangle$ is a coherent motional state defined in appendix D as

$$|\alpha(t)\rangle = e^{\frac{-|\alpha(t)|^2}{2}}\sum_{n=0}^{\infty}\frac{\alpha(t)^n}{\sqrt{n!}}|n\rangle \tag{7.21}$$

where $\alpha(t)$ is given by

$$\alpha(t) = \frac{Fx_0}{\hbar\delta}(1 - e^{i\delta t}) \tag{7.22}$$

where $x_0 = \sqrt{\frac{\hbar}{2mv}}$, m is the ions mass and the state dependent force $\text{F} = \sqrt{2}\eta_{eff}\hbar\Omega$.

An ion in the $|0\rangle$ state is in a superposition of $|\phi_0\rangle$ and $|\phi_1\rangle$,

$$|0\rangle = \frac{|\phi_0\rangle + |\phi_1\rangle}{\sqrt{2}} \tag{7.23}$$

and will therefore evolve when acted on by the Hamiltonian given in equation 7.16 as

$$|0\rangle \rightarrow \frac{1}{\sqrt{2}}\left(e^{i\Phi(t)}\,|\alpha(t)\rangle\,|\phi_0\rangle + e^{i\Phi(t)}\,|-\alpha(t)\rangle\,|\phi_1\rangle\right) \tag{7.24}$$

$$= e^{i\Phi(t)}\left(|\alpha(t)\rangle + |-\alpha(t)\rangle\right)|0\rangle + ie^{i\Phi(t)}\left(|\alpha(t)\rangle - |-\alpha(t)\rangle\right)|1\rangle\,. \tag{7.25}$$

The probability of finding the ion in the $|1\rangle$ state at time, t, after a force in the $\sigma_{\frac{\pi}{2}}$ direction is applied to an ion initially in the $|0\rangle$ state is therefore given by

$$P(|1\rangle) = \left|ie^{i\Phi(t)}\left(|\alpha(t)\rangle - |-\alpha(t)\rangle\right)\right|^2. \tag{7.26}$$

This can be simplified using the coherent state identity $\langle\alpha|\beta\rangle = e^{-\frac{|\alpha|^2}{2}}e^{-\frac{|\beta|^2}{2}}e^{\alpha^*\beta}$ [108] to give

$$P(|1\rangle) = \frac{1}{2}\left(1 - e^{-2|\alpha(t)|^2}\right). \tag{7.27}$$

This probability will equal zero when

$$t_c = n_r\frac{2\pi}{\delta} \tag{7.28}$$

where n_r is an integer corresponding to the number of rotations made by the motional states in phase space. As discussed in chapter 5, when a state dependent force is applied to the ion, the motional states of two orthogonal states, in this case $|\phi_0\rangle$ and $|\phi_1\rangle$ will follow opposite circular trajectories in phase space. After a time t_c, the motional states have returned to their initial phase space positions and the ion will return to its initial state, $|0\rangle$, with the addition of a phase, Φ_T, given by equation 5.35. The probability of being in $|1\rangle$ at these times is therefore equal to zero.

The derivation of the equation 7.27 did not take into account the effects of temperature or heating on the ions evolution. These are explored in [70] and result in the following modified version of equation 7.27,

$$P(|1\rangle) = \frac{1}{2}\left(1 - e^{-\frac{1}{2}\dot{n}t\left(\frac{2F}{\hbar\delta}\right)^2 - \left(\overline{n}+\frac{1}{2}\right)|2\alpha(t)|^2}\right) \tag{7.29}$$

where $\overline{n}$ is the ions average motional state and $\dot{n}$ is the heating rate of the ion.

Figure 7.15 shows the experimental probability of an ion initially in the $|0\rangle$ state being in the $|1\rangle$ state after two microwave fields have been incident on the ion for a fixed time,

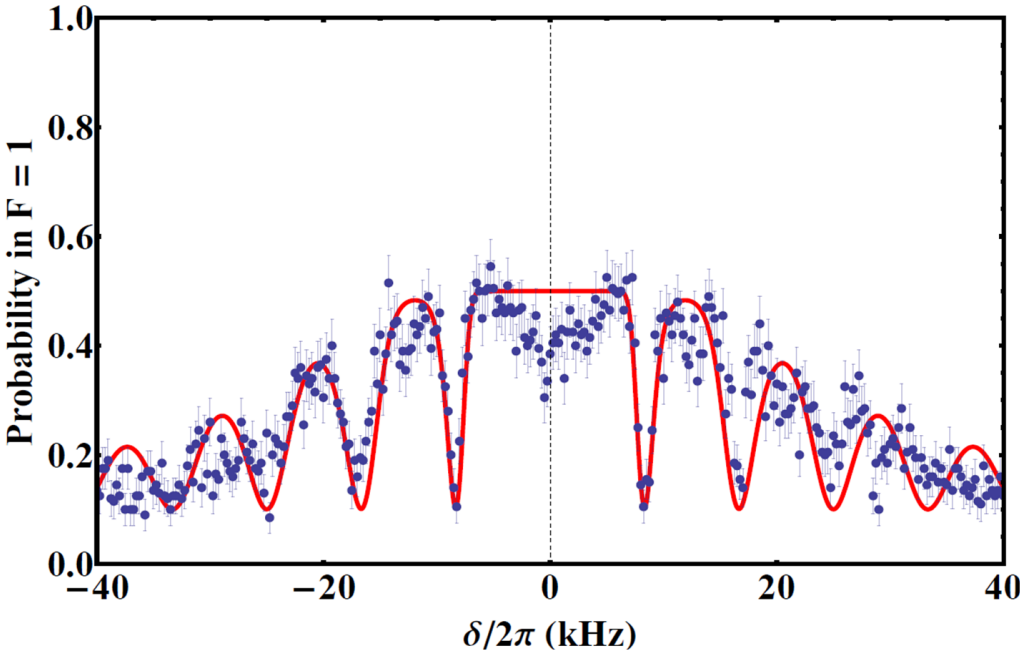

Figure 7.15: Probability of an ion initially in the $|0\rangle$ state being in the $|1\rangle$ state after two microwave fields resonant with the first red and blue sidebands of the $|0\rangle$ to $|+1\rangle$ transition plus/minus a detuning, δ, are applied simultaneously for a time, $t_c = 180\mu s$. The carrier Rabi frequency was measured to be $2\pi \times 41$ kHz and the secular frequency was measured to equal $2\pi \times 267$ kHz giving a $\eta_{eff} = 0.009$. Each point is an average of 200 measurements. A fit to equation 7.29 is also shown with $\overline{n} = 400$ and $\dot{n} = 10000$ quanta per second.

$t_c = 180\mu s$. The frequencies of these two fields are resonant with the red and blue motional sidebands of the ion with the respective addition and subtraction of a variable detuning, δ. The pulse sequence is given in figure 7.16.

As expected, periodic dips are present in the probability. The ions motional states are therefore moving in phase space which confirms the presence of a state dependent force.

The fit to equation 7.29 of the data in figure 7.15 gives $\bar{n} = 400$ and $\dot{n} = 10000$. While these are both very high, it should be noted that they are overestimates for two main reasons. Firstly, due to the short pulse time, the effect of heating on the ion will be minimal, therefore the error on the fit is quite high, while $\dot{n} = 10000$ was the best fit to the data, it was found that any fit with an $\dot{n}$ between 0 and 10000 would fit within the error bars of the data. Secondly, equation 7.29 did not take into account other sources of decoherence which can effect the ion in a similar way to a high $\bar{n}$ and $\dot{n}$. Due to the use of a magnetic field sensitive state, magnetic field fluctuations will be the main source of decoherence and result in a decoherence time of less than 500 μs (see chapter 3). This is less than three times the time the state dependent force is applied for in figure 7.15 and therefore decoherence effects will be expected. Nevertheless, the $\bar{n}$ and $\dot{n}$ should be

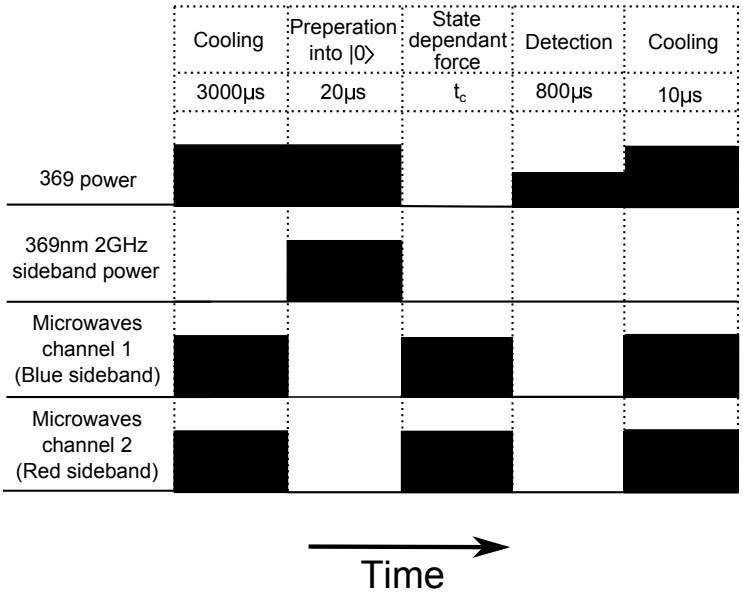

Figure 7.16: The pulse sequence used to produce a σ_ϕ state dependent force. The results of the application of this pulse sequence are given in figure 7.15

minimised to achieve the maximum possible gate fidelity[11].

As discussed in section 7.3.1, to first reduce $\bar{n}$ to the Doppler limit, experimental effects such as micromotion and power fluctuations need to be minimised. The Doppler limit at a secular frequency of $2\pi \times 267\,\text{kHz}$ equals 37. To reduce $\bar{n}$ further, the ion can be sideband cooled.

A high heating rate, $\dot{n}$ is caused by a large amount of unwanted electric field noise coupling to the ions motional modes [109]. This noise could be a result of, for example, electrical noise on the trap electrodes [109]. The effect of this noise can be reduced by using the stretch mode of two ions [110]. When the stretch mode is excited, the ions move out of phase with each other. As a result, the excitation of this mode by uniform electric fields which can excite and therefore cause heating in the centre of mass and single ion modes, is significantly reduced. While the mode is still susceptible to differential electric fields as well as heating of the radial modes, the heating rate of the stretch mode can be up to two orders of magnitude less than the centre of mass mode [110].

As shown in figure 7.15, a dip in probability is present at $\delta = 0$. This dip is repeatable and not predicted by the theory. Investigations into this have included potential power and detuning differences between the two microwave fields, magnetic field noise and micromotion. All investigations have however thus far remained inconclusive and this remains an area for further study.

[11] A detailed discussion of the infidelities within a σ_ϕ phase gate caused by being outside the Lamb-Dicke regime as well as having a high heating rate is given in [63]

7.3.5 Motional coupling within the dressed states

As discussed in chapter 6, to reduce decoherence due to magnetic field fluctuations, dressed state qubits can be used. Figure 7.17 shows a frequency sweep of the RF over the $|0'\rangle$ to $|D\rangle$ transitions of the dressed state qubit. This is analogous to the experiment shown in figure 6.15 however now a magnetic field gradient is present which allows the motional sidebands to be seen. Six peaks are observed which correspond to the six different motional transitions as shown in figure 7.18. This confirms that while insensitive to magnetic field fluctuations, the effective Lamb-Dicke parameter from the magnetic field gradient is still present for the dressed state qubit.

Similarly to the non dressed qubit, the red and blue sidebands in figure 7.17 are all of a similar height which suggests a high $\bar{n}$. The sideband widths are however smaller for the dressed state qubit in relation to the bare state qubit. This is due to the smaller Rabi frequency.

To produce a σ_ϕ state dependent force on the dressed state qubit, RF frequencies resonant with either ω_{r1} and ω_{b1} or ω_{r2} and ω_{b2} as labeled in figure 7.18 would be applied simultaneously to the dressed ion. The motional states of the dressed qubit will then evolve in time as described by equation 7.29.

7.4 Future work: two ion entanglement

The following describes the additional experimental setup required to use the magnetic field gradient to produce a two ion entanglement gate which is insensitive to magnetic field fluctuations.

To produce a two ion gate on the dressed state qubit, firstly two ions need to be simultaneously prepared into the dressed state. RF frequencies near resonant with the stretch mode sidebands of the two dressed state qubits will then need to be applied to produce the required state dependent force on the two ions. Finally a method to detect the final state of the two ions is required.

Dressing two ions

Firstly the two ions need to be simultaneously prepared into the dressed state, $|D\rangle$, to shield them from decoherence caused by magnetic field fluctuations. Due to the Zeeman effect, the $|-1\rangle$ and $|+1\rangle$ states will be at different frequencies for each of the two ions therefore four dressing fields are required as shown in figure 7.19. Two STIRAP operations,

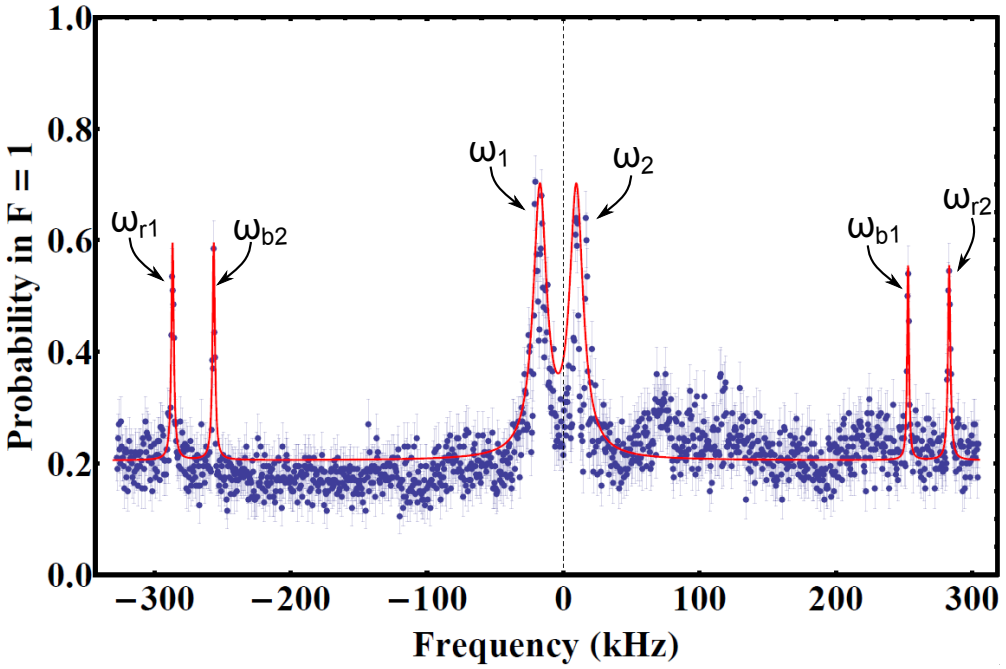

Figure 7.17: RF frequency sweep over the $|0'\rangle$ to $|D\rangle$ transitions while the dressing fields resonant with the $|0\rangle$ to $|\pm 1\rangle$ transitions are incident on the ion. Six peaks are present which correspond to the six first order motional transitions as shown in figure 7.18. The data was taken with a RF pulse time equal to $400\,\mu$s. The Rabi frequency of the carrier and sidebands was found to equal $2\pi \times 7\,$kHz and $2\pi \times 1\,$kHz respectively. Each point is an average of 200 measurements.

one for each qubit, will need to be performed simultaneously. This can be produced by simply replicating the setup present before the combiner in figure 6.4 to produce a second set of STIRAP pulses and adding these to the combiner.

Applying the two ion state dependent force

In order to apply a state dependent force simultaneously to the two dressed state qubits, RF frequencies resonant with the red and blue stretch mode motional sidebands of a $|0'\rangle$ to $|D\rangle$ transition of both ions need to be applied to the ion. An example set of these required frequencies are shown in figure 7.20. These will be produced separately by RF frequency supplies, combined, amplified and sent through a resonant LCR circuit similar to that described in section 6.3.3 and as before, the RF fields will be applied to the ion using the inductor coil. The circuit needs to be able to withstand high power and have a bandwidth wide enough to allow all four frequencies to be applied simultaneously.

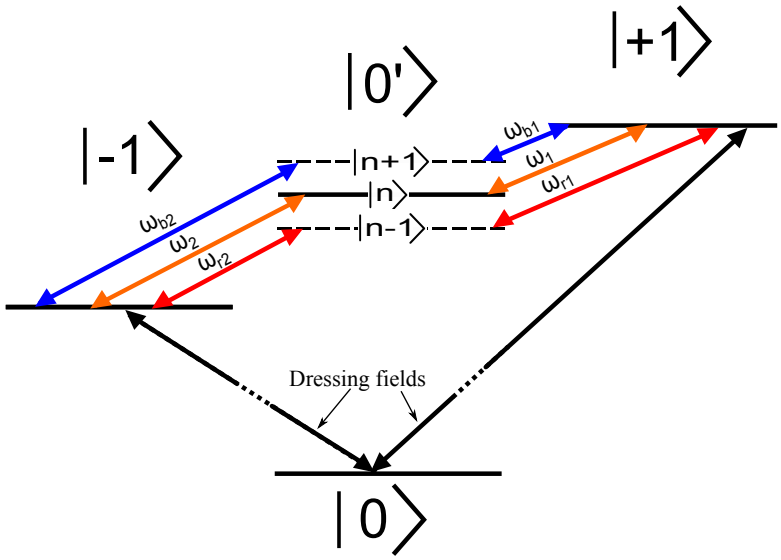

Figure 7.18: The origin of the six first order motional transitions on the $|0'\rangle$ to $|D\rangle$ qubit.

Two ion detection

During detection, the photons from both ions will be collected by the imaging optics and incident on the same PMT. The resultant detection histogram is shown in figure 7.21 for the four possible states. The $|01\rangle$ and $|10\rangle$ states both consist of one dark and one bright ion and therefore give the same photon distribution and cannot be distinguished. To determine the state of an ion, two discriminators are needed. The first discriminator, d_1 lies between the $|00\rangle$ and $|01\rangle/|10\rangle$ distributions and the second discriminator d_2 lies at the crossing point of the $|01\rangle/|10\rangle$ and $|11\rangle$ distributions. The number of photons collected during detection, n_p will therefore imply the ion is in the $|00\rangle$ state if $n_p \leq d_1$, the $|01\rangle/|10\rangle$ state if $d_1 < n_p \leq d_2$ or the $|11\rangle$ state if $n_p > d_2$.

Assuming background scatter is negligible, the optimum value of d_1 will always be equal to zero (see section 3.2). Figure 7.22 shows the detection fidelity[12] of two ion detection as a function of detection time when $d_1 = 0$ and d_2 equals 10 (orange), 30 (yellow), 50 (blue), 70 (green) and 90 (purple) for a 369 nm intensity equal to $0.1\,\mathrm{I}_{sat}$. This graph is simulated by comparing the detectable photon distributions given off by $|00\rangle$, $|01\rangle$ and $|11\rangle$ states during detection with d_1 and d_2. These photon distributions are found by combining the single ion photon distributions from equations 3.23 and 3.24 and using the rate equation program using the method described in section 3.2.

Figure 7.22 shows that, for a fixed d_2, as the detection time is increased, the fidelity will initially increase as the increasing number of photons emitted by the bright ions

[12]The probability that the ions state is correctly determined by comparing n_p, d_1 and d_2

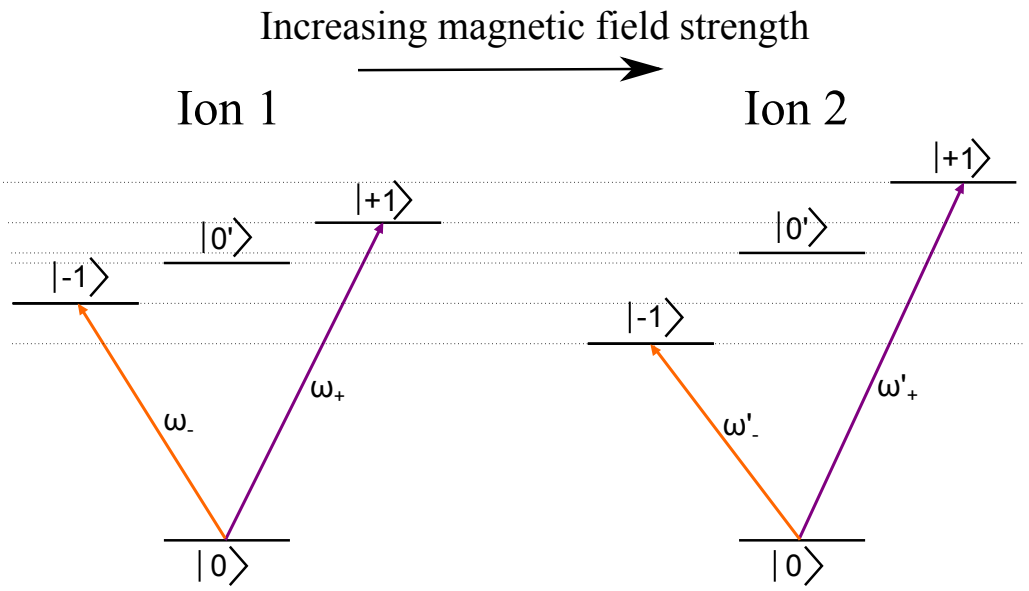

Figure 7.19: Frequencies required to prepare two adjacent ions into the $|D\rangle$ state.

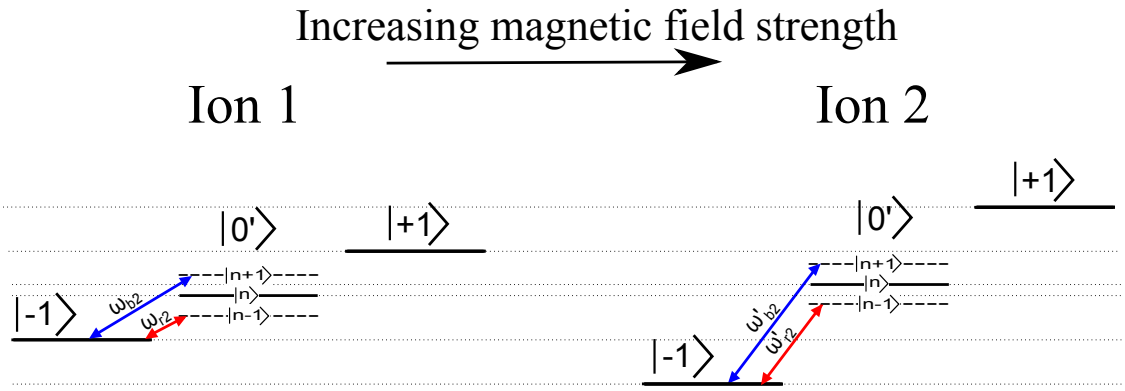

Figure 7.20: An example of the RF frequencies required to simultaneously apply a σ_ϕ force to two dressed state ion qubits.

separate out the photon distributions. When the detection time becomes such that the crossing point between the $|01\rangle$ / $|10\rangle$ and $|11\rangle$ distributions reaches d_2, the fidelity reaches its maximum value. The fidelity then decreases again as the $|01\rangle$ / $|10\rangle$ distribution begins to cross over d_2. The plateau in fidelity at around 66 % is present when both the $|01\rangle$ / $|10\rangle$ and $|11\rangle$ distributions lie above d_2. At high detection times, off resonant scattering results in a further decrease in fidelity. As shown in figure 7.22, an optimum d_2 and detection time exist which give the maximum fidelity. These optimum values depend on the 369 nm intensity. Figure 7.23 shows the optimum fidelity, detection time and d_2 value for 369 nm intensities equal to 10 (orange), 1 (green), 0.1 (black), 0.01 (blue) and 0.001 (red). Figure 7.23 shows that, as with single ion detection, to obtain the maximum fidelity, the 369 nm intensity needs to be as low as possible. This does however result in larger detection times

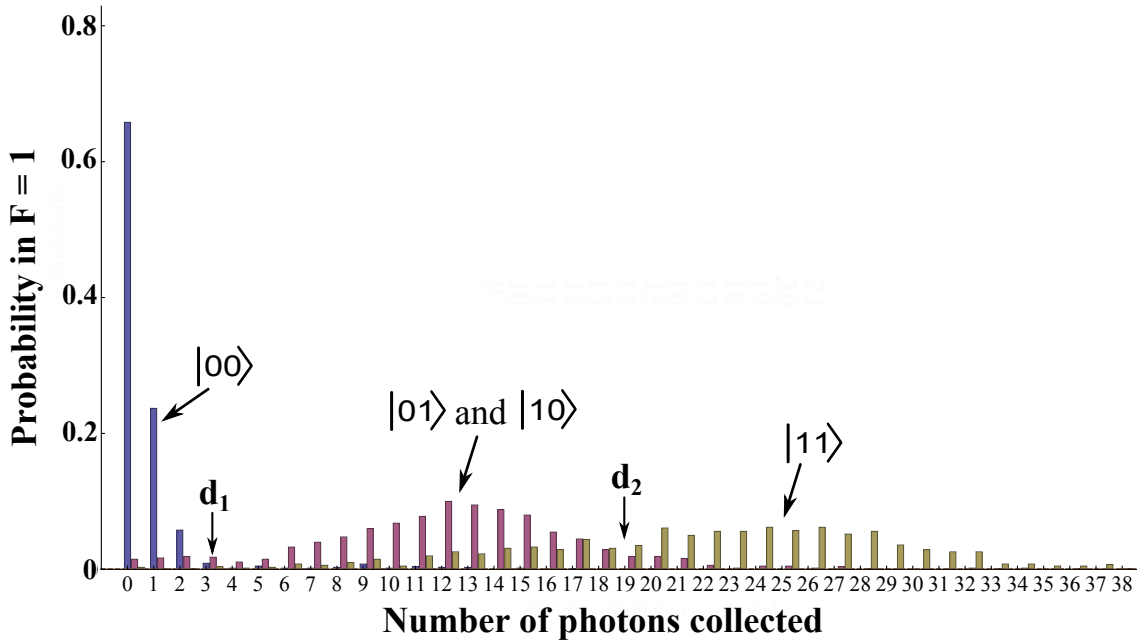

Figure 7.21: State detection histogram for two ions after the ion has been prepared in the $|00\rangle$, $|01\rangle$ and $|11\rangle$ states. The $|00\rangle$ state was prepared with 60μW of 369 nm light focused down to 60μm with 45 % of this light contained within the 2 GHz sidebands. The $|01\rangle$ and $|11\rangle$ states were prepared by applying microwave pulses on the magnetic field sensitive $|0\rangle$ to $|+1\rangle$ transition of the particular ions. During detection 1.2μW of 369 nm light was focused down to a beam waist of 60μW for 3 ms. The 935 nm beam intensity was equal to $500\,\mathrm{I}_{sat}$. The graph is an average of 1000 measurements.

being required.

As shown in figure 7.23, the maximum detection fidelity is only approximately 90 %. The relatively large infidelity compared with single ion detection is due to the significant overlap in the $|01\rangle/|10\rangle$ and $|11\rangle$ photon distributions. It should also be noted that in reality, the infidelity will be higher due to effects of background scatter such as the broadening of the $|00\rangle$ photon distribution as demonstrated within figure 7.21.

To counter this infidelity, normalisation techniques can be used such as the method outlined in [111].

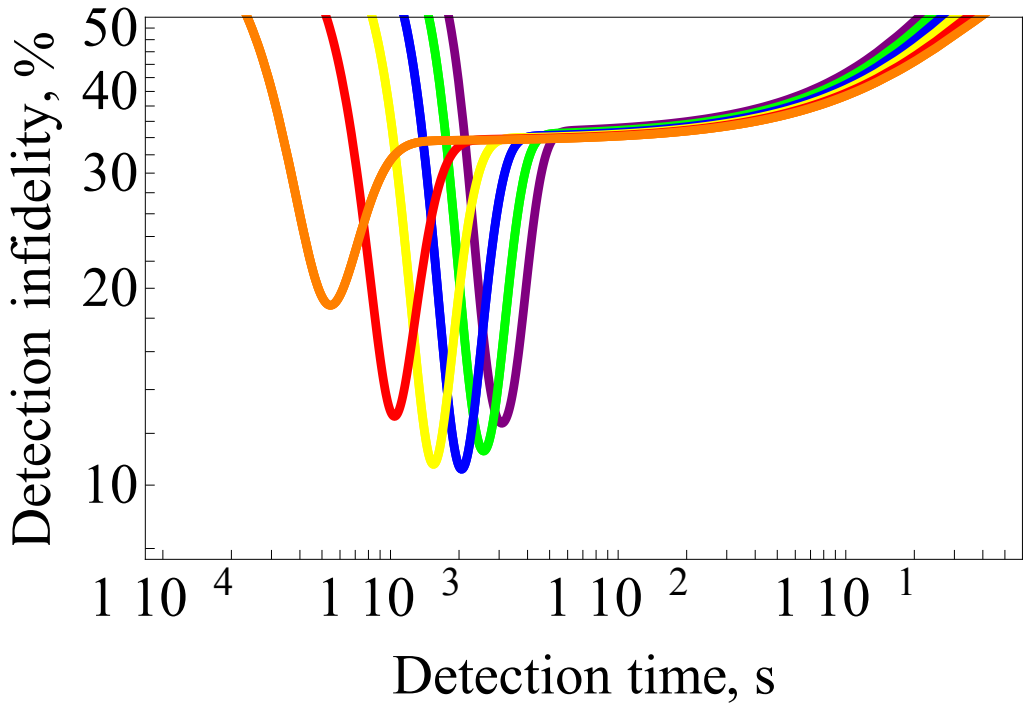

Figure 7.22: Graph showing the detection infidelity vs detection time of two ion detection with $d_1 = 0$ and $d_2 = 10$ (orange), 30 (yellow), 50 (blue), 70 (green) and 90 (purple). The 369 nm and 935 nm intensities were set to equal 0.1 I_{sat} and 10 I_{sat} respectively.

7.5 Summary

This chapter has showed the progress towards a high fidelity two ion entanglement gate using microwave and RF fields. Firstly a magnetic field gradient of 24.4 Tm^{-1} has been produced using in vacuum permanent magnets and used to individually address ions. The presence of this gradient creates an effective Lamb-Dicke parameter which allows the microwave fields to couple the internal and motional states of the ion. This has been used to produce a state dependent force on a single ion which is the key ingredient required for a geometric phase gate. The coupling of the internal states of a dressed state qubit to the ion's motional states is also performed using RF fields. This confirms that the effect of the magnetic field gradient is felt by the dressed qubit which allows the gate to be performed while being shielded from decoherence due to magnetic field fluctuations. Finally, the remaining experimental steps required to perform a two ion entanglement gate are summarised. Additions to the experimental setup will be required in order to address the additional frequencies associated with the second ion.

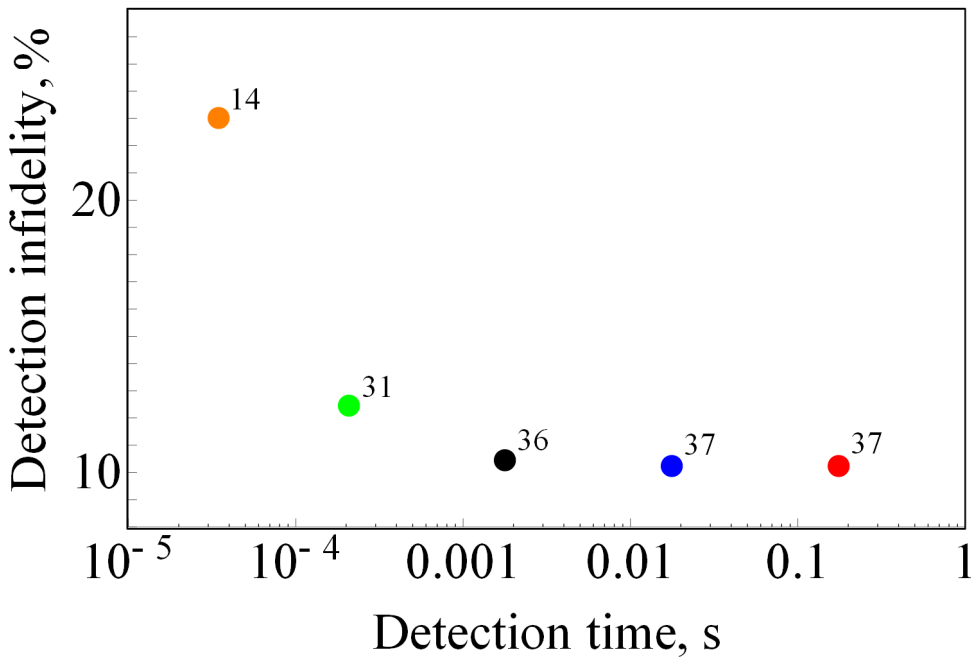

Figure 7.23: Graph showing the optimum detection infidelity and detection time for 369 intensities equal to 10 (orange), 1 (green), 0.1 (black), 0.01 (blue) and 0.001 (red). The numbers beside the points indicate the value of d_2 required to obtain these maximum values. The 935 nm intensity was set to equal 10 I_{sat}.

Chapter 8

Conclusion

In this thesis I have shown the progress towards the implementation of a two qubit entanglement gate using trapped ytterbium ions.

Firstly the experimental setup used to successfully trap ytterbium ions was introduced and described. This includes a macroscopic RF Paul trap which provides the trapping potential, an ultra high vacuum system to reduce decoherence due to particle collisions, lasers required for laser cooling and optical pumping and an imaging system to magnify, observe and measure the photon count rate from the ions.

Next I introduced the $^{171}Yb^{+}$ qubit as the hyperfine sublevels of the $^{2}S_{\frac{1}{2}}$ level and used rate equations to optimise the state preparation and detection. As a result of the Zeeman effect, the $F=1$ sublevel of the $^{2}S_{\frac{1}{2}}$ level is split and separate magnetic field sensitive and insensitive qubits were presented. Coherent manipulation on both these qubits was performed and the coherence time of the magnetic field insensitive qubit was found using a Ramsey method to be 1.5 seconds. The coherence time of the magnetic field sensitive qubit is however found to be several orders of magnitude smaller due to decoherence from magnetic field fluctuations.

I then investigated the effect of fluctuations in the frequency of the 369 nm laser during state preparation and detection and built a system to stabilise these fluctuations to the required level. This system begins by stabilising a 780 nm laser using saturated absorption spectroscopy of a rubidium vapor cell and then uses this to stabilise a Fabry-Perot cavity. The 739 nm laser, which is doubled to form the 369 nm laser, is then stabilised to this cavity using a dual resonance cavity lock. The users guide for the system is also presented.

I review the main experimental methods of two ion entanglement including the Cirac and Zoller gate [61], the geometric phase gate using lasers [27,62,63] or microwaves within a magnetic field gradient [34] and the ultrafast gate using a pulsed laser system [64]. A

comparison of the methods finds that a geometric phase gate using microwaves within a static magnetic field gradient is the most suitable way forward for our laboratory as it avoids the main sources of decoherence present in laser gates, namely spontaneous emission as well as intensity and frequency fluctuations. In addition, the use of microwaves allows for a higher degree of scalability compared with lasers. The magnetic field gradient creates an effective Lamb-Dicke parameter which allows microwave radiation to couple to the motional states of magnetic field sensitive qubit states. The use of magnetic field sensitive states does however leave the system susceptible to a high degree of decoherence due to magnetic field fluctuations.

To reduce this decoherence, I then present a method to shield the ion from magnetic field fluctuations using microwave dressed states. Dressing the ion with microwaves allows the use of a new qubit which suppresses magnetic field fluctuations while still allowing motional coupling using microwaves as a result of a magnetic field gradient. The preparation of this qubit is described and optimised and two methods of coherent manipulation of this new qubit using RF fields is presented. This includes a new method which allows for arbitrary rotations around the Bloch sphere.

I then go on to present the experimental progress towards a two ion entanglement gate within these microwave dressed states. Firstly in-vacuum permanent magnets were attached to the RF Paul trap. The magnetic field gradient given by these magnets was measured to equal $24\,\mathrm{Tm}^{-1}$ which is currently the highest recorded static magnetic field gradient at the position of a trapped ion. Individual addressing of ions using this gradient is then shown and the entanglement of a single ion's internal and motional states within the bare qubit states is demonstrated in the form of Schrodinger cat states.

Finally, the first ever observation of motional coupling of the microwave dressed state qubit is presented and the remaining steps required for two ion entanglement are discussed.

Bibliography

[1] S. Olmschenk. Quantum teleportation between distant matter qubits. *Ph.D. thesis, University of Michigan*, 2009.

[2] S. Webster. Raman sideband cooling and coherent manipulation of trapped ions. *Ph.D. thesis, University of Oxford*, 2005.

[3] W. C. Campbell, J. Mizrahi, Q. Quraishi, C. Senko, D. Hayes, D. Hucul, D. N. Matsukevich, P. Maunz, and C. Monroe. Ultrafast gates for single atomic qubits. *Phys. Rev. Lett.*, 105:090502, 2010.

[4] J. Mizrahi, B. Neyenhuis, K. Johnson, W. C. Campbell, C. Senko, D. Hayes, and C. Monroe. Quantum control of qubits and atomic motion using ultrafast laser pulses. *Applied Physics B*, 114(1):45–61, 2014.

[5] H. G. Dehmelt. Radiofrequency spectroscopy of stored ions. *Adv. At. Mol. Phys.*, 3:53, 1967.

[6] Wolfgang Paul. Electromagnetic traps for charged and neutral particles. *Rev. Mod. Phys.*, 62:531–540, Jul 1990.

[7] M. Chwalla, J. Benhelm, K. Kim, G. Kirchmair, T. Monz, M. Riebe, P. Schindler, A. S. Villar, W. Hänsel, C. F. Roos, R. Blatt, M. Abgrall, G. Santarelli, G. D. Rovera, and Ph. Laurent. Absolute frequency measurement of the $^{40}Ca^{+}4s^{2}S_{1/2}$-$3d^{2}D_{5/2}$ clock transition. *Phys. Rev. Lett.*, 102:023002, Jan 2009.

[8] S. A. Webster, P. Taylor, M. Roberts, G. P. Barwood, and P. Gill. Kilohertz-resolution spectroscopy of the $^{2}S_{1/2}-^{2}F_{7/2}$ electric octupole transition in a single $^{171}Yb^{+}$ ion. *Phys. Rev. A*, 65:052501, Apr 2002.

[9] Th. Udem, S. A. Diddams, K. R. Vogel, C. W. Oates, E. A. Curtis, W. D. Lee, W. M. Itano, R. E. Drullinger, J. C. Bergquist, and L. Hollberg. Absolute frequency

measurements of the Hg^+ and ca optical clock transitions with a femtosecond laser. *Phys. Rev. Lett.*, 86:4996–4999, May 2001.

[10] M. Keller, B. Lange, K. Hayasaka, W. Lange, and H. Walther. Deterministic cavity quantum electrodynamics with trapped ions. *J. Phys. B: At. Mol. Opt. Phys.*, 36:2099–2105, 2003.

[11] D.J Douglas, AJ Frank, and DM Mao. Linear ion traps in mass spectrometry. *Mass Spectrometry Reviews*, 24:1–29, 2005.

[12] R. P. Feynman. Simulating physics with computers. *International Journal of Theoretical Physics*, 21:467–488, 1982.

[13] D. Deutsch. Quantum theory, the church-turing principle and the universal quantum computer. *Proc. R. Soc. Lond. A*, 400:97–117, 1985.

[14] P. W. Shor. Algorithms for quantum computation: discrete logarithms and factoring. In *Proceedings of the 35th Annual Symposium on Foundations of Computer Science*, SFCS '94, pages 124–134. IEEE Computer Society, 1994.

[15] Lov K. Grover. A fast quantum mechanical algorithm for database search. In *STOC '96 Proceedings of the twenty-eighth annual ACM symposium on Theory of computing*, pages 212–219, 1996.

[16] David Deutsch and Richard Jozsa. Rapid solution of problems by quantum computation. *Proceedings of the royal society*, 439(1907):553–558, 1907.

[17] David P. DiVincenzo. The physical implementation of quantum computation. *Fortschritte der Physik*, 48(9-11):771–783, 2000.

[18] D. Deutsch. Quantum computational networks. *Proc. R. Soc. Lond. A*, 425, 1989.

[19] J. Clarke and F. K. Wilhelm. Superconducting quantum bits. *Nature*, 451:1031, 2008.

[20] P. Kok, W. J. Munro, K. Nemoto, T. C. Ralph, J. P. Dowling, and G. J. Milburn. Linear optical quantum computing with photonic qubits. *Rev. Mod. Phys.*, 79:135–174, 2007.

[21] Rainer Blatt and David Wineland. Entangled states of trapped atomic ions. *Nature*, 453:1008–1015, June 2008.

[22] I. Bloch. Quantum coherence and entanglement with ultracold atoms in optical lattices. *Nature*, 453:1016, 2008.

[23] Advanced Research and Development Activity (ARDA). A quantum information science and technology roadmap. 2004.

[24] M. Acton, K. A. Brickman, P. C. Haljan, P. J. Lee, L. Deslauriers, and C. Monroe. Near-perfect simultaneous measurement of a qubit register. *Quantum Information and Computation*, 6(6):465–482, 2006.

[25] T. P. Harty, D. T. C. Allcock, C. J. Ballance, L. Guidoni, H. A. Janacek, N. M. Linke, D. N. Stacey, and D. M. Lucas. High-fidelity preparation, gates, memory and readout of a trapped-ion quantum bit. *arXiv:1403.1524*, 2014.

[26] F. Schmidt-Kaler, S. Gulde, M. Riebe, T. Deuschle, A. Kr euter, G. Lancaster, C. Becher, J. Eschner, H. H Ìˆaffner, and R. Blatt. The coherence of qubits based on single ca ions. *J. Phys. B: At. Mol. Opt. Phys.*, 36:623, 2003.

[27] D. Leibfried, B. DeMarco, V. Meyer, D. Lucas, M. Barrett, J. Britton, W. M. Itano, B. Jelenkovic, C. Langer, T. Rosenband, and D. J. Wineland. Experimental demonstration of a robust, high-fidelity geometric two ion-qubit phase gate. *Nature*, 422:412–415, 2003.

[28] P. W. Shor. Fault-tolerant quantum computation. *Proc. 37th Annual Symposium on Foundations of Computer Science, IEEE Computer Society Press*, pages 56–65, 1996.

[29] A. M. Steane. Error correcting codes in quantum theory. *Phys. Rev. Lett.*, 77:793–797, Jul 1996.

[30] Austin G. Fowler, Matteo Mariantoni, John M Martinis, and Andrew N. Cleland. Surface codes: Towards practical large-scale quantum computation. *Phys. Rev. A.*, 86:032324, 2012.

[31] A. H. Myerson, D. J. Szwer, S. C. Webster, D. T. C. Allcock, M. J. Curtis, G. Imreh, J. A. Sherman, D. N. Stacey, A. M. Steane, and D. M. Lucas. High-fidelity readout of trapped-ion qubits. *Phys. Rev. Lett.*, 100:200502, May 2008.

[32] Chr. Wunderlich, Th. Hannemann, T. Koerber, H. Haeffner, Ch. Roos, W. Haensel, R. Blatt, and F. Schmidt-Kaler. Robust state preparation of a single trapped ion by adiabatic passage. *Journal of Modern Optics*, 54:1541–1549, 2007.

[33] S. Olmschenk, K. C. Younge, D. L. Moehring, D. N. Matsukevich, P. Maunz, and C. Monroe. Manipulation and detection of a trapped Yb^+ hyperfine qubit. *Phys. Rev. A*, 76:052314, Nov 2007.

[34] Florian Mintert and Christof Wunderlich. Ion-trap quantum logic using long-wavelength radiation. *Phys. Rev. Lett.*, 87(25):257904, Nov 2001.

[35] Samuel Earnshaw. On the nature of the molecular forces which regulate the constitution of the luminiferous ether. *Trans. Camb. Phil. Soc.*, 7:97–112, 1842.

[36] Marcus D. Hughes, Bjoern Lekitsch, Jiddu A. Broersma, and Winfried K. Hensinger. Microfabricated ion traps. *Contemporary Physics*, 52(6):505–529, 2011.

[37] J. McLoughlin. Development and implementation of an Yb^+ ion trap experiment towards coherent manipulation and entanglement. *Ph.D. thesis, University of Sussex*, 2011.

[38] M. Abramowitz and I. A. Stegun. Handbook of mathematical functions. *Dover Publications*, 1972.

[39] D. J. Berkeland, J. D. Miller, J. C. Bergquist, W. M. Itano, and D. J. Wineland. Minimization of ion micromotion in a paul trap. *Journal of applied physics*, 83, May 1998.

[40] W. Winkworth. A compact rf resonator for cryogenic operation and an electronic setup for compensation of micromotion in ion traps. *Masters thesis, University of Sussex*, 2013.

[41] Chr. Balzer, A. Braun, T. Hannemann, Chr. Paape, M. Ettler, W. Neuhauser, and Chr. Wunderlich. Electrodynamically trapped Yb^+ ions for quantum information processing. *Phys. Rev. A*, 73:041407, Apr 2006.

[42] D. J. Berkeland and M. G. Boshier. Destabilization of dark states and optical spectroscopy in zeeman-degenerate atomic systems. *Phys. Rev. A*, 65:033413, Feb 2002.

[43] J. D. Siverns, L. R. Simkins, S. Weidt, and W. K. Hensinger. On the application of radio frequency voltages to ion traps via helical resonators. *Applied Physics B*, 106, 2012.

[44] A Einstein. On the quantum theory of radiation. *Physikalische Zeitschrift*, 18(p121-128), 1917.

[45] Simon Hooker and Colin Webb. *Laser Physics*. Oxford University Press, 2010.

[46] Yehuda B. Band. *Light and Matter*. Wiley, 2006.

[47] J. A. Jones. Quantum information lecture notes. *University of Oxford*, 2010.

[48] Rachel Noek, Caleb Knoernschild, Justin Migacz, Taehyun Kim, Peter Maunz, True Merrill, Harley Hayden, C.S. Pai, and Jungsang Kim. Multi-scale optics for enhanced light collection from a point source. *Opt. Lett.*, 35(2460), 2010.

[49] G. Shu, N. Kurz, M. R. Dietrich, and B. B. Blinov. Efficient fluorescence collection from trapped ions with an integrated spherical mirror. *Phys. Rev. A*, 81(042321), 2010.

[50] Erik W. Streed1, Benjamin G. Norton1, Andreas Jechow1, Till J. Weinhold, and David Kielpinski1. Imaging of trapped ions with a microfabricated optic for quantum information processing. *Phys. Rev. Lett*, 106(010502), 2011.

[51] J True Merrill1, Curtis Volin, David Landgren, Jason M Amini, Kenneth Wright, S Charles Doret, C-S Pai, Harley Hayden, Tyler Killian, Daniel Faircloth, Kenneth R Brown, Alexa W Harter, and Richart E Slusher. Demonstration of integrated microscale optics in surface-electrode ion traps. *New. J. Phys*, 13(103005), 2011.

[52] Robert Maiwald, Andrea Golla, Martin Fischer, Marianne Bader, Simon Heugel, BenoÃ®t Chalopin, Markus Sondermann, and Gerd Leuchs. Collecting more than half the fluorescence photons from a single ion. *Phys. Rev. A*, 86(043431), 2012.

[53] Rachel Noek, Geert Vrijsen, Daniel Gaultney, Emily Mount, Taehyun Kim, Peter Maunz, and Jungsang Kim. High speed, high fidelity detection of an atomic hyperfine qubit. *arXiv*, (:1304.3511v1), 2013.

[54] Rüdiger Paschotta. *Encyclopedia of Laser Physics and Technology*, volume 1. Wiley, October 2008.

[55] R. Sterling. Ytterbium ion trapping and microfabrication of ion trap arrays. *Ph.D. thesis, University of Sussex*, 2011.

[56] Wolfram. Wolfram mathematica 9 documentation center.

[57] Phidgets Inc. Allan deviation primer. 2012.

[58] Karl Johan Aström and Richard M. Murray. *Feedback Systems:An Introduction for Scientists and Engineers*. Princeton University Press, 2008.

[59] C. J. Foot. Atomic physics. *Oxford University Press, New York*, 2005.

[60] Stanford research systems. Application notes: lock-in amplifiers.

[61] J. I. Cirac and P. Zoller. Quantum computations with cold trapped ions. *Phys. Rev. Lett.*, 74:4091–4094, May 1995.

[62] J Lee, P, K-A Brickman, L Deslauriers, C Haljan, P, L-M Duan, and C Monroe. Phase control of trapped ion quantum gates. *Journal of Optics B*, 7:S371–383, 2005.

[63] Anders Sørensen and Klaus Mølmer. Entanglement and quantum computation with ions in thermal motion. *Phys. Rev. A*, 62(2):022311, Jul 2000.

[64] J.J. Garcia-Ripoll, P. Zoller, and J.I.Cirac. Speed optimized two-qubit gates with laser coherent control techniques for ion trap quantum computing. *Phys. Rev. Lett.*, 91(157901), 2003.

[65] J. I. Cirac and P. Zoller. A scalable quantum computer with ions in an array of microtraps. *Nature*, 404:579–581, 2000.

[66] M. Riebe, K. Kim, P. Schindler, T. Monz, P. O. Schmidt, T. K. Korber, W. Hnsel, H. Haner, C. F. Roos, and R. Blatt. Effective quantum spin systems with trapped ions. *Phys. Rev. Lett.*, 97:220407, 2006.

[67] Ferdinand Schmidt-Kaler, Hartmut Häffner, Mark Riebe, Stephan Gulde, Gavin P. T. Lancaster, Thomas Deutschle, Christoph Becher, Christian F. Roos, Jürgen Eschner, and Rainer Blatt. Realization of the Cirac-Zoller controlled-NOT quantum gate. *Nature*, 422:408–411, 2003.

[68] Anders Sørensen and Klaus Mølmer. Quantum computation with ions in thermal motion. *Phys. Rev. Lett.*, 82:1971–1974, Mar 1999.

[69] F. Carruthers and M. M. Nieto. Coherent states and the forced quantum oscillator. *Am. J. Phys.*, 33:537–544, 1965.

[70] P. J. Lee. Quantum information processing with two trapped cadmium ions. *Ph.D. thesis, University of Maryland*, 2006.

[71] David Tannor. *Introduction to Quantum Mechanics: A Time-dependent Perspective.* University Science Books, 2007.

[72] Klaus Mølmer and Anders Sørensen. Multiparticle entanglement of hot trapped ions. *Phys. Rev. Lett.*, 82:1835–1838, Mar 1999.

[73] E. Jaynes and F. Cummings. Comparison of quantum and semiclassical radiation theories with application to the beam maser. *Proceedings of the IEEE*, 51:89, 1963.

[74] J. Randall. Quantum logic in trapped ions. *MRes project report, Imperial College*, 2012.

[75] Jan Benhelm, Gerhard Kirchmair, Christian F. Roos, and Rainer Blatt. Towards fault-tolerant quantum computing with trapped ions. *Nat. Phys*, 4:463–466, 2008.

[76] R. C. Steele. Optical phase-locked loop using semiconductor laser diodes. *Electron. Lett.*, 19(69), 1983.

[77] Xu Z, Zhang X, Huang K, and Lu X. A digital optical phase-locked loop for diode lasers based on field programmable gate array. *Rev Sci Instrum.*, 83(093104), 2012.

[78] H. R. Telle and H. Li. Phase-locking of laser diodes. *Electron. Lett.*, 26(858), 1990.

[79] D. Hayes, D. N. Matsukevich, P. Maunz, D. Hucul, Q. Quraishi, S. Olmschenk, W. Campbell, J. Mizrahi, C. Senko, and C. Monroe. Entanglement of atomic qubits using an optical frequency comb. *Phys. Rev. Lett.*, 104, 2010.

[80] G. Breit and I. I. Rabi. Measurement of nuclear spin. *Phys. Rev.*, 38, 1931.

[81] J.R. Schrieffer and P.A. Wolff. Relation between the anderson and kondo hamiltonians. *Phys. Rev*, 149(491), 1966.

[82] B. Lekitsch. Development of microfabricated ion traps for scalable microwave quantum technology. *Ph.D. thesis, University of Sussex*, 2013.

[83] J.J. Garcia-Ripoll, P. Zoller, and J.I.Cirac. Coherent control of trapped ions using off-resonant lasers. *Phys. Rev. A*, 71(062309), 2004.

[84] L.-M. Duan. Scaling ion trap quantum computation through fast quantum gates. *Phys. Rev. Lett.*, 93(100502), 2004.

[85] J. A. Mizrahi. Ultrafast control of spin and motion in trapped ions. *Ph.D. thesis, University of Maryland*, 2013.

[86] N.Rosen and C.Zener. Double stern-gerlach experiment and related collision phenomena. *Phys. Rev. Lett.*, 40:502, 1932.

[87] Gerald F. Thomas. Validity of the rosen-zener conjecture for gaussian-modulated pulses. *Phys. Rev. A*, 27(5):2744–2746, May 1983.

[88] Dong Mao, Xueming Liu, Zhipei Sun, Hua Lu, Dongdong Han, Guoxi Wang, and Fengqiu Wang. Flexible high-repetition-rate ultrafast fiber laser. *Scientific Reports*, 3:3223, 2013.

[89] H. C. Nagerl, D. Leibfried, H. Rohde, Thalhammer, J. Eschner, F. Schmidt-Kaler, and R. Blatt. Laser addressing of individual ions in a linear paul trap. *Phys. Rev. A*, 60, July 1999.

[90] A. Steane, C. F. Roos, D. Stevens, A. Mundt, D. Leibfried, F. Schmidt-Kaler, and R. Blatt. Speed of ion-trap quantum-information processors. *Phys. Rev. A*, 62:042305, 2000.

[91] D. Leibfried. Individual addressing and state readout of trapped ions utilizing rf micromotion. *Phys. Rev. A*, 60, Nov 1999.

[92] Q. A. Turchette, C. S. Wood, B. E. King, C. J. Myatt, D. Leibfried, W. M. Itano, C. Monroe, and D. J. Wineland. Deterministic entanglement of two trapped ions. *Phys. Rev. Lett*, 81, Oct 1998.

[93] D. Kielpinski, C.R. Monroe, and D.J. Wineland. Architecture for a large-scale ion-trap quantum computer. *Nature*, 417:709–711, 2002.

[94] J. Benhelm, G. Kirchmair, C. F. Roos, and R. Blatt. Experimental quantum-information processing with $^{43}Ca^{+}$ ions. *Phys. Rev. A*, 77:062306, 2008.

[95] Ch. Piltz, B. Scharfenberger, A. Khromova, A. F. Varón, and Ch. Wunderlich. Protecting conditional quantum gates by robust dynamical decoupling. *Phys. Rev. Lett.*, 110:200501, May 2013.

[96] N. Timoney, I. Baumgart, M. Johanning, A. F. Varon, M. B. Plenio, A. Retzker, and Ch. Wunderlich. Quantum gates and memory using microwave-dressed states. *Nature*, 476:185–188, 2011.

[97] Bruce Shore. *Manipulating Quantum Structures Using Laser Pulses*. Cambridge University Press, 2011.

[98] J Oreg. Adiabatic following in multilevel systems. *Phys. Rev. A*, 29(2):690–698, Feb 1984.

[99] Roman Krems, Bretislav Friedrich, and William C Stwalley. *Cold Molecules: Theory, Experiment, Applications*. Taylor and Francis group, 2009.

[100] G. S. Vasilev, A. Kuhn, and N. V. Vitanov. Optimum pulse shapes for stimulated raman adiabatic passage. *Phys. Rev. A*, 80:013417, July 2009.

[101] G. K. Woodgate. Elementary atomic structure. *Second Edition*, 2002.

[102] S. C. Webster, S. Weidt, K. Lake, J. J. McLoughlin, and W. K. Hensinger. Simple manipulation of a microwave dressed-state ion qubit. *Phys. Rev.Lett.*, 111:143504, 2013.

[103] Alex Nicol. Iqt summer research placement report. *University of Sussex*, 2012.

[104] J. Randall. Quantum logic in trapped ions. *MRes project report, Imperial College*, 2012.

[105] M. C. Engineering. Samarium cobalt. *http://www.mceproducts.com*.

[106] D.F.V. James. Quantum dynamics of cold trapped ions with application to quantum computation. *Applied Physics B*, 66, 1998.

[107] H. Metcalf and P. Van Der Straten. Laser cooling and trapping. *Springer*, ISBN 9780387987268, 1999.

[108] Rodney Loudon. *The quantum theory of light*. Oxford science publications, 2000.

[109] Q. A. Turchette, Kielpinski, B. E. King, D. Leibfried, D. M. Meekhof, C. J. Myatt, M. A. Rowe, C. A. Sackett, C. S. Wood, W. M. Itano, C. Monroe, and D. J. Wineland. Heating of trapped ions from the quantum ground state. *Phys. Rev. A*, 61(6):063418, May 2000.

[110] B. E. King, C .S. Wood, C .J. Myatt, Q. A. Turchette, D. Leibfried, W. M. Itano, C. Monroe, and D. J. Wineland. Cooling the collective motion of trapped ions to initialize a quantum register. *Phys. Rev. Lett.*, 81:1525–1528, 1998.

[111] J. Home. Entanglement of two trapped-ion spin qubits. *Ph.D. thesis, University of Oxford*, 2006.

[112] Jeff Sauro and James R Lewis. *Quantifying the User Experience: Practical Statistics for User Research*. Elsevier Ltd, 2012.

[113] M Schubert and B Wilhelmi. *Nonlinear Optics and Quantum Electronics*. Wiley, New York, 1986.

Appendix A

Rate equation program

The following is the Mathematica code used to solve the rate equation of $^{171}Yb^{+}$ as described in chapter 3.

Defining variables

Wavelengths and frequencies being applied.

```
λ369 = 369.52604 10^-9;
λ935 = 935.18768 10^-9;
sb369 = 2.1049 10^9;
sb935 = 3.06950 10^9;
eom = 14.747712124 10^9;
```

Intensities of the lasers in terms of I_{sat}.

```
I369 = 0.1;
I935 = 10;
```

Frequencies present at the ion

```
f1 = spl/λ369;
f2 = f1 + sb369;
f3 = f1 - sb369;
f4 = f1 + eom;
f5 = f1 - eom;
f6 = spl/λ935;
f7 = f6 + sb935;
f8 = f6 - sb935;
```

Set the relative fraction of the power within sidebands

fr1 = 1;

fr2 = (1 − fr1)/2;

fr3 = (1 − fr1)/2;

fr4 = 0;

fr5 = 0;

fr6 = 1;

fr7 = (1 − fr6)/2;

fr8 = (1 − fr6)/2;

Set polarisation axis of 369 nm light.

frsm = 1/3;

frp = 1/3;

frsp = 1 − frsm − frp;

Magnetic field present

T=0.00034; dbf=T mu/h;

Defining constants

hbar=1.05457148 10^{-34};

h=hbar 2 π ;

spl=2.99792458 10^{8};

mu=9.274 10^{-24};

Required wavelengths and frequencies

thλ369=369.52604 10^{-9};

thλ935=935.18768 10^{-9};

thsb369=2.1049 10^{9};

thsb935=3.06950 10^{9};

thsb9352=0.862 10^{9};

thmw=12.64 10^{9};

Frequencies which resonate with transitions within $^{171}Yb^{+}$

thf1=spl/ thλ369;

thf2=thf1+thsb369;

thf4=thf1+thmw;

thf6=spl/ thλ935;

thf7=thf6-thsb935;

thf8=thf1+thmw+thsb369;

thf10=thf6-thsb9352;

thf9=thmw;

Defining matrices for state to state transitions

Selection rules: polerisation.

pol = {{0, 0, 0, 0, 0, 0, 0, 0, 0, 0, 0, 0}, {1, 0, 0, 0, 0, 0, 0, 0, 0, 0, 0, 0},
{1, 0, 0, 0, 0, 0, 0, 0, 0, 0, 0, 0}, {1, 0, 0, 0, 0, 0, 0, 0, 0, 0, 0, 0},
{0, frsp, frp, frsm, 0, 0, 0, 0, 0, 0, 0, 0}, {frsm, frp, frsm, 0, 0, 0, 0, 0, 0, 0, 0, 0},
{frp, frsp, 0, frsm, 0, 0, 0, 0, 0, 0, 0, 0}, {frsp,0, frsp, frp, 0, 0, 0, 0, 0, 0, 0, 0},
{0, 0, 0, 0, 0, 0, 0, 0, 0, 0, 0, 0}, {0, 0, 0, 0, 0, 0, 0, 0, 0, 0, 0, 0},
{0, 0, 0, 0, 0, 0, 0, 0, 1, 1, 0, 0}, {0, 0, 0, 0, 0, 0, 0, 0, 1, 0, 0, 0}};

Selection rules:Δ F = 0, $\pm$1, F = 0 -x-> F = 0.

beta = {{0, 1, 1, 1, 0, 1, 1, 1, 0, 0, 1, 0}, {0, 0, 0, 0, 1, 1, 1, 0, 0, 0, 1, 1},
{0, 0, 0, 0, 1, 1, 0, 1, 0, 0, 1, 1}, {0, 0, 0, 0, 1, 0, 1, 1, 0, 0, 1, 1},
{0, 0, 0, 0, 0, 0, 0, 0, 0, 0, 0, 0},{0, 0, 0, 0, 0, 0, 0, 0, 0, 0, 0, 0},
{0, 0, 0, 0, 0, 0, 0, 0, 0, 0, 0, 0}, {0, 0, 0, 0, 0, 0, 0, 0, 0, 0, 0, 0},
{0, 0, 0, 0, 1, 1, 1, 1, 0, 0, 1, 1}, {0, 0, 0, 0, 0, 1, 1, 1, 0, 0, 1, 0},
{0, 0, 0, 0, 0, 0, 0, 0, 0, 0, 0, 0}, {0, 0, 0, 0, 0, 0, 0, 0, 0, 0, 0, 0}};
alpha= {{0, 0, 0, 0, 0, 0, 0, 0, 0, 0, 0, 0}, {1, 0, 0, 0, 0, 0, 0, 0, 0, 0, 0, 0},
{1, 0, 0, 0, 0, 0, 0, 0, 0, 0, 0, 0}, {1, 0, 0, 0, 0, 0, 0, 0, 0, 0, 0, 0},
{0, 1, 1, 1, 0, 0, 0, 0, 0, 0, 0, 0}, {1, 1, 1, 0, 0, 0, 0, 0, 0, 0, 0, 0},
{1, 1, 0, 1, 0, 0, 0, 0, 0, 0, 0, 0}, {1, 0, 1, 1, 0, 0, 0, 0, 0, 0, 0, 0},
{0, 0, 0, 0, 0, 0, 0, 0, 0, 0, 0, 0}, {0, 0, 0, 0, 0, 0, 0, 0, 0, 0, 0, 0},
{0, 0, 0, 0, 0, 0, 0, 0, 1, 1, 0, 0}, {0, 0, 0, 0, 0, 0, 0, 0, 1, 0, 0, 0}};

Branching ratios

dkj={{0,1,1,1,0,0.332,0.332,0.332,0,0,0.2455,0},
{0,0,0,0,0.332,0.332,0.332,0,0,0,0.2455,0.327},
{0,0,0,0,0.332,0.332,0,0.332,0,0,0.2455,0.327},
{0,0,0,0,0.332,0,0.332,0.332,0,0,0.2455,0.327},
{0,0,0,0,0,0,0,0,0,0,0,0},{0,0,0,0,0,0,0,0,0,0,0,0},
{0,0,0,0,0,0,0,0,0,0,0,0},{0,0,0,0,0,0,0,0,0,0,0,0},
{0,0,0,0,0.004,0.002,0.002,0.002,0,0,0.009,0.018},
{0,0,0,0,0,0.002,0.002,0.002,0,0,0.009,0},
{0,0,0,0,0,0,0,0,0,0,0,0},{0,0,0,0,0,0,0,0,0,0,0,0}};

Decay rates

$$\text{decayrate} = \{3.17\ 10^{-8}, 3.17\ 10^{-8}, 3.17\ 10^{-8}, 3.1710^{-8}, 3.17\ 10^{-8},$$
$$(1/\ (8.1210^{-9})), (1/(8.12\ 10^{-9})), (1/(8.12\ 10^{-9})), (1/(8.12\ 10^{-9})),$$
$$(1/(52.7\ 10^{-3})), (1/(52.7\ 10^{-3})), (1/(37.7\ 10^{-9})), (1/(37.7\ 10^{-9}))\};$$

Resonant frequencies

$$\text{res} = \{\{0, \text{thf9}, \text{thf9}, \text{thf9}, 0, \text{thf8} - \text{dbf}, \text{thf8}, \text{thf8} + \text{dbf}, 0, 0, 0, 0\},$$
$$\{0, 0, 0, 0, \text{thf1} + \text{dbf}, \text{thf2}, \text{thf2} + \text{dbf}, 0, 0, 0, 0, 0\},$$
$$\{0, 0, 0, 0, \text{thf1}, \text{thf2} - \text{dbf}, 0, \text{thf2} + \text{dbf}, 0, 0, 0, 0\},$$
$$\{0, 0, 0, 0, \text{thf1} - \text{dbf}, 0, \text{thf2} - \text{dbf}, \text{thf2}, 0, 0, 0, 0\},$$
$$\{0, 0, 0, 0, 0, 0, 0, 0, 0, 0, 0, 0\}, \{0, 0, 0, 0, 0, 0, 0, 0, 0, 0, 0, 0\},$$
$$\{0, 0, 0, 0, 0, 0, 0, 0, 0, 0, 0, 0\}, \{0, 0, 0, 0, 0, 0, 0, 0, 0, 0, 0, 0\},$$
$$\{0, 0, 0, 0, 0, 0, 0, 0, 0, 0, \text{thf10}, \text{thf6}\}, \{0, 0, 0, 0, 0, 0, 0, 0, 0, 0, \text{thf7}, 0\},$$
$$\{0, 0, 0, 0, 0, 0, 0, 0, 0, 0, 0, 0\}, \{0, 0, 0, 0, 0, 0, 0, 0, 0, 0, 0, 0\}\};$$

State populations

$$\text{Npop} = \{\{\text{n1}\}, \{\text{n2}\}, \{\text{n3}\}, \{\text{n4}\}, \{\text{n5}\}, \{\text{n6}\}, \{\text{n7}\}, \{\text{n8}\}, \{\text{n9}\}, \{\text{n10}\}, \{\text{n11}\}, \{\text{n12}\}\};$$

Defining array for fields present at the ion

$$\text{Intensity} = \{\text{I369fr1}, \text{I369fr2}, \text{I369fr3}, \text{I369fr4}, \text{I369fr5}, \text{I935fr6}, \text{I935fr7}, \text{I935fr8}\};$$
$$\text{frequency} = \{\text{f1}, \text{f2}, \text{f3}, \text{f4}, \text{f5}, \text{f6}, \text{f7}, \text{f8}\};$$

Forming the rate equations

```
For[k=1,k<13,k++,
For[ t=1,t<13,t++,
rateeee[k,t]=alpha[[k,t]] pol[[k,t]] decayrate[[k]] decayrate[[k]] decayrate[[k]]
(dkj[[t, k]] + dkj[[k, t]])Sum[Intensity[[i]]/(4ππ((res[[t, k]] + res[[k, t]]) − frequency[[i]])^2
+decayrate[[k]]decayrate[[k]]/4),{i,8}]/4
+alpha[[t,k]]pol[[t,k]] decayrate[[t]] decayrate[[t]] decayrate[[t]] (dkj[[t,k]]+dkj[[k,t]])
Sum[Intensity[[i]]/(4ππ((res[[t, k]] + res[[k, t]]) − frequency[[i]])^2
+decayrate[[t]] decayrate[[t]]/4),{i,8}]/4+beta[[k,t]] decayrate[[t]]dkj[[k,t]]]];

a=MatrixForm[Array[rateeee,{12,12}]];
ar1=Array[rateeee,{12,12}];

For[y=1,y<13,y++,
ar=Total[ar1[[All,y]]]; rateee[y,y]=ar;For[z=1,z¡13,z++,
If[y==z,rateee[y,z]=rateee[y,z],rateee[y,z]=0]]]

b=MatrixForm[Array[rateee,{12,12}]];
ar2=Array[rateee,{12,12}];

For[z = 1, z < 13, z++, For[y = 1, y < 13, y++, ratematrix[y, z] = ar1[[y, z]] − ar2[[y, z]]]]
ar4=Array[ratematrix,{12,12}];
c=MatrixForm[ar4];
```

State evolution

Initial state populations

```
n1 = 0;
n2 = 0;
n3 = 1;
n4 = 0;
n5 = 0;
n6 = 0;
n7 = 0;
n8 = 0;
```

```
n9 = 0;
n10 = 0;
n11 = 0;
n12 = 0;
```

Step size and number of steps

```
dt = 1 10^-6;
num=10000;
```

Forming solution

```
ar5 = MatrixExp[ar4dt];
nb = 0;
For[i = 1, i < num, i++, For[y = 1, y < 13, y++, nb = n1ar5[[y, 1]] + n2ar5[[y, 2]]
+n3ar5[[y, 3]] + n4ar5[[y, 4]] + n5ar5[[y, 5]] + n6ar5[[y, 6]] + n7ar5[[y, 7]] + n8ar5[[y, 8]]
+n9ar5[[y, 9]] + n10ar5[[y, 10]] + n11ar5[[y, 11]] + n12ar5[[y, 12]]; na[i, y] = nb];
n1 = na[i, 1]; n2 = na[i, 2]; n3 = na[i, 3]; n4 = na[i, 4]; n5 = na[i, 5]; n6 = na[i, 6];
n7 = na[i, 7]; n8 = na[i, 8]; n9 = na[i, 9]; n10 = na[i, 10]; n11 = na[i, 11]; n12 = na[i, 12]]
```

Forming arrays of the population of each state over time set by step size and number of steps

```
pop=Array[na,{num-1,12}];
n1b=pop[[All,1]];
n2b=pop[[All,2]];
n3b=pop[[All,3]];
n4b=pop[[All,4]];
n5b=pop[[All,5]];
n6b=pop[[All,6]];
n7b=pop[[All,7]];
n8b=pop[[All,8]];
n9b=pop[[All,9]];
n10b=pop[[All,10]];
n11b=pop[[All,11]];
n12b=pop[[All,12]];
```

Appendix B

Binomial confidence interval

Upon measurement, a qubit in the state

$$|\phi\rangle = a\,|0\rangle + b\,|1\rangle \tag{B.1}$$

will collapse into the $|0\rangle$ or $|1\rangle$ state with probability $|a|^2$ or $|b|^2$ respectively. To determine the absolute values of a and b and thus a qubits final state at the end of an experiment, the experiment is repeated a large number, N, of times. The collapsed state after each repetition is then measured. The average of these measurements, p, will therefore give the ratio of a and b.

The error on p will depend on the value of N and is calculated using a binomial confidence interval [112]. This assumes that each experiment is identical and makes the approximation that the data follows a normal distribution around the averaged value. The error on the calculated value, p, is therefore [112]

$$E(p) = \sqrt{\frac{1}{N}p(1-p)} \tag{B.2}$$

where $p \pm E(p)$ gives a confidence interval equal to one standard deviation (approximately 70 %).

Appendix C

General solution to the two level optical Bloch equations

The following derivation gives the solution to the two level optical Bloch equations given by equations 3.49 and 3.50 in chapter 3,

$$\dot{q}_0 = iq_1\frac{\Omega}{2}e^{i(\Delta t+\phi)} \tag{C.1}$$

$$\dot{q}_1 = iq_0\frac{\Omega}{2}e^{-i(\Delta t+\phi)} \tag{C.2}$$

This derivation is based on that found in [1]. Differentiating equation C.1 with respect to time gives

$$\ddot{q}_0 = i\dot{q}_1\frac{\Omega}{2}e^{i(\Delta t+\phi)} - q_1\frac{\Delta\Omega}{2}e^{i(\Delta t+\phi)} \tag{C.3}$$

Substituting in equations C.1 and C.2 gives the following second order differential equation,

$$\ddot{q}_0 + i\dot{q}_0\Delta + q_0\left(\frac{\Omega}{2}\right)^2 = 0 \tag{C.4}$$

The general solution to a second order differential equation is given by

$$q_0 = ae^{\alpha_- t} + be^{\alpha_+ t} \tag{C.5}$$

where a and b are constants which depend on the initial conditions and $\alpha_\pm$ are roots of equation C.4 given by,

$$\alpha_\pm = \frac{-i\Delta \pm i\sqrt{\Delta^2+\Omega^2}}{2} \tag{C.6}$$

q_1 can then be found by substituting equation C.5 into equation C.1,

$$q_1 = -2\frac{i}{\Omega}\frac{a\alpha_- e^{\alpha_- t} + b\alpha_+ e^{\alpha_+ t}}{e^{i(\Delta t+\phi)}}. \tag{C.7}$$

For the moment, we will assume the ion is initially in the $|0\rangle$ state (where $q_0 = 1$ and $q_1 = 0$ when $t = 0$). The constants a and b can be found by simultaneously solving equations C.5 and C.7 at $t = 0$. This gives,

$$\begin{aligned} a &= -\frac{\alpha_+}{\alpha_- - \alpha_+}, \\ b &= \frac{\alpha_-}{\alpha_- - \alpha_+} \end{aligned} \tag{C.8}$$

The solution to the Bloch equations when the ion is initially in $|0\rangle$ is therefore equal to

$$q_0 = -\frac{\alpha_+}{\alpha_- - \alpha_+}e^{\alpha_- t} + \frac{\alpha_-}{\alpha_- - \alpha_+}e^{\alpha_+ t} \tag{C.9}$$

and

$$q_1 = -2\frac{i}{\Omega}e^{-i(\Delta t+\phi)}\frac{\alpha_+\alpha_-}{\alpha_- - \alpha_+}(e^{\alpha_+ t} - e^{\alpha_- t}) \tag{C.10}$$

which can be expanded and then simplified using equation C.6 to give,

$$q_0 = e^{\frac{i\Delta t}{2}}\left(\cos\left(0.5t\sqrt{\Delta^2+\Omega^2}\right) - \frac{\Delta i}{\sqrt{\Delta^2+\Omega^2}}\sin\left(0.5t\sqrt{\Delta^2+\Omega^2}\right)\right) \tag{C.11}$$

and

$$q_1 = \frac{i\Omega}{\sqrt{\Delta^2+\Omega^2}}e^{-\frac{i\Delta t}{2}}e^{-i\phi}\sin\left(0.5t\sqrt{\Delta^2+\Omega^2}\right). \tag{C.12}$$

The solutions to the Bloch equations when the ion is initially in the $|1\rangle$ state (where $q_0 = 0$ and $q_1 = 1$ when $t = 0$)are found in a similar way and are equal to,

$$q_0' = \frac{i\Omega}{\sqrt{\Delta^2+\Omega^2}}e^{\frac{i\Delta t}{2}}e^{i\phi}\sin\left(0.5t\sqrt{\Delta^2+\Omega^2}\right) \tag{C.13}$$

and

$$q_1' = e^{-\frac{i\Delta t}{2}}\left(\cos\left(0.5t\sqrt{\Delta^2+\Omega^2}\right) + \frac{\Delta i}{\sqrt{\Delta^2+\Omega^2}}\sin\left(0.5t\sqrt{\Delta^2+\Omega^2}\right)\right). \tag{C.14}$$

An ion initially in the superposition state, $|\psi\rangle = n|0\rangle + m|1\rangle$, will therefore evolve in time

according the following equation

$$|\psi(t)\rangle = \begin{pmatrix} q_0 & q_1 \\ q_0' & q_1' \end{pmatrix} \begin{pmatrix} n \\ m \end{pmatrix}. \tag{C.15}$$

These equations describe oscillations between $|0\rangle$ and $|1\rangle$ with a frequency equal to $\sqrt{\Delta^2 + \Omega^2}$, These are known as Rabi oscillations.

Increasing the detuning will increase the Rabi frequency however, the amplitude of the Rabi oscillations is proportional to $\frac{\Omega}{\sqrt{\Delta^2+\Omega^2}}$, therefore as the detuning is increased, the amplitude of the Rabi oscillations will decrease.

Appendix D

Motional states

The motion of an ion trapped within a potential well is quantised into a series of motional energy levels. These are known as Fock states and are discussed in section D.1. The application of a oscillating force to the trapped ion results in the production of coherent states. These are linear superpositions of Fock states and are discussed in section D.2.

D.1 Fock states

A ion trapped within a potential well can be approximated to a quantum harmonic oscillator. This has the Hamiltonian

$$\hat{H} = \hbar v \left(a^{\dagger} a + \frac{1}{2} \right) \tag{D.1}$$

where $a^{\dagger}$ and a are the creation and annihilation operators respectively. The energy eigenvalues of such a system are equal to

$$\hat{E} = \hbar v \left(n + \frac{1}{2} \right) \tag{D.2}$$

where the corresponding eigenstates are given by $|n\rangle$ where n is an integer. These are known as Fock states and are shown in figure D.1.

The application of creation and annihilation operators to Fock states result in movement between states

$$a^{\dagger} |n\rangle = \sqrt{n+1} \, |n+1\rangle \tag{D.3}$$

$$a \, |n\rangle = \sqrt{n} \, |n-1\rangle \tag{D.4}$$

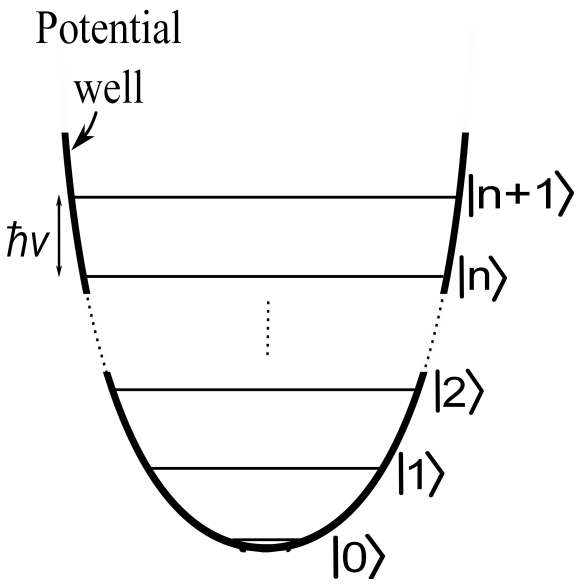

Figure D.1: Diagram showing the Fock states of an ion trapped within a potential well.

and as a result any Fock state can be written in terms of the motional ground state as follows

$$|n\rangle = \frac{1}{\sqrt{n!}}(a^\dagger)^n |0\rangle . \tag{D.5}$$

D.2 Coherent states

The motional states of a trapped ion can also be expressed in terms of coherent states. A coherent state, $|\alpha\rangle$, is defined as an eigenstate of $\hat{a}$,

$$\hat{a} |\alpha\rangle = \alpha |\alpha\rangle \tag{D.6}$$

where $\langle\alpha|\alpha\rangle = 1$ and α is a complex number.

It follows that the expectation value for the Fock state of an ion within a coherent state is given by

$$\langle n\rangle = \langle\alpha |\hat{n}| \alpha\rangle \tag{D.7}$$

$$= \langle\alpha|\hat{a}\hat{a}^\dagger|\alpha\rangle \tag{D.8}$$

$$= |\alpha|^2 . \tag{D.9}$$

$|\alpha\rangle$ can be expressed in terms of Fock states as [108]

$$|\alpha\rangle = e^{\frac{-|\alpha|^2}{2}} \sum_{n=0}^{\infty} \frac{\alpha^n}{\sqrt{n!}} |n\rangle . \tag{D.10}$$

Using equation D.5, a coherent state can also be written in terms of the motional ground state as

$$|\alpha\rangle = e^{\frac{-|\alpha|^2}{2}} \sum_{n=0}^{\infty} \frac{(\alpha a^\dagger)^n}{n!} |0\rangle \tag{D.11}$$

$$= e^{\alpha \hat{a}^\dagger - \frac{1}{2}|\alpha|^2} |0\rangle . \tag{D.12}$$

Using the Campbel-Baker-Hausdorff relation, [113]

$$e^{\hat{A}+\hat{B}} = e^{\hat{A}} e^{\hat{B}} e^{[\hat{A}\hat{B}]/2}, \tag{D.13}$$

where $\hat{A}$ and $\hat{B}$ are operators which satisfy the condition $\left[\hat{A}\left[\hat{A},\hat{B}\right]\right] = 0$, equation D.12 can be rewritten as [108]

$$|\alpha\rangle = e^{\alpha \hat{a}^\dagger - \alpha^* \hat{a}} |0\rangle . \tag{D.14}$$

A coherent state, $|\alpha\rangle$, can therefore be thought of as being the result of applying the displacement operator, $D(\alpha)$, to the motional ground state where $D(\alpha)$ is given by

$$D(\alpha) = e^{\alpha \hat{a}^\dagger - \alpha^* \hat{a}}. \tag{D.15}$$

The displacement operator can be produced by applying a force to a trapped ion, this is explored in chapter 5.

D.2.1 Phase space

The dynamics of coherent states are often visualised by plotting α on an Argand diagram as shown in figure D.2. The expectation values of the position and momentum of a coherent motional state are equal to the real and imaginary parts of α respectively [108].

$$Re(\alpha) = \langle x \rangle \tag{D.16}$$

$$Im(\alpha) = \langle p \rangle \tag{D.17}$$

The application of the displacement operator to $\hat{a}$ results in the addition of a displacement,

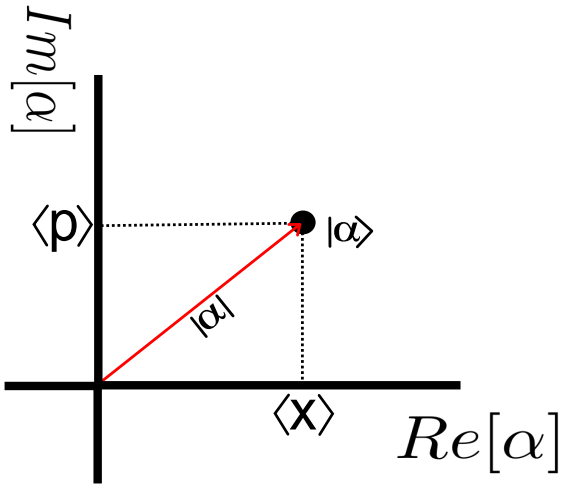

Figure D.2: The position of a coherent motional state can be represented using an Argand diagram. This is also known as the phase space picture and is often viewed in interaction picture with respect to the ions secular motion.

α [108],

$$\hat{D}^{\dagger}(\alpha)\hat{a}\hat{D}(\alpha) = \hat{a} + \alpha. \tag{D.18}$$

This means that the application of $D(\beta)$ to a coherent state, $|\alpha\rangle$, which is an eigenstate of $\hat{a}$, results in a displacement of the coherent state in phase space by β. This is shown in figure D.3. In addition to this displacement, the coherent state will gain a phase, $e^{\alpha\beta^* - \alpha^*\beta}$. This phase is the key to the production of a geometric phase gate as explored in chapter 5.

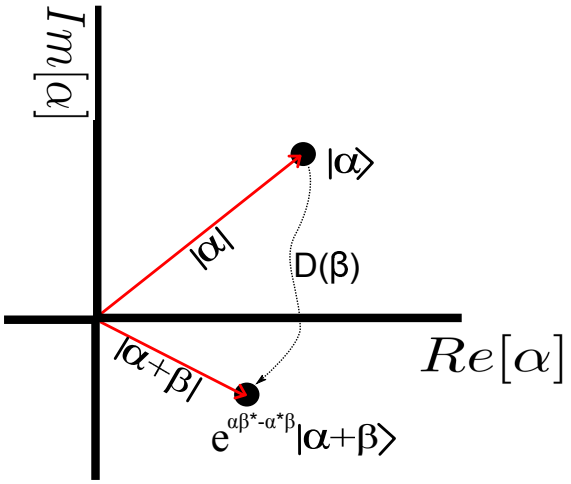

Figure D.3: Displacement in phase space of a coherent state, $|\alpha\rangle$, after application of a displacement operator $D(\beta)$.